A Hundred Times Sharper Than Hubble:

Stellar Imaging with Intensity Interferometry

Hannes Jensen

Lund Observatory
Lund University

2010-EXA41

Degree project of 60 higher education credits (for a degree of Master)
June 2010

Lund Observatory
Box 43
SE-221 00 Lund
Sweden

Abstract

Imaging of stellar surfaces in visible wavelengths is one of the current frontiers in astronomy. With a few exceptions, stars can not be seen in visible light as anything but point objects with current technology. Being able to properly image stars would open up the door to a vast field of new discoveries, permitting direct studies of phenomena such as rotationally deformed stars, circumstellar disks and clouds, stellar winds and wind collision zones, mass accretion structures, pulsating stars etc.

Ground based phase interferometers have been able to produce images of a few large stars in infrared light by connecting several telescopes over distances of ∼100 m, but are limited by the need to keep the optical path constant down to a fraction of the wavelength of the light over very large distances. Intensity interferometry works around these problems by measuring correlations in light intensity fluctuations, essentially removing the need for high-quality optics and making the system virtually immune to atmospheric disturbances, permitting the connection of a great number telescopes to form one giant kilometer-scale hypertelescope. This comes at the cost of higher light intensity requirements and the loss of the phase of the Fourier transform of the stellar surface brightness.

Invented in the 1940's by Robert Hanbury Brown, intensity interferometry has not been used in astronomy since the 1970's (though the physical principle behind it has become very important in particle physics), due to the requirement for very large flux collectors and fast photo-detectors. However, recent technological advances and new mathematical algorithms for image reconstruction have sparked a renewed interest in this technique.

A "digital revival" of intensity interferometry would enable visible-light imaging of stellar objects at resolutions that are orders of magnitude better than what is possible today or in the foreseeable future. An interesting possibility is to use air Cherenkov telescopes – which happen to share many requirements with intensity interferometry.

In this thesis, the theory and history behind intensity interferometry are laid out and a number of astrophysically interesting targets of study are identified. A new method for simulating intensity interferometry measurements, valid for modern photon-counting detectors, is derived and implemented as a simulation software package. It is also shown how this method can be extended to higher-order correlations. The simulation software is applied to a number of astronomical objects with extra attention given to the use of the upcoming European mega-project CTA (Cherenkov Telescope Array) as an intensity interferometer. Finally, the results from laboratory experiments at Lund Observatory are presented.

Populärvetenskaplig sammanfattning

Trots att det gått mer än 400 år sedan teleskopet uppfanns är det fortfarande praktiskt taget omöjligt att avbilda stjärnor som annat än punktobjekt med dagens teknik. De flesta stjärnor som är synliga på natthimlen har en vinkelstorlek på omkring 1 millibågsekund (en 3600000-dels grad), vilket på ett ungefär motsvarar en ärta i Paris sedd från Lund.

För att avbilda ytstrukturer på så otroligt små objekt krävs att man kopplar samman flera teleskop över stora avstånd genom s.k. interferometri. Dagens interferometrar är dock tekniskt mycket komplicerade och fungerar i praktiken bara i infrarött ljus och med (i sammanhanget) relativt korta teleskopavstånd.

En alternativ (eller kanske snarare kompletterande) teknik, intensitetsinterferometri, utnyttjar ljusets kvantmekaniska egenskaper för att ta sig runt de tekniska svårigheterna hos vanlig interferometri. Med denna teknik – som nu håller på att återupplivas med modern utrustning, efter att inte ha använts inom astronomi på flera decennier p.g.a. de höga krav som ställs på bl.a. snabba ljus-detektorer och stora teleskop – är det möjligt att koppla ihop hundratals teleskop till ett enda kilometerstort hyperteleskop.

En sådan kilometerstor intensitetsinterferometer skulle ge en bildskärpa hundratals gånger bättre än dagens största teleskop och skulle kunna avbilda en lång rad fenomen som tidigare endast kunnat studeras indirekt, exempelvis snabbt roterande, deformerade stjärnor, cirkumstellära skivor och gasmoln, kolliderande stjärnvindar, pulserande stjärnor etc.

I det här examensarbetet ger jag en översikt av teorin bakom intensitetsinterferometri och de vetenskapliga möjligheter som tekniken medför. Jag presenterar ett datorprogram för simuleringar av intensitetsinterferometriska mätningar av stjärnor och använder detta för att simulera mätningar och avbildningar av ett antal astronomiska objekt. En studie gällande möjligheterna att använda det planerade europeiska jätteprojektet CTA (Cherenkov Telescope Array, ett instrument primärt för detektion av kosmisk gammastrålning) för intensitetsinterferometri presenteras också. Slutligen jämförs de teoretiska resultaten med resultat från laboratorie-experiment utförda i Lund.

Acknowledgements

First and foremost I would like to thank Dainis Dravins for being an excellent supervisor. He has been incredibly helpful and supportive.

I would also like to thank everyone working with intensity inteferometry at the University of Utah. I am especially thankful to Paul Nuñez for letting me use his image reconstruction software and for answering all my questions regarding it.

Finally, I would like to thank everyone at Lund Observatory, especially the other Master students for making this an enjoyable time. Thanks also to David Hobbs for proof-reading this thesis, and to Torbjörn Wiesel and Nels Hansson for helping out in the lab.

Contents

Nomenclature

Most of the abbreviations and symbols used in the text are described here.

Symbols

τ_c	The coherence time of light
l_c	The coherence length of light
V	The visibility of interference fringes
$\Gamma_{12}(\tau)$	The mutual coherence function of light at points 1 and 2 for time delay τ
$\gamma_{12}(\tau)$	The complex degree of coherence of light at points 1 and 2 for delay time τ
γ_{12}	The complex degree of coherence of light at points 1 and 2 for $\tau = 0$
α	The quantum efficiency of a detector
θ	The angular diameter of a star
x^*	The complex conjugate of x
$\langle x \rangle$	The time average of x

Abbreviations

AGIS	Advanced Gamma-Ray Imaging System
APD	Avalanche Photo Diode
BSC	Bright Star Catalog
CTA	Cherenkov Telescope Array
GA	Genetic Algorithm
HBT effect	Hanbury Brown & Twiss effect
IACT	Imaging Air Cherenkov Telescope
II	Intensity interferometry
mas	Milli-arcseconds
μas	Micro-arcseconds
PMT	Photomultiplier Tube
SII	Stellar intensity interferometry

Chapter 1

Introduction

1.1 The Potential of Intensity Interferometry

Ever since Galileo first pointed his telescope towards the skies 400 years ago, the ability to visually observe and image celestial objects has played an enormously important role in the advance of astronomy as a science. Virtually every significant breakthrough in telescope technology has brought with it not only a better understanding of already known phenomena, but also a range of serendipitous discoveries. Seen from this perspective, it is interesting to note that, with a few exceptions, astronomy – literally the science of stars – is still not able to image stars.

The angular diameter of the bright stars visible in the sky is typically on the order of 1 milliarcsecond (mas) or $4.8 \cdot 10^{-9}$ radians. The Rayleigh criterion tells us that to resolve such a stellar disk at 500 nm under perfect atmospheric conditions, we would need a telescope with a diameter:

$$D = 1.22\frac{\lambda}{\theta} = 1.22\frac{500 \text{ nm}}{4.8 \cdot 10^{-9}} \approx 125 \text{ m}.$$

This is an order of magnitude larger than what exists today, and such a telescope is unlikely to be constructed within the foreseeable future.

However, as we shall see in the following chapters, a revival of intensity interferometry, using digital technology, offers a way around the technical difficulties and promises affordable and feasible stellar imaging down to and even beyond milliarcsecond resolution.

The maximum obtainable resolutions of some of the world's major observatories – both planned and in operation – are shown in different wavelength regions in Fig. 1.1. The red line shows what could be achieved if a telescope array such as the upcoming CTA (Cherenkov Telescope Array) was used for intensity interferometry. It is clear from this figure alone, that this technique represents a step into a completely uncharted region of the wavelength-angular resolution plane.

From stellar simulations and observations we know that we can expect to see a wealth of features if stars could be imaged at mas level. Supergiants like Betelgeuse, which has an angular diameter of around 40 mas, have been (at least partially) resolved by current

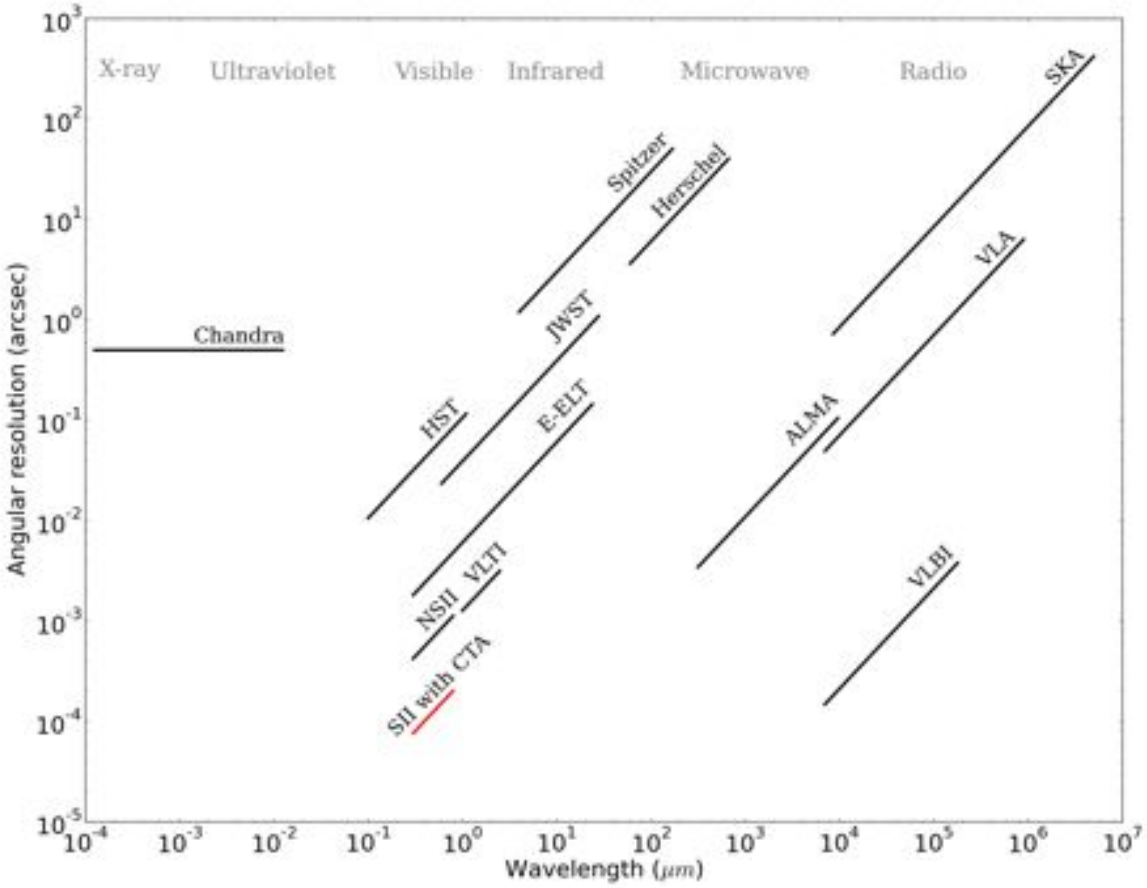

Figure 1.1: Angular resolutions for some existing and future observatories in different wavelength regions. For all instruments except Chandra, the resolutions have been calculated using the Rayleigh criterion – i.e. it is the highest physically obtainable (diffraction-limited) resolution. For VLBI, a baseline corresponding to the diameter of the Earth was assumed.
Legend: HST – Hubble Space Telescope; JWST – James Webb Space Telescope; NSII – Narrabri Stellar Intensity Interferometer; E-ELT – European Extremely Large Telescope; VLTI – Very Large Telescope Interferometer; SKA – Square Kilometer Array; VLA – Very Large Array; ALMA – Atacama Large Millimeter Array; VLBI – Very Long Baseline Interferometry; CTA - Cherenkov Telescope Array.

telescopes and display features drastically different from the Sun. Betelgeuse shows very different diameters for different spectral passbands, and various hot spots on the surface. The hot spots are interpreted as low-density areas in the atmosphere where the hotter interior of the star shines through [1]. All of this tells us that these kinds of supergiants generally do not have a smooth spherical surface like the Sun, but are fuzzy and irregularly shaped.

Stellar models also indicate that rapid rotation will greatly affect the shape and nature of a star. Recent phase interferometry studies of for example Achernar[2] and Altair [3] show a significant rotational flattening of the stars. In some cases the rotation also results in a disk around the star.

Other, more exotic effects are predicted to occur in stars with differential rotation. Such stars might take on a "donut-like" shape [4], but this has yet to be confirmed by observations.

Further targets of study might include pulsating stars, supernova candidates, stars with hot stellar winds and mass transfer in binaries. Since intensity interferometry is especially sensitive to hot targets, it might even be possible to observe exotic objects such as ultra-hot white dwarfs, which can reach temperatures of hundreds of thousands of Kelvin. However, since these stars are extremely faint, this will likely not be feasible with first generation instruments.

Compared to conventional phase interferometry, intensity interferometry has several advantages (and some disadvantages). While phase interferometry is extremely sensitive to atmospheric disturbances and optical imperfections, an intensity interferometer can operate with fairly coarse optics and is virtually immune to atmospheric scintillation effects.

One downside is that the technique requires very large flux collectors and very fast electronics. Also, while a phase interferometer measures a complex quantity called the *visibility* – essentially the Fourier transform of the the target's intensity distribution – an intensity interferometer can only measure the square of this complex quantity, meaning that the phase information from the image is lost. However, as we shall see in the coming chapters, all of these challenges should be possible to overcome, making intensity interferometry a very cost-effective alternative (or complement) to phase interferometry and extremely large telescopes.

Chapter 2

Theory and History of Intensity Interferometry

This chapter covers the basics of the theory behind interferometry in general and intensity interferometry in particular. Since intensity interferometry shares many basic concepts with regular phase interferometry, the basic theory of coherent light and phase interferometry is dealt with first. A full description of the physics behind intensity interferometry requires a quantum-optical approach, which is mostly beyond the scope of this thesis. However, the classical theory presented here will suffice for most basic purposes.

2.1 Coherence of Light

All interferometry experiments rely on a basic property of light called *coherence*. Put simply, the coherence is the degree to which properties of the light such as its phase and amplitude can be predicted in the future (or the past) given knowledge of them at the present. Since coherence is such an important concept, we will start with a slightly more thorough treatment below.

For the sake of simplicity, light waves are often described in basic level physics textbooks as single-frequency plane waves on the form $E(x,t) = \sin(kx - \omega t)$. While sometimes a convenient simplification, this description is not a very realistic one. Real light consists of a superposition of many such monochromatic waves, and in addition it undergoes frequent phase shifts.

A more realistic way of looking at light is as a sum of many individual *wavetrains*, or harmonic pulses of duration Δt, each having the form:

$$E(x) = \begin{cases} E_0 \cos \omega_p t & \text{when } -\Delta t/2 \leq t \leq \Delta t/2 \\ 0 & \text{when } |t| > \Delta t/2 \end{cases} \tag{2.1}$$

Each such pulse is a (quasi-)monochromatic wave extending a certain length in space and time, i.e. a truncated sinusoidal function. The frequency contents of such a pulse is

given by its Fourier transform, which can be shown (e.g. [5]) to be:

$$A(\omega) = E_0 \frac{\Delta t}{2} \operatorname{sinc}\left[(\omega_p - \omega)\Delta t/2\right] \tag{2.2}$$

where $\operatorname{sinc}(x) = \sin(x)/x$.

From Eq. (2.2) it is clear that the longer the pulse, the narrower its Fourier transform, and the smaller its frequency content. In the limit $\Delta t \to \infty$ – a pulse of infinite duration – we get back to the idealized case of a single monochromatic wave.

With this model of light as a series of finite wavetrains, we can proceed to define a number of useful concepts. The average time that a wavetrain exists, τ_c, is called the *coherence time* of the light. Within a time interval smaller than the coherence time, the light is roughly sinusoidal and both the phase and the amplitude are predictable. In other words, if we know the phase at some time t, we can calculate it at a time t' as long as $t' - t$ is at most about the same as τ_c. However, if $t' > t + \tau_c$, we can not say anything about the phase at t'

The spatial equivalent of the coherence time is called the *coherence length*, $l_c = c\tau_c$. This is just the spatial extent of the average wavetrain.

The coherence time can be approximated as the inverse of the frequency bandwidth $\Delta\nu$, which is the width of Eq. (2.2). Thus, the ideal monochromatic light wave, having $\Delta\nu = 0$, will have an infinite coherence time and coherence length, meaning the phase and amplitude is completely predictable at any time and place. Since $\tau_c = \Delta\nu^{-1}$, we may think of the coherence time and length as measures of the spectral purity of the light. The closest one can get (with current technology) to a monochromatic wave is a laser. However, even laser light will have a finite coherence length and time.

2.2 Visibility and Coherence Functions

When (partially) coherent light beams interfere they form alternating dark and light bands known as interference fringes. The interference of the light in all sorts of interference experiments thus gives rise to a varying intensity distribution on the screen. The contrast between the brightest and the darkest parts on the screen is called the *visibility*. This quantity is what is measured directly in a phase interferometer, and – as we shall see – indirectly by an intensity interferometer. Formally, the visibility is defined as:

$$V = \frac{I_{max} - I_{min}}{I_{max} + I_{min}} \tag{2.3}$$

As we can see from Eq. (2.3), the visibility ranges from 0 (no fringes) to 1 (when $I_{min} = 0$). See figure 2.1 for an illustration of varying visibility.

2.2.1 A Look at Young's Double Slit Experiment

There is a fundamental relationship between the visibility and the coherence of light, which will be outlined below (the derivation here is a rough outline of that in [5], and the

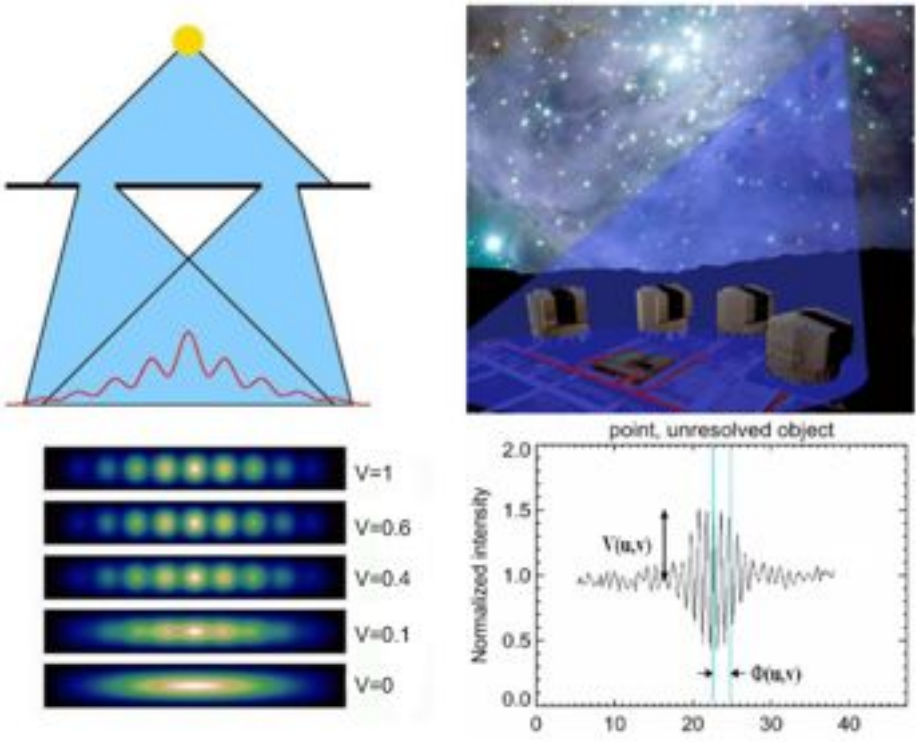

Figure 2.1: Young's double slit experiment (left) as compared to a stellar phase interferometer (exemplified here by the VLTI). In the phase interferometer, the telescopes play the same role as the slits in the double slit experiment. However, instead of simply letting the light pass through to a plane, it is guided to detectors through an elaborate system of mirrors and delay lines. The contrast of the fringes gives the magnitude of the visibility, and their position along the optical path gives the phase. Figure from [6].

reader is referred there for more details). We consider the famous Young's experiment (figure 2.2), where an extended source σ illuminates two small holes S_1 and S_2 in a screen. We will call the light field from σ $E(\mathbf{r}, t)$, and the fields at S_1 and S_2 will be $E_1(t)$ and $E_2(t)$ respectively. The light reaching a point P on the screen is then

$$E_P = K_1 E_1(t - r_1/c) + K_2 E_2(t - r_2/c),$$

where the constants K_1 and K_2 are so-called propagators, depending on the sizes and locations of the apertures S_1 and S_2.

The intensity at P is then simply the average of the light amplitude times its complex conjugate averaged over some time interval:

$$I = \langle E_P(t) E_P^*(t) \rangle, \tag{2.4}$$

where $\langle\rangle$ denotes averaging over time. Since we are assuming that the fields are stationary, i.e. they do not change their statistical nature over time, we may start measuring at any time origin. In other words a term such as $\langle E_1(t - t_1) E_1^*(t - t_1) \rangle$ is equivalent to $\langle E_1(t) E_1^*(t) \rangle$. With this in mind, we may insert the expression for E_P into (2.4) and rewrite it as:

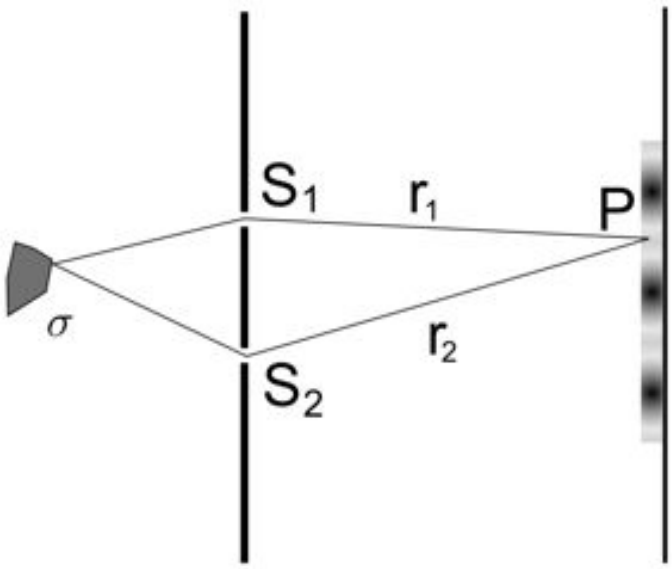

Figure 2.2: Young's double slit experiment.

$$I = K_1K_1^*\langle E_1(t-t_1)E_1^*(t-t_1)+\rangle K_1K_1^*\langle E_2(t-t_2)E_2^*(t-t_2)\rangle + \tag{2.5}$$
$$K_1K_2^*\langle E_1(t-t_1)E_2^*(t-t_2)\rangle + K_2K_1^*\langle E_2(t-t_2)E_1^*(t-t_1)\rangle \tag{2.6}$$
$$= K_1K_1^*I_{S_1} + K_2K_2^*I_{S_2} + 2\mathrm{Re}[K_1K_2^*\langle E_1(t+\tau)E_2^*(t)\rangle]. \tag{2.7}$$

In the last step, the symbols $\tau = t_2 - t_1$ and $I_{S_1} = \langle E_1(t)E_1^*(t)\rangle$, $I_{S_2} = \langle E_2(t)E_2^*(t)\rangle$ have been introduced. The two last terms are then just a quantity plus its complex conjugate, which is equal to twice its real part.

The time average part in the last term in (2.5) is a cross-correlation between E_1 and E_2. This function is called the *mutual coherence function* of the light at S_1 and S_2, and is denoted:

$$\Gamma_{12}(\tau) = \langle E_1(t+\tau)E_2^*(t)\rangle. \tag{2.8}$$

If we write the cross-correlation out explicitly it becomes:

$$\Gamma_{12}(\tau) = \frac{1}{T}\int_0^T E_1(t+\tau)E_2^*(t)\,\mathrm{d}t.$$

Note here that if $E_1(t+\tau)$ and $E_2(t)$ do not depend on each other in any way, the integral will tend to zero as the integration time increases. However, if they vary in more or less the same way, i.e. they are both large at the same time and small at the same time, the integral will not be zero. So a cross-correlation will be a measure on how similar one function is to another shifted by a time τ.

Now, making use of the fact that the K factors are purely imaginary and setting $I_1 = |K_1|^2 I_{S_1}$ and likewise for I_2, we end up with the following for the intensity at P:

$$I = I_1 + I_2 + 2|K_1||K_2|\text{Re}\,\Gamma_{12}(\tau). \tag{2.9}$$

Now consider the special case where S_1 and S_2 are made to coincide. The optical path difference of the two light beams will be zero and the mutual coherence function will be an auto-correlation:

$$\Gamma_{11}(0) = \langle E_1(t)E_1^*(t)\rangle = I_{S_1} \text{ and } \Gamma_{22}(0) = \langle E_2(t)E_2^*(t)\rangle = I_{S_2}$$

From (2.9) we know then that $|K_1|^2 = I_1/\Gamma_{11}(0)$ and similarly for $|K_2|^2$. This gives:

$$|K_1||K_2| = \frac{\sqrt{I_1 I_2}}{\sqrt{\Gamma_{11}(0)\Gamma_{22}(0)}},$$

which makes it convenient to introduce the *complex degree of coherence*, which is the normalized version of the mutual coherence function:

$$\gamma_{12}(\tau) = \frac{\Gamma_{12}(\tau)}{\sqrt{\Gamma_{11}(0)\Gamma_{22}(0)}} = \frac{\langle E_1(t+\tau)E_2^*(t)\rangle}{\sqrt{\langle|E_1|^2\rangle\langle|E_2^2|\rangle}}, \tag{2.10}$$

leading to the final expression for the intensity distribution on the screen:

$$I = I_1 + I_2 + 2\sqrt{I_1 I_2}\text{Re}\,\gamma_{12}(\tau). \tag{2.11}$$

Finally, if we note the fact that γ_{12} is a complex function, and rewrite it as $\gamma_{12}(\tau) = |\gamma_{12}(\tau)|e^{i\Phi_{12}(\tau)}$, for some phase angle Φ_{12}, we see from Eq. (2.11) that

$$I_{max} = I_1 + I_2 + 2\sqrt{I_1 I_2}|\gamma_{12}|$$

and

$$I_{min} = I_1 + I_2 - 2\sqrt{I_1 I_2}|\gamma_{12}|.$$

Thus we can relate the coherence function to the visibility, using (2.3):

$$V = \frac{I_{max} - I_{min}}{I_{max} + I_{min}} = \frac{2\sqrt{I_1 I_2}}{I_1 + I_2}|\gamma_{12}(\tau)|, \tag{2.12}$$

or, if $I_1 = I_2$:

$$V = |\gamma_{12}(\tau)|. \tag{2.13}$$

To sum things up, if we measure the contrast of the interference fringes, i.e. V, we can deduce the coherence function of the light. And as Eq. (2.10) tells us, this says something about the statistical coherence of the two light fields. As we shall see shortly, knowing the coherence function allows us to say a lot about the source, and even reconstruct its intensity distribution.

2.3 Phase Interferometry

2.3.1 The Michelson Stellar Interferometer

The first interferometric device successfully used in astronomy was the Michelson stellar interferometer (or simply Michelson interferometer[1]), conceived in 1890 by A.A. Michelson, and first used in real measurements in the 1920's [7]. The operation of a Michelson interferometer is outlined in Fig. 2.3 and bears many similarities to Young's double slit experiment discussed above.

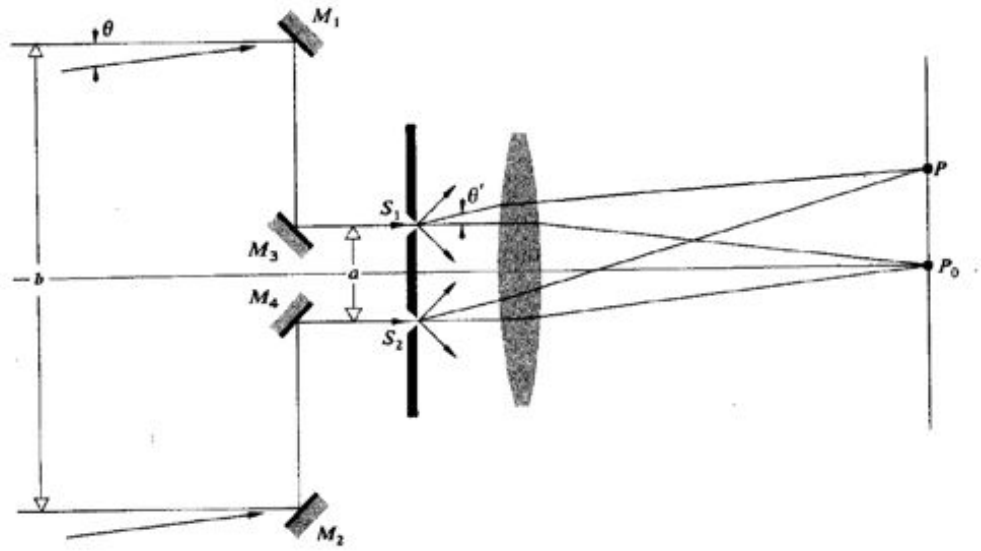

Figure 2.3: Outline of a phase interferometer. Figure from [5].

Instead of simply letting the light pass through two apertures as before, light is now collected into a telescope using two movable mirrors. The light is focused onto a screen, and if the light source is a point source, e.g. a distant star, the intensity on the screen will look like that in Young's experiment, Eq. (2.11).

Now, let's say we observe two nearby point sources, for example a close binary star. If some sort of filter is used, the light will be of narrow-bandwidth, centered around some wavelength λ_0. Light from the first star will go through the interferometer and produce a fringe pattern at a point P_0 on the screen. Light from the other star will come in at a (very small) angle θ to the optical axis and form another fringe pattern at some point P. Because it's slightly off-axis, this light will be delayed by a time approximately equal to $b\theta/c$, which means it will be out of phase by $2\pi b\theta/\lambda_0$.

The two point-sources are completely incoherent, and their respective fringe patterns will simply add up. If the separation between the mirrors, b, is varied, the separation

[1]Usually, the term Michelson interferometer refers to a different instrument from the same inventor, used to measure the effects of the Earth's motion on the speed of light. Here however, we shall use the term to denote Michelson's stellar interferometer.

between P and P_0 will vary. If the light from star 1 comes in along the optical axis it will have a fringe maximum at the center of the screen. If the mirror separation is increased until the phase difference is π, the pattern from star 2 will have a minimum at the center and the two patterns will cancel each other out, bringing the visibility to a minimum. If the intensities of the two stars are equal, V will be zero. This all happens when $2\pi b\theta/\lambda_0 = \pi$, or

$$b = \frac{\lambda_0}{2\theta} \;\Rightarrow\; \theta = \frac{\lambda_0}{2b}. \tag{2.14}$$

So, by starting at a very small mirror separation, or *baseline*, b, and gradually increasing it until the first visibility minimum occurs, one can measure angular separation with great accuracy using a Michelson interferometer. Notice here that the two point sources are completely incoherent and are not interfering with each other. What we are measuring is just the sum of the two *individual* interference patters.

If the light source is not just two points, but rather an extended source, such as a stellar disk, the visibility can be found by treating the source as consisting of many small point sources. For a circular source of uniform intensity, it can be shown (e.g. [5]) that the visibility takes the form:

$$V = |\gamma_{12}(0)| = 2\left|\frac{J_1(\pi b\theta/\lambda_0)}{\pi b\theta/\lambda_0}\right|, \tag{2.15}$$

where J_1 is the Bessel function of first order (V is plotted in Fig. 2.4). This function has its first zero at $\pi b\theta/\lambda_0 = 3.83$, meaning that the fringes will disappear when

$$b = 1.22\frac{\lambda_0}{\theta}.$$

This equation looks very similar to the familiar Rayleigh criterion, which gives the resolution of a telescope as a function of wavelength and telescope diameter. This means that the resolution of a Michelson interferometer with baseline b is $1.22\lambda_0/b$ – the same as a telescope of diameter b. In other words, an interferometer with baseline b will have the same resolution as a telescope with a diameter equal to the separation of the interferometer mirrors!

2.3.2 The van Cittert-Zernike Theorem

The Michelson interferometer described above works best if the target is about the same size as the resolution of the interferometer. If the target is very small or very large, no useful information will be gained. However, the baseline can be varied so that the resolution matches the size of the target. Thus, one might suspect that by combining measurements from interferometers with different baselines, one might be able to reconstruct information about both large and small scale structures of an extended target. The English radio astronomer Sir Martin Ryle pursued this idea in the 1960's, leading to the development of the technique called *aperture synthesis*, for which he received the 1974 Nobel Prize in physics.

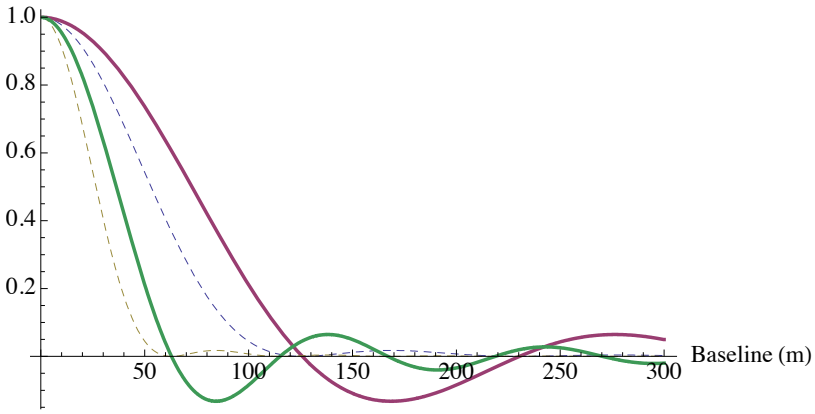

Figure 2.4: Visibility (solid lines) and squared visibility (dashed lines) as a function of baseline for light with $\lambda = 500$ nm. Inner curves are for a solid disk of angular size 2 mas, and outer curves are for a disk of size 1 mas.

Consider an electric field $E(\mathbf{R}, t)$ at some point $\mathbf{R}$ in space (we are ignoring polarization effects here). Such a field can be divided into its Fourier components $E_\nu(\mathbf{R})$, so that:

$$E_\nu(\mathbf{r}) = \iiint K_\nu(\mathbf{R}, \mathbf{r}) E_\nu(\mathbf{R})\, \mathrm{d}x\, \mathrm{d}y\, \mathrm{d}z$$

where K is again a propagator, and $\mathbf{r}$ is the position of the observer. Assuming that the source lies on a two-dimensional celestial sphere of radius $R = |\mathbf{R}|$ (R is large), we can simplify this to:

$$E_\nu(\mathbf{r}) = \int_S \mathcal{E}_\nu(\mathbf{R}) \frac{e^{2\pi i \nu |\mathbf{R}-\mathbf{r}|/c}}{|\mathbf{R}-\mathbf{r}|}\, \mathrm{d}S \tag{2.16}$$

where $\mathcal{E}_\nu$ is the surface brightness of the source. The explicit form of the propagator K comes from Huygen's principle and is valid if polarization is ignored and the space between the target and the observer is assumed to be empty (see [8] for details).

We can now relate this to the correlation function $\Gamma_{12} = \langle E_\nu(\mathbf{r}_1) E_\nu^*(\mathbf{r}_2) \rangle$. Inserting Eq. (2.16) into this expression gives:

$$\Gamma_{12} = \Big\langle \iint \mathcal{E}_\nu(\mathbf{R}_1) \mathcal{E}_\nu^*(\mathbf{R}_2) \frac{e^{2\pi i \nu |\mathbf{R_1}-\mathbf{r_1}|/c}}{|\mathbf{R_1}-\mathbf{r_1}|} \frac{e^{2\pi i \nu |\mathbf{R_2}-\mathbf{r_2}|/c}}{|\mathbf{R_2}-\mathbf{r_2}|}\, \mathrm{d}S_1\, \mathrm{d}S_2 \Big\rangle. \tag{2.17}$$

Taking $\mathbf{s} = \mathbf{R}/R$ and the observed intensity $I_\nu = R^2 \langle |\mathcal{E}(\mathbf{s})|^2 \rangle$ and assuming that the source is spatially incoherent, i.e. $\langle \mathcal{E}_\nu(\mathbf{R}_1) \mathcal{E}_\nu^*(\mathbf{R}_2) \rangle = 0$ if $\mathbf{R}_1 \neq \mathbf{R}_2$, this last equation can be simplified with some manipulation (again, see[8] for details):

$$\Gamma_{12} \approx \int I_\nu(\mathbf{s}) e^{-2\pi i \nu \mathbf{s} \cdot (\mathbf{r_1}-\mathbf{r_2})/c}\, \mathrm{d}\Omega, \tag{2.18}$$

where $\mathrm{d}\Omega = |\mathbf{R}|^{-2}\, \mathrm{d}S$ is a small angular element.

We now measure the separation $\mathbf{r_1} - \mathbf{r_2}$ in some plane perpendicular to the line of observation, so that $\mathbf{r_1} - \mathbf{r_2} = (u\lambda, v\lambda, 0)$, and use coordinates (l, m) for the (angular)

positions on the target. After some more manipulation, one eventually ends up with the following expression for the correlation:

$$\Gamma(u,v) = \iint I_\nu(l,m) e^{-2\pi i(ul+vm)} \,\mathrm{d}l \,\mathrm{d}m. \tag{2.19}$$

Equation (2.19) is a form of the van Cittert-Zernike theorem, which is the backbone of all interferometric imaging. It tells us that the quantity measured by an interferometer for a given baseline is a component of the Fourier transform of the surface intensity distribution of the source. Note that we can expand the concept of visibility to be a complex quantity, with a magnitude equal to the previous definition, and a phase corresponding to the position of the interference fringes (see Fig. 2.1). Since Eq. (2.19) is a Fourier transform, it can be inverted:

$$I_\nu(l,m) = \iint V(u,v) e^{2\pi i(ul+vm)} \,\mathrm{d}u \,\mathrm{d}v. \tag{2.20}$$

The result is remarkable. By using many different separations and orientations of a single (or – as is more often the case – several) interferometers we can sample the $(u,v)-$plane and reconstruct the source image with a resolution equal to that of a telescope with a diameter of the longest baseline. This is the technique known as aperture synthesis.

2.3.3 Modern Day Phase Interferometry, Possibilities and Limitations

The idea of using interferometry to measure stellar diameter was first suggested by Fizeau in 1868, and carried out by Stephan in 1874, using a mask placed over his 80 cm reflector at Marseille Observatory, effectively turning it into a two-aperture 80 cm-baseline interferometer. He found out, however, that it was impossible to resolve any stars for this small aperture [9]. Instead, Michelson is usually given credit as the first person to perform useful interferometric measurements of astronomical objects. His 6-meter interferometer, described above, operated in the 1920's, mounted on the Hooker telescope on Mt. Wilson, while his later 15-meter instrument proved too unstable to be usable [7].

However, the challenges involved in maintaining the optical path differences during observations and making sure that the entire optical system was accurate down to a fraction of a wavelength of the light proved enormous. Because of this, the technique lay dormant for almost half a century following the pioneer work done by Michelson.

It wasn't until 1975 that Labeyrie succeeded in measuring directly the interference fringes between two different telescopes (as opposed to the two mirrors feeding a single telescope in Michelson's interferometer). His instrument, Interféromètre à Deux Télescopes (I2T) [9] made observations in both visible and near-IR wavelengths during the 1970's and 1980's, and its successor, Grand Interféromètre à Deux Télescopes (GI2T) was in operation until 2006 [10].

Phase interferometry has seen great progress during the last decade, and as of 2006, 9 optical and infrared interferometers were in operation all over the world [11]. Among the

foremost of these is ESO's Very Large Telescope Interferometer (VLTI) at Cerro Paranal in Chile [12]. The VLTI connects the four 8 m main telescopes of the VLT and four 1.8 m Auxiliary Telescopes (AT's) using an elaborate system of delay lines consisting of movable mirrors on rails in underground tunnels. The instrument has been used to measure the shapes of stars (see Sec. 5.4.1), and recently even aperture-synthesized milliarcsecond resolution images in the infrared [13].

The system currently providing the longest operational baselines is the CHARA array on Mount Wilson, consisting of six 1 meter telescopes with a maximum baseline of 330 m. Figure 2.6 shows an example of the extremely high resolution images possible with this array.

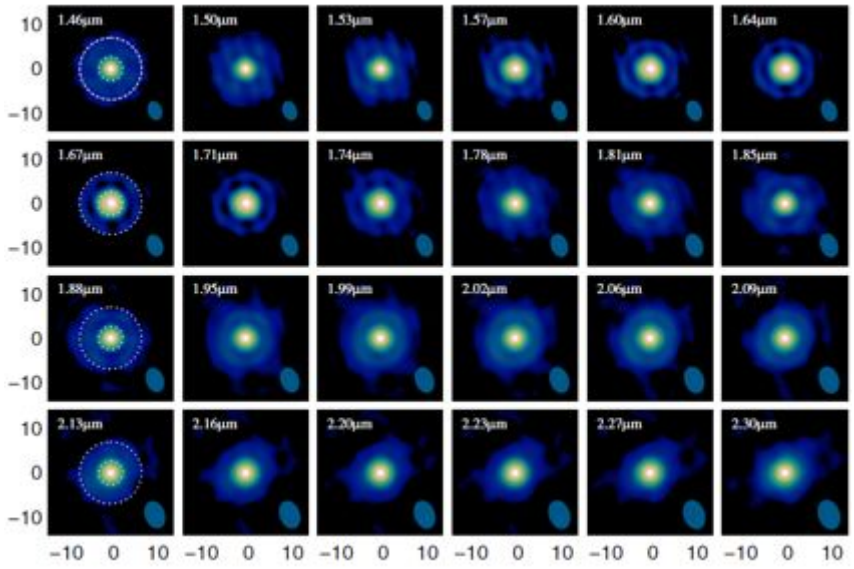

Figure 2.5: These reconstructed images of the Mira variable T Leporis obtained with the VLTI at different wavelengths are an example of current state-of-the-art stellar imaging. The star is imaged in infrared light, revealing molecular clouds surrounding the star. The scale is in mas. Figure from [13].

Despite this recent progress within phase interferometry, there are still some inherent difficulties with the technique when it comes to shorter wavelengths. The entire system – telescopes, delay lines and instrumentation – needs to be perfect down to a fraction of a wavelength. Even vibrations of a single micrometer can ruin measurements in visible light. This puts enormous demands on high quality mirrors, top-notch adaptive optics systems and extremely high-precision delay lines. Thus, even state-of-the-art systems like the VLTI cannot conduct measurements like the one in Fig. 2.5 using visible light.

As we shall see, intensity interferometry eliminates many of the difficulties with phase interferometry, and might soon fill the niche of ultra-high-resolution imaging of hot and bright stars in visible wavelengths.

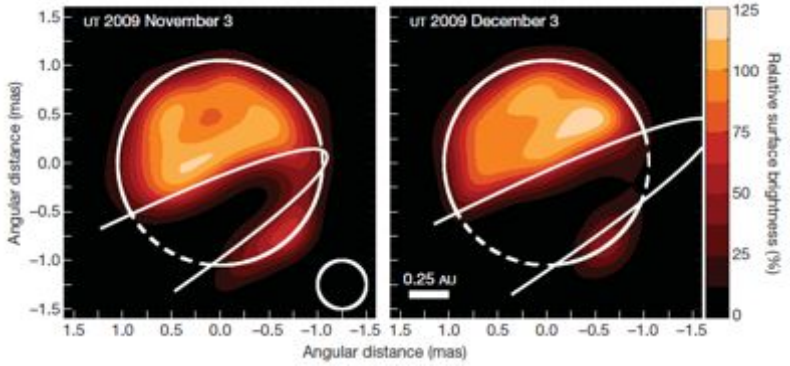

Figure 2.6: Aperture synthesized infrared images produced with the CHARA array showing the obscuring circumstellar disk of ϵ Aurigae. Note the angular scale! Figure from [14].

2.4 Intensity Interferometry

2.4.1 Hanbury Brown and the Narrabri Interferometer

As we saw in the previous section, phase interferometry can produce some fantastic scientific results, but it quickly becomes an extremely expensive and technically demanding technique when long baselines are required. This problem was addressed by Robert Hanbury Brown in 1949 [2]. As he was pondering over how to measure the angular sizes of the radio sources Cassiopeia A and Cygnus A (which were not resolvable by phase interferometers available at the time), he was struck with the basic idea: if the phases of two light beams are correlated, shouldn't there also exist a correlation between the *intensities*? In other words, if two simple square law detectors were brought close to each other and pointed at the same target they should see the same intensity fluctuations. If they are then moved apart, the intensity correlation should decrease, and the rate of decrease will be a measure of the spatial correlation, and thus the angular size of the target.

By using intensity correlations rather than phase interference, Hanbury Brown hoped to simplify the problem of the very precise timing required in long baseline phase interferometry. Together with Richard Twiss, he worked out the underlying mathematics and set out to build a simple radio interferometer. While Cassiopeia A and Cygnus A turned out to be so large that they could actually have been measured using only slight modifications to contemporary phase interferometers ("we had used a sledge-hammer to crack a nut") Hanbury Brown and Twiss soon realized that their invention had some very interesting unforeseen properties. They had noticed that even when there were serious atmospheric disturbances and the radio sources were scintillating violently, the correlations were hardly affected at all. After looking over the mathematics again (see Sec. 2.4.2), Richard Twiss concluded that this was to be expected, and that insensitivity

[2] The entire story behind the invention of intensity interferometry can be found in Hanbury Brown's book *The Intensity Interferometer*[15]

to atmospheric disturbances was actually an inherent property of an intensity interferometer.

This realization sparked the idea of an intensity interferometer working in optical wavelengths. The initial calculations were disappointing however – the telescopes needed to achieve adequate fluxes would need to be larger (and more expensive) than anything that existed at the time, and to top it all off one of them would need to be mobile. It took them half a year to realize that while the telescopes indeed had to be very large, the optical quality was not important. There was no need to form a conventional image – the telescopes needed only to serve as "light-buckets" collecting as much light as possible and focusing it on the detectors. This meant that the whole project could be done on a much smaller budget.

After proving the concept in laboratory experiments (e.g. [16]) and by measuring the angular diameter of Sirius using two World War II searchlights as "telescopes" [17], they proceeded to seek funding for a full-scale optical intensity interferometer.

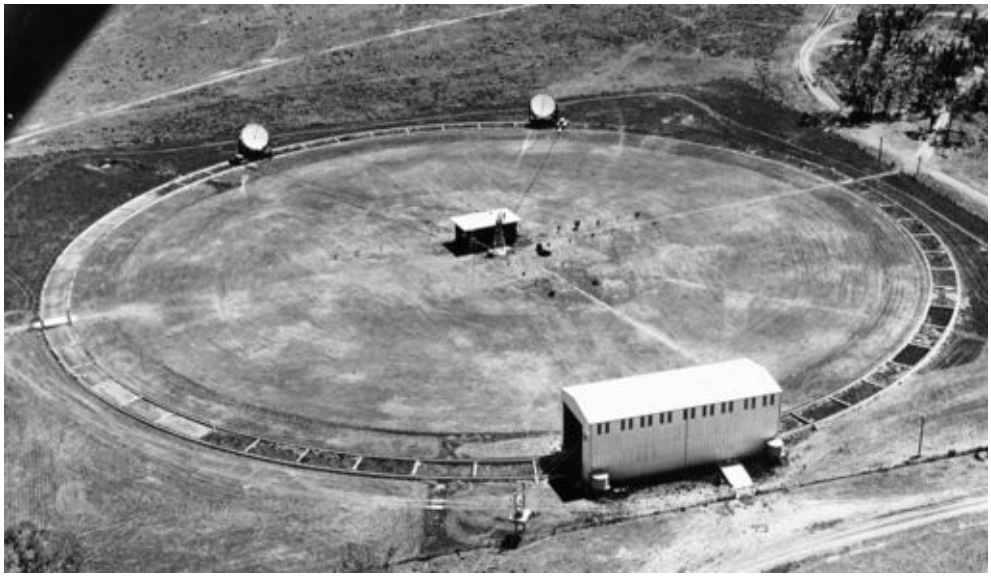

Figure 2.7: View of the Narrabri Stellar Intensity Interferometer showing the two 6.5-meter flux collectors on the circular track. The building in the middle is the control building and the one at the lower part of the picture is the garage for the reflectors. Figure from [15].

The final result was the Narrabri Stellar Intensity Interferometer (NSII), constructed at Narrabri, Australia in the early 1960's. The NSII consisted of two 6.5-meter reflectors, constructed from many smaller hexagonal mirrors, standing on a circular track (188 m diameter) and connected to a central control building. The telescopes were movable on the track, making it possible to vary the baseline. The observatory was operating between 1965 and 1972, measuring the angular diameters of 32 single stars along with other measurements including binary star separations, emission zones around hot stars and the effects of limb-darkening. A detailed description of the results from NSII can be found in [15].

Having done all the measurements that were possible with the flux collectors at Narrabri, planning was started for a successor to the instrument with bigger reflectors and longer baselines [18]. However, it was eventually decided that the new science that could be gained from a better interferometer did not justify the costs involved. To this day, the SII at Narrabri remains the only astronomical intensity interferometer to ever have been in operation doing real science.

2.4.2 Basic Theory of Intensity Interferometry

Intensity Correlations

As mentioned above, the basic idea behind an intensity interferometer is that if light is coherent when it comes to the phase, the amplitude (and thus the intensity) of the light shouldn't be completely random. As it turns out, for quasi-monochromatic thermal light, both the phase and the amplitude are relatively slowly changing functions of time. Typically the light wave will undergo a few tens of thousands of oscillations before there is a phase shift, and the phase shift is generally accompanied by a shift in amplitude. While the amplitude itself is impossible to detect, one should be able to study the changes in intensity and somehow relate these to the coherence of light.

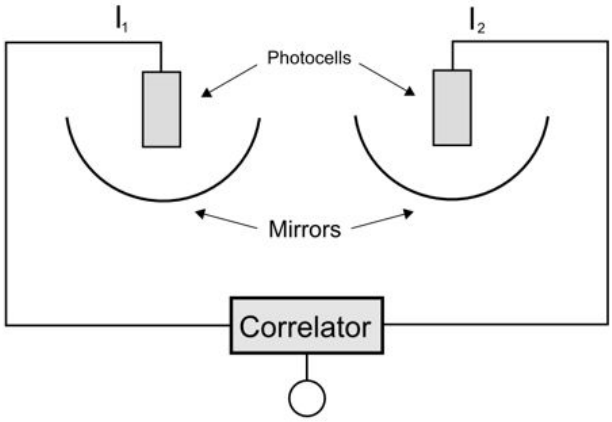

Figure 2.8: The basic components of an intensity interferometer.

In its simplest form an intensity interferometer consists of two flux collectors, each with an attached square-law detector feeding one channel of a correlator (Fig. 2.8). The intensities at detectors 1 and 2 will be:

$$I_1(t) = E_1^*(t)E_1(t) \qquad I_2(t) = E_2^*(t)E_2(t).$$

And the correlation between the intensities will be

$$\langle I_1(t)I_2(t+\tau)\rangle = \langle E_1(t)^*E_1(t)E_2(t)^*E_2(t)\rangle \tag{2.21}$$

Equation (2.21) can be expanded if the complex field amplitudes are divided into their real and imaginary parts. Here we must make an assumption that is fundamental to the operation of an intensity interferometer: that the light is thermal. If the light is thermal, the real and imaginary parts of E_1 and E_2 are Gaussian random variates, i.e. the values of E_1 and E_2 measured at different times can be treated as random variables following a normal distribution. If this is the case, one can use the so-called Gaussian moment theorem, which relates all higher order correlations of Gaussian variates to products of their lower-order correlations (the mathematics of this is described in detail by Mandel [19], and discussed more in chapter 4). It is possible to show then, that:

$$\langle I_1(t+\tau)I_2(t)\rangle = \langle I_1\rangle\langle I_2\rangle + |\Gamma_{12}(\tau)|^2, \tag{2.22}$$

or

$$\langle I_1(t+\tau)I_2(t)\rangle = \langle I_1\rangle\langle I_2\rangle(1 + |\gamma_{12}|^2). \tag{2.23}$$

If we define the intensity fluctuations ΔI as:

$$\Delta I_1(t) = I_1(t) - \langle I_1\rangle \qquad \text{and} \qquad \Delta I_2(t) = I_2(t) - \langle I_2\rangle,$$

Eq. (2.23) becomes:

$$\langle \Delta I_1(t+\tau)\Delta I_2(t)\rangle = \langle I_1\rangle\langle I_2\rangle|\gamma_{12}(\tau)|^2, \tag{2.24}$$

since $\langle \Delta I\rangle = 0$. It should be noted that we have not taken polarization into account here. As it turns out[5], Eq. (2.24) holds for linearly polarized light. In the case of unpolarized light, a factor $1/2$ enters on the right-hand side of the equation.

Relation to Phase Interferometry

One thing that is notably absent from the previous section about intensity interferometry are interference terms. In fact, an intensity interferometer is not really an interferometer at all – it only measures intensity correlations – and the name was given to illustrate the analogy in usage with phase interferometry. There is however a fundamental relationship to phase interferometry. As Eq. (2.24) shows, we can find the square of the coherence function by measuring the intensity correlations. If we relate this to Eq. (2.13), we get:

$$|V| = |\gamma_{12}(\tau)| = \sqrt{\frac{\langle \Delta I_1(t+\tau)\Delta I_2(t)\rangle}{\langle I_1\rangle\langle I_2\rangle}}. \tag{2.25}$$

So we can actually measure the visibility of the interference fringes without doing any interference experiments. This means that one can use for example (2.14) to determine angular sizes of distant objects with a resolution equal to that of a phase interferometer, as illustrated in Fig. 2.4. One significant advantage of the intensity interferometer is that the intensity fluctuations are virtually unaffected by atmospheric disturbances. While a phase interferometer needs very high quality optics and usually adaptive optics systems and baselines that are kept accurate down to a fraction of the wavelength of the light, intensity interferometry is possible using very crude optics. Generally, irregularities in mirrors and baselines up to a few centimeters can be tolerated.

One major disadvantage is of course that only the modulus of the visibility is measured – the phase information is lost. Since the phase information is needed in the van Cittert-Zernike theorem, one would think that aperture synthesis is impossible. Indeed, that was long thought to be the case, but more recent research has shown that clever mathematical tricks can be utilized to (at least partially) recover the phase information if certain assumptions are made. We shall see more about this in coming sections.

Intensity Interferometry in Practice

The equations above are quite idealized and in a real instrument the situation is obviously quite different. A thorough treatment of noise properties and similar issues in the simple interferometer described above was done by Hanbury Brown (see for example [15], [16]). Parts of this are no longer relevant due to technological advancements (a much more in-depth discussion of the ins-and-outs of more modern components will be given in chapter 3). However, some of the results of Hanbury Brown are still worth taking note of.

The description so far has been a classical one, where light is treated as a wave. Regardless of how one detects the light, the signal will always be discretized by the detectors as it is converted to an electrical current (you either emit a photoelectron or you don't). If the probability of emitting a photoelectron is taken to be proportional to the intensity of the light, the current in a detector will be:

$$i(t) = \alpha e I(t),$$

where e is the charge of an electron and α is the quantum efficiency of the detector. The noise in the detector can be divided into two principal components: the *wave noise* and the *shot noise*. The wave noise is due to fluctuations in the classical wave and the shot noise is due to the discretization in the detector and the randomness in emission of photoelectrons. It should be noted that the wave noise is a property of the incoming light, whereas the shot noise arises in the detectors. Thus the wave noise will be correlated while the shot noise will not.

Furthermore, a photodetector can never detect any "true" instantaneous value of the intensity – due to finite response times and the discrete nature of light itself the measured quantity will always be a time average over some time T. As it turns out, this will reduce the correlation by a factor τ_c/T, where τ_c is the coherence time of the light. It can be shown [15] that the correlations between the two photocurrents can be written:

$$\bar{c}(d) = \langle \Delta i_1 \Delta i_2 \rangle = \alpha^2 A^2 e^2 n^2 |\gamma_d(0)|^2 (\Delta f / \Delta \nu), \tag{2.26}$$

where $\bar{c}(d)$ is the time average of the correlation at baseline d; Δf is the electrical bandwidth of the detector; $\Delta\nu$ is the spectral bandwidth of the light; A is the area of the detectors and n is the intensity in number of photons per seconds. This expression is valid for the type of detectors used at Narrabri. For digital photon-counting detectors the noise properties will be a little different, but the general picture is the same.

If the shot noise is assumed to be equally large in both detectors it can further be shown that the r.m.s. noise in the output of one detector is:

$$N(T) = \sqrt{2} e^2 A \alpha n \Delta\nu \sqrt{\Delta f / T}$$

which gives the following expression for the signal-to-noise ratio of the instrument:

$$(S/N)_{rms} = \frac{\bar{c}(d)T}{N(T)} = A\alpha n|\gamma_d(0)|^2(\Delta f T/2)^{1/2}. \tag{2.27}$$

An interesting thing to note here is that the spectral bandwidth $\Delta\nu$ vanished from the signal-to-noise ratio. Making the spectral filter narrower gives less light so one might expect a lower signal. However, squeezing the bandwidth together produces more spectrally pure light with a longer coherence time which compensates for the lower intensity. As we shall see later on, this provides some interesting scientific opportunities.

Also worth considering is what happens if one of the detectors in Fig. 2.8 is moved a small distance $x < \lambda$. This will induce a phase-shift $\Phi = 2\pi x/\lambda$ in the light reaching that detector. From Eq. (2.26) we see that the measured correlation is proportional to the square of the modulus of the coherence. Now, when the phase shift is introduced, the new coherence function γ_0' will be:

$$\gamma_0'(0) \approx \gamma_0(0)e^{i\Phi}.$$

But since we only measure the modulus of the coherence and $|\gamma_0(0)e^{i\Phi}| = |\gamma_0(0)|$, the correlation will not be affected at all by small path differences like these. It can further be shown that the loss of coherence from longer path differences are on the order of 10^5 times smaller than for a Michelson interferometer. Thus, an intensity interferometer is virtually immune to atmospheric disturbances, and optical imperfections can be big (up to centimeter scales) before they have any significant impact.

Semiclassical Treatment of Photodetection

One of the key points in understanding the relationship between a quantum view of light and the classical description derived above is in the physics of photoelectric detection of light. A semiclassical theory on photoelectric detection is derived by Leonard Mandel in [19], and the reader is referred there for a comprehensive treatment of the subject.

One way of detecting light is by using a photomultiplier, in which electrons are emitted from a cathode through the photoelectric effect. When light impinges on the photomultiplier, there is a probability P that a photoelectron will be emitted:

$$P = \frac{1}{\hbar^2}\left|\int_{t_0}^{t_0+\Delta t}\langle E|\hat{H}_I(t_1)|E_0\rangle\right|^2, \tag{2.28}$$

where $|E\rangle$ and $|E_0\rangle$ are the different energy levels of the electron and $\hat{H}_I(t_1)$ is the interaction energy – a property of the light [19]. If reasonable assumptions are made, it can be shown [19] that for a short measurement interval, Δt, this probability can be approximated as

$$P(t) \approx \alpha I(t)\Delta t, \tag{2.29}$$

where α is a constant depending on the detector properties and I is the light intensity. For two independent detectors this becomes:

$$P(t_1, t_2) = \alpha_1\alpha_2 I_1(t_1)I_2(t_2)\Delta t_1\Delta t_2. \tag{2.30}$$

The details in the physics will vary for different types of detectors, but Eq. (2.29) remains valid. In other words, the probability of detecting a photon within a small time interval in a photon-counting detector is proportional to the intensity of the light (provided Δt is small). But the intensity of the light is proportional to the square of the amplitude of the light's E-vector, which is a wave. Therefore, it is a mistake to regard the light as consisting of separate photons when it is on its way to the detector. The light must be treated as a wave phenomenon before detection, and we see the quantum effects only at the detector when a photo-electron is or is not emitted.

In practice, one is often interested not in the probability of one detection occurring in a very small time interval but rather in the expected number of detections within a larger interval. This number is readily found by simply dividing the detection time into many small intervals and integrating:

$$\langle n \rangle = \alpha \int_t^{t+T} I(t')\,\mathrm{d}t'. \tag{2.31}$$

This number can now go well beyond one, and can of course no longer be interpreted as a probability. Writing down the probability $p(n,t,T)$ of detecting n photoelectrons during a time interval t to $t+T$ is straightforward however. If the detection events are assumed to be independent, the probability will follow a Poisson distribution with a mean value of $\langle n \rangle$. Inserting the expression for $\langle n \rangle$:

$$p(n,t,T) = \frac{1}{n!} < n >^n e^{-<n>} = \tag{2.32}$$

$$= \frac{1}{n!} \left[\alpha \int_t^{t+T} I(t')\,\mathrm{d}t' \right]^n \exp\left[-\alpha \int_t^{t+T} I(t')\,\mathrm{d}t' \right]. \tag{2.33}$$

From the equation above we see that randomness comes into the act of photoelectric detection in two ways. First, the detection process is random, with the intensity of the light determining the probability of detecting a photon. Second, the intensity itself is fluctuating in a random manner. It is by determining the characteristics of these latter fluctuations that an intensity interferometer can be used to measure the coherence of light.

The equations above will be valid only for *one realization of an ensemble* of possible intensities. Practically meaningful results can be obtained by taking the ensemble average, denoted by $\langle\rangle$:

$$P(t) \approx \alpha \langle I(t) \rangle \Delta t$$

$$\langle n \rangle = \alpha \int_t^{t+T} \langle I(t') \rangle\,\mathrm{d}t'. \tag{2.34}$$

For our purposes, it is safe to assume that the field is stationary, i.e. its statistics are independent of the time. Thus the average $\langle I(t) \rangle$ does not depend on the time and can be moved out from the integral:

$$\langle n \rangle = \alpha \langle I(t) \rangle T. \tag{2.35}$$

This means that Eq. (2.30) becomes:

$$P(t_1, t_2) = \alpha_1 \alpha_2 \langle I_1(t_1) I_2(t_2) \rangle. \tag{2.36}$$

But in general

$$\langle I_1(t_1) I_2(t_2) \rangle \neq \langle I_1(t_1) \rangle \langle I_2(t_2) \rangle, \tag{2.37}$$

which means that

$$P_{12}(t_1, t_2) \neq P_1(t_1) P_2(t_2). \tag{2.38}$$

In other words, if the probabilities of detecting a photon in detector A and B are P_A and P_B respectively, the probability of both detectors registering an event at the same time is not necessarily $P_A P_B$. The difference in probability will depend on the statistics of the light field.

For thermal (chaotic) light, one can usually assume that the field follows Gaussian statistics. In this case it can be shown that

$$\langle I_1(t_1) I_2(t_2) \rangle = \langle I_1 \rangle \langle I_2 \rangle (1 + |\gamma_{12}|^2), \tag{2.39}$$

which we have already seen as Eq. (2.23).

2.4.3 Relation to Quantum Optics

While both the scientific results and underlying theory of Hanbury Brown's and Twiss' first intensity interferometer, operating in radio wavelengths, were accepted by the astronomical community more or less immediately, significant controversy arose when the concept was expanded to optical wavelengths. At the time, no complete theory of the quantum nature of light existed, and many physicists believed that the idea of intensity correlations violated fundamental quantum mechanical principles, confused partly by the fallacy of regarding photons as little "bullets of light", and failing to see how these little bullets could interfere with each other. Since photoelectric devices are intrinsically tied to the quantized nature of light it was not at all obvious at the time that the correlation would be preserved in the process of photoelectric emission. Several papers were published disputing the claims of Hanbury Brown and Twiss and it took several laboratory experiments ([17], [16]) and a short but convincing article by Purcell [20] to silence the critics. Eventually the whole situation was resolved when Roy Glauber developed a quantum theory of optical coherence in the 1960's (a theory which earned him the 2005 Nobel Prize in physics).

Photon Bunching and Antibunching

Since we have already seen that the modulus of the coherence of light, $|\gamma|$, can only be between zero and one, Eq. (2.39) would seem to imply that the probability of detecting two photons close to each other (in time or space) is always greater than or equal to the sum of the individual detection probabilities (i.e. the probability one would expect from completely non-coherent light). This tendency for photons to appear close to each other

is known as the *Hanbury Brown-Twiss effect* (HBT effect) or *photon bunching*. It occurs only in fluctuating fields, such as those from thermal light sources, and is attributed to the boson nature of thermal photons [19].

This is however one point where the (semi-)classical treatment breaks down. Contrary to what one would expect from Eq. (2.39) there is also such a thing as photon *anti*-bunching – a tendency for photons to avoid each other. An understanding of this requires a full quantum mechanical description of the light (and not just of the detection process) which is beyond the scope of this report. One can find such a treatment in [19].

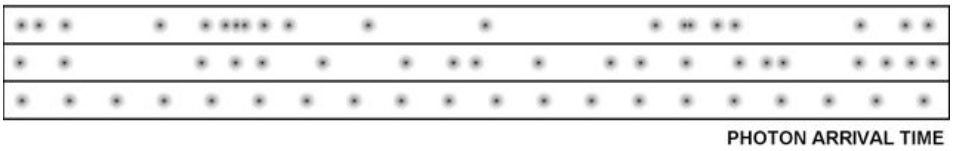

Figure 2.9: Photon arrival times in light beams with different quantum-mechanical statistics. The top row shows thermal (Bose-Einstein distributed) photons, which tend to "buch together". The middle row shows antibunched photons, resulting from a light source that is not in thermodynamic equilibrium. Bottom row shows idealized laser light. Figure from [21].

2.4.4 Digital Revival

The progress in instrumentation technology since the Narrabri Interferometer was abandoned has been enormous. Today, high-resolution photon-counting detectors and hardware correlators are commercially available, and new mathematical algorithms permit (partial) reconstruction of the visibility phase, allowing for image reconstruction. The most expensive components – large flux collectors – exist in the form of Cherenkov telescopes. All of this has sparked a renewed interest in astronomical intensity interferometry in the recent years.

In 2008, the SII (Stellar Intensity Interferometry) Working Group, within commission 54 of the International Astronomical Union, was formed. The group first met at the August 2008 SPIE meeting in Marseilles. Following this meeting, a workshop on stellar intensity interferometry was held at the University of Utah in January 2009 (see e.g. chapter 5). The envisioned path [22] towards the revival of SII as a modern astronomical technique can be roughly divided into four (possibly overlapping) phases:

1. **Initial Prototype Phase (-2010).** Present work, conducted by groups in both the US and in Europe, consists mainly of development and testing of equipment, such as correlators, photo-detectors and optical fibers. One aspect of these efforts (and an important point for this thesis) is the need to properly understand the noise properties and limitations of an intensity interferometer. When planning and seeking funding for an instrument it is of course necessary to know what equipment is needed and what one can do with a given set of instrumentation.

A test facility – StarBase Utah – is being set up by the University of Utah outside Salt Lake City. This facility, which as of spring 2010 is very close to being in full operation, consists of two 3 m reflectors on a 23 m baseline. It will serve as a test environment in which instrumentation can be tried out and its performance evaluated.

2. **IACT Array "Piggyback" Phase (2011-2013).** Once more is known about the technical requirements, it will be possible to use arrays of Cherenkov Telescopes, so-called Imaging Air Cherenkov Telescopes (IACTs), to conduct intensity interferometry on a larger scale. This is described in more detail in Sec. 3.2.1.

3. **CTA/AGIS Phase (2013-2020)**. The Cherenkov Telescope Array (CTA) is a European project to construct a giant array of some 50-100 flux collectors spread over more than a square kilometer. Work is being done to ensure that CTA is capable of SII from the start (see Sec. 3.2.1). In this phase it is reasonable to expect the first results of real scientific value, such as reconstructed images.

4. **Dedicated SII Facility (2020-)**. If results from the CTA phase are good, the ultimate goal would be a dedicated SII facility. Such a facility might consist of a large number of flux collectors over a large area, likely with capabilities for time-tagging and recording of individual photons, high-bandwidth data transfer systems and distributed computer farms for offline calculation of correlation functions in software.

While phase 4 is still highly hypothetical, phase 3 is much more likely to happen. And as we shall see in the coming chapters, already an array like the CTA, if equipped for SII, will be capable of completely new science, allowing studies of stellar objects in unprecedented detail.

Non-Astronomical Intensity Interferometry

It is worth mentioning that while intensity interferometry has not been used as an astronomical technique for many decades, it has been adopted and developed by particle physics (see e.g. [23], [24]), and is now a widely used method for studying atomic and sub-atomic structures (here, the technique is often referred to as *femtoscopy* or sometimes *Hanbury Brown-Twiss (HBT) interferometry*).

The crucial point here is that the HBT effect is not limited to photons, but applies to all quantum-mechanical particles. Bosons (such as photons) tend to 'clump together' in space and time, which can be (partly) understood through the classical interpretation outlined above. However, a full quantum-mechanical description (e.g. [23]) reveal other effects that can not be understood classically. It turns out, for example, that fermions behave in a manner opposite to that of bosons – i.e. they tend to arrive separated in space and time. Figure 2.10 shows the results from an experiment illustrating this effect.

Just as it is possible to draw conclusions about the intensity distribution of astronomical objects with very small angular diameters by correlating photons, it is possible

to measure the space-time geometry of very small particle emission regions by detecting and correlating the particles emitted from them. Such an emission region could for example be the collision zone in a particle collision experiment.

The terminology and mathematical formalism of particle physicists differ significantly from those of astronomers, which is somewhat of an obstacle for astronomers wishing to draw upon the experience and theoretical insights gained by particle physicists. Nevertheless,this sort of inter-disciplinary collaboration could prove to be very important in reviving intensity interferometry as a modern astronomical technique.

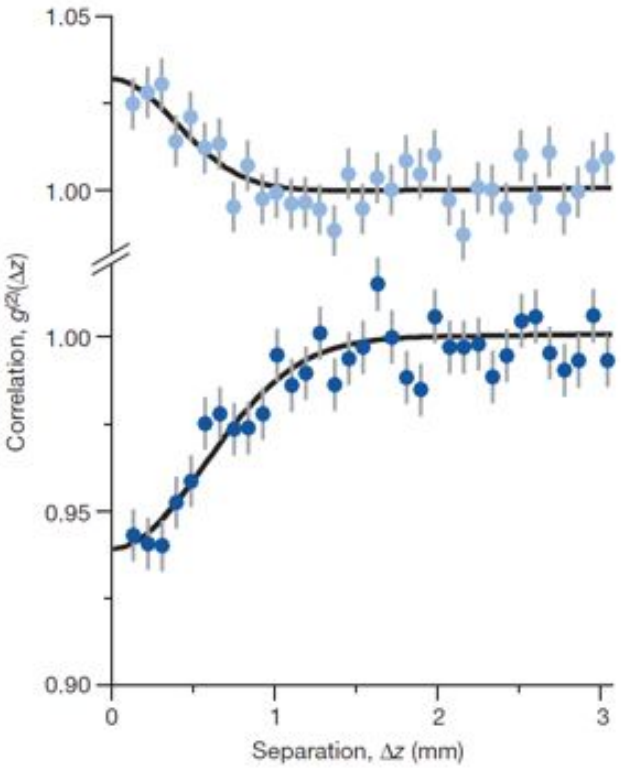

Figure 2.10: Experimental evidence of the difference between fermions and bosons. In this experiment, clouds of ^{4}He (bosons) and ^{3}He (fermions) were produced and launched towards a detector area. The amount of particle pairs detected at a given separation Δz is plotted as a function of separation. The bosons (upper plot) tend to favor arrival in close pairs (i.e. they are 'bunched'), while fermions (lower plot) show a decreased probability of arriving in close pairs ('anti-bunching'). This anti-bunching effect requires a full quantum-mechanical description to explain [25].

Chapter 3

The Components of an Intensity Interferometer

This chapter gives an overview of the different components needed for a modern intensity interferometer. It describes the functionality and performance of the instruments and detectors that exist today and of some that are planned for the future.

3.1 Overview – a Modern Intensity Interferometer

As mentioned above, no astronomical intensity interferometer has been in scientific operation since the Narrabri SII closed down in 1972. However, just like phase interferometry was resurrected when technology had progressed enough, hopes are now high [26] that the technological advances made since the 1970's will make a revival of intensity interferometry worthwhile. Already, all the components needed for a modern intensity interferometer exist and have been proven to work.

In very general terms, an intensity interferometer can be divided into three main parts: flux collectors to collect light from the target, photo-detectors to detect and time-tag photons, and a data handling system to calculate correlation functions and do data analysis such as image reconstruction (see Fig. 2.8). The calculation of correlation functions is a time-consuming process, but can be handled in real-time with specialized hardware correlators. The rest of this chapter gives a more in-depth description of these components.

3.2 Telescopes and Flux Detectors

Intensity interferometry requires the measurement of the second-order correlation of light. This means that the sensitivity scales as the square of the received flux. This all means that the collection of light is extremely important to get a good signal. Very large flux collectors are needed. Luckily though, optical quality is less important. As we have already seen, an intensity interferometer can tolerate optical defects up to a few centimeters.

3.2.1 Air Cherenkov Telescopes

One class of already existing, large flux collectors are the so-called Imaging Air Cherenkov Telescopes, IACTs. These instruments are arrays of very large reflectors that detect the Cherenkov light induced from very high energy cosmic gamma ray photons. The gamma rays produce a cascade of relativistic, charged particles – a so-called shower – when they enter the atmosphere. The charged particles in turn give rise to a flash of Cherenkov light. By using several connected telescopes it is possible to calculate an approximate direction to the source of the shower. The Cherenkov light is very faint, typically only a few tens of photons per m^2. This means that the flux collectors have to be very large.

Today, several large IACTs (see e.g. [27]) are in operation. Among these are H.E.S.S. in Namibia (four 13 m telescopes, one 28 m dish under construction), MAGIC on La Palma (two 17 m telescopes), CANGAROO-III in Woomera, Australia (four 10 m telescopes) and VERITAS in Arizona (four 12 m telescopes).

IACTs happen to share many basic requirements with intensity interferometry – they have large flux collectors where light gathering capability is more important than optical quality, and the telescopes are typically spaced around 100 meters apart (approximately the baseline needed for a resolution of 1 mas).

All this means that Cherenkov arrays can be converted to SII receivers with relatively small (and non-permanent) modifications. All that is required is in principle an optical collimator, a filter, a photo-detector at the focal plane and some sort of data acquisition and processing system [22]. Another advantage from an SII point of view is that Cherenkov light can only be detected when there is little or no moonlight, which means that for a significant amount of time each year, the telescopes are not in use.

In October 2007, the VERITAS array was used for intensity interferometry experiments, the first ever case of optical telescopes being connected digitally rather than optically [28].

While arrays such as VERITAS may be suitable for testing of equipment, the baselines and number of telescopes are too small to offer much new science. This might change in the near future as the proposed American project AGIS and the European Cherenkov Telescope Array, CTA, become a reality.

CTA will consist of up to a hundred flux collectors of varying sizes, spread out over more than a square-kilometer. It will provide a great number of baselines, the longest of which might be more than a kilometer, enabling very good (u, v)-coverage. A special workgroup within the CTA collaboration, led by Dainis Dravins, is currently working to assure that intensity interferometry capabilities are considered from the beginning in the design of CTA. At the point of writing, the CTA SII group has recently submitted a CTA Phase A design study for enabling SII capability for CTA. The design requirements include some way of easily attaching and removing detectors at the telescopes and the possibility to focus the telescopes at infinity [29]. If all goes well, CTA might become the world's first square-kilometer optical stellar imager within the coming decade(s).

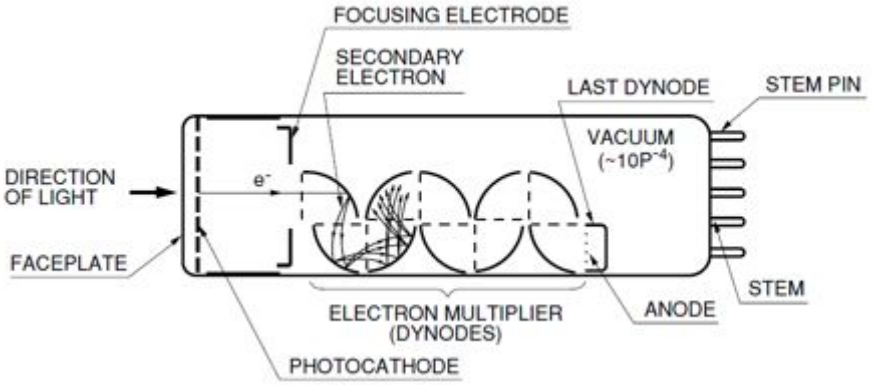

Figure 3.1: Basic outline of a photomultiplier tube. Fig. from [30].

3.3 Photon-counting Detectors

With the telescopes in place the next part in the chain is a device to detect the intensity of the light and feed it to the correlator.

Most light sensing in modern astronomy is done with charge-coupled devices, CCDs. These devices have revolutionized astronomy with their excellent properties for imaging. However, the readout time for a CCD is often on the order of seconds or more, and thus they are not suitable for intensity interferometry where intensity fluctuations on nanosecond levels need to be measured.

There are a number of detector types that can be used for this type of high-time-resolution measurements. In broad terms they can be divided into two groups: photomultiplier tubes (PMTs) and avalanche photo-diodes (APDs).

3.3.1 Photomultipliers

Photomultiplier tubes (PMTs), or simply photomultipliers, have been around for more than seven decades (this is the type of detectors used by Hanbury Brown at Narrabri). The basic structure of a PMT is outlined in Fig. 3.1.

The device consists of a glass tube with vacuum inside. When an incident photon strikes the photocathode, an electron is emitted through the photoelectric effect. The emitted electron is then focused onto the electron multiplier, consisting of several dynodes. When it strikes the first dynode, a secondary electron is emitted (so-called *secondary emission*). The secondary electron is then accelerated by an electric field and strikes the second dynode with a much higher energy, resulting in several new emitted electrons. These are in turn accelerated onto the third dynode and so on, each time with more electrons emitted, resulting in a large number of electrons reaching the anode [30].

In the end, the PMT produces an electrical current proportional to the light intensity, or number of photons per second.

3.3.2 Avalanche Photo-diodes

Avalanche photo-diodes, APDs, are an alternative to PMTs. They are semiconductor devices containing a p-n junction. When an incoming photon is absorbed in the depletion layer in the junction, an electron-hole pair is created. If the device is operating in so-called avalanche mode, or photoconductive mode, a large reverse voltage is applied to the diode. This means that there is a large probability that the electron or hole will trigger an avalanche breakdown where more and more electrons or holes are created in a chain reaction eventually causing the diode to be conductive and producing an electrical pulse [31].

Typically, the current pulses produced in APDs are converted by electronics into standard TTL voltage pulses making them simple to feed into digital electronics such as correlators (3.4.1).

Detectors combining many APDs into an array are just now starting to become feasible. These devices – referred to as solid-state photomultipliers (SSPMs) – will combine the high time-resolution of APDs with some of the imaging capabilities of CCDs.

3.3.3 Properties of Photon-counting Detectors

Both APDs and PMTs have a large number of characteristics that are important to understand their performance and characteristics. Some of the most important in the context of this work are listed below:

- **Quantum efficiency**. In simple terms, this is the percentage of incident photons that are detected. PMTs suffer from quite low quantum efficiencies, typically on the order of 15 % depending on photocathode material [30], while APDs often reach up to 50% and sometimes even as high as 95 % [31].

- **Time resolution**. APDs will have a dead time after each detection where the device is reset to its original state, during which nothing is detected. This means that the detector will start to miss photons when the number of incoming photons per second is on the order of one over the dead time, or time resolution.

  For PMTs, the ability to detect rapid fluctuations in the light intensity is commonly expressed as the *electric bandwidth* of the detector. A high bandwidth means that photons can be detected with a good time resolution.

  For modern detectors, both PMTs and APDs, the time resolution can be as small as picoseconds, but is typically on the order of nanoseconds.

- **Dark current**. In both types of detector, there is always the possibility of an electron becoming thermally excited (as opposed to emitted through the photo-electric effect) and triggering a detection. This is known as *dark current* and can be minimized by cooling the detector. Since intensity interferometry requires high count rates, the dark current (which is a small constant background independent of the light intensity) is typically not a big issue, except perhaps for very faint targets.

- **Afterpulsing**. Due to imperfections in materials, there is always a possibility of electrons being "trapped" in impurities and re-released after some time, which can cause false detection a small time interval after the real detection. This is a potential problem since such false detections mimic correlation signals.

3.4 Data Handling and Software

3.4.1 Hardware Correlators

One very time consuming part of the data processing is the calculation of correlation functions. If A_i and B_i are the recorded (discrete) intensity series and $N = T/\Delta t$ (T is the total integation time, and Δt is the time resolution of the data aquisition system) is the number of samples, then the normalized correlation function calculated by a digital correlator for delay time τ will be:

$$c(\tau) = N \frac{\sum_{i=1}^{N} A_i B_{i+\tau/\Delta t}}{\sum_{i=1}^{N} A_i \sum_{i=1}^{N} B_{i+\tau/\Delta t}} \tag{3.1}$$

Depending on the sampling time, this will result in several hundred millions of multiplications for each recorded second and delay time.

Today, a large selection of dedicated digital hardware correlators are commercially available. Manufacturers include Becker & Hickl, PicoQuant, Brookhaven Instruments, Photocor Instruments and correlator.com. Hardware correlators exist in a variety of forms, both as internal PCI cards and as stand-alone modules connected to the USB port of the computer. They are usually marketed for use in various biochemical applications, such as the study of decay times of florescent biomolecules, but they are also very well suited for astronomical uses.

At the time of writing, Lund Observatory has four digital hardware correlators from correlator.com. Two of these are custom-built units capable of handling 8 input channels at a time resolution of 1.4 ns, calculating auto- and cross-correlation functions with sample times ranging from 1.4 ns up to several hours, in real time.

Figure 3.2 outlines the basic operations of a digital hardware correlator and how it calculates Eq. 3.1. The memory register $n(t_{i-k}), k = 1, 2, 3, \ldots$ keeps track of the number of counts k time intervals ago. The storage counters contain the raw (un-normalized correlation) for different delay times (τ).

Standard TTL pulses from the photon detector are fed to a counter, which counts the number of photons $n(t_i)$ in a time interval. It multiplies this value with the values $n(t_{i-1}), n(t_{i-2}) \ldots$ in its memory and adds these products to the values in the storage counters 1 through L. Finally it shifts all the values in the memory register one step to the right and places the value $n(t_i)$ at the leftmost place, and repeats for the next time interval. This way, the values in the storage counters will contain the raw correlation for $\tau = \Delta t, 2\Delta t, 3\Delta t \ldots$, i.e. the numerator in Eq. 3.1. To get the normalized correlation, one also needs to store the total number of counts in each channel.

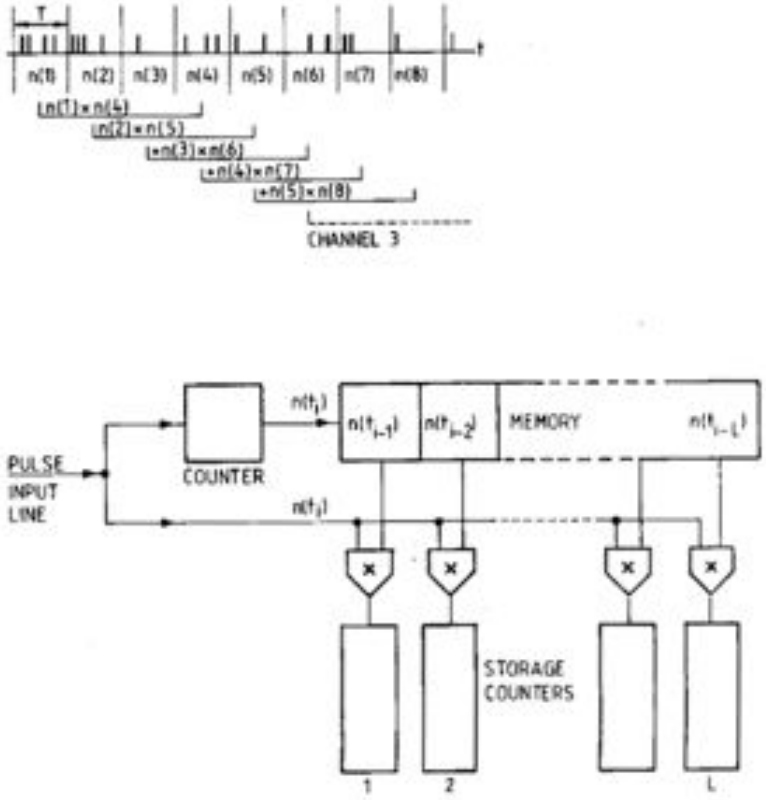

Figure 3.2: Outline of the principles behind a digital correlator. Figure from [32].

The process described above will give the auto-correlation of the input. For the calculation of a cross-correlation, two different counters are needed – one feeding the memory register and one providing the numbers to multiply with.

Today, most correlators consist of many modules like the one above, each with an increasing sample time. The first module might have sample time Δt, the next one $2\Delta t$, then $4\Delta t$, $8\Delta t$ and so on. This is known as a *multiple-τ* correlator. Using the multiple-τ scheme, it is possible for a correlator to keep track of correlations for delay times ranging from very small (nanoseconds) up to very long (several hours) in a single measurement.

Other Uses for Hardware Correlators

As mentioned above, hardware correlators have a wide range of uses. Whenever one wants to study variability in a signal, these instruments perform all the heavy number crunching needed in real time. In July 2009 correlators belonging to Lund Observatory were tried out along with the OPTIMA high speed photon counting instrument [33] at Skinakas Observatory, Crete. The idea was to observe variabilities in astronomical sources such as pulsars in real time.

While the count rate from the detectors of OPTIMA turned out to be too low to use

the hardware correlators for any astronomically interesting measurements, we found that the correlators were excellent for monitoring different sources of errors in the telescope, such as wind shake. An example of this is shown in Fig. 3.3. The autocorrelation of the signal shows a clear spike at around 0.1 s due to wind shake in the telescope. A smaller signal is seen at a period of around 27 s. This is due to some unidentified, likely mechanical, noise source in the telescope system.

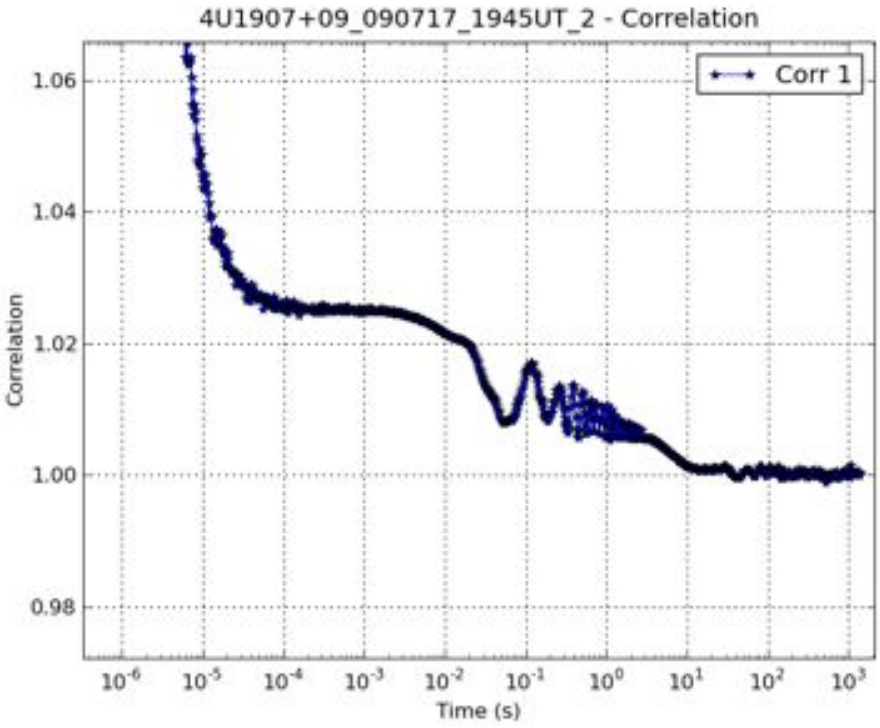

Figure 3.3: Autocorrelation of signal from high mass X-ray binary 4U1907+09.

3.4.2 Software Correlators

Hardware correlators have the advantage of being very fast and relatively affordable. However, they also have some significant drawbacks. The most obvious one is that photon series are not saved, only the correlation functions. This means that one discards a certain amount of information, for example everything that is contained in the higher-order correlations.

In theory, therefore, storing all the output from the detectors and calculating the correlation functions "offline" is highly desirable [34]. Software correlators are not a new concept, and are not very complicated to implement (in principle, all that is needed is a computer program that evaluates Eq. 3.1). However, the amount of data processing and storage required adds significant costs to the system.

As an example, a system of 50 telescopes, each with a detector running at 10 MHz would produce data rates of 500 MB/s (assuming one byte per detected photon) and over 14 TB of raw data for an 8 hour observation run. On top of this there are $50 \cdot 49/2 = 1229$ second-order correlations, $50 \cdot 49 \cdot 48/(3 \cdot 2) = 19600$ third-order correlations etc to be calculated. The bandwidth and storage required are high but not unrealistically so, but the calculation of the correlation functions will require a great amount of computer power to be feasible in any reasonable amount of time. Even if the calculations could be done with the same speed as a dedicated hardware correlator (i.e. 1 h computing time for 1 h of data), the second-order correlations alone would take $1229 \cdot 8$ h = 409 days.

However, very similar issues are currently being faced, and overcome, for example at the LOFAR project [35], which aims to connect a great number of very simple radio antennas to form a gigantic "software telescope". While hardware correlators are probably the least complicated and most cost-effective way of realizing an intensity interferometry system at this stage, technology developed in projects such as LOFAR combined with a few more years of Moore's law will likely make software correlation the way of the future.

3.4.3 Data Extraction and Image Reconstruction

The "raw" output from an intensity interferometer is a set of correlations for a number of points in the Fourier plane (see Sec. 4.4.2). Each such correlation is directly proportional to the magnitude of the Fourier transform of the intensity distribution of the target.

As discussed above, a data handling system could work either using hardware correlators, saving only correlations, or by saving the complete photon recording history and doing the correlations offline in software. The first approach would be fast, simple, and relatively inexpensive but would throw away some potentially useful information, while the second approach would retain all recorded information at the cost of highly complex and expensive data handling systems.

Once the correlations – i.e. the Fourier magnitude – are obtained, there is the question on how to interpret the data. At the Narrabri SII, data were used exclusively for model fitting [15]. In most cases the model was a uniform circular disk, and the data points were used to find the radius of the disk, i.e. θ in Eq. (2.15).

Modern phase interferometry often work in a similar fashion. In principle, model-independent image reconstruction is possible here since the full Fourier transform (including the phase) is measured, but since the sampling of the Fourier plane if often very sparse, better results are often obtained by making assumptions about the target.

Upcoming Cherenkov telescope arrays such as the CTA will consist of up to a hundred telescopes, meaning several thousands of baselines (as contrasted by the single baseline of the Narrabri interferometer). Using Earth rotation synthesis (Sec. 4.4.2) with such a system makes it possible to get a very dense sampling of the (u, v)-plane. It is easy to believe that the lack of phase information makes model-independent image reconstruction impossible for intensity interferometry. However, this is not the case, and in Sec. 4.5 two different methods for image reconstruction from SII data are presented.

Chapter 4

Computer Simulations

One of the main goals of this project was to develop a computer program to simulate intensity interferometry observations. In this section, a method for simulating the measured intensity correlation between pairs of telescopes is derived, and a complete simulation software is presented. Different methods for image reconstruction from the measured correlation are discussed, and finally the simulation software is applied to a set of candidate configurations for the upcoming Cherenkov Telescope Array (CTA) to evaluate the performance of these if used for intensity interferometry.

4.1 Theory

We begin by considering only correlations measured by two telescopes.

A two-telescope intensity interferometer will measure the second-order correlation function $\langle I(\mathbf{r}_1,t_1)I(\mathbf{r}_2,t_1)\rangle/(\langle I(\mathbf{r}_1,t_1)\rangle\langle I(\mathbf{r}_2,t_1)\rangle)$ where $I(\mathbf{r}_1,t)$ and $I(\mathbf{r}_2,t)$ are the intensities measured by the telescopes at $\mathbf{r}_1$ and $\mathbf{r}_2$ respectively and angle brackets denote time average.

If we assume that we detect the light using some photon-counting detector with a (small) sample time Δt, then the probability of detecting a photon within a time interval Δt is [19], as we have already seen:

$$P_1(\mathbf{r}_1) = \alpha\langle I(\mathbf{r}_1,t)\rangle\Delta t, \tag{4.1}$$

where α is the quantum efficiency of the detector. We assume here that the light field fluctuates on a timescale much less than Δt, so that $\langle I(t)\rangle$ is independent of t. It is also necessary that the intensity is low enough that the resulting probability $P_1 \ll 1$, or the detector will not be in its linear regime.

For two independent detectors, the probability of detecting one photon in each during the same time interval will be:

$$P_2(\mathbf{r}_1,\mathbf{r}_2,t_1,t_2,\Delta t) = \alpha_1\alpha_2\langle I(\mathbf{r}_1,t_1)I(\mathbf{r}_2,t_2)\rangle\Delta t^2. \tag{4.2}$$

That is, the probability of joint detections depends on the correlation of the two field intensities. If the statistical properties of the fields are known, it is possible to obtain a

relationship between the correlation of the fields and the coherence function of the light. In particular, for thermal light the fields follow Gaussian statistics, and the correlation function can be shown to be [19]:

$$\langle I_1(t_1)I_2(t_2)\rangle = \langle I_1(t_1)\rangle\langle I_2(t_2)\rangle[1 + |\gamma_{12}(t_2 - t_1)|^2] \tag{4.3}$$

for polarized light, where $I_1(t) = I(\mathbf{r}_1, t)$ and $I_2(t) = I(\mathbf{r}_2, t)$ and $\gamma_{12}(\tau)$ is the complex degree of coherence between the points $\mathbf{r}_1$ and $\mathbf{r}_2$ for time delay $\tau \equiv t_2 - t_1$. Inserting into equation (4.2) we obtain a new expression for the joint detection probability per time:

$$P_2(\mathbf{r}_1, \mathbf{r}_2, \tau) = \alpha_1\alpha_2\langle I_1(t)\rangle\langle I_2(t + \tau)\rangle[1 + |\gamma_{12}(\tau)|^2]. \tag{4.4}$$

Note here that since the light fields are stationary, the terms $\langle I_1(t)\rangle$ and $\langle I_2(t)\rangle$ will not depend on the time and can be regarded as constants. In the future we will write $\langle I_1\rangle \equiv \langle I_1(t)\rangle$.

It is clear that we need to know two things to simulate a measurement process:

1. How to calculate the coherence function γ from the stellar intensity distribution.

2. How the photon arrival time statistics depend on γ.

4.1.1 Stellar Coherence Functions

The relation between the stellar surface intensity distribution and the measured correlation (or interferometric visibility) is fundamental to interferometry, both optical and in radio wavelengths. Two telescopes separated by a vector (x, y) in a plane perpendicular to the line of sight measure the coherence function for a point in the Fourier-plane, or (u, v)-plane, where $x = \lambda u$ and $y = \lambda v$. The coherence function is the Fourier transform of the stellar brightness distribution $I(l, m)$ [8]:

$$\gamma(u, v) = \iint I(l, m)e^{-2i\pi(ul+vm)}\,\mathrm{d}l\,\mathrm{d}m. \tag{4.5}$$

Here, l and m are dimensionless (angular) coordinates on the stellar surface, and the integration is to be taken over the entire sky.

For our purposes, the brightness distribution will be a discrete bitmap where $I(l, m)$ corresponds to the pixel value at pixel (l, m). The integral then takes on the form of a sum:

$$\gamma(u, v) \approx \sum_l \sum_m I(l, m)e^{-2i\pi(ul+vm)}\Delta l\Delta m. \tag{4.6}$$

The coherence function is now a discrete Fourier transform, and will thus repeat itself with regular intervals. This can be a problem for measurements at long baselines, but it is easily avoided by using a sufficiently high resolution image.

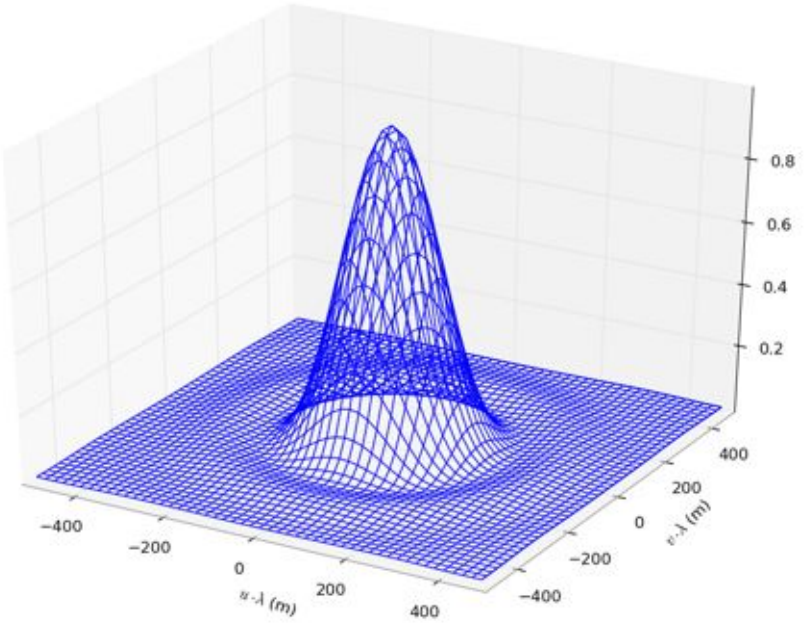

Figure 4.1: Normalized coherence function of a circular uniform disk of angular diameter $\theta = 0.5$ mas, calculated using equation (4.6). The $z-$axis shows $|\gamma|^2$. Compare to the one-dimensional plots in Fig. 2.4.

4.1.2 Photon Statistics

We consider now a situation where two photon-counters A and B are measuring light from a star. The setup is such that there is no time delay between the two detectors – a plane wavefront will strike them both at exactly the same time. The intensities at each detector are $I_A(t)$ and $I_B(t)$ respectively. For each small time interval Δt there is a probability P_A that detector A will detect a photon, a probability P_B that detector B will detect one and a probability P_{AB} that they both will detect one photon.

Equation (4.1) tells us that

$$P_A = \alpha_A \langle I_A \rangle \Delta t$$

$$P_B = \alpha_B \langle I_B \rangle \Delta t$$

We know from Eq. (4.4) that P_{AB} will be slightly larger than $P_A P_B$ if $\gamma \neq 0$. Since we are measuring over a time interval Δt which is generally much longer than the coherence time of the light, we will need to integrate the probability over a detection time interval to obtain the probability of a joint detection:

$$P_2(\mathbf{r}_A, \mathbf{r}_B, \Delta t) = \left(\alpha_A \alpha_B \langle I_A \rangle \langle I_B \rangle \int_{-\Delta t/2}^{\Delta t/2} (1 + |\gamma_{AB}(\tau)|^2) \, \mathrm{d}\tau \right) \Delta t. \tag{4.7}$$

If the light is cross-spectrally pure[1], the coherence term $|\gamma_{AB}(t)|^2$ can be factorized into a spatial and a temporal part (see [19]):

$$|\gamma_{AB}(\tau)|^2 = |\gamma_{AB}(0)|^2 |\gamma(\tau)|^2. \tag{4.8}$$

The spatial part $|\gamma_{AB}(0)|^2$ follows from the geometric layout of the telescopes and the spatial intensity distribution of the target. The temporal part $|\gamma(\tau)|^2$ is unity for $\tau = 0$ and negligibly small for values larger than the coherence time of the light, τ_c. Thus, if $\Delta t \gg \tau_c$ it is reasonable [19] to set:

$$\int_{-\Delta t/2}^{\Delta t/2} |\gamma(\tau)|^2 \, \mathrm{d}\tau \approx \int_{-\infty}^{\infty} |\gamma(\tau)|^2 \, \mathrm{d}\tau = \tau_c. \tag{4.9}$$

So the probability of a joint detection in A and B within a time interval Δt will be:

$$\begin{aligned} P_{AB} &= \alpha_A \alpha_B \langle I_A \rangle \langle I_B \rangle [1 + |\gamma_{AB}|^2 \frac{\tau_c}{\Delta t}] \Delta t^2 = \\ &= P_A P_B + \alpha_A \alpha_B \langle I_A \rangle \langle I_B \rangle |\gamma_{AB}|^2 \frac{\tau_c}{\Delta t} \Delta t^2, \end{aligned} \tag{4.10}$$

where we have written $\gamma_{AB}(0) \equiv \gamma_{AB}$ for brevity. We see that the joint detection probability will be $P_A P_B$ plus a factor that depends on the coherence.

4.2 An Intensity Interferometry Simulation Algorithm

We assume that we have a situation with photon counters that can only detect one or zero photons in each time interval. The raw correlation $\langle I_A I_B \rangle$ will then simply be the number of coincidences, i.e. the number of times when both detectors detect a photon simultaneously. The normalized correlation function can then be written:

$$g^{(2)} = \frac{N_{AB}}{N_A N_B} N, \tag{4.11}$$

where N_A and N_B are the number of counts in detectors A and B respectively, N_{AB} is the number of coincidences and $N = T/\Delta t$ (again, T is the total integration time, and Δt is the time resolution of the detectors) is the number of sampled time intervals. We can treat a measurement of the second-degree coherence as an experiment where three random numbers N_A, N_B and N_{AB} are drawn from three different probability distributions.

For each time interval of length Δt, we know from above that there is a probability P_A of detection in A, a probability P_B of detection in B and a probability P_{AB} of a joint detection. It then follows that N_A, N_B and N_{AB} will follow Poisson distributions with mean values $\lambda_A = P_A \cdot N$, $\lambda_B = P_B \cdot N$ and $\lambda_{AB} = N_{AB} \cdot N$ respectively.

[1] Cross-spectral purity is a concept that was introduced by Mandel. In short, it means that the spectral distribution of the light at some point in the plane of observation is of the same form as the spectral distribution at the pinholes in a double slit type experiment. The full details can be found in [19].

However, since we are normally dealing with very large values for N, it is reasonable to approximate these as normal distributions with mean value $\mu_A = \lambda_A$ and standard deviation $\sigma_A = \sqrt{\mu_A}$ and similarly for N_B and N_{AB}.

We can then simulate a measurement by an intensity interferometer using the following method:

1. Start with an intensity distribution of a star and use this to calculate the spatial coherence, γ_{AB}.
2. Calculate the received intensities $\langle I_A \rangle$ and $\langle I_B \rangle$ from the properties of the star and atmosphere.
3. Use γ_{AB} to calculate the probabilities P_A, P_B and P_{AB} as described above.
4. Draw three random numbers N_A, N_B and N_{AB} from three normal distributions, as described above.
5. The 'measured' correlation will then be $g^{(2)} = \frac{N_{AB}}{N_A N_B} N$.

4.2.1 Signal-to-Noise Estimates

Since the distributions of N_A, N_B and N_{AB} are known, it is in principle possible to derive a probability distribution for the correlation itself, which would directly give an estimation of the signal-to-noise. However, the mathematics become very awkward, and we have not been able to find an analytical form for this expression.

A simpler (although more time consuming) approach is to use a Monte-Carlo method. A large number n of correlation measurements are performed for zero baseline and stored in a list $\mathbf{C}_1$. A second list $\mathbf{C}_2$ is then produced in the same way for a very long baseline (zero coherence). The vector $\mathbf{C} = \mathbf{C}_1 - \mathbf{C}_2$ is then regarded as the signal, and the signal-to-noise ratio taken as the mean of the signal divided by the standard deviation of the signal:

$$\frac{S}{N} = \frac{\bar{\mathbf{C}}}{\sqrt{\frac{1}{n}\sum_{i=1}^{n}(\mathbf{C}_i - \bar{\mathbf{C}})^2}}. \tag{4.12}$$

4.3 Three-Telescope Measurements

Normally, measurements would only be made for two telescopes at a time. Even when using arrays of many telescopes, these are typically correlated in pairs. There are however some applications for higher-order correlations (e.g. [36]), and the method above can be generalized to correlations of arbitrary degree, although the mathematics quickly get a little awkward for higher degrees. Below, we derive a method for simulating a measurement of the third-order correlation, $g^{(3)}$, by a system of three telescopes. This section is not essential to the rest of the project, and the results here are not used in the simulations; it is included mostly to show how these higher-order could potentially be studied, should one want to in the future. It is possible to skip to Sec. 4.4.

In analogy with Eq. (4.2), the probability of a simultaneous detection in three detectors will be

$$P_3(\mathbf{r}_1, \mathbf{r}_2, \mathbf{r}_3, t_1, t_2, t_3 \Delta t) = \alpha_1 \alpha_2 \alpha_3 \langle I(\mathbf{r}_1, t_1) I(\mathbf{r}_2, t_2) I(\mathbf{r}_3, t_3) \rangle \Delta t^3. \tag{4.13}$$

What we need then, is a way of expressing the third-order correlation, $\langle I(\mathbf{r}_1, t_1) I(\mathbf{r}_2, t_2) I(\mathbf{r}_3, t_3) \rangle$, in terms of the individual (mean) intensities and the complex degree of coherence.

We start by treating the (polarized) light field as an analytic signal $V(\mathbf{r}, t)$ with zero mean. Following [19], we then define a correlation function of order (M, N) as:

$$\Gamma^{(M,N)}(x_1, x_2, \ldots, x_M; y_1, y_2, \ldots, y_N) = \\ \langle V^*(x_1) V^*(x_2) \ldots V^*(x_M) V(y_1) V(y_2) \ldots V(y_N) \rangle, \tag{4.14}$$

where x_m and y_m are space-time points, $x_m = (\mathbf{r}_m, t_m)$. We are mainly interested in correlations where $M = N$, and we will set $\Gamma^{(M)} \equiv \Gamma^{(M,M)}$.

If the fields are Gaussian, it is possible to use the Gaussian moment theorem [19] to express higher-order correlations as products of first-order correlations:

$$\Gamma^{(M)}(x_1, x_2, \ldots, x_M; y_1, y_2, \ldots, y_M) = \\ \sum_{\text{All permutations}} \Gamma^{(1)}(x_{i1}, y_{j1}) \Gamma^{(1)}(x_{i2}, y_{j2}) \ldots \Gamma^{(1)}(x_{iM}, y_{jM}). \tag{4.15}$$

The subscripts i_p and j_p are integers in the range $1 \leq i_p, j_p \leq M$ and the summation is to be taken over the $M!$ possible permutations of i_p and j_p.

For the third-order correlation this becomes:

$$\begin{aligned} &\Gamma^{(3)}(x_1, x_2, x_3; y_1, y_2, y_3) = \\ &\quad \Gamma^{(1)}(x_1, y_1) \Gamma^{(1)}(x_2, y_2) \Gamma^{(1)}(x_3, y_3) + \Gamma^{(1)}(x_1, y_2) \Gamma^{(1)}(x_2, y_3) \Gamma^{(1)}(x_3, y_1) + \\ &\quad \Gamma^{(1)}(x_1, y_3) \Gamma^{(1)}(x_2, y_1) \Gamma^{(1)}(x_3, y_2) + \Gamma^{(1)}(x_1, y_1) \Gamma^{(1)}(x_2, y_3) \Gamma^{(1)}(x_3, y_2) + \\ &\quad \Gamma^{(1)}(x_1, y_2) \Gamma^{(1)}(x_2, y_1) \Gamma^{(1)}(x_3, y_3) + \Gamma^{(1)}(x_1, y_3) \Gamma^{(1)}(x_2, y_2) \Gamma^{(1)}(x_3, y_1). \end{aligned}$$

Since we only consider measurements in three points simultaneously, we now put $x_i = y_i;\ i = 1, 2, 3$. We also note that

$$\Gamma^{(1)}(x_m, x_m) = \langle V^*(x_m) V(x_m) \rangle = \langle I(x_m) \rangle$$

and that

$$\Gamma^{(1)}(x_m, x_n) = [\Gamma^{(1)}(x_n, x_m)]^* \ \Rightarrow\ \Gamma^{(1)}(x_m, x_n) \Gamma^{(1)}(x_n, x_m) = |\Gamma^{(1)}(x_m, x_n)|^2.$$

We then get:

$$\begin{aligned} &\Gamma^{(3)}(x_1, x_2, x_3) = \\ &\quad \langle I(x_1) \rangle \langle I(x_2) \rangle \langle I(x_3) \rangle \\ &\quad + \langle I(x_1) \rangle |\Gamma^{(1)}(x_2, x_3)|^2 + \langle I(x_2) \rangle |\Gamma^{(1)}(x_1, x_3)|^2 + \langle I(x_3) \rangle |\Gamma^{(1)}(x_1, x_2)|^2 \\ &\quad + \Gamma^{(1)}(x_1, x_2) \Gamma^{(1)}(x_2, x_3) \Gamma^{(1)}(x_3, x_1) \\ &\quad + \Gamma^{(1)}(x_2, x_1) \Gamma^{(1)}(x_3, x_2) \Gamma^{(1)}(x_1, x_3). \end{aligned}$$

Finally, we replace the correlation functions with the normalized version defined by:

$$\gamma^{(1)}(x_1, x_2) \equiv \frac{\Gamma^{(1)}(x_1, x_2)}{\sqrt{\langle I(x_1)\rangle}\sqrt{\langle I(x_1)\rangle}}.$$

After some algebraic manipulation, this results in the following:

$$\begin{aligned}\Gamma^{(3)}(x_1,&x_2, x_3) = \\ &\langle I(x_1)\rangle\langle I(x_2)\rangle\langle I(x_3)\rangle[1 + |\gamma^{(1)}(x_1, x_2)|^2 + |\gamma^{(1)}(x_2, x_3)|^2 \\ &|\gamma^{(1)}(x_1, x_3)|^2 + 2\mathrm{Re}(\gamma^{(1)}(x_1, x_2)\gamma^{(1)}(x_2, x_3)\gamma^{(1)}(x_3, x_1))].\end{aligned}$$

Using Eq. (4.13) we end up with an expression for the probability of a triple detection within a time interval Δt (cf. Eq. (4.7)):

$$\begin{aligned}P_3(\mathbf{r}_1,&\mathbf{r}_2, \mathbf{r}_3, \Delta t) = \\ &\alpha_1\alpha_2\alpha_3\langle I_1(t)\rangle\langle I_2(t + \tau_1)\rangle\langle I_2(t + \tau_2)\rangle \int_{-\Delta t/2}^{\Delta t/2}\int_{-\Delta t/2}^{\Delta t/2}[1+ \\ &|\gamma_{12}(\tau_1)|^2 + |\gamma_{23}(\tau_2 - \tau_1)|^2 + |\gamma_{13}(\tau_2)|^2+ \\ &2\mathrm{Re}(\gamma_{12}(\tau_1)\gamma_{13}(\tau_2)\gamma_{23}(\tau_2 - \tau_1))]\,\mathrm{d}\tau_1\,\mathrm{d}\tau_2 \cdot \Delta t.\end{aligned} \tag{4.16}$$

The squared coherence terms inside the integral can be treated as before (see Eq. (4.9)):

$$\int_{-\Delta t/2}^{\Delta t/2} |\gamma_{12}(\tau)|^2\,\mathrm{d}\tau = |\gamma_{12}|^2 \int_{-\infty}^{\infty} |\gamma(\tau)|^2\,\mathrm{d}\tau \approx |\gamma_{12}|^2\tau_c. \tag{4.17}$$

$|\gamma(\tau)|^2$ will have a bell-shaped form symmetric around the origin. Thus, if we change the argument to, say, $\tau_2 - \tau_1$, this only translates the curve along the τ-axis, it does not affect the value of the indefinite integral in (4.17).

The last term inside the integral in (4.16) requires some extra thought. We begin by splitting the coherence terms into their spatial and temporal parts, so that the last part of the integral becomes:

$$\int_{-\Delta t/2}^{\Delta t/2}\int_{-\Delta t/2}^{\Delta t/2} \mathrm{Re}[\gamma_{12}\gamma_{13}\gamma_{23}\gamma(\tau_1)\gamma(\tau_2)\gamma(\tau_2 - \tau_1)]\,\mathrm{d}\tau_1\,\mathrm{d}\tau_2 \tag{4.18}$$

The important part here is the temporal coherence $\gamma(\tau)$. For values of τ larger than the coherence time τ_c, $\gamma(\tau)$ can be considered to be zero, so we need only integrate over a time interval where $|\tau| < \tau_c$. For smaller values of τ, $\gamma(\tau)$ is approximately periodic. According to [19], it can be written as:

$$\gamma(\tau) = e^{-2\pi i\bar{\nu}\tau}, \tag{4.19}$$

where $\bar{\nu}$ is the mean frequency of the light.

The integral (4.18) then becomes:

$$\int_{-\Delta t/2}^{\Delta t/2}\int_{-\Delta t/2}^{\Delta t/2} \mathrm{Re}[\gamma_{12}(0)\gamma_{13}(0)\gamma_{23}(0)e^{-4i\pi\bar{\nu}(\tau_1+\tau_2+\tau_2-\tau_1]}\,\mathrm{d}\tau_1\,\mathrm{d}\tau_2 = \tag{4.20}$$
$$= \Delta t \int_{-\Delta t/2}^{\Delta t/2} \mathrm{Re}[\gamma_{12}(0)\gamma_{13}(0)\gamma_{23}(0)e^{-4i\pi\bar{\nu}\tau_2}]\,\mathrm{d}\tau_2.$$

All of this gives us then the final expression for the probability of a triple detection:

$$\begin{aligned} P_3(\mathbf{r}_1,\mathbf{r}_2,\mathbf{r}_3,\Delta t) = \alpha_1\alpha_2\alpha_3\langle I_1\rangle\langle I_2\rangle\langle I_2\rangle[1+ \\ \tau_c/\Delta t(|\gamma_{12}|^2+|\gamma_{13}|^2+|\gamma_{23}|^2)+ \\ 2/\Delta t\int_{-\tau_c}^{\tau_c}\mathrm{Re}(\gamma_{12}\gamma_{23}\gamma_{32}e^{-4\pi\bar{\nu}\tau})\,\mathrm{d}\tau]\Delta t^3. \end{aligned} \tag{4.21}$$

The last integral is hard to evaluate analytically, but there are no reasons why it should not be possible to evaluate it numerically.

4.4 Implementation

The method for simulations described in Sec. 4.2 was implemented as a Python program, using `numpy` [2] for numerical calculations. The program takes as input information about a star (a bitmap image, angular diameter, apparent V magnitude and effective temperature), information about the instrumentation (detector sample time and quantum efficiency, telescope diameter, filter wavelength and bandwidth), a baseline in (x, y)-coordinates and an integration time. From this it calculates the coherence function and the received intensity from the star. It then scales the intensity by calculating the intensity that would equal one photon per Δt, i.e. $I_0 = hc/(\lambda_f \Delta t)$, where λ_f is the filter wavelength, and expressing the received intensity as a fraction of this. Finally, it produces a measured correlation and a signal-to-noise ratio according to the method described above. The coherence time of the light is taken to be:

$$\tau_c = \frac{1}{\Delta\nu_f} \approx \frac{\lambda_f^2}{c\Delta\lambda_f}, \tag{4.22}$$

where $\Delta\lambda_f$ is the filter bandwidth. This assumes that the light has a spectral density that is approximately constant over the filter passband.

Figures 4.2 and 4.3 show two sample simulations of different surface intensity distributions and with varying integration times (given for each data point). Both input images were taken to be 1 mas across. The apparent V magnitude was 6 and the effective temperature 13000 K. The simulations where done for a telescope diameter of 15 m, a 550 nm filter of 1 nm bandwidth and a detector with a sampling time of 0.1 ns and a quantum efficiency of 70 %.

[2] `http://www.numpy.scipy.org`

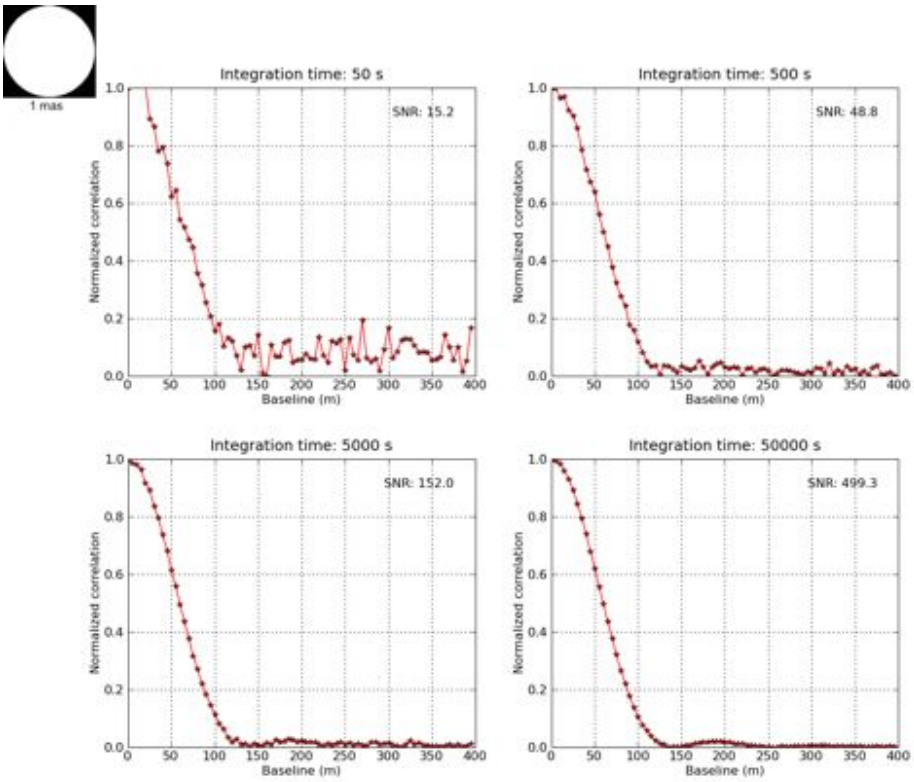

Figure 4.2: Simulated measurements of a uniform circular stellar disk. Input image, 1 mas across, is shown in the top-left corner.

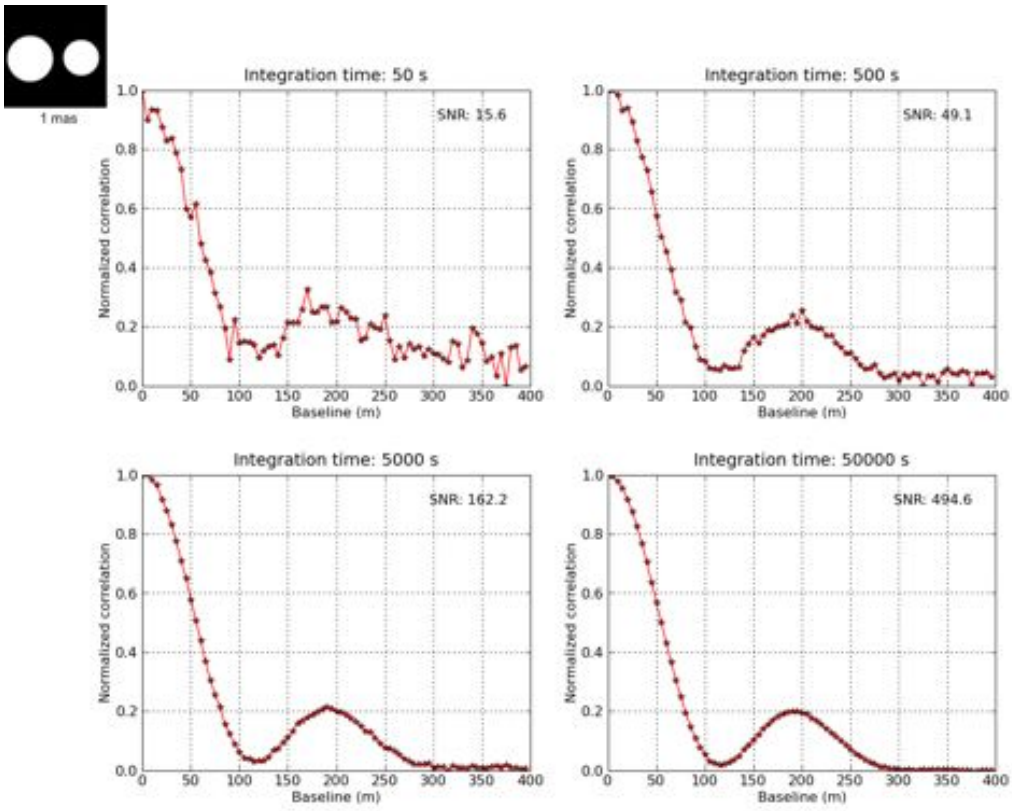

Figure 4.3: Simulated measurements of a binary system. Input image, 1 mas across, is shown in the top-left corner.

4.4.1 Comparison with Results from Narrabri

As a sanity check, it is interesting to see that the simulations give results that are comparable to those obtained by Hanbury Brown et al. at Narrabri [15]. Figure 4.4(b) shows the output from a simulation of a circular uniform stellar disk with properties corresponding to those of Sirius ($\theta = 5.6$ mas, $T_{eff} = 10000$ K, $m_V = -1.46$). The simulation was done for two 6.5 m reflectors, at 450 nm with a spectral bandwidth of 1 nm. The detectors were taken to have a quantum efficiency of 10 % and a time resolution of 10 ns (i.e. an electrical bandwidth of 100 MHz), and the the observation time was 40 hours for each data point.

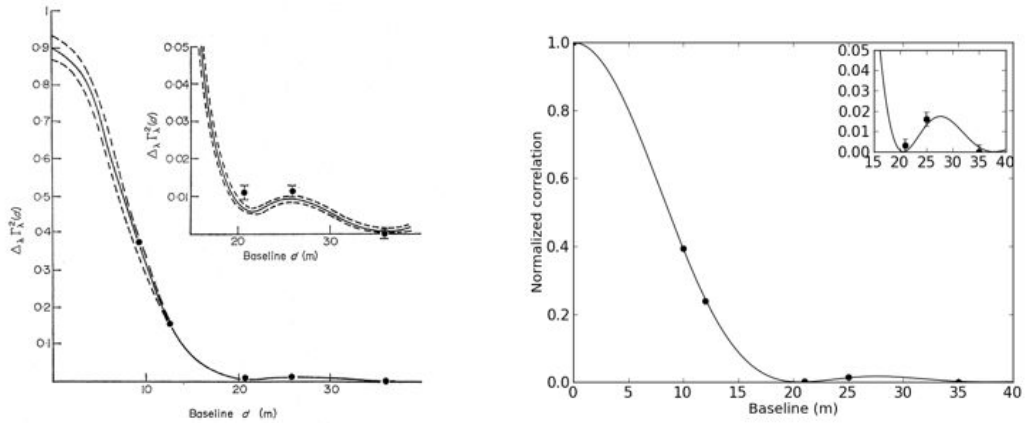

(a) Measurements by Hanbury Brown et al. [37]

(b) Simulated measurements.

Figure 4.4: Observations of Sirius by Hanbury Brown et al. as compared to simulations with similar input parameters. The lines show the theoretical correlation curves. Error bars in the simulation plot were calculated using Eq. (4.12).

The simulation parameters were chosen to be as similar as possible to those used in Fig. 4.4(a). As we see, the results look very similar (there is a small difference in the shape of the correlation curves which is due to the more sophisticated model used by Hanbury Brown et al., incorporating effects such as limb darkening; for the simulations a simple circular uniform disk was used).

It should be noted, however, that it is difficult to make exact comparisons between these simulations and the measurements from Narrabri. For a bright star such as Sirius, digital detectors will start to saturate (i.e. they approach or exceed one photon per time resolution interval) and some sort of light attenuation device will have to be used, unless the spectral filter is very narrow. Therefore, the filter bandwidth will affect the signal-to-noise for very bright stars, in a way that may be quite different from the situation when analog detectors are used (as was the case at Narrabri).

All in all, a direct numerical comparison of simulation results with the measurements at Narrabri is not very meaningful, but we note from Fig. 4.4.1 that the results look reasonable, and are at least not off by orders of magnitude.

4.4.2 Telescope Arrays and Rotation of the Earth

The simulation code described in the previous section only works for two telescopes with the star fixed at Zenith (which of course is unrealistic). In a real-world scenario, we will usually have an array of telescopes, which will usually be correlated in pairs. An array consisting of n telescopes will give rise to $n(n-1)/2$ pairs, or *baselines*, though they are not necessarily all unique. Each such baseline represents a point in the (u, v)- (Fourier-) plane.

One way of increasing the coverage of the (u, v)-plane is to move one or several of the telescopes around. This is what was done at the Narrabri interferometer. However, making a telescope mobile greatly increases the technical difficulties in its construction. A different approach is so-called *Earth rotation synthesis*. Due to the Earth's rotation, stars will move across the sky, and give rise to many different projected baselines, see Fig. 4.5. Making use of this allows one to measure a great number of points in the uv-plane.

Figure 4.5: As the Earth rotates, the projected baseline will change. Each such projected baseline represents a point in the Fourier plane. By having many pairs of telescopes, it is possible to cover a large part of the Fourier plane simply by making use of the Earth's rotation.

A baseline can be expressed as a vector $\mathbf{B} = (B_{north}, B_{east}, B_{up})$ in an Earth-centric coordinate system. Here, B_{north} and B_{east} denote the telescope separations along the north-south and east-west directions respectively. B_{up} is the difference in elevation between the telescopes (so if the telescopes are located on a flat field, $B_{up} = 0$). As the target of observation moves along the sky due to the Earth's rotation, the projected baseline is [38]:

$$\mathbf{B}_p = \mathbf{P} \begin{pmatrix} B_{north} \\ B_{east} \\ B_{up} \end{pmatrix} \tag{4.23}$$

where

$$\mathbf{P} = \begin{pmatrix} -\sin l \sin h & \cos h & \cos l \sin h \\ \sin l \cos h \sin \delta + \cos l \cos \delta & \sin h \sin \delta & -\cos l \cos h \sin \delta + \sin l \cos \delta \\ -\sin l \cos h \cos \delta + \cos l \sin \delta & -\sin h \cos \delta & \cos l \cos h \cos \delta + \sin l \sin \delta \end{pmatrix}$$

Here h is the hour angle of the star (h=0 for the southern meridian), l is the latitude of the telescope and δ is the declination of the star. From this we get the point in the

Fourier plane as:

$$\begin{pmatrix} u \\ v \\ w \end{pmatrix} = \frac{\mathbf{B}_p}{\lambda}. \tag{4.24}$$

The w component will be directed along the line of sight towards the target of observation. Thus, it does not affect the projected baseline, but is just a measure of the optical path difference between the two telescopes. In a real-world scenario, a time-delay needs to be introduced into one telescope whenever $w \neq 0$.

As h increases, a star will trace out an ellipse in the (u, v)-plane. The coherence in a point (u, v) will always be the same as in $(-u, -v)$, so each baseline will give measurements for two points in the (u, v)-plane.

In these simulations, the ellipses traced out were treated as series of discrete points, and the methods described above were then applied to each such point. As an example, Fig. 4.6 shows the (u, v)-coverage of the VERITAS 4-telescope array as a star moves across the sky through the zenith, as measured during an 8 hour period.

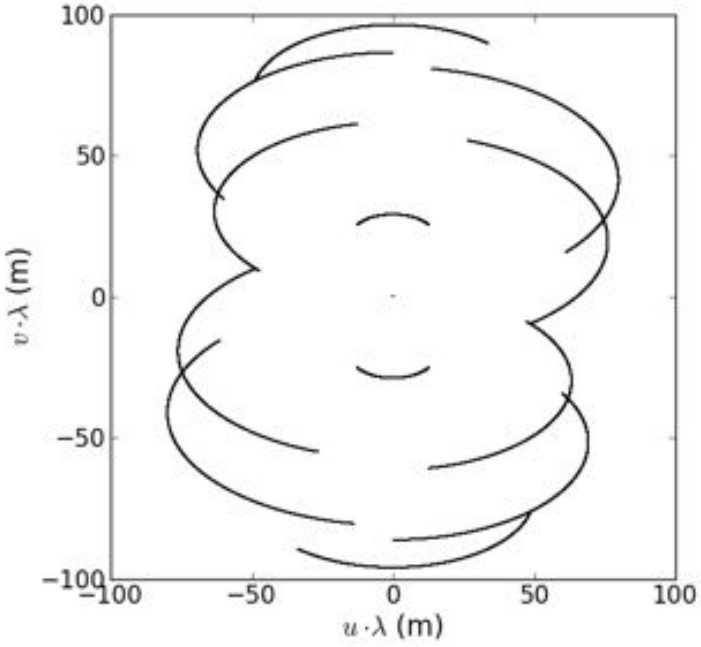

Figure 4.6: Simulated Fourier plane coverage of the VERITAS array for an 8 hour period.

With the method for simulating measured correlations and calculating the (u, v)-coverage of a telescope array described above, it is now possible to simulate a realistic measurement of a real astronomical target with a large scale telescope array. A pristine image of the target is fed to the program in the form of a bitmap image and the output is a large number of data points, spread out over the Fourier plane, each one containing the measured correlation function for a specific baseline.

These points are samples from the magnitude of the two-dimensional Fourier transform of the target surface brightness distribution. Working with a discrete set of non-uniformly spread out points is not very convenient. For any sort of data analysis, it would be much better to have the Fourier magnitude on a dense and uniform grid (approximating a continuous function). There are several ways to solve this problem, but one of the most straightforward is to make a triangulation and a linear interpolation.

A triangulation is a connection of a set of points into triangles, see Fig. 4.7 for an example. A commonly used triangulation is the so-called Delaunay triangulation, which connects the points in such a way as to maximize the minimum angle of the triangles.

Once a triangulation is made, it is possible to evaluate the Fourier magnitude anywhere in the plane. Because each triangle specifies a plane, one can perform a linear interpolation to find the value of the function in any point. Several algorithms for performing a Delaunay triangulation exist (see e.g. [39]), but fortunately, the numerical package `numpy`, which is used here, has its own built-in function `griddata` which triangulates a set of points and interpolates over an evenly spaced grid.

The structure and function of this full simulation code is outlined in Fig. 4.9.

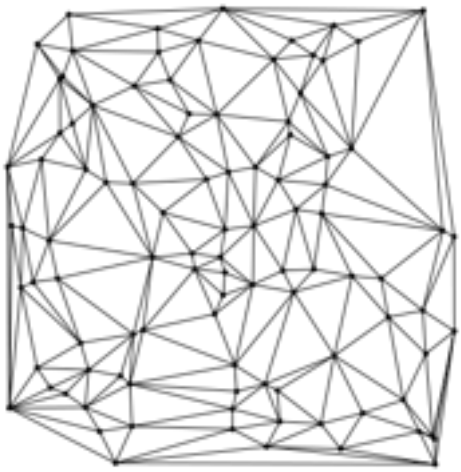

Figure 4.7: Example of a Delaunay triangulation of a set of points randomly scattered in a plane.

Figure 4.8 shows an example of the output from the program. The simulated target is a binary star, measured with one of the envisioned CTA array configurations. Each point in the plot is a correlation measurement, and the underlying contour plot is simply the interpolation of all the points, resulting from the Delaunay triangulation.

4.5 Image Reconstruction

4.5.1 Cauchy-Riemann Image Reconstruction

Since only the magnitude of the Fourier transform of the intensity distribution is measured in intensity interferometry, images can not be obtained directly from the van Cittert-

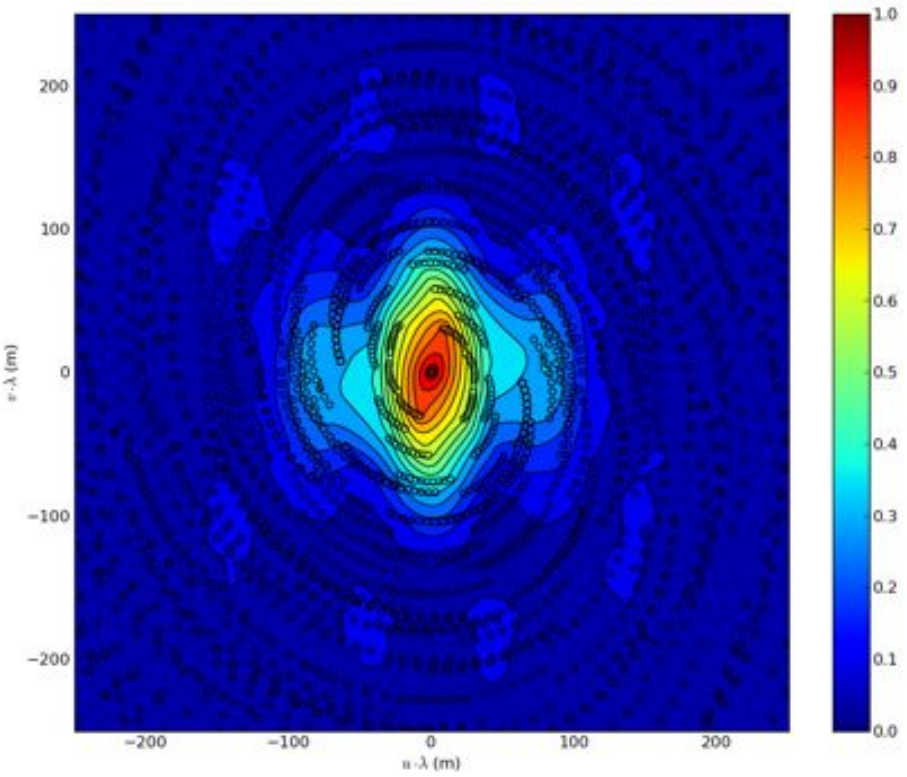

Figure 4.8: Simulated measurement of a binary star with a CTA-type telescope array. The color scale shows normalized correlation. Each point represents one baseline. In reality, these would not be discrete points, but would be parts of ellipses, traced out in the Fourier plane as the target moves across the sky. However, in these simulations, the ellipses are treated as consisting of many discrete points.

Figure 4.9: Rough outline of the simulation software.

Zernicke theorem (2.20). However, there exist a number of methods for recovering the phase of a complex function when only the magnitude is known.

A method of phase retrieval specifically intended for intensity interferometry was proposed by Holmes and Belen'kii [40]. The basic ideas behind this method are outlined below, but interested readers are referred to [40] for the details.

Starting from Eq. (2.19), the Fourier transform $\Gamma(u,v)$ can be written as:

$$\begin{aligned}\Gamma(u,v) &= \iint I_\nu(l,m)e^{-2\pi i(ul+vm)}\,\mathrm{d}l\,\mathrm{d}m = \\ &= \Delta l\Delta m\sum_{j,k} I(j\Delta\theta, j\Delta\theta)z_u^j z_v^k + \epsilon(u,v),\end{aligned} \tag{4.25}$$

where $z_u = \exp(-2\pi iu\Delta\theta)$, $z_v = \exp(-2\pi iv\Delta\theta)$ and $\epsilon(u,v)$ is the error from using a discrete Fourier transform. Because the Fourier transform is a polynomial in the two complex variables z_u and z_v, it is also an analytical function, and so the Cauchy-Riemann equations apply. Setting $\Gamma = R\exp(i\Phi)$ and $z_u = \xi + i\psi$ (or equivalently for z_v) the Cauchy-Riemann equations give:

$$\frac{\partial[R\exp(i\Phi)]}{\partial\xi} = \frac{\partial[R\exp(i\Phi)]}{\partial(i\Psi)}. \tag{4.26}$$

By splitting this up in real and imaginary parts and equating these, one obtains:

$$\frac{\partial\Phi}{\partial\psi} = \frac{\partial s}{\partial\xi} \tag{4.27}$$

$$\frac{\partial\Phi}{\partial\xi} = -\frac{\partial s}{\partial\psi} \tag{4.28}$$

where $s \equiv \ln(R)$. These two equations give a relation between the phase Φ and the magnitude R. Since the magnitude is sampled at discrete points, this must be written in finite form:

$$\Delta\Phi = (\Delta s/\Delta\xi)\Delta\psi \tag{4.29}$$

$$\Delta\Phi = -(\Delta s/\Delta\psi)\Delta\xi. \tag{4.30}$$

A further constraint on the phase is given by the fact that it satisfies Laplace's equation in the (ξ,ψ) plane:

$$\frac{\partial^2\Phi}{\partial\xi^2} + \frac{\partial^2\Phi}{\partial\Psi^2} = 0. \tag{4.31}$$

A problem here is the presence of zeros in the magnitude which will give rise to singularities, since $s = \ln(R)$ will not be defined at these points. In practice however, one can usually get around this by a clever sampling of the Fourier plane (but even near-zeros will introduce errors to the reconstructed phase). Most of the time, the phase of an image can be reconstructed with only a translational and mirror-flip ambuigity [40].

Reconstruction of two-dimensional images from intensity interferometry measurements are currently being actively researched at the University of Utah [41]. A work-in-progress version of image reconstruction software developed by Paul Nuñez was used

to reconstruct images from simulated II data; some results from this are shown later on in Secs. 4.6 and 5.5. It should be stressed however, that by the time of this writing, the image reconstruction software was not in a "finished" state, and so imperfections in the reconstruction probably do not represent fundamental limitations in the Cauchy-Riemann method, but may simply be due to practical issues with the implementation.

4.5.2 Genetic Algorithm Image Reconstruction

About Genetic Algorithms

As part of this project, a different method for image reconstruction was tried out, using a genetic algorithm. Genetic algorithms (GAs) are a type of computational methods which utilize concepts from evolutionary biology to obtain solutions to problems such as optimization problems (see e.g. [42]), and are a subset of the much larger field of evolutionary computing. These types of algorithms are particularly useful for problems with a large solution space where there exists a way of assessing the quality of an individual solution, but where there is no easy way to arrive at the best solution.

An example of a problem that lends itself well to a GA is the well-known Travelling Salesman Problem (given a number of cities on a map, find the shortest route connecting them all visiting each city only once). The number of possible solutions is large ($n!/2$ for n cities), it is possible to compute the quality of a given solution by simply calculating the length of the route, but there is no easy way of determining the shortest route.

Taking its terminology largely from biology, GAs treat each solution as an "individual" with a genome, which in turn gives rise to a phenotype. A set of individuals – a *population* – is created, and new generations are obtained by repeatedly selecting the best individuals and cross-breeding and mutating them. In general, a GA consists of the following:

- A method for encoding a solution as a *chromosome* in some suitable format. A common format is a binary string, but other encodings, such as matrices can also be used.
- A *fitness function*, $f(x)$, which gives the fitness or quality of chromosome (solution) x.
- A method for mutating (i.e. randomly altering) a chromosome. In the case of a binary string encoding, this might be as simple as flipping a few of the bits.
- A method for crossover – the creation of a new individual from two parents. For binary strings this is often done by splitting the strings at some random point and splicing the first part of the first string with the second part of the second one.
- A selection method for selecting parents from a population. Usually individuals are assigned a selection probability proportional to its fitness.

Typically a GA starts by generating a first generation of some size. The fitness function is then calculated for each individual. New generations are then formed by

using the selection method to select two parents and doing a crossover to produce a new individual until the new generation reaches a sufficient size. For each new individual there is also a probability (usually fairly low) of a mutation occurring. Often, so-called *elitism* is also applied, where the best individuals are carried over directly to the new generation so as not to lose any good solutions.

The iteration process can then be continued for a set number of iterations or until a sufficient fitness level is reached. When done, the best individual of the last generation is taken as the solution to the problem.

Application to Image Reconstruction

In the case of image reconstruction from the Fourier magnitude the solution space is the set of all possible images. If the image size is fixed to, say, 100x100 pixels and each pixel is represented by a byte, i.e., 256 possible (gray scale) values, we end up with 255^{10000} possible solutions. The fitness function should tell us how well the Fourier magnitude of the solution matches the observed Fourier magnitude.

Using GAs for image reconstruction from Fourier magnitudes seems to be an area that is not very well explored. A paper by Yoshimori et al. from 2001 [43] discusses a method for applying genetic algorithms to other phase reconstruction algorithms to prevent these from getting stuck at local minima. This method seems to work very well at least for their test cases, but it assumes that the Fourier magnitude is fully known rather than sparsely sampled.

Here, a few different somewhat simplified versions of the algorithm of Yoshimori et al. were implemented and tried out on simulated II data. One implementation was done using the free GA package `pyevolve`[3], and another was written in Python from scratch in an attempt to parallelize the code and take advantage of multi-core CPUs. No big qualitative difference was visible in the results from these two implementations.

Images were encoded simply as 100x100 matrices with each value being an integer between 0 and 255. Other encodings, such as binary strings could also be used, but since a major idea behind GAs is to transfer "useful building blocks" of solutions to later generations [42] it makes more sense to have a two-dimensional encoding. This is also the approach used in [43].

The crossover mechanism can also be implemented in a straightforward manner. A position along the parent image's vertical axis is chosen at random and everything above this location is taken from the first parent, while everything below is taken from the second parent.

When it comes to the mutation method, there are many different possibilities, and a few different approaches were tried out. The obvious and most general way is to randomly change the values of a few individual pixels. This was found to work decently for small images (around 10x10 pixels), but the algorithm tended to converge very slowly for higher resolution images. A different approach where shapes such as rectangles and circles of random sizes and (possibly negative) grayscale values were "painted" onto the

[3] `http://pyevolve.sourceforge.net/`

image proved more successful. This method did however tend to produce some ugly artifacts in the images, as is clearly seen in the chopped-off part of the right star in Fig. 4.11(b).

For the selection of parents, a method known as *Roulette Wheel Selection* was used. In this method, the probability p of a chromosome x with fitness $f(x)$ of being selected is $p = f(x)/\sum_i f(x_i)$. This means that even chromosomes with a lower fitness have a chance of being selected, which in theory should minimize the risk of the algorithm getting stuck in a local minimum. In addition, a strictly elitistic version, where the best parents were always selected, was also tried out [4]. It was found that, at least for the test cases used here, the choice of selection method did not matter much.

Lastly, there's the fitness function. From the simulated observations we have values of the Fourier magnitude in a number of points scattered across the (u, v)-plane. From these values one can interpolate and the the Fourier magnitude evaluated over a regular grid (see Sec. 4.4.2). One suitable choice of fitness function is $f(x) = |\mathcal{F}_x - \mathcal{F}_{\text{obs}}|$, where $\mathcal{F}_x$ is the Fourier magnitude of the image x and $\mathcal{F}_{\text{obs}}$ is the observed (interpolated) Fourier magnitude. Note that for this choice of fitness function, a lower value of $f(x)$ means a better solution. In practice, the reciprocal value of the sum of residuals was used so that higher values means better fitness. This simplifies the implementation of the Roulette wheel selection.

Results

Figures 4.10 and 4.11 shows two examples of GA reconstructions – a binary star and a circular disk observed with a CTA-like array. The simulations did not include any measurement noise, the only imperfections in the observed Fourier magnitude was from the sparse sampling of the (u, v)-plane.

The results are far from perfect, but the general shape and size of the pristine images are reconstructed fairly well, and it is clear that it is possible to reconstruct images from II data with this method.

There are some serious drawbacks to the usage of GAs for image reconstruction. They are computationally heavy and take a long time (several hours in most of the examples tried here) to finish. Also, one is not guaranteed to end up with the best solution.

However, there are also some appealing aspects. These types of algorithms are conceptually simple and require very little mathematical knowledge to implement. This means that it is easy to replace parts of the code and try out different encodings, different mutation methods, different fitness functions etc.

One niche where GAs might fit in is as a hybrid between model-fitting and true image reconstruction. Images could be constrained in various ways – for example an image could be assumed to consist of 0-n ellipses, 0-k rectangles etc, each with different positions, sizes and intensities. Mutating an image would then mean altering not individual pixel values, but rather the properties of the shapes constituting the image. This would of

[4] With this selection method, the algorithm is no longer a GA in a strict sense, but rather a "Random Search Algorithm".

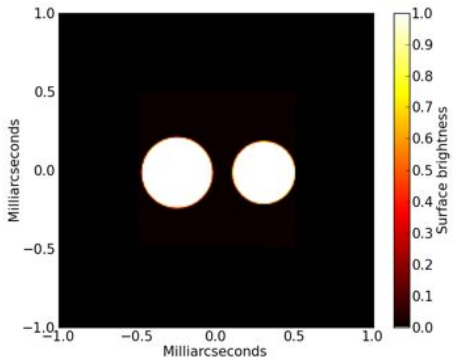

(a) Pristine image

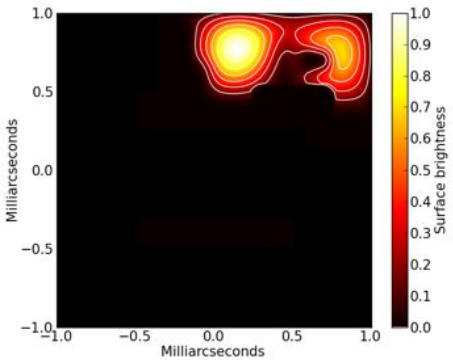

(b) Reconstructed image

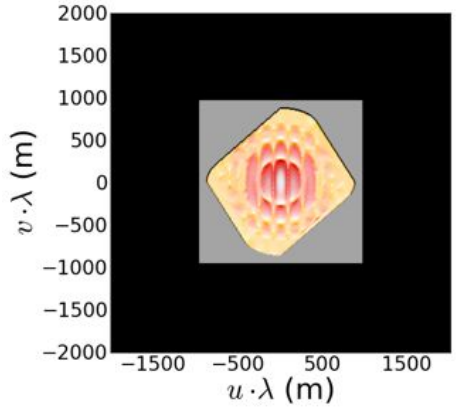

(c) Observed Fourier log-magnitude

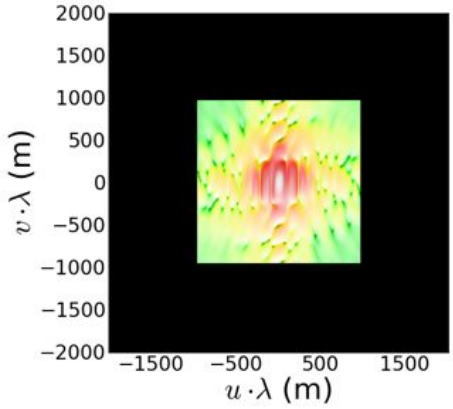

(d) Fourier log-magnitude of reconstructed image

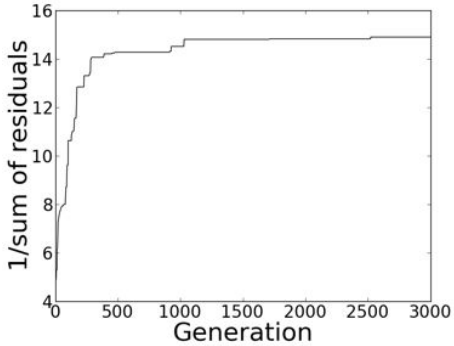

(e) Evolution of fitness function.

Figure 4.10: GA reconstruction of a binary star, observed with a CTA-like telescope array. Note that Fourier magnitudes are invariant to translation, so there's no way to reconstruct the exact position of the target. Figure 4.11(e) shows the improvement of the fitness function (difference between observed and reconstructed Fourier magnitude) as the algorithm progresses.

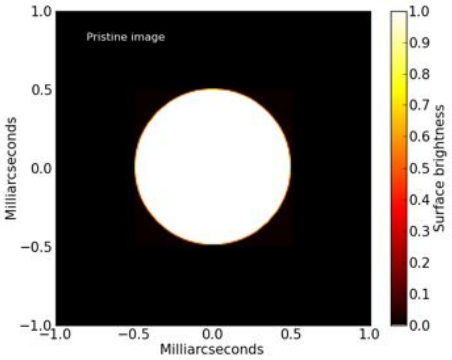

(a) Pristine image

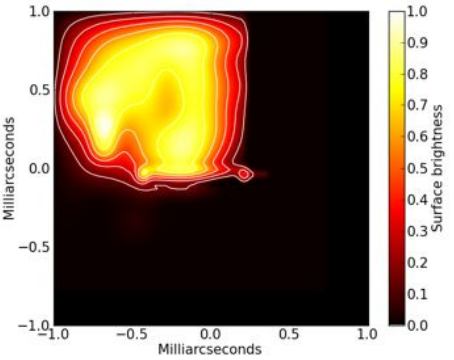

(b) Reconstructed image

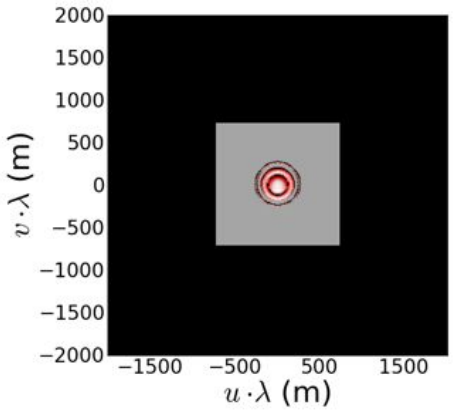

(c) Observed Fourier log-magnitude

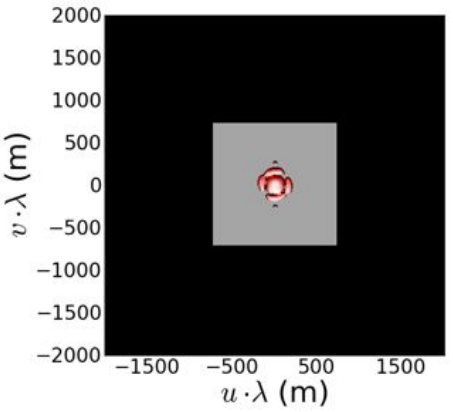

(d) Fourier log-magnitude of reconstructed image

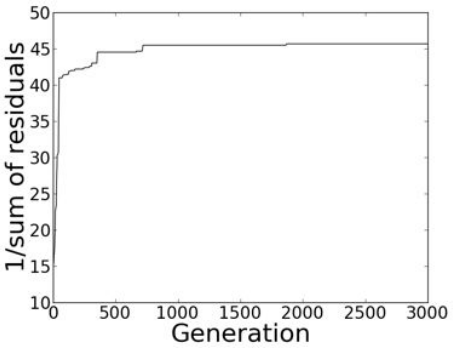

(e) Evolution of fitness function.

Figure 4.11: GA reconstruction of a uniform circular disk, observed with a CTA-like telescope array.

course make the reconstruction less general and more dependent on assumptions, but it would bring down the number of degrees of freedom by several orders of magnitude.

4.6 CTA Telescope Array Layouts

4.6.1 About CTA and Telescope Placement

The upcoming European CTA (Cherenkov Telescope Array, see Sec. 3.2.1) has the potential to become the first modern intensity interferometer to conduct scientifically interesting studies. The final design for CTA when it comes to telescope sizes and placement has yet to be finalized, and a number of candidate configurations are currently being evaluated with regard to their performance in the γ-ray regime, see Fig. 4.14. However, the relative performance of these candidate arrays for γ-ray astronomy (which will of course be the main function of CTA) is not necessarily the same as for intensity interferometry.

Optimizing the telescope placement in an interferometric array is a highly complex and widely studied problem (see e.g. [44], [45]). In short, the situation can be summarized as following: each separation between a pair of telescopes (a baseline) corresponds to one point in the Fourier plane – long baselines provide high-frequency components (i.e. small details in the target of study), and short baselines provide low-frequency components (i.e. larger field of view). An array with n telescopes will have $n(n-1)/2$ baselines, though these are not all necessarily unique. The sampling of the Fourier plane is further affected by the Earth's rotation, the latitude of the array and the declination of the observed object, following Eq. (4.23).

The optimal telescope configuration is thus dependent upon the task at hand. If the objective is to study very small structures, then long baselines are required. If, on the other hand, one wishes to measure large-scale structures, shorter baselines are necessary. For a general-purpose array, it is usually preferable to have a healthy mixture of short and long baselines, sampling the (u, v)-plane as uniformly as possible. In any case it is almost always best to avoid regularly spaced telescopes, since such placement will result in duplicate baselines.

In intensity interferometry, the main targets of study are bright stars ($m_V \lesssim 6$), and thus it is crucial to know something about their angular extent. Figure 4.12 shows the relationship between angular diameter, apparent magnitude, and effective temperature, assuming circular stellar disks of uniform surface brightness radiating as perfect blackbodies. The grey, dashed lines show the baselines at which different angular diameters are resolved.

Figure 4.13 shows the angular diameters of the stars in the Bright Star Catalogue (essentially all the stars that are visible to the naked eye). As we see, most of the brightest stars in the sky have angular diameters on the order of one milliarcsecond, which is resolved by a baseline of ~ 100 m. This means that a telescope array will need baselines at least as long as 100 meters to image any stellar surface features, but it also means that an array that lacks baselines as short as this will be unable to image the shapes of most suitable targets. Thus, perhaps somewhat surprisingly, for kilometer-scale telescope arrays the number of *short* baselines can be a strongly limiting factor

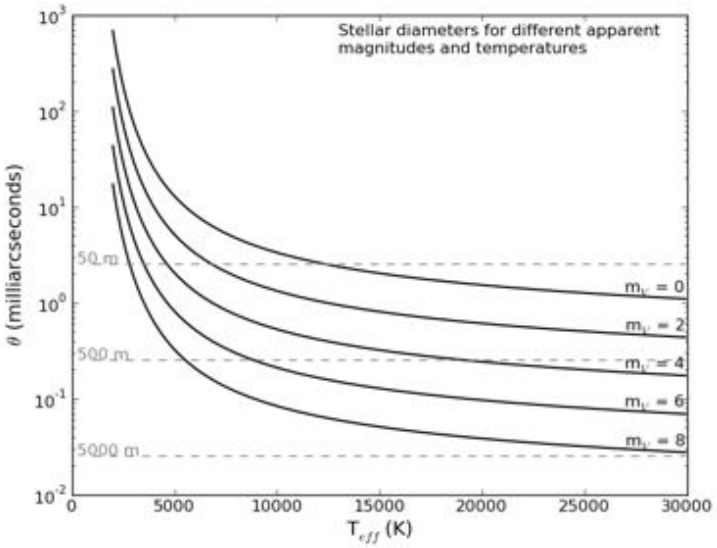

Figure 4.12: Relationship between stellar diameter and effective temperature for different apparent magnitudes. Stars were assumed to be perfect blackbodies with uniform circular disks, observed in the V band (545 nm).
Dashed grey lines show the baselines at which different diameters are resolved, i.e. where the first minimum of the coherence function (Eq. (2.15)) is reached.

when it comes to imaging stars.

4.6.2 Candidate Configurations

A number of candidate array layouts for the CTA are being studied within its design study, of which some are shown in Fig. 4.14. Each of these candidate layouts is a subset of an all-encompassing larger array, shown in the bottom-right corner. Note that several among the configurations are not fundamentally different from each other. Already from a quick glance at Fig. 4.14 one can roughly divide the layouts into three groups: A, B, F and G, whose telescopes are concentrated in a fairly small area and which lack longer baselines; C, D and J which contain telescopes more sparsely spread out over a large area; and E, H, I and K which contain a larger number of telescopes and provide both long and short baselines. For this project, the configurations B, D and I were selected for more detailed study, as "representatives" of the three groups.

The left column in Fig. 4.15 shows the telescope placement of the three configurations, B, D and I (from top to bottom). The middle column shows a "snapshot" (u, v)- (Fourier) coverage of the arrays at an instant in time for a star in the zenith. In the right column, the effect in the (u, v) plane of the star moving 20 degrees to the west is shown.

Already from Fig. 4.15 and Table 4.1 a few things can be said about the candidate designs if applied to intensity interferometry. Configuration B samples the central parts of the Fourier plane very densely and would provide a field-of-view that is fully capable of

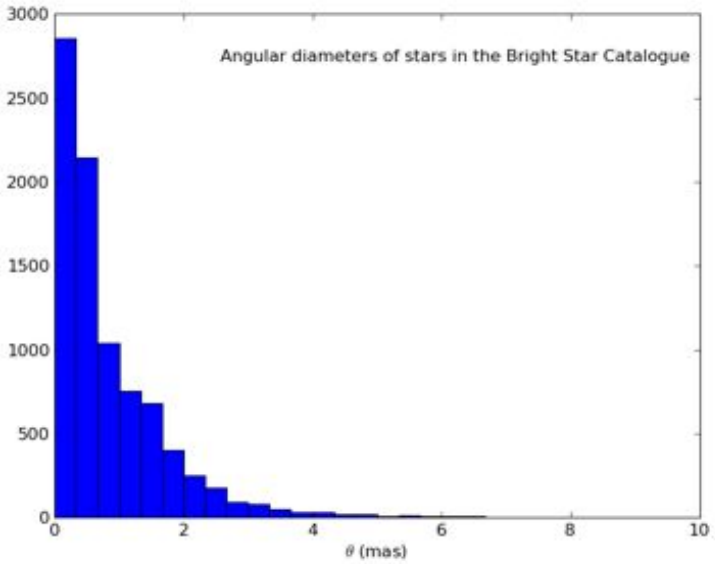

Figure 4.13: Approximated angular diameters of the stars in the Bright Star Catalogue (BSC), containing all the stars in the sky with $m_V < 6.5$. Effective temperatures of the stars were estimated by fitting a polynomial to data relating T_{eff} and $B - V$ color index from [46] and inserting the color indices of the BSC into this. The effective temperatures were then used to calculate the angular diameters assuming the stars are blackbodies with uniform circular disks.

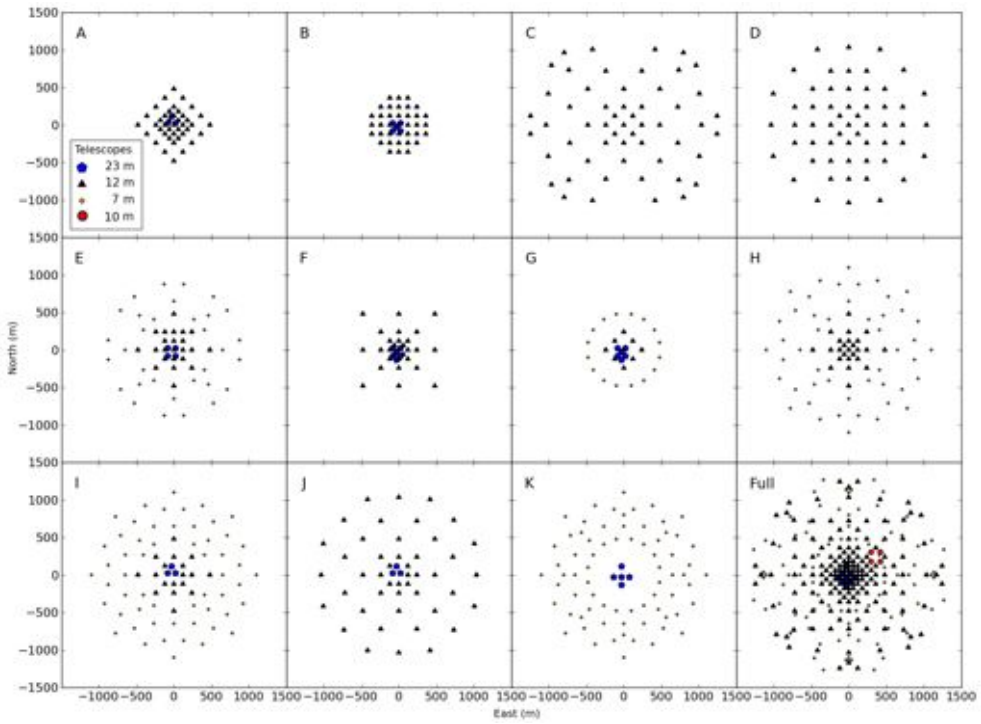

Figure 4.14: Overview of candidate configurations for CTA. Each configuration is a subset of a larger superset configuration (bottom-right corner) produced by Konrad Bernlöhr. In this work, configurations B, D, and I are compared and their performance for intensity interferometry evaluated.

imaging the shapes of almost any stellar object. However, it is lacking longer baselines, making it unable to resolve details smaller than ∼200 μas.

Configuration D on the other hand provides baselines out to 2180 m, permitting studies of very detailed structures, down to around 50 μas. The shortest baseline is 170 m, however, which means that any structures larger than ∼0.75 mas will be lost. This makes it unsuitable for most stars.

Configuration I seems to provide the best of two worlds. It has baselines short enough to measure the shapes of the disks of most stellar objects, while still providing very long baselines and a very good resolution.

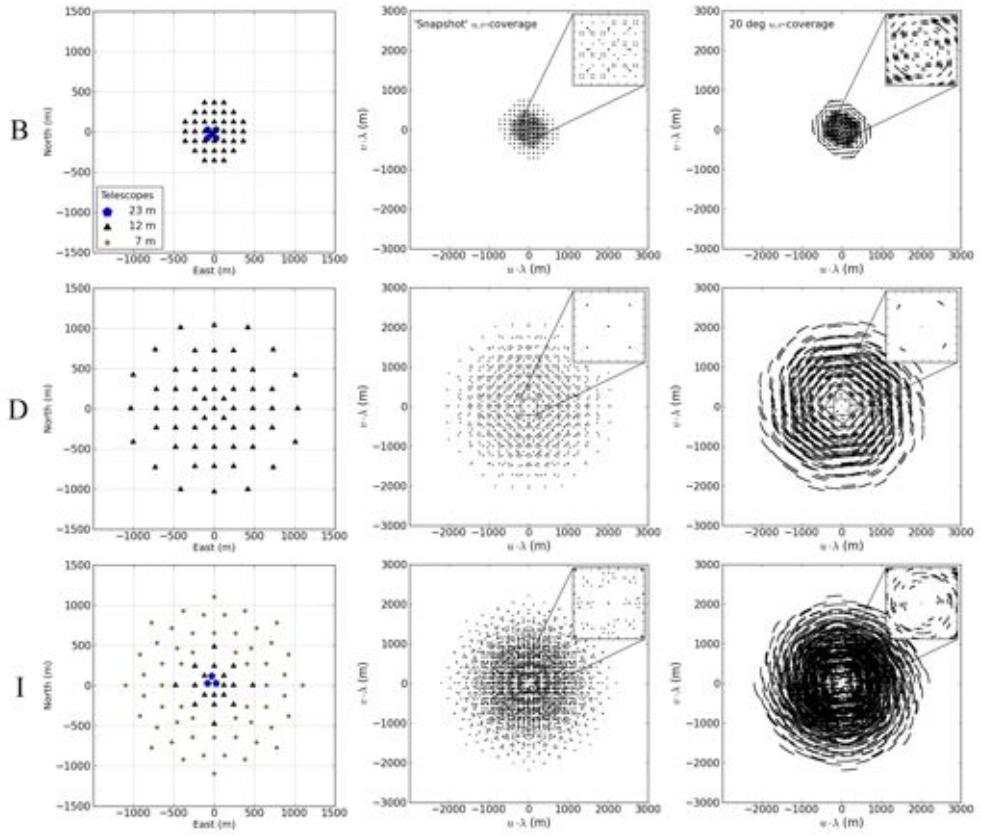

Figure 4.15: Left column: Telescope placement for the three candidate configurations examined: B, D and I from the top to the bottom.
Middle column: (u, v)-plane coverage at an instant in time for a star in the zenith. Upper right-hand squares show the central 400x400 m area.
Right column: (u, v)-plane coverage for a star starting in the zenith and moving 20 degrees to the west.

Table 4.1: Properties of the three examined candidate configurations. The resolution range is the minimum and maximum angular sizes that can be resolved with the array, according to the Rayleigh criterion: $\theta = 1.22D/\lambda$.

	Conf. B	Conf. D	Conf. I
Number of telescopes	42	57	77
Unique baselines	253	487	1606
Shortest baseline	32 m	170 m	90 m
Longest baseline	759 m	2180 m	2200 m
Resolution range @500nm	0.16 - 3.9 mas	0.05 - 0.75 mas	0.06 - 1.4 mas

4.6.3 Simulated Observations

Varying Target Magnitude

The simulation code from Sec. 4.4 was applied to the candidate configurations using the binary star in Fig. 4.16 as input.

Figure 4.17 shows the results of varying the magnitude of the target. The simulations were carried out with the star starting at the zenith and moving 50 degrees to the west in steps of 5 degrees, with an integration time of 2 hours for each time step (thus corresponding to several nights of observations). The observation wavelength was 500 nm with a filter bandwidth of 1 nm, and the detectors were assumed to have a time resolution of 1 ns and a quantum efficiency of 0.7.

The data from the simulations are shown in the Fourier plane. To better illustrate the locations of low-amplitude structures and noise in the Fourier plane, the data were logarithmized and normalized after performing a linear interpolation between the points in the plane to obtain the Fourier magnitude evaluated over a regular grid (see Sec. 4.4.2). A 3D shading was then applied to the data to further highlight the locations of structures. The absolute values of the measured correlations are not of any real significance in this context.

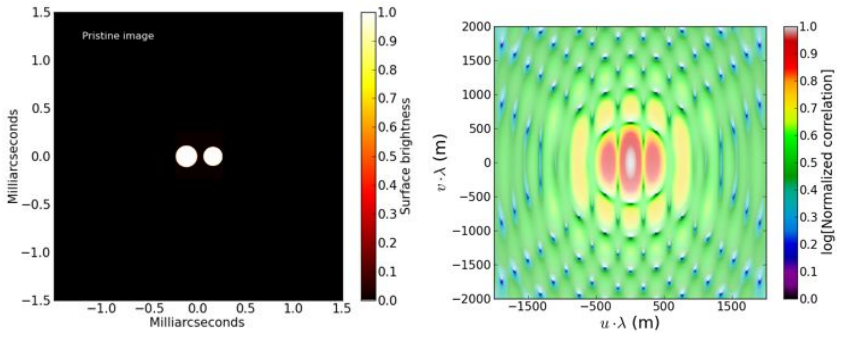

(a) Image (b) Fourier magnitude

Figure 4.16: Test image used for simulations and its (logarithmized) Fourier magnitude.

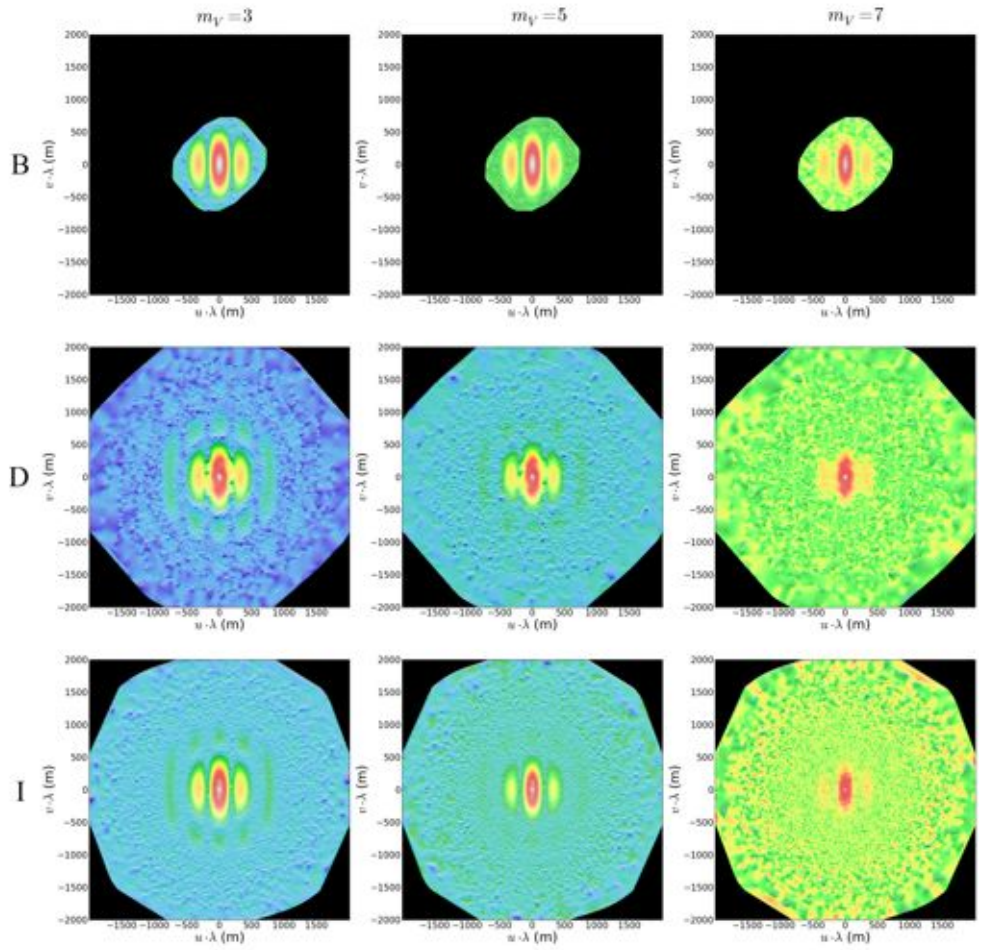

Figure 4.17: Output from simulated observations of the binary star in Fig. 4.16 with configuration B (top row), D (middle row) and I (bottom row).

Figure 4.17 illustrates the relationship between features in the image plane (Fig. 4.16(a)) and the Fourier plane. We see clearly the shortcomings of configuration B in resolving the higher-frequency components.

Configuration D measures the higher-frequency components very well but even for a target with such a small angular extent as this, the central parts of the Fourier plane – which determine the overall shape of the object – are distorted due to poor sampling.

Configuration I samples the whole Fourier plane well, but its smaller telescopes (see Fig. 4.15) make it a bit more sensitive to target magnitude.

Observations with Subsets of the Configurations

Figure 4.19 shows the output from simulations of the binary star in Fig. 4.16(a) using only subsets of the candidate configurations. The subsets (shown in Fig. 4.18) were

generated by selecting telescopes from the full configurations in a pseudo-random fashion, attempting to preserve the general shape of the arrays. In the left column half of the telescopes have been selected, in the middle column one in four, and in the right column one in eight.

The simulation parameters are the same as in Fig. 4.17 except that the magnitude of the star is now fixed at 5 and the integration time has been increased to 10 hours per timestep in order to highlight sampling effects rather than measurement noise.

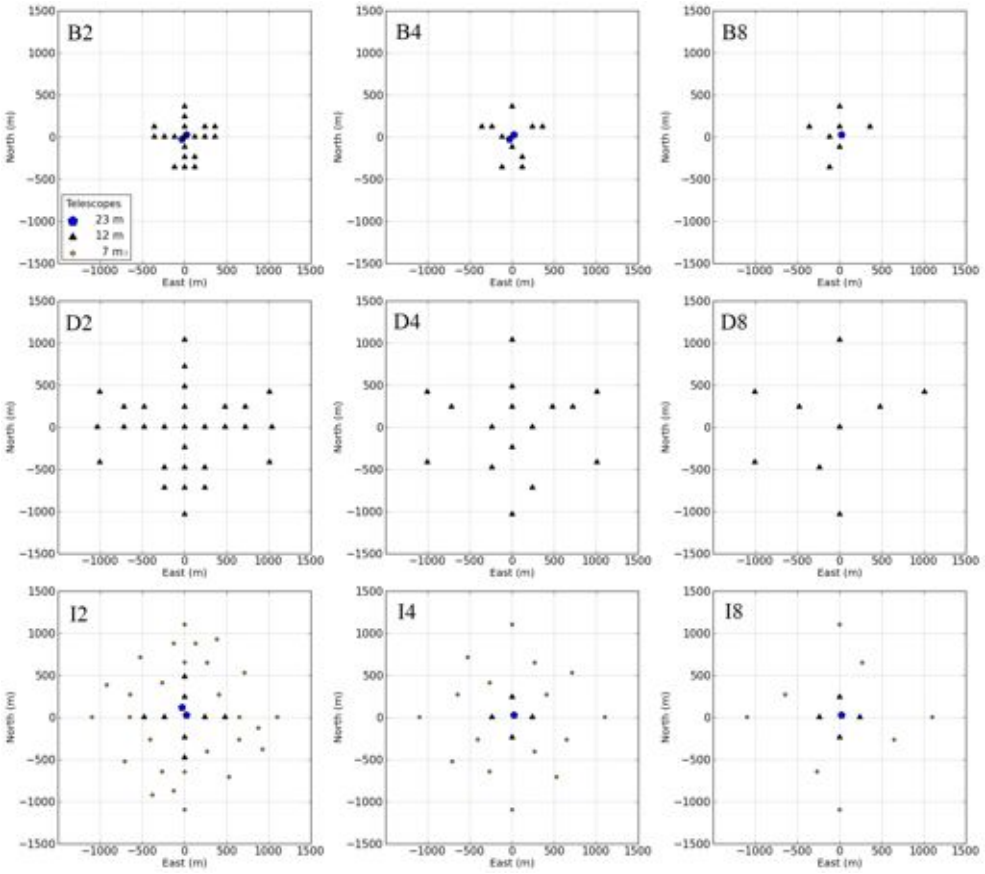

Figure 4.18: Subsets of the candidate configurations (B, D, I from top to bottom). In the leftmost column half the telescope of the superset configuration was selected in a pseudo-random fashion. In the middle column, one in four telescopes was selected, and in the rightmost column one in eight.

It is obvious that more telescopes are better in terms of Fourier plane sampling, and too few telescopes can completely ruin the results as illustrated by the observation by D8. It should be noted, however, that no attempt was made here to optimize the selection of telescopes in order to improve the sampling.

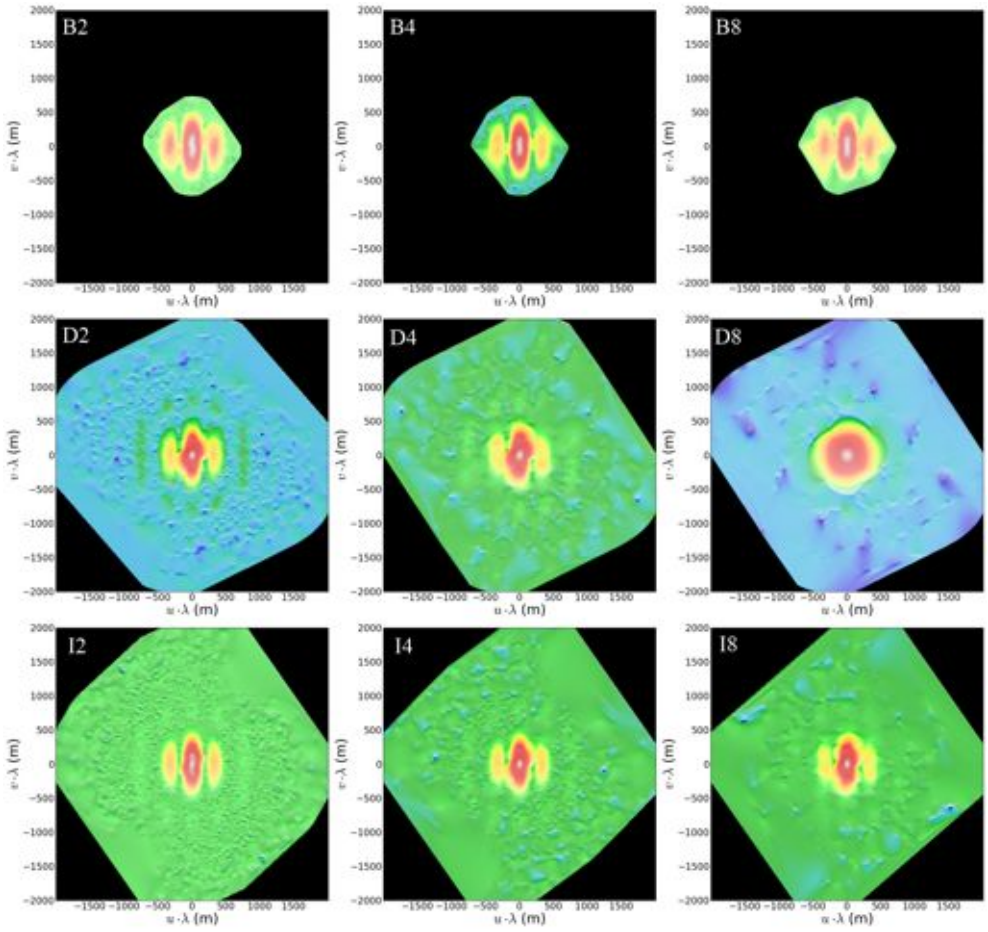

Figure 4.19: Output from simulated observations of the binary star in Fig. 4.16 with subsets of configuration B (top row), D (middle row) and I (bottom row).

Image Reconstruction

The discussion above has only dealt with Fourier magnitudes, which is what is directly measured by an intensity interferometer. Fourier magnitudes alone can be used to fit model parameters such as stellar diameters, binary separations, circumstellar disk thicknesses etc. As we saw in Sec. 4.5, model-independent image reconstruction from the Fourier magnitude alone is indeed possible (though with some limitations).

A number of proof-of-concept examples of images reconstructed from simulated data using the candidate configurations are shown later on, in Sec. 5.5. However, image reconstruction is an active area of research and many practical issues remain to be improved. Thus, it is difficult at this stage to determine whether imperfections in reconstructed images are due to fundamental limitations of the algorithms used or simply due to practical issues that can be solved. Because of this, there is a great risk that a comparison between reconstructed images from the different candidate arrays would be misleading,

which is why the focus here is placed on the algorithm-independent Fourier magnitudes instead.

4.6.4 Conclusions

An instrument such as the CTA will likely be able to produce excellent scientific data if used as an intensity interferometer, providing measurements of spatial structures on scales down to a few tens of μas – orders of magnitude better than what is possible today in visible light.

The candidate configurations examined here – while not optimized for intensity interferometry – all provide very dense sampling of the (u, v)-plane due to the sheer number of telescopes. Apart from the simulations described above, a number of other tests were carried out to determine the effects of varying the declination of the star and the geographic orientation of the telescope array. It was found that the very large number of telescope make the effects of any such variations negligible.

It should be noted however, that an array such as configuration D will be severely crippled by its lack of short baselines, essentially limiting the instrument to studying stars smaller than $\sim$0.5 mas.

Chapter 5

Hot Stars as Targets for Intensity Interferometry

The following chapter describes a brief investigation of possible suitable targets for intensity interferometry that was presented at the 2009 Workshop on Stellar Intensity Interferometry in Salt Lake City. It is also summarized in [47].

The simulation code from the preceding chapter was applied to models similar to these targets; the results from these simulations are presented at the end of this chapter.

5.1 Background

The signal to noise ratio of an intensity interferometer improves with the temperature of the target. Since SII is insensitive to atmospheric disturbances, observations in the violet or blue pose no problem. Eliminating the "Achilles' Heel" of standard phase interferometry will enable high resolution studies of hot stars over very long geometric baselines.

As a small step in the ongoing evaluation of the scientific potential of SII, a list of a handful of bright, hot and astronomically interesting stars was produced. These targets provide a quick overview of some of the things that are reasonable to observe with SII within the not-too-distant future. Such a list might also be useful as a rough starting point for future observing programs.

5.2 Selection of Objects

As a starting point, the Bright Star Catalogue (BSC) was used. This catalog, shown as a color-magnitude plot in Fig. 5.1, contains the brightest stars in the sky, down to an apparent magnitude of around 7.

To get a rough estimate of the effective temperatures of the stars in the BSC, table values from [46] were used to acquire a polynomial fit relating color index to effective temperature. The hotter part of the BSC, $T_{eff} \gtrsim 9000$ K, is shown in Fig. 5.2 with color index converted to effective temperature.

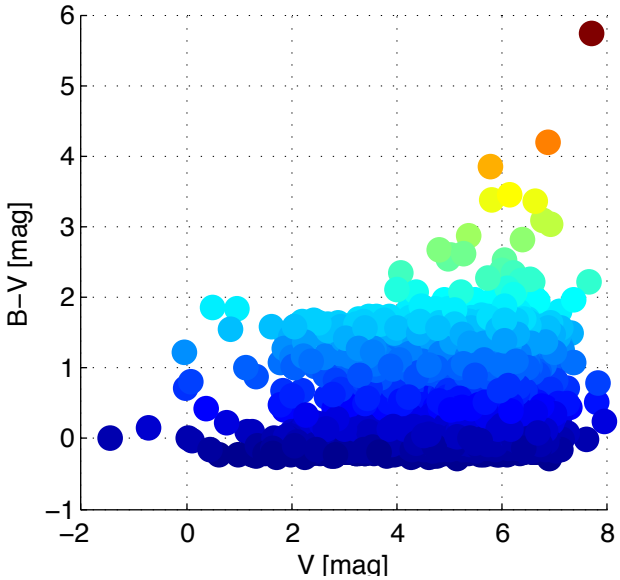

Figure 5.1: The entire Bright Star Catalogue

In the sky, approximately 2600 stars exist that are brighter than visual magnitude 7 and hotter than 9000 K. This is an interesting number to note, as all of these stars would likely be realistic targets even for a fairly modest intensity interferometer.

To narrow the list down, hot and bright objects with $T_{eff} > 9000\ K$ and $V < 2$ were selected along with extremely hot ones, $T_{eff} > 25000$K. To this new list, a few other interesting targets were then added manually. Finally, the angular diameters of the targets were looked up in CHARM2, a compilation of angular diameter measurements from different sources [48].

It should be noted that the selection criteria used are not based upon any calculations on what is possible to observe. Rather, they were decided upon in order to extract a few of the "best" targets that exist. The list should thus *not* be interpreted as an evaluation of what can be seen, but rather as an exemplification of a few stars that can be considered "prime observational targets".

5.3 List of Objects

After the selection process described above, the list of targets contained 37 objects, plotted in Fig. 5.3. The sizes of the circles indicate the angular diameter. A cross in the circle indicates that no entry was found in CHARM2.

Table A.1 shows the list of targets along with some data and notes highlighting their scientific relevance. In very general terms, a target should have some sort of features on a (sub-)milli-arcsecond level to be considered astronomically interesting in this context.

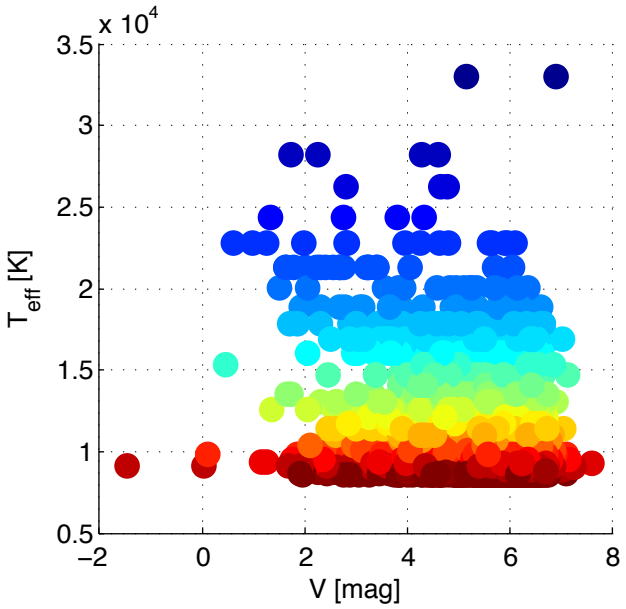

Figure 5.2: The hotter part of the Bright Star Catalogue

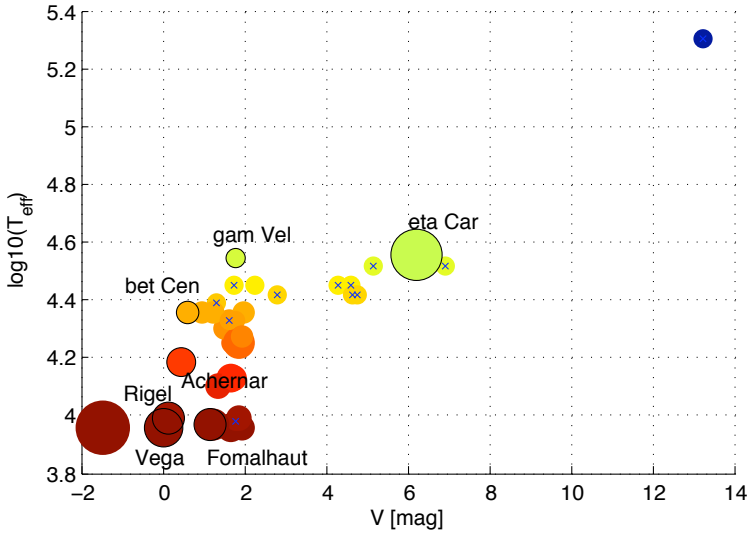

Figure 5.3: The final selection of stars

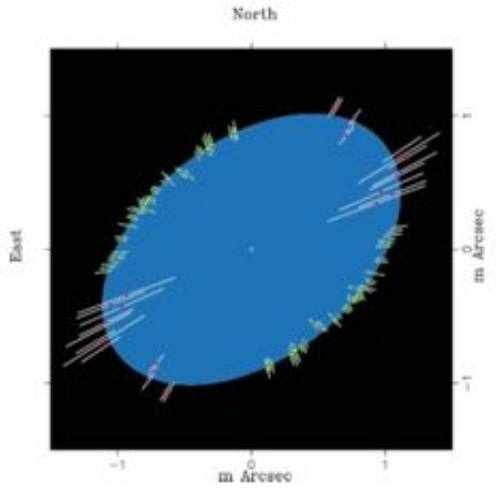

Figure 5.4: The flattened shape of α Eridani as revealed by the VLTI. Each 'line' along the edge of the star represents a measurement (with error bars) of the stellar diameter at different angles. Figure from [2].

These features could be, for instance, deformation due to rapid rotation, pulsation, stellar disks, hot stellar winds, mass accretion etc.

5.4 Some Specific Targets

Of the stars in table A.1 a few especially interesting ones were singled out for further investigation. The literature was examined for relevant previous studies. These stars are presented below, along with some brief notes on their science potential for SII.

5.4.1 Achernar (α Eridani)

Achernar is a rapidly rotating Be-star ($v \sin i$ = 250 km/s). Long-wavelength studies with the VLTI (Fig. 5.4) have recently revealed the flattened shape of the star – a direct result of the rotation [2].

In addition to the flattening, the rapid rotation of Achernar results in other effects, such as a complex stellar wind and a circumstellar disk with H-alpha emission lines. The presence of bright emission lines is especially interesting in this context; since the S/N of an intensity interferometer is independent of the spectral passband, studies in the continuum may be combined with observations centered around the emission line.

5.4.2 Rigel (β Orionis)

Rigel is the nearest blue supergiant (240 pc). It is a very dynamic object with variable absorption/emission lines and oscillations on many different timescales – from minutes to weeks [49]. The physical properties of Rigel have recently been shown to be very similar to the supernova progenitor of SN1987A. This realization makes understanding the dynamical nature of Rigel highly relevant.

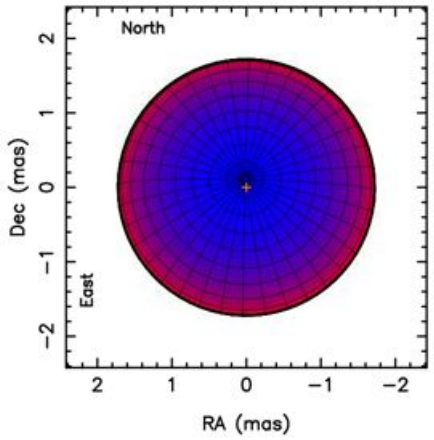

Figure 5.5: Intensity distribution at 500 nm at the surface of Vega.

5.4.3 β Centauri

β Centauri is a binary system consisting of two very hot, very massive variable stars. Both components are variable both spatially and in their line profiles.

The intricate nature of the system has led to it being called "a challenge for current evolution scenarios in close binaries", and studies of this object on a (sub-)milliarcsecond level will no doubt yield valuable information for stellar evolution modeling [50].

5.4.4 Vega (α Lyrae)

While one of the most fundamental stars in the sky for calibration purposes, the nature of Vega has proven to be more complicated than previously thought. Recent phase interferometry studies suggest an 18-fold drop in intensity at 500 nm from center to limb (Fig. 5.5), consistent with a rapidly rotating pole-on model, as contrasted to the 5-fold drop predicted by non-rotating models [51]. Intensity interferometry will allow direct studies of the intensity distribution at shorter wavelengths and in different passbands. Such observations will lead to a better understanding of the link between rotation and limb darkening in different wavelength regions.

5.4.5 η Carinae

η Carinae is the most luminous star known in the Galaxy, and an extremely unstable and complex object. Recent VLTI studies have revealed asymmetries in the stellar winds due to the rapid rotation of the star [52]. Like Rigel, η Carinae is believed to be on the verge of exploding as a core-collapse supernova.

5.4.6 γ^2 Velorum

γ^2 Velorum is a binary consisting of a hot O-type star and a Wolf-Rayet star. The proximity to the O-type star creates a situation where two stellar winds interact, creating a wealth of interesting phenomena such as wind collision zones, wind-blown cavities and

eclipses of spectral lines [53]. The bright emission lines of WR stars make them suitable for comparative studies in different passbands, as discussed above.

5.5 Simulated Observations

To study what could actually be observed with a given set of instrumentation, the simulation code from Chapter 4 was applied to models of targets similar to the ones singled out above. The plots below are generally on the same format as Fig. 4.17, i.e. they show the logarithm of the measured correlation interpolated over a grid and with 3D shading applied to highlight structures and noise in the Fourier plane. Given the Fourier magnitude, which is the "raw data" of an intensity interferometer, one can go in several directions: one can for example try to reconstruct the image of the source, or one can use prior knowledge of the target and attempt to fit a model with one or several parameters to the data.

In this chapter, focus is placed on the Fourier magnitude. Just by looking at the measured correlations, we can say something about what can be observed and where in the Fourier plane most of the important information is located for some interesting types of astronomical targets.

A few reconstructed images are also shown, created using the software package SI-ISoft v0.11 courtesy of Paul Nuñez, University of Utah. This software uses the Cauchy-Riemann method described in Sec. 4.5.1. It should be noted that the difference between the pristine and the reconstructed image depends on a number of factors:

- The area in the Fourier plane sampled by the telescope array. Any frequencies too high or low to be covered will naturally be beyond recovery. In other words, the reconstructed image can never be better than the pristine image convolved with the point-spread function of the array.
- The density and uniformity of the Fourier plane sampling.
- Measurement noise.
- Issues with the image reconstruction algorithm itself.

As the version number indicates, this software was not in a "finished" state as of this writing. It is stressed therefore that imperfections in the reconstructed images do not necessarily represent fundamental limitations with II or even with the algorithm used, but may simply be due to minor issues with this particular implementation.

5.5.1 Simulation Parameters

The simulations take the following parameters as input (the notation here will be used in the rest of the section):

- m_V – The V band apparent magnitude of the target.
- T_{eff} – The effective temperature of the target.

- h – The hour angle range for the simulation. $h = (0\,^\circ, 50\,^\circ)$ means that the target started in the south and moved 50 degrees west during the observation.
- Δh – The hour angle step, see Sec. 4.4.2 and Fig. 4.6 for an explanation.
- δ The declination of the star.
- T – The observation time *per hour angle step.*
- Δt – The time resolution of the detectors.
- QE – The quantum efficiency of the detectors.
- λ_f – The filter wavelength.
- $\Delta\lambda$ – The filter bandwidth.
- l – The latitude of the telescope array.
- Array – The telescope array used. In this section the candidate layouts CTA B, CTA B and CTA I were used. These configuration are shown in Fig. 4.15.

5.5.2 Stellar Diameters and Binary Separations

The main purpose of the Narrabri Intensity Interferometer was to measure the angular diameters of stars. Even with only two telescopes, this was done with great accuracy. It was also possible to study such things as binary separations by fitting models to the data [15].

A modern intensity interferometer using a CTA-like array would be able to perform these sorts of measurements in a much more accurate and model-independent manner, since such an array samples the Fourier plane in thousands of points as compared to the ∼5 points for typical measurements at Narrabri. This will also make it possible to study a much wider range of features including rotational deformation and mass transfer regions.

Binary Radii

Figure 5.5.2 shows the results from simulations of three binary stars with the radius of one of the stars being varied (simulation parameters are listed in the image caption). The radius of the secondary changes by only a few tens of micro-arcseconds, but still this change is clearly visible in the Fourier magnitude, and even the reconstructed images reproduce the stellar diameters and separations with remarkable accuracy.

Binary Separations

Figure 5.7 shows three frames from an image sequence of an eclipsing binary. Input parameters, similar to those in the previous simulations, are given in the figure caption. Once again, it is evident that properties such as stellar diameters and binary separations are very well reconstructed.

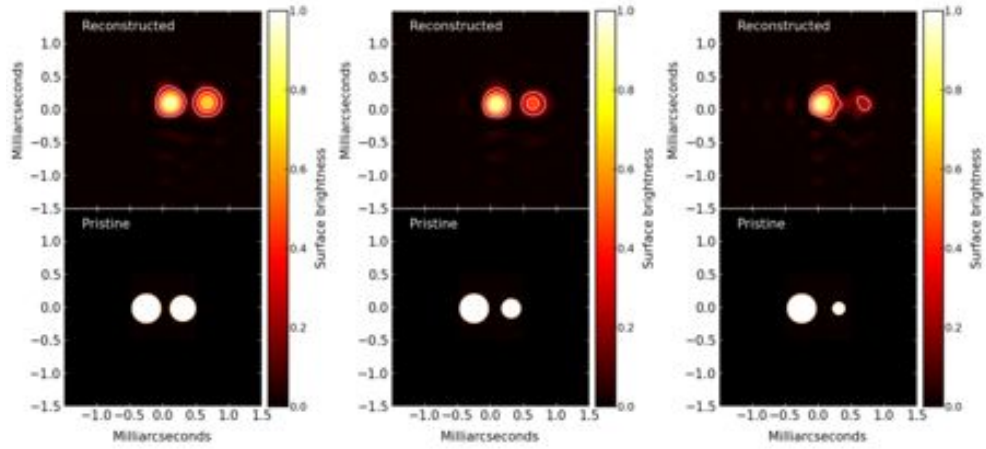

(a) Reconstructed images

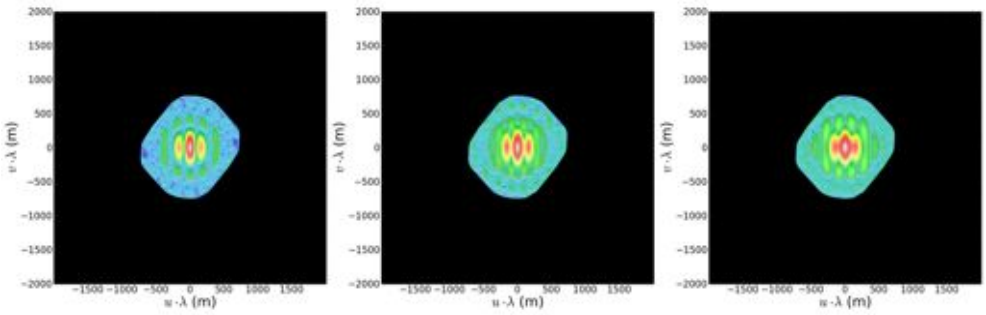

(b) Fourier magnitudes

Figure 5.6: Simulation of binary stars with different radii.
Simulation parameters: $m_V = 3$; $T_{eff} = 7000$ K; $h = (-50\,^\circ, 50\,^\circ)$; $\Delta h = 10\,^\circ$; $\delta = 30\,^\circ$; $T = 5$ h; $\Delta t = 1$ ns; $\lambda_f = 500$ nm; $\Delta\lambda = 1$ nm; QE= 0.7; $l = 30\,^\circ$; Array= CTA B

Hot, Rapidly Rotating Star

Figure 5.8 gives a showcase of what could be possible with a large telescope array. It shows a rotationally flattened star, a mere 200 μas from pole to pole. This is similar to a visible-light version of Fig. 5.4, but the resolution here is about 10 times better and the reconstruction is completely model-independent.

5.5.3 Dark Surface Features

The dense sampling of the Fourier plane provided by CTA-like telescope arrays enables studies going beyond simple determination of stellar shapes and diameters, to image surface features such as starspots and obscuring dust disks (cf. Fig. 2.6).

A number of simulations of such features were carried out, and the general conclusion is that dark surface features need to be large to be observed. Imaging such phenomena

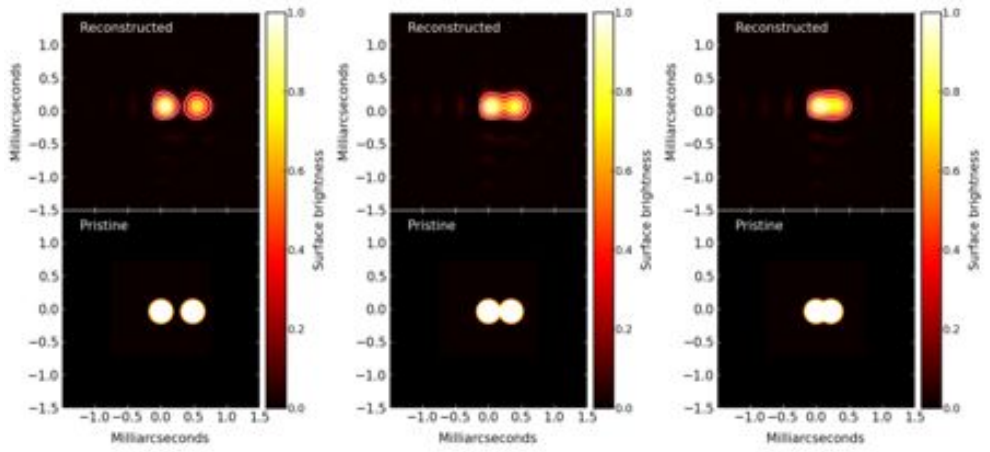

(a) Reconstructed images

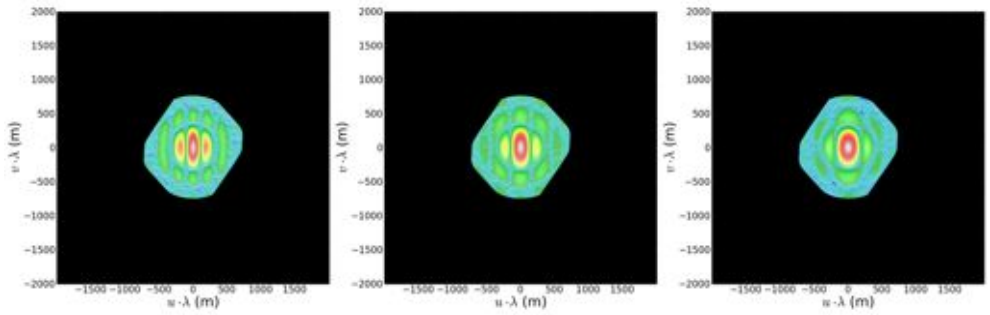

(b) Fourier magnitudes

Figure 5.7: Simulation of binary stars with different separations.
Simulation parameters: $m_V = 3$; $T_{eff} = 7000$ K; $h = (-75\,^\circ, 75\,^\circ)$; $\Delta h = 10\,^\circ$; $\delta = 30\,^\circ$; $T = 10$ h; $\Delta t = 1$ ns; $\lambda_f = 500$ nm; $\Delta\lambda = 1$ nm; QE= 0.7; $l = 30\,^\circ$; Array= CTA B

as planetary transits will likely be very challenging and will probably not be realistic in the foreseeable future.

Figures 5.9 and 5.10 show two examples of what is nevertheless possible – a flattened star with an obscuring disk, and a circular star with a large dark spot. Comparing the shape of the Fourier magnitude in Fig. 5.9(b) with Fig. 5.8(b), we see that the case with a disk is clearly distinguishable from the case without a disk, and likewise the Fourier magnitude in Fig. 5.10(b) is different from the case of a uniform circular disk (which gives rise to a circularly symmetric Fourier magnitude).

The reconstructed images are somewhat less than perfect, but as stressed earlier this can not yet be interpreted as being due to any fundamental limitations.

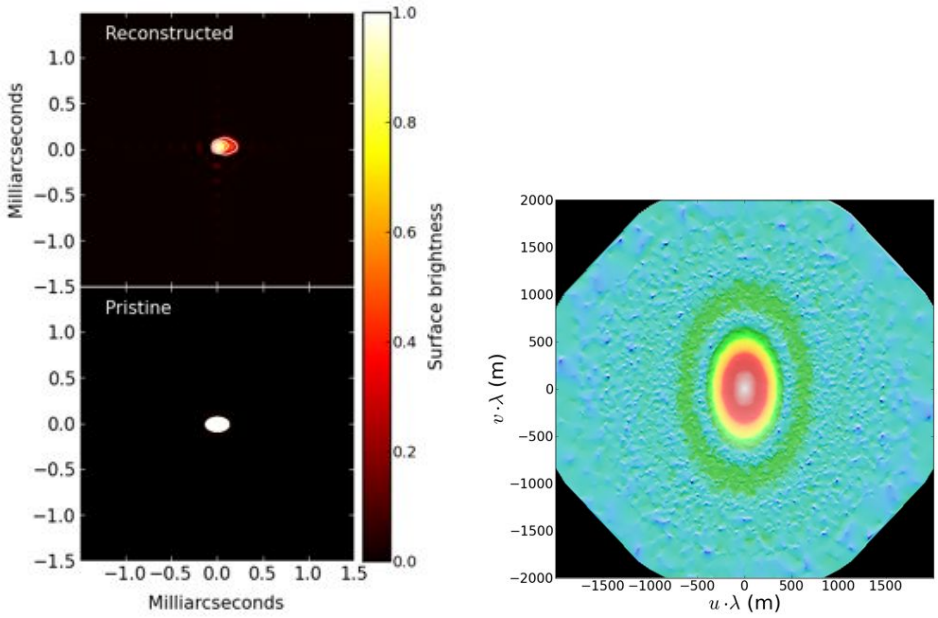

(a) Reconstructed image (b) Fourier magnitude

Figure 5.8: Simulation of a rotationally flattened hot star.
Simulation parameters: $m_V = 5$; $T_{eff} = 12000$ K; $h = (-50\,^\circ, 50\,^\circ)$; $\Delta h = 10\,^\circ$; $\delta = 30\,^\circ$; $T = 10$ h; $\Delta t = 1$ ns; $\lambda_f = 500$ nm; $\Delta\lambda = 1$ nm; QE= 0.7; $l = 30\,^\circ$; Array= CTA D

5.5.4 Emission-Line Features

One interesting feature of intensity interferometry is that the signal-to-noise is independent of spectral passband. A narrow filter will let through less light, but it will contain less frequencies and have a longer coherence time and these two effects exactly compensate for each other (to a first order approximation).

Thus, if the target has emission-line features the signal-to-noise can be greatly increased by observing in a narrow spectral range centered around the emission line. For example, Be-stars typically reach fluxes up to 6 times above the continuum level in the emission lines [54]. Observing such a star in an emission line would be equivalent to continuum observations of a star 6 times (or roughly 2 magnitudes) brighter.

This property of intensity interferometry was exploited already at Narrabri by Hanbury Brown et al [15] when measuring the stellar diameters of γ^2 Velorum (Sec. 5.4.6).

Figure 5.12 shows a Be star with emission lines coming from a thin circumstellar disk. The flux from the emission line was assumed to be 6 times stronger than the continuum. The disk is only 20 μas thick but gives rise to very distinct structures in the Fourier plane at long baselines.

Another possibility, perhaps a bit more far-fetched, is to exploit the insensitivity to optical passband to image non-radial higher-mode pulsations in stars such as Cepheids. Such stars will have some regions moving outwards at high velocities, while other areas will move inwards [55]. In white light, the differences between these regions will be

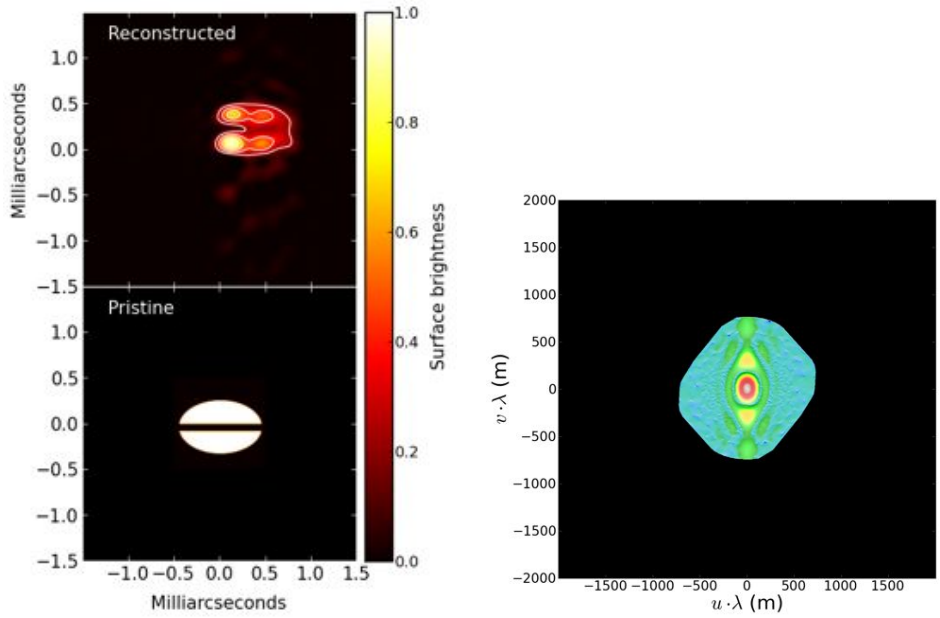

(a) Reconstructed image (b) Fourier magnitude

Figure 5.9: Simulation of a rotationally flattened star with an obscuring disk.
Simulation parameters: $m_V = 3$; $T_{eff} = 9000$ K; $h = (-50\,^\circ, 50\,^\circ)$; $\Delta h = 10\,^\circ$; $\delta = 30\,^\circ$; $T = 3$ h; $\Delta t = 1$ ns; $\lambda_f = 500$ nm; $\Delta\lambda = 1$ nm; QE= 0.7; $l = 30\,^\circ$; Array= CTA B

negligible. However, if the star is observed in a very narrow passband centered on an absorption line, then light emitted from rapidly moving areas may be Doppler shifted enough to avoid the absorption line, and the result will be a large contrast between inwards-moving and outwards-moving areas.

Figure 5.13 shows a simulated observation of a star with non-radial pulsations, with stellar diameters resembling those of the Cepheid l Car. A theoretical surface map of the perturbations from a $m = 4$, $l = 5$ mode pulsation from Jankov et al. [55] was mapped onto a sphere to create the pristine image (Fig. 5.13(c)). An absorption line depth of $\sim$50% was assumed.

A clearly visible problem here is that Cepheids are relatively cool stars, and bright Cepheids will thus have large angular diameters, putting all the structures in the Fourier plane within a very small area (see Fig. 5.13(a)). A second simulation of a hypothetical hot Cepheid-like star, with angular diameter $\theta = 1$ mas, is shown in Fig. 5.13(b). The Fourier magnitude is clearly distinct from the circularly symmetric case, suggesting that the study of phenomema like this are not completely unrealistic.

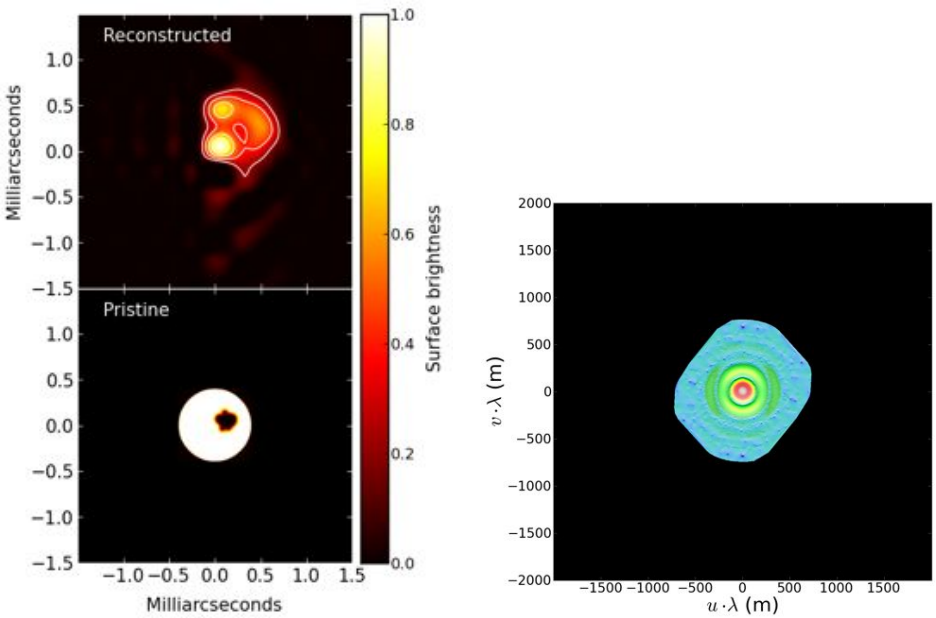

(a) Reconstructed image (b) Fourier magnitude

Figure 5.10: Simulation of a star with a large dark spot.
Simulation parameters: $m_V = 3$; $T_{eff} = 10000$ K; $h = (-50\,^\circ, 50\,^\circ)$; $\Delta h = 10\,^\circ$; $\delta = 30\,^\circ$; $T = 10$ h; $\Delta t = 1$ ns; $\lambda_f = 500$ nm; $\Delta\lambda = 1$ nm; QE= 0.7; $l = 30\,^\circ$; Array= CTA B

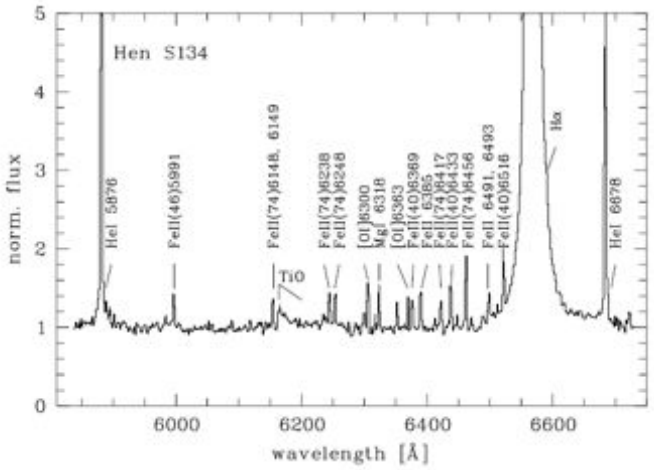

Figure 5.11: Spectrum of the typical B[e] star HD38489. The flux in the emission lines are many times stronger than the continuum, so II observations in emission lines can be equivalent of increasing the intensity by several magnitudes. Figure from [54].

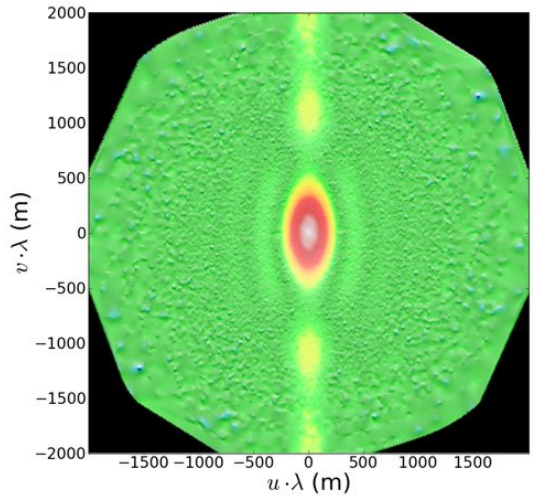

(a) Fourier magnitude, emission line

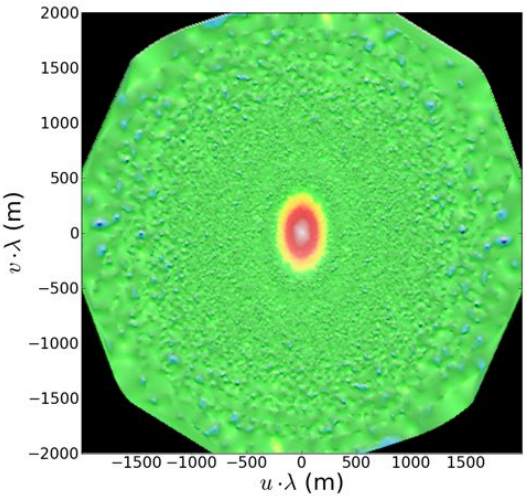

(b) Fourier magnitude, continuum

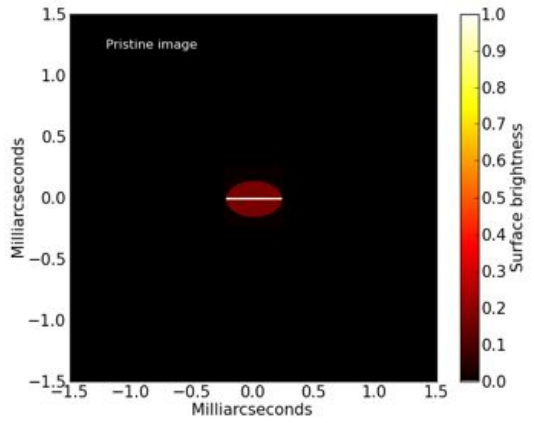

(c) Input image

Figure 5.12: Simulation of a flattened star with emission line disk. Figure 5.12(a) shows observation at HeI emission line at 587 nm. Figure 5.12(b) shows the same target observed in the continuum. Simulation parameters: $m_V = 6$; $T_{eff} = 7000$ K; $h = (0\,^\circ, 50\,^\circ)$; $\Delta h = 10\,^\circ$; $\delta = 30\,^\circ$; $T = 10$ h; $\Delta t = 1$ ns; $\lambda_f = 587$ nm; $\Delta\lambda = 1$ nm; QE= 0.7; $l = 30\,^\circ$; Array= CTA I

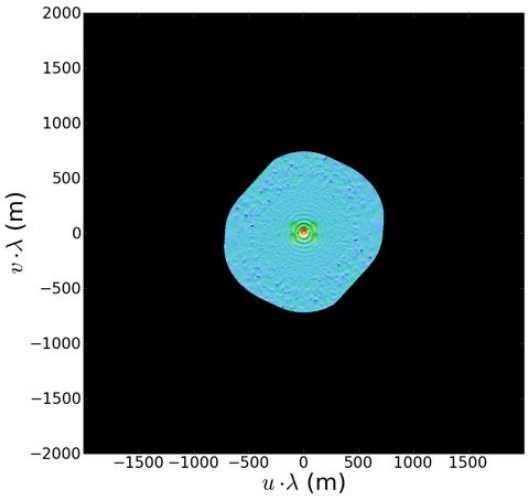

(a) Fourier magnitude

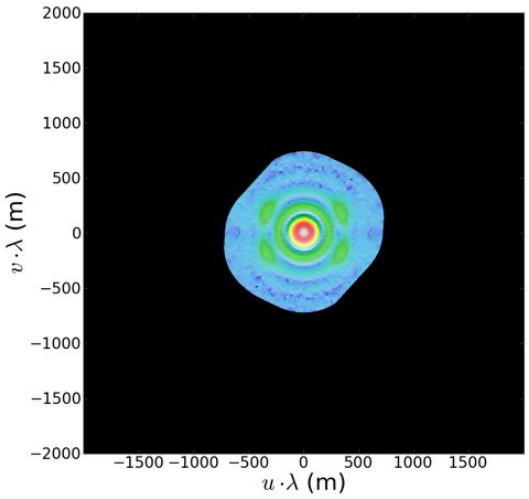

(b) Fourier magnitude of small star

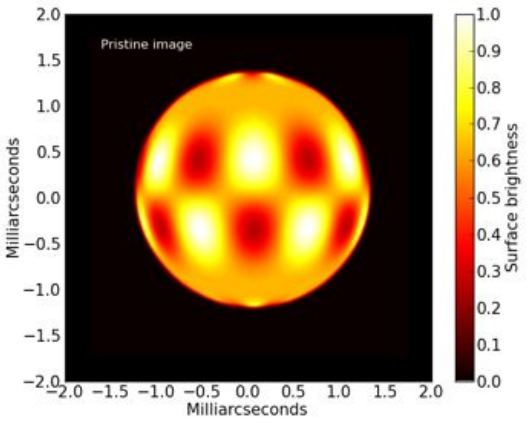

(c) Input image

Figure 5.13: Simulation of Cepheid-like star. Figure 5.13(b) shows the same as fig. 5.13(a) but with the angular diameter of the target decreased to 1 mas.
Simulation parameters: $m_V = 3.4$; $T_{eff} = 7000$ K; $h = (-75\,^\circ, 75\,^\circ)$; $\Delta h = 5\,^\circ$; $\delta = 30\,^\circ$; $T = 10$ h; $\Delta t = 1$ ns; $\lambda_f = 500$ nm; $\Delta\lambda = 1$ nm; QE= 0.7; $l = 30\,^\circ$; Array= CTA B

Chapter 6

Laboratory Experiments

While the main focus of this project was on theory and simulations, some attempts were also made to carry out laboratory experiments in order to identify potential practical problems with the instrumentation and to verify results from the simulations. Unfortunately, the equipment used turned out to give flux rates that were not sufficient to measure any real intensity interferometric signal. Nevertheless, some results were obtained, and these are presented in this chapter along with some of the experiences gained and some thoughts on how these experiments could be improved in the future.

6.1 Laboratory Setup and Equipment

A laboratory experiment – similar in principle to the outline of a simple intensity interferometer in Fig. 2.8, but with modern digital equipment – was set up in the optics laboratory at Lund Observatory.

In the first version of the experiment, a mercury arc lamp shining through a 25 μm pinhole acted as an "artificial star". Light from the lamp was gathered by two $\sim$3 cm refractors and focused on the light sensitive areas of two photon counting detectors. The signals from these two detectors were then fed to a digital correlator connected to a computer. The whole setup is outlined in Fig. 6.1.

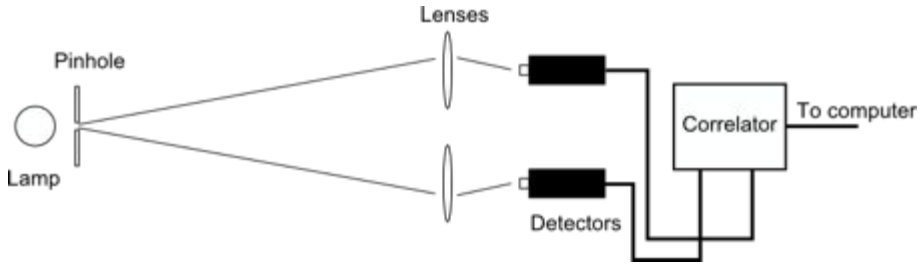

Figure 6.1: Outline of the laboratory experiment.

The correlation measured will be proportional to the optical coherence, so by making measurements while increasing the detector separation, one should obtain something like

the dashed lines in Fig. 2.4, though for a 25 μm pinhole at a distance of 4 m the coherence function will reach its first minimum at around 10 cm.

6.1.1 Practical Issues

One big practical issue was the problem with focusing the light form the arc lamp onto the very small light sensitive area of the detectors (this area is on the order of 0.1x0.1 mm for most detectors). The light from the lamp was too faint to be seen by the naked eye and monitoring the received light intensity required a computer which is a problem since the light from the computer screen was much brighter than the light from the arc lamp.

To deal with this problem, a simple computer program was written using dll interface files from the correlator manufacturer correlator.com. This program monitors the received light intensity and emits short beeps twice a second with a frequency proportional to the photon count rate. Using this program it is possible to do all the focusing in complete darkness by just adjusting the positions of lenses and detectors until the beeps reach a maximum tone height.

A second – and as it would turn out, more serious – issue was the received flux from the lamp. To get a good signal (i.e. a detectable difference in correlation between different detector separations), a high flux within a low spectral passband is required. Furthermore, the light source must have a very small spatial extent to provide a diffraction pattern of reasonable size (since the detectors could not practically be brought closer to each other than $\sim$5 cm). The light must also be chaotic in nature (as discussed in the theory section) ruling out lasers. The Hg arc lamp was selected for this purpose: it reaches temperatures of up to 3000 K, which gives it an extremely high surface brightness. A narrow-band optical filter was selected singling out the brightest emission line, at 546 nm, so as to increase the spectral purity of the light while keeping the flux as high as possible.

However, the count rates obtained were not enough to detect a real signal within a reasonable integration time. Figure 6.2 shows signal-to-noise ratios simulated using the method described in Sec. 4.2.1 for different count rates. Clearly, count rates of a few MHz would be desirable; however the actual received count rates were only on the order of a few hundred kHz.

Nevertheless, it was possible to do some experiments relating to the noise properties of the setup, even though the count rates were too low to give any measurable HBT correlation. These are described below.

6.2 Experimental Results

6.2.1 Systematic Effects from Detectors

Although the Hg arc lamp turned out to give too low count rates to see any differences in correlation between different detector separations, it was possible to examine some properties of the noise. A digital correlator, as described in Sec. 3.4.1, generally stores

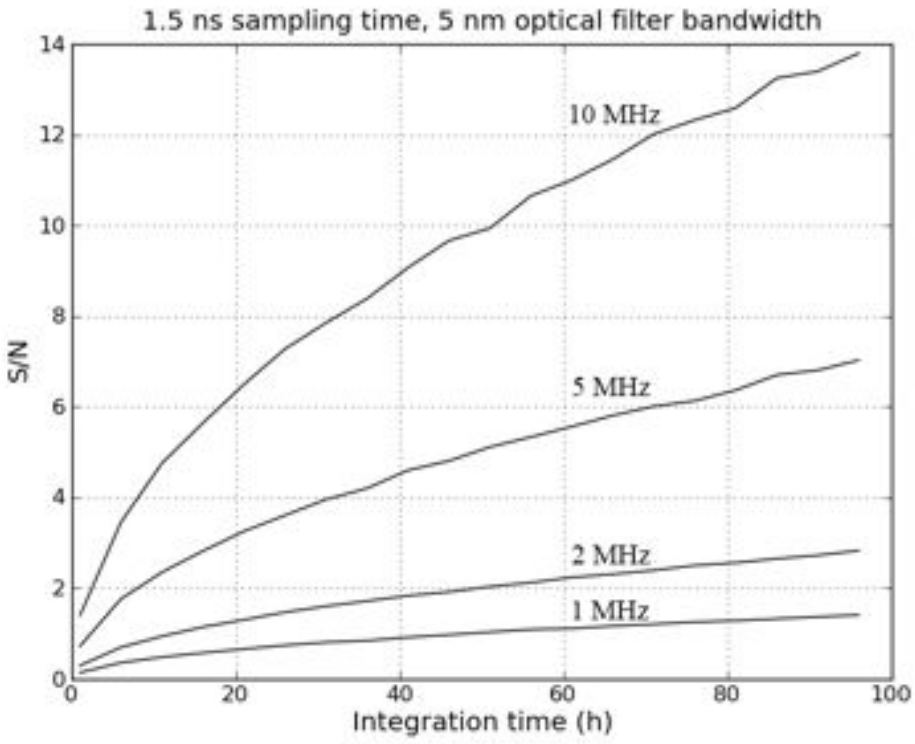

Figure 6.2: Simulated signal-to-noise ratios for different count rates and integration times. The noise rates were calculated using Eq. (4.12).

correlation in many channels with semi-exponentially increasing delay times. For II, the most interesting channels are the ones with short delay times, especially the first channel. In theory, for measurements such as these, with no sources of correlation present, one would expect all the channels to be centered around a value of 1.0.

However, measurements showed that systematic effects were present, causing different channels to center around different values. Figures 6.3 and 6.4 show superimposed plots of the first 10 channels of the output from the correlator (a Flex 03-LQ01 from correlator.com) with two different types of detectors. The measurements were carried out under identical conditions, with the same integration times (200 s for each measurement).

Cleary, the patterns depend on which type of detector is used, but they look very consistent between different measurements. Further experiments confirmed that the curves looked very similar for a given type of detector even when measurement conditions were being varied. Presumably the difference arises from some sort of detector effects, such as after-pulsing and/or defects in the shape of the TTL pulse. However, since the effects seem systematic and consistent, calibrating and adjusting for them should be possible.

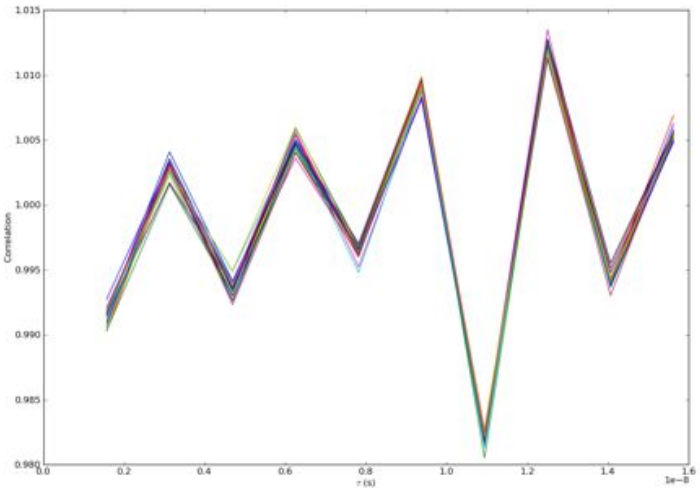

Figure 6.3: First 10 channels of the digital correlator for 20 measurements with id-Quantique id100-50 detectors.

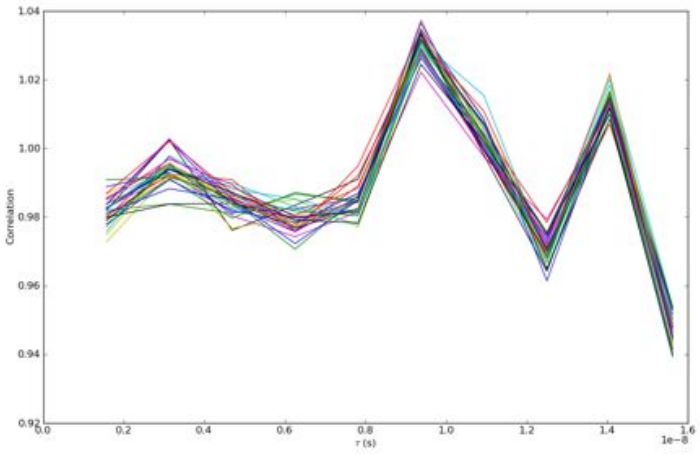

Figure 6.4: First 10 channels of the digital correlator for 20 measurements with SensL detectors.

6.2.2 Scaling of Noise Levels

It was also possible to test some aspects of the computer simulations even with these low count rates. Even if no correlation is expected, simulations should still give reasonable variations in noise levels. To test this, four series of measurements were carried out, with two different types of detectors. For each detector type, one series of thirty 100-second measurements and one series of twenty 200-second measurements were performed.

Then, a large number (10 000) of simulated experiments were carried out and their results plotted as a histogram along with the measured correlations.

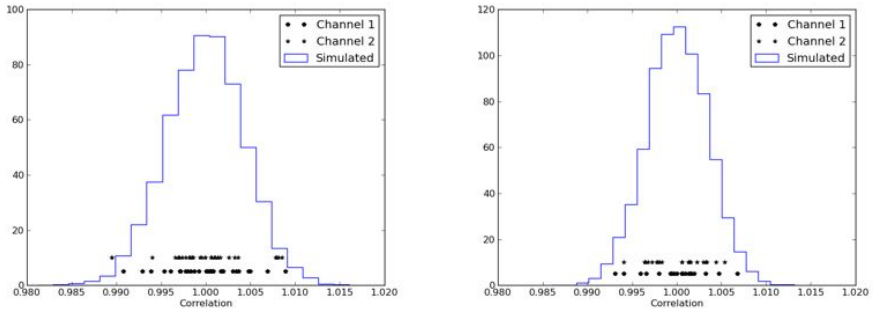

(a) 100 second integration time (b) 200 second integration time

Figure 6.5: Simulated and measured differences between 100 and 200 seconds integration time. The dots show the two first correlator channels from measurements with SensL detectors at 7.5 cm separation (the different locations of the dots on the y axis were chosen simply for clarity). We do not expect any difference between these two channels since the flux rates were too low to give any HBT signal. We do however expect the spread of the correlations to decrease when the integration time increases (i.e. the histogram should get narrower), and this is exactly what is seen. It seems also that this decrease in spread is accurately predicted by the simulations.

Figure 6.5 shows the results from two of these experiments (the plots from the other two were nearly identical), using SensL detectors. The output from the correlator has been centered around 1 to compensate for the effects described in the previous section, so that only the spread in data remains. Only the two first channels from the correlator are shown. The scale on the y-axis is arbitrary (only relative numbers matter for the histograms, and for the measurement points the y-axis positions were chosen simply for clarity). From these figures, it would seem that at least the scaling with integration time is predicted more or less correctly by the simulations.

6.3 Thoughts for the Future

Unfortunately it proved impossible to reach sufficient flux rates with Hg arc lamp. One could imagine a number of ways to work around this problem:

- The “telescopes” could be make bigger, directly increasing the flux rates.
- A low-pressure lamp with very narrow spectral lines could be used. Some experiments were performed with a Na lamp in the hope that the higher spectral purity of the light would compensate for the lower flux. For this particular lamp, the light turned out to be too faint however.
- The light source could be moved closer to the detectors, but this would cause the diffranction pattern to become very small and some way of practically moving the detectors closer together would have to be devised.

- Light from a laser could be made pseudo-thermal by shining it through an emulsion of micro-particles undergoing Brownian motion. A set of micro-spheres of different sizes were ordered for this purpose as part of this project, but arrived too late for any experiments to be carried out.

  In theory however, this method appears very promising as one can essentially obtain any coherence time desired by adjusting the sizes and concentrations of the micro-particles.

Chapter 7

Summary and Conclusions

Already, phase interferometry is beginning to open the door to a completely new area of astronomical research – imaging of stellar surfaces. To extend this field to visible light and even better resolutions, intensity interferometry seems to be the most promising method.

In this thesis I have shown that the science case for sub-milliarcsecond imaging in visible wavelengths is solid, and that this can be realistically achieved with intensity interferometry. All of the required instrumentation exists today. Both fast photo-detectors and digital correlators are commercially available and the most critical component – large telescope arrays – will be built in the near future in the form of giant Cherenkov telescopes such as the CTA.

I have shown in this thesis that a facility such as the CTA, if used for intensity interferometry, would be able to study stellar surfaces at an unprecedented level of detail. I have also shown that new image reconstruction algorithms, such as the Cauchy-Riemann method, perform well and are robust enough to function with realistic noise levels in the data and with the sparsity in the Fourier plane sampling imposed by a CTA-like array. Furthermore, the genetic algorithm reconstruction method presented here – while seemingly inferior to the Cauchy-Riemann method – proves that the problem of image reconstruction from the Fourier magnitude can be tackled with a multitude of approaches.

In short, most of the results so far seem good – a digital revival of intensity interferometry appears to be worthwhile, and one can only hope to see the first real scientific results within the next decade or so.

Bibliography

[1] Young, J. S., Baldwin, J. E., Boysen, R. C., Haniff, C. A., Lawson, P. R., Mackay, C. D., Pearson, D., Rogers, J., St.-Jacques, D., Warner, P. J., Wilson, D. M. A., and Wilson, R. W., "New views of Betelgeuse: multi-wavelength surface imaging and implications for models of hotspot generation," *Mon. Not. Royal Astron. Soc.* **315**, 635–645 (2000).

[2] Domiciano de Souza, A., Kervella, P., Jankov, S., Abe, L., Vakili, F., di Folco, E., and Paresce, F., "The spinning-top Be star Achernar from VLTI-VINCI," *Astron. & Astrophys.* **407**, L47–L50 (2003).

[3] Monnier, J. D., Zhao, M., Pedretti, E., Thureau, N., Ireland, M., Muirhead, P., Berger, J., Millan-Gabet, R., Van Belle, G., ten Brummelaar, T., McAlister, H., Ridgway, S., Turner, N., Sturmann, L., Sturmann, J., and Berger, D., "Imaging the Surface of Altair," *Science* **317**, 342pp (2007).

[4] MacGregor, K. B., Jackson, S., Skumanich, A., and Metcalfe, T. S., "On the Structure and Properties of Differentially Rotating, Main-Sequence Stars in the 1-2 $M_{\odot}$ Range," *Astrophys. J.* **663**, 560–572 (2007).

[5] Hecht, E., [*Optics, 4th ed.*], Addison Wesley, San Francisco (2002).

[6] Malbet, F., "Interferometric science results on young stellar objects," *ArXiv e-prints* (2009).

[7] Hariharan, P., [*Optical interferometry*], Academic Press, New York (1985).

[8] Clark, B. C., "Coherence in Radio Astronomy," in [*Synthesis Imaging in Radio Astronomy*], R. A. Perley, F. R. Schwab, & A. H. Bridle, ed., *Astronomical Society of the Pacific Conference Series* **6**, 1pp (1989).

[9] Quirrenbach, A., "Optical Interferometry," *Annu. Rev. Astron. Astrophys.* **39**, 353–401 (2001).

[10] Mourard, D., Blazit, A., Bonneau, D., Chevassut, J. L., Clausse, J. M., Le Bouquin, J. B., Maire, J., Merlin, G., Rousselet-Perraut, K., Borgnino, J., Nardetto, N., Patru, F., Rondeau, X., Stee, P., Tallon-Bosc, I., Thiébaut, E., Vakili, F., and Ziad, A., "Recent progress and future prospects of the GI2T interferometer," in [*Society of Photo-Optical Instrumentation Engineers (SPIE) Conference Series*], *Presented at the Society of Photo-Optical Instrumentation Engineers (SPIE) Conference* **6268** (2006).

[11] Davis, J., "Forty Years of Progress in Long-Baseline Optical Interferometry: 2005 Robert Ellery Lecture," *Publ. Astron. Soc. of Australia* **23**, 94–104 (2006).

[12] Haguenauer, P., Abuter, R., Alonso, J., Argomedo, J., Bauvir, B., Blanchard, G., Bonnet, H., Brillant, S., Cantzler, M., Derie, F., Delplancke, F., Di Lieto, N., Dupuy, C., Durand, Y., Gitton, P., Gilli, B., Glindemann, A., Guniat, S., Guisard, S., Haddad, N., Hudepohl,

G., Hummel, C., Jesuran, N., Kaufer, A., Koehler, B., Le Bouquin, J., Léveque, S., Lidman, C., Mardones, P., Ménardi, S., Morel, S., Percheron, I., Petr-Gotzens, M., Phan Duc, T., Puech, F., Ramirez, A., Rantakyrö, F., Richichi, A., Rivinius, T., Sahlmann, J., Sandrock, S., Schöller, M., Schuhler, N., Somboli, F., Stefl, S., Tapia, M., Van Belle, G., Wallander, A., Wehner, S., and Wittkowski, M., "The Very Large Telescope Interferometer: an update," in [*Society of Photo-Optical Instrumentation Engineers (SPIE) Conference Series*], *Presented at the Society of Photo-Optical Instrumentation Engineers (SPIE) Conference* **7013** (2008).

[13] Le Bouquin, J., Lacour, S., Renard, S., Thiébaut, E., Merand, A., and Verhoelst, T., "Pre-maximum spectro-imaging of the Mira star T Leporis with AMBER/VLTI," *Astron. & Astrophys.* **496**, L1–L4 (2009).

[14] Kloppenborg, B., Stencel, R., Monnier, J. D., Schaefer, G., Zhao, M., Baron, F., McAlister, H., Ten Brummelaar, T., Che, X., Farrington, C., Pedretti, E., Sallave-Goldfinger, P. J., Sturmann, J., Sturmann, L., Thureau, N., Turner, N., and Carroll, S. M., "Infrared images of the transiting disk in the ϵ Aurigae system," *Nature* **464**, 870–872 (2010).

[15] Hanbury Brown, R., [*The Intensity Interferometer*], Taylor & Francis, London (1974).

[16] Hanbury Brown, R. and Twiss, R., "Correlation between Photons in two Coherent Beams of Light," *Nature* **177**, 27–29 (1956).

[17] Hanbury Brown, R. and Twiss, R., "A Test of a New Type of Stellar Interferometer on Sirius," *Nature* **178**, 1046–1048 (1956).

[18] Davis, J., "A Proposed Successor to the Narrabri Stellar Intensity Interferometer," in [*Dudley Observatory Report*], A. G. D. Philip & D. S. Hayes, ed., 199pp (1975).

[19] Mandel, L. and Wolf, E., [*Optical Coherence and Quantum Optics*], Cambridge University Press, Cambridge (1995).

[20] Purcell, E. M., "The question of correlation between photons in coherent light rays," *Nature* **178**, 1449 – 1450 (1956).

[21] Dravins, D., "Photonic Astronomy and Quantum Optics," in [*Astrophysics and Space Science Library*], D. Phelan, O. Ryan, & A. Shearer, ed., *Astrophysics and Space Science Library* **351**, 95pp (2008).

[22] Daniel, M., de Wit, W. J., Dravins, D., Kieda, D., LeBohec, S., Nunez, P., and Ribak, E., "Towards the Intensity Interferometry Stellar Imaging System," *ArXiv e-prints* (2009).

[23] Baym, G., "The Physics of Hanbury Brown–Twiss Intensity Interferometry: from Stars to Nuclear Collisions," *Acta Physica Polonica B* **29**, 1839pp (1998).

[24] Boal, D. H., Gelbke, C.-K., and Jennings, B. K., "Intensity interferometry in subatomic physics," *Rev. Mod. Phys.* **62**(3), 553–602 (1990).

[25] Jeltes, T., Mcnamara, J. M., Hogervorst, W., Vassen, W., Krachmalnicoff, V., Schellekens, M., Perrin, A., Chang, H., Boiron, D., Aspect, A., and Westbrook, C. I., "Comparison of the Hanbury Brown-Twiss effect for bosons and fermions," *Nature* **445**, 402–405 (2007).

[26] LeBohec, S., Barbieri, C., de Wit, W., Dravins, D., Feautrier, P., Foellmi, C., Glindemann, A., Hall, J., Holder, J., Holmes, R., Kervella, P., Kieda, D., Le Coarer, E., Lipson, S., Malbet, F., Morel, S., Nuñez, P., Ofir, A., Ribak, E., Saha, S., Schoeller, M., Zhilyaev, B., and Zinnecker, H., "Toward a revival of stellar intensity interferometry," in [*Society of Photo-Optical Instrumentation Engineers (SPIE) Conference Series*], *Presented at the Society of Photo-Optical Instrumentation Engineers (SPIE) Conference* **7013** (2008).

[27] Djannati-Ataï, A., "Status of very high energy γ-ray Astronomy as of early 2008," *Nuclear Instruments and Methods in Physics Research A* **602**, 28–33 (2009).

[28] Dravins, D. and LeBohec, S., "Toward a diffraction-limited square-kilometer optical telescope: digital revival of intensity interferometry," in [*Society of Photo-Optical Instrumentation Engineers (SPIE) Conference Series*], *Presented at the Society of Photo-Optical Instrumentation Engineers (SPIE) Conference* **6986** (2008).

[29] Dravins, D., "Enabling the CTA for intensity interferometry and high time-resolution astrophysics," Internal note for the PHYS work package for CTA (2009).

[30] Hamamatsu Photonics K.K., *Photomultiplier Tubes – Basics and Applications*, 3rd ed. (2006).

[31] Paschotta, R., "Encyclopedia of laser physics and technology," (retr. 2010-04-13). http://www.rp-photonics.com/photodiodes.htm.

[32] Saleh, B., [*Photoelectron Statistics*], Springer Verlag, Berlin (1978).

[33] Straubmeier, C., Kanbach, G., and Schrey, F., "OPTIMA: A Photon Counting High-Speed Photometer," *Experimental Astronomy* **11**, 157–170 (2001).

[34] Ofir, A. and Ribak, E. N., "Offline, multidetector intensity interferometers - I. Theory," *Mon. Not. Royal Astron. Soc.* **368**, 1646–1651 (2006).

[35] de Vos, M., Gunst, A. W., and Nijboer, R., "The LOFAR Telescope: System Architecture and Signal Processing," *IEEE Proceedings* **97**, 1431–1437 (2009).

[36] Marathay, A. S., Hu, Y., and Shao, L., "Phase function of spatial coherence from second-, third-, and fourth order intensity correlations," *Opt. Eng.* **33**, 3265–3271 (1994).

[37] Hanbury Brown, R., Davis, J., Lake, R. J. W., and Thompson, R. J., "The effects of limb darkening on measurements of angular size with an intensity interferometer," *Mon. Not. Royal Astron. Soc.* **167**, 475–484 (1974).

[38] Ségransan, D., "Observability and UV coverage," *New Astron. Rev.* **51**, 597–603 (2007).

[39] Press, W., Teukolsky, S., Vetterling, W., and Flannery, B., [*Numerical Recipes*], Cambridge University Press, Cambridge, 3rd ed. (2007).

[40] Holmes, R. B. and Belenḱii, M. S., "Investigation of the Cauchy-Riemann equations for one-dimensional image recovery in intensity interferometry," *J. Opt. Soc. Am.* **21**(5), 697pp (2004).

[41] Nuñez, P. D., LeBohec, S., Kieda, D. B., et al., "Stellar intensity interferometry: Imaging capabilities of air Cherenkov telescope arrays," *Proc. SPIE* **7734**, 7734–47 (2010).

[42] Mitchell, M., [*An Introduction to Genetic Algorithms*], MIT Press, Boston (1998).

[43] Yoshimori, S., Terauchi, A., Yoshinao, T., and Omatu, S., "Genetic relaxed iterative Fourier transform algorithm for image reconstruction from Fourier transform magnitude," *Systems and Computers in Japan* **32**(5), 55pp (2001).

[44] Keto, E., "The Shapes of Cross-Correlation Interferometers," *Astrophys. J.* **475**, 843–852 (1997).

[45] Millour, F., "All you ever wanted to know about optical long baseline stellar interferometry, but were too shy to ask your adviser," *New Astron. Rev.* **52**, 177–185 (2008).

[46] Bessell, M. S., Castelli, F., and Plez, B., "Model atmospheres broad-band colors, bolometric corrections and temperature calibrations for O - M stars," *Astron. & Astrophys.* **333**, 231–250 (err. **337** p. 321) (1998).

[47] Barbieri, C., Daniel, M. K., de Wit, W. J., Dravins, D., Jensen, H., Kervella, P., Le Bohec, S., Malbet, F., Nunez, P., Ralston, J. P., and Ribak, E. N., "New Astrophysical Opportunities Exploiting Spatio-Temporal Optical Correlations," in [*astro2010: The Astronomy and Astrophysics Decadal Survey*], *Astronomy* **2010**, 61pp (2009).

[48] Richichi, A., Percheron, I., and Khristoforova, M., "CHARM2: An updated Catalog of High Angular Resolution Measurements," *Astron. & Astrophys.* **431**, 773–777 (2005).

[49] Stewart, H. A., Guinan, E. F., Wasatonic, R., Engle, S. G., and McCook, G. P., "Multi-Frequency Photometric Analyses of Rigel, the nearest Blue Supergiant and Supernova Progenitor," in [*Bulletin of the American Astronomical Society*], *Bulletin of the American Astronomical Society* **41**, 207pp (2009).

[50] Ausseloos, M., Aerts, C., Uytterhoeven, K., Schrijvers, C., Waelkens, C., and Cuypers, J., "beta Centauri: An eccentric binary with two beta Cep-type components," *Astron. & Astrophys.* **384**, 209–214 (2002).

[51] Peterson, D. M., Hummel, C. A., Pauls, T. A., Armstrong, J. T., Benson, J. A., Gilbreath, G. C., Hindsley, R. B., Hutter, D. J., Johnston, K. J., Mozurkewich, D., and Schmitt, H. R., "Vega is a rapidly rotating star," *Nature* **440**, 896–899 (2006).

[52] Weigelt, G., Kraus, S., Driebe, T., et al., "Near-infrared interferometry of η Carinae with spectral resolutions of 1 500 and 12 000 using AMBER/VLTI," *Astron. & Astrophys.* **464**, 87–106 (2007).

[53] Millour, F., Petrov, R. G., Chesneau, O., et al.

[54] Lamers, H. J. G. L. M., Zickgraf, F., de Winter, D., Houziaux, L., and Zorec, J., "An improved classification of B[e]-type stars," *Astron. & Astrophys.* **340**, 117–128 (1998).

[55] Jankov, S., Vakili, F., Domiciano de Souza, Jr., A., and Janot-Pacheco, E., "Interferometric-Doppler imaging of stellar surface structure," *Astron. & Astrophys.* **377**, 721–734 (2001).

Appendix A

List of Hot and Bright Stars

Name	θ (mas)	v_{rot} (km/s)	Spec. class	T_{eff} (K)	V [mag]	Notes
Achernar, α Eri, HR472	1.9	250	B3Ve	15000	0.46	High rotational velocity, Be-star
Rigel, β Ori, HR1713	2.4	30	B8Iab	9800	0.12	Emission line star, SN candidate
λ Lep, HR 1756		70	B0.5IV	28000	4.29	
Bellatrix, γ Ori, HR 1790	0.7	60	B2III	21300	1.64	
Elnath, β Tau, HR 1791	1.5	70	B7III	13500	1.65	
ν Ori, HR 1855		20	B0V	28000	4.62	
HR 1887, HD 36960		40	B0.5V	26000	4.78	
Alnilam, ϵ Ori, HR 1903	0.7	90	B0Iab	18000	1.7	
μ Col, HR 1996		150	O9.5V	33000	5.17	High v_{rot}
β CMa, HR 2294	0.5	35	B1II/III	23000	1.98	Short period β Cep variable
Alhena, γ Gem, HR 2421	1.4	30	A0IV	9100	1.93	
S Mon, HR 2456		60	O7Ve	26000	4.66	
Sirius, α CMa, HR 2491	5.9	10	A1V	9100	-1.46	Very bright, well studied
EZ CMa, HR 2583			WN4	33000	6.91	Highly variable W-R star
Adara, ϵ CMa, HR 2618	0.8	40	B2Iab	20000	1.5	Double star
Naos, ζ Pup, HR 3165	0.4	210	O5Ia	28000	2.25	High v_{rot}
γ^2 Vel, HR 3207	0.4		WCv+	21300	1.78	
β Car, HR 3685	1.5	130	A2IV	9100	1.68	
Regulus, α Leo, HR 3982	1.4	330	B7V	12000	1.35	High v_{rot}
Acrux, α^1 Cru, HR 4730		120	B0.5IV	24000	1.33	
Acrux, α^2 Cru, HR 4731		200	B1V	28000	1.73	High v_{rot}
β Cru, HR 4853	0.7	40	B0.5IV	23000	1.25	
ϵ UMa, HR 4905		40	A0p	9500	1.77	
Spica, α Vir, HR 5056	0.9	160	B1III-IV+	23000	0.98	High v_{rot}
Alcaid, η UMa, HR 5191	<2	200	B3V	18000	1.86	High v_{rot}
β Cen, HR 5267	0.9	140	B1III	23000	0.61	
τ Sco, HR 6165		25	B0.2V	26000	2.82	
λ Sco, HR 6527		160	B2IV+	21000	1.63	High v_{rot}
Kaus Astr., ϵ Sgr, HR 6879	1.4	140	B9.5III	9800	1.85	
Vega, α Lyr, HR 7001	3.2	15	A0V	9100	0.03	Bright, well studied, rotating
Peacock, α Pav, HR 7790	0.8	40	B2IV	19000	1.94	Spectroscopic binary
Deneb, α Cyg, HR 7924	2.2	20	A2Iae	9300	1.25	α Cyg variable
α Gru, HR 8425	1.0	230	B6V	13000	1.74	High v_{rot}
Fomalhaut, α PsA, HR 8728	2	100	A4V	9300	1.16	First exo-planet imaged in visible light
η Car, HR 4210	5.0 (shell)		pec	36000	6.21	Many extreme properties
WD 0005+511				200000	13.23	Hottest WD known

Table A.1: List of stars with $(T_{eff} > 9000\ K \wedge V < 2) \vee T_{eff} > 25000\ K$

Appendix B

Presentations and Publications

B.1 Workshop on Stellar Intensity Interferometry

Salt Lake City, January 2009. Presentation *Hot Stars as Targets for Intensity Interferometry.*
`http://www.physics.utah.edu/~lebohec/SIIWGWS/`

B.2 Astro 2010 White Paper

Barbieri C., Daniel M. K., de Wit W. J., Dravins D., Jensen H.,Kervella P., LeBohec S., Malbet F., Nunez P., Ralston J. P., Ribak E. N., Ridgway S. T. 2009, *New Astrophysical Opportunities Exploiting Spatio-Temporal Optical Correlations*, Astro2010 Science White Paper, `arXiv:0903.0062`

B.3 Astronomdagarna 2009

Poster *Digital Revival of Intensity Interferometry* presented at Astronomdagarna, Stockholm, September 2009

B.4 SPIE Conference on Astronomical Instrumentation, San Diego, June-July 2010

- Jensen, H., Dravins, D., LeBohec, S.L. and Nuñez, P.D., 2010, *Stellar intensity interferometry: Optimizing air Cherenkov telescope array layouts*, Proc. SPIE 7734, 7734-64

- Nuñez, P. D., LeBohec, S. L., Kieda, D. B., Holmes, R., Dravins, D. and Jensen, H., 2010, *Stellar intensity interferometry: Imaging capabilities of air Cherenkov telescope arrays*, Proc. SPIE 7734, 7734-47

- LeBohec, S., Nuñez, P. D., Kieda, D. B. et al., 2010, *Stellar intensity interferometry: Experimental steps toward long-baseline observations* Proc. SPIE 7734, 7734-48

- Dravins D., Jensen, H., LeBohec, S., Nuñez, P.D. 2010, *Stellar Intensity Interferometry: Astrophysical targets for sub-milliarcsecond imaging*, Proc. SPIE 7734, 7734-9

Hot Stars as Targets for Intensity Interferometry

Hannes Jensen
Lund Observatory, Sweden

LUND UNIVERSITY

Aims

- Given recent progress in phase interferometry:
  which should be the prime observational targets for II?
- What is least difficult to observe?
- Starting point for observing programs, white papers, etc.

Selection Criteria

What makes a target suitable for II?

- **Bright**
  High above background noise level, moonlight etc.
- **Hot**
  S/N improves greatly with target temperature
- **Astronomically interesting**
  Features on a (sub)milliarcsecond level.
  Deformation due to rapid rotation, pulsation, disks, winds, etc.

The Bright Star Catalogue

The Bright Star Catalogue contains the ~9000 brightest stars.

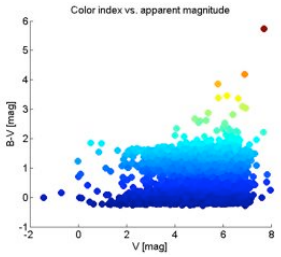

Temperatures

Effective temperatures were approximated with a polynomial fit to values from [Bessel et al, 1998, A&A333].

~2600 objects are hotter than 9000 K and brighter than V=7

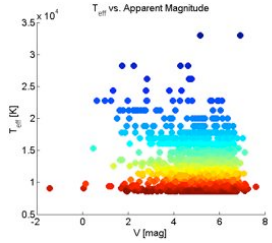

Final selection

- 34 stars exist with $(T_{eff} > 9000\ K \wedge V < 2) \vee T_{eff} > 25000\ K$
- A few other interesting objects were added
- Angular diameters from the CHARM2 compilation.
  [Richichi et a.l., 2005, A&A431, 773]

Selected objects

Temperature vs. apparent magnitude of selected stars.
Circle size indicates angular diameter where available.

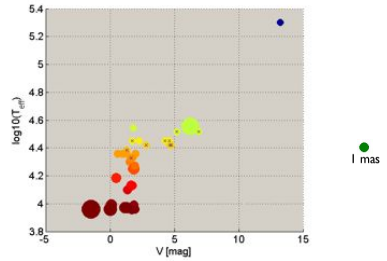

List of Objects

Name	Angular size (mas)	Rot. vel.* [km/s]	Spec. class	T_{eff} [K]	V [mag]	Notes
Achernar, HR 472	1.9	250	B3Ve	15000	0.46	High rotational velocity,Be-star
Rigel, HR 1713	2.4	30	B8Iab	9800	0.12	Emission line star,SN candidate
Lambda Lup, HR 1756		70	B0.5IV	28000	4.29	
Bellatrix, HR 1790	0.7	60	B2II	21000	1.64	Variable star
Mirach, HR 1791	1.5	70	B7III	13000	1.65	Star in double system
HR 1855		20	B0V	28000	4.62	Variable star
HR 1887		38	B0.5V	26000	4.78	Star in double system
Alnilam A, HR 1903	0.7	87	B0Iab	18000	1.7	Emission line star
HR 1996		153	O9.5V	33000	5.17	High rotational velocity
Beta CMa	0.5	36	B1III/II	23000	1.98	Short period beta Cep variable
Alhena, HR 2421	1.4	30	A0IV	9100	1.93	Star in double system
S Mon, HR 2456		60	O7Ve	36000	4.66	
Sirius, HR 2491	5.9	13	A1 V	9100	-1.46	Bright, well studied,high angular size
EZ CMa, HR 2583		?	WN4	33000	6.91	Highly variable W-R star
Adara, HR 2618	0.8	44	B2ab	20000	1.5	Star in double system
Naos, HR 3165	0.4	211	O5Ia	38000	2.25	BY Dra variable, high rot. vel.
HR 3207	0.4		WCv	21000	1.78	Double or multiple star
HR 3685	1.5	133	A2IV	9100	1.68	

* $v_{rot} \sin i$

List of Objects, contd.

Name	Angular size (mas)	Rot. vel. [km/s]	Spec. class	T_{eff} [K]	V [mag]	Notes
Beta Cen, HR 5267	0.9	264	B1III	23000	0.61	Beta Cep variable
Tau Sco, HR 6165		24	B0.2V	26000	2.82	
Lambda Sco, HR 6527		163	B2IV	21000	1.63	Beta Cep variable
Kaus Austr., HR 6879	1.4	147	B9.5III	9800	1.85	Star in double system
Vega, HR 7001	3.2	?	A0V	9100	0.03	Bright, well studied
Peacock, HR 7790	0.8	39	B2IV	19000	1.94	Spectroscopic binary
Deneb, HR 7924	2.2	21	A2Iae	9300	1.25	Alpha Cyg variable
HR 8425	1.0	236	B6V	13000	1.74	High rotational velocity
Fomalhaut, HR 8728	2	100	A4V	9300	1.16	First optically imaged exo-planet
Eta Car, HR 4210	5.0 (CSS)	?	pec	36000	6.21	Highly unstable, SN candidate?
WD 0005+511		?		200 000	13.23	Hottest WD known
Gamma Vel, HR 3207	0.4		WC8+O9I		1.8	WR-O binary
Regulus, HR 3982	1.4	329	B7V	12000	1.35	High rotational velocity
Acrux, HR 4730		117	B0.5V	24000	1.33	Spectroscopic binary
HR 4721		197	B1V	28000	1.73	High rotational velocity
Beta Cru, HR 4853	0.7	38	B0.5V	23000	1.25	Beta Cep variable
Eps UMa, HR 4905		38	A0p	9500	1.77	Variable star
Spica, HR 5056	0.9	159	B1III-IV	23000	0.98	High rotational velocity variable
Alcaid, HR 5191	< 2.	205	B3V	18000	1.86	High rotational velocity variable

Selected objects

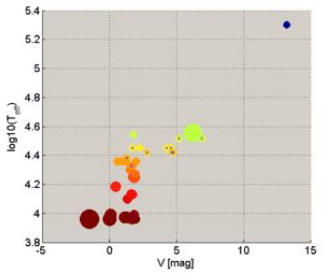

Achernar (B3Ve)

T_{eff}	15 000 K
V [mag]	0.46
v sin *i*	250 km/s
θ	1.85 mas

- Very rapidly rotating Be-star
- Highly deformed due to rotation, observed with VLTI
  [de Souza et al., 2003, A&A 407, 47]
- Complex stellar winds due to rotation
  [e.g., Kervella et al., 2008]
- Circumstellar disk may be studied with II in its Hα emission
- Companion star suggested
  [Kervella & de Souza, 2007, A&A 474, 49]

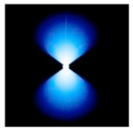

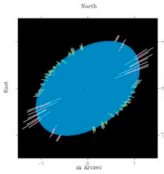

[Kervaen et al., 2008, A&A, 486]

Rigel (B8Iab)

T_{eff}	10 000 K
V [mag]	0.12
v sin *i*	30 km/s
θ	2.4 mas

- The nearest blue supergiant
- Nearest type II supernova progenitor? [Stewart et al., 2009]
- Periodic oscillations on many timescales
  [Stewart et al., 2009]
- Variation in absorption/emission in Hα lines [Morrison et al., 2009]

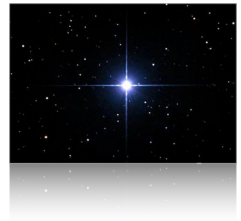

β Centauri (B1III)

T_{eff}	22 000 K*
V [mag]	0.61
v sin *i*	140 km/s
θ	0.9 mas

*both components approx. equal mass and temp.

- The brightest β Cep variable
- Oscillations, line profile variations
- Highly complex spectroscopic binary, both components variable
  [Ausseloos et al., 2006, A&A 455]
- "A challenge for current evolution scenarios in close binaries"
  [Ausseloos et al., 2002 A&A 209]
- Orbits measured with Sydney University Stellar Interferometer (SUSI)
  [Davis et al, 2005, MNRAS 256 1362]

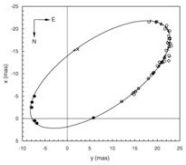

Vega (A0 V)

T_{eff}	9 000 K
V [mag]	0.03
v sin *i*	15 km/s
θ	3.2 mas

- Widely studied standard star. "Arguably the second most important star in the sky after the Sun" [Gulliver et al., 94, ApJ 429]
- Realized to be a rapidly rotating pole-on star
- Center-limb intensities: 18x drop at 500 nm, compared to 5x drop for non-rotating model
  [Peterson et al., 2006, Nature 440, 896]

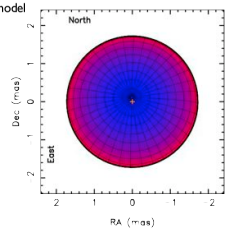

Fomalhaut (A4V)

T_{eff}	9 000 K
V [mag]	1.16
v sin *i*	100 km/s
θ	2 mas

- Host star of an optically imaged exoplanet
- Debris disk with planet(s)

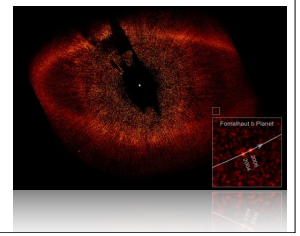

η Carinae

T_{eff}	36 000 K
V [mag]	6.21
v sin *i*	?
θ	5 mas*

* Circumstellar shell

- Most luminous star known in the Galaxy
- Highly unstable, "doomed to explode within 100 000 years"
- Imaged with HST and VLT to some 0.1 arcsec;
- VLTI data to milliarcsecond level shows asymmetries in winds due to rapid rotation
  [Weigelt et al., 2007, A&A, 464, 87]

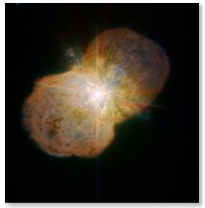

Images: eso.org

γ^2 Velorum (WC8+O9I)

T_{eff}	35 000 K
V [mag]	1.8
v sin *i*	?
θ	0.4 mas

- Closest and brightest Wolf-Rayet star.
- WR-O binary, important for understanding stellar evolution
  [North et al., 2007, MNRAS 377]
- Excellent system for studying massive stars and their interacting winds
  [Millour et al., 2007, A&A 464]
- Already observed at Narrabri by Hanbury Brown et al.: Angular size in C III-IV emission at 465 nm shows stellar envelope five times larger than stellar disk in the continuum

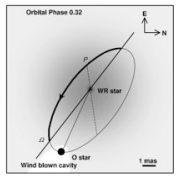

Conclusions

- Observationally suitable and exciting targets exist all over the sky
- Much to be gained from sub-milliarcsecond measurements
  - way more than just stellar diameters!

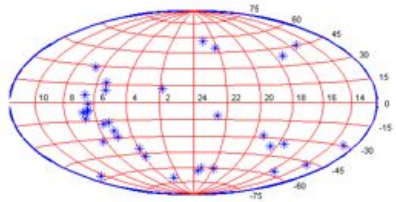

New Astrophysical Opportunities Exploiting Spatio-Temporal Optical Correlations

C. Barbieri[1], **M. K. Daniel**[2], **W. J. de Wit**[3], **D. Dravins**[4], **H. Jensen**[4], **P. Kervella**[5], **S. Le Bohec**[6], **F. Malbet**[7,8], **P. Nunez**[6], **J. P. Ralston**[9], **E. N. Ribak**[10] *for the working group on stellar intensity interferometry (IAU commission 54)*

[1] University of Padova, Italy; [2] Durham University, UK; [3] University of Leeds, UK; [4] Lund Observatory, Sweden; [5] LESIA, France; [6] University of Utah, USA; [7] LAOG, France; [8] Caltech, USA; [9] University of Kansas, USA; [10] Technion, Israel

Abstract. The space-time correlations of streams of photons can provide fundamentally new channels of information about the Universe. Today's astronomical observations essentially measure certain amplitude coherence functions produced by a source. The spatial correlations of wave fields has traditionally been exploited in Michelson-style amplitude interferometry. However the technology of the past was largely incapable of fine timing resolution and recording multiple beams. When time and space correlations are combined it is possible to achieve spectacular measurements that are impossible by any other means. Stellar intensity interferometry (SII) is ripe for development and is one of the few unexploited mechanisms to obtain potentially revolutionary new information in astronomy. As we discuss below, the modern use of SII can yield unprecedented measures of stellar diameters, binary stars, distance measures including Cepheids, rapidly rotating stars, pulsating stars, and short-time scale fluctuations that have never been measured before.

1. Introduction

More than 40 years ago the basic principles of *intensity interferometry* were developed and proven through the measurement of stellar diameters with sub-milli-arcsecond resolution [1, 2]. Yet this breakthrough ran its course due to technological limitations. The old technology was limited to two telescope beams, and integration of correlations was done by the elegantly primitive device of counting the turns of an electric motor. In the interim the technology of photon detection has exploded, and the ability to handle and correlate multiple beams with exquisite time resolution has been perfected. It is hard to overstate the advantages now possible with current and future detection technology, both in real-time and off-line, both with simple pairs and with multiple detector arrays.

SII works by comparing the random intensity fluctuations of light waves entering separated detectors. Nothing special is needed from the source, and black-body, thermal correlations are ideal. While quantum properties derived from the statistics of photon arrival times (e.g. photon bunching behavior) add extra information, the effect is robust, and works whether or not quanta are well-resolved. Statistical correlations of beams of a given wavelength λ separated by a given distance D allows resolution of structure at the Rayleigh criterion $\Delta\theta \sim \lambda/D$. This is how measurements equivalent to 100 meter telescopes were made with SII 40 years ago [3]. The exacting match of optical path lengths needed in amplitude (Michelson) interferometry is completely unnecessary, because different phase properties dominate SII. Troublesome sensitivity to path length differences caused by atmospheric turbulence is completely eliminated for the same reason. Vast quantities of photons are however required and the visual wavelength region is most appropriate. Several algorithms are available for phase recovery in a multi-beam set-up, permitting model independent imaging [4, 5]. Current detection technology allow

therefore a revolution in SII: multiple telescope, long baseline optical *intensity interferometry*. A system can be devised [6, 7] that would consist of hundreds of large flux gathering surfaces spread out over kilometers of baseline that would enable to make the next big step in astronomy: optical imaging at μ-arcsecond resolution.

2. Astrophysical applications for μ-arcsecond imaging SII

Properly imaging stellar surfaces constitutes a major break-through in stellar astrophysics. Stars have angular sizes of tens of milli-arcseconds or less, and until now, apart from the sun, only Betelgeuse and Altair have been imaged albeit with a modest number of resolution elements (at maximum ten). Technical requirements for SII are such that one can easily be looking at hundred resolution elements with an order of magnitude increase in angular resolution. Stellar physics has been waiting for a long time to make this leap forward, and it is similar to the impact realized by Hanbury Brown and Twiss when they measured 32 stellar diameters with the first and only application of SII in astronomy [3]. Modern SII would undoubtedly extend solar physics to the realm of the stars. Moreover, feasibility studies indicate that SII may not be limited to resolving Galactic sources only. We present therefore an overview of core galactic and extra-galactic science drivers:

- Stellar surface phenomena and dynamo action
- Conditions for planet formation around young stars
- Cepheid properties and the distance scale
- Mass loss and fast rotation of massive hot stars and supernova progenitors
- Nuclear optical emission from AGN
- Structure of gamma-ray bursts

Of course, feasibility of these science topics depends on the design of the intensity interferometer. For practical purposes we adopt a conservative limiting visual magnitude $m_v < 8^m$ and a resolution of a 0.1 milli-arcsecond, and we detail the science that would be opened up within these limits.

Stellar surface phenomena, star formation and binaries Pre-main sequence (PMS) objects are young stars that are contracting towards the main-sequence, still lacking internal hydrogen combustion. Key questions relating to the physics of mass accretion and PMS evolution can be addressed by means of very high resolution imaging. Spatially resolved studies would involve the absolute calibration of PMS tracks, the mass accretion process, continuum emission variability, and stellar magnetic activity. The technique may allow spot features on the stellar surface to be resolved. Hot spots deliver direct information regarding the accretion of material onto the stellar surface. Cool spots, on the other hand, may cover 50% of the stellar surface, and they are the product of the slowly decaying rapid rotation of young stars. Imaging them will constrain the interplay of rotation, convection, and chromospheric activity as traced by cool spots and need not be limited to PMS stars only. It may also provide direct practical application as the explanation for the anomalous photometry observed in young stars [10].

In the last decade several young coeval stellar groups have been discovered in close proximity ($\sim$50 pc) to the sun. Famous examples are the TW Hydra and β Pic comoving groups. The majority of the spectral types within reach range between A and G-type, and about 50 young stars have $m_v < 8^m$. Their ages lie within the range 8 to 50 Myr (see [11] for an overview). The age intervals ensures that a substantial fraction of the low-mass members are still in their PMS contraction phase. Key targets for calibration of evolutionary PMS tracks in the Hertzsprung-Russell diagram are spectroscopic binaries. Resolving binaries delivers the inclination of the system and hence access to the mass of the components. This is a

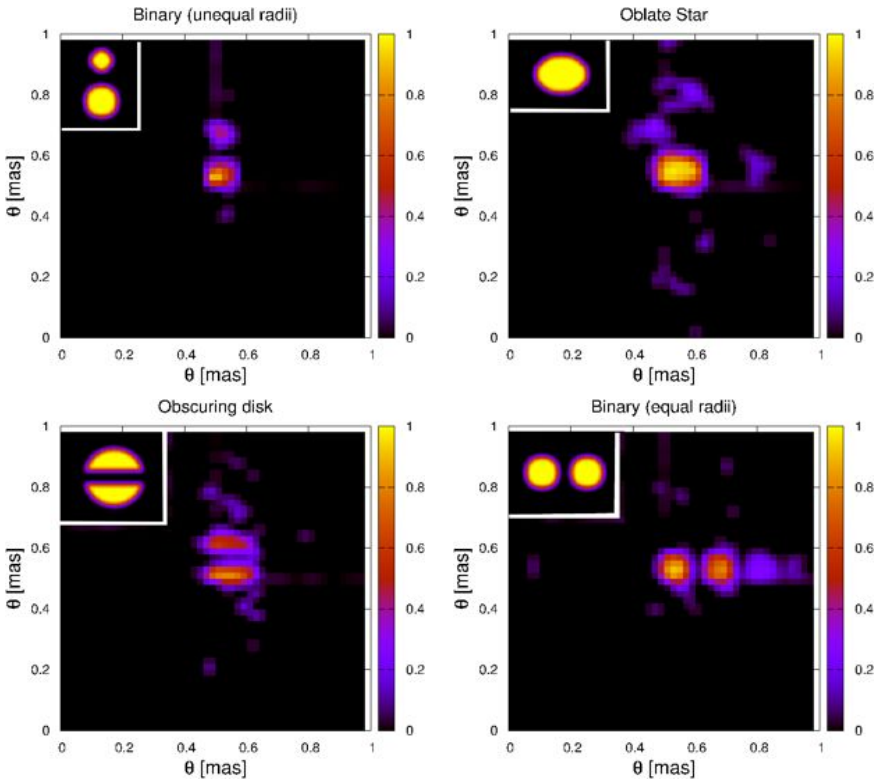

Figure 1. Four examples of images reconstructed from *SII* data as would be recorded with an array that operates at a wavelength of $\sim 400\,\mathrm{nm}$ with one hundred telescopes and a telescope separation of $\sim 100\,\mathrm{m}$. The pristine image is shown at the top left in each example. The images were produced [8] using an algorithm based on the Cauchy-Riemann equations [9]. The analysis does not yet include a realistic noise component, which is still actively being investigated.

fundamental exercise not only for PMS stars but for all spectroscopic binaries in any evolutionary stage. Measurement of angular sizes of individual PMS stars in combination with a distance estimate (e.g. GAIA) allows a direct comparison between predicted and observed sizes of these gravitationally contracting stars. The proximity of the comoving groups ensures that their members are bright. Their proximity renders the comoving group also relatively sparse making them very suitable, unconfused targets. The sparseness is also the reason for incomplete group memberships, making it likely that the number of young stars close to the sun will increase with the years to come.

Distance scale and pulsating stars Measuring diameters of Cepheids is a basic method with far reaching implications for the calibration of the distance scale. A radius estimate of a Cepheid can be obtained using the Baade-Wesselink method. The Baade-Wesselink method relies on the measurement of the ratio of the star size at times t_1 and t_2, based on the luminosity and color. Combined with a simultaneous measurement of the radial velocity, this method delivers the difference in the radius between t_1 and t_2. With the known difference and ratio of the radius at two times, one can derive the radius of the Cepheid. Combining *SII* angular size measurement with the radius estimate one obtains the distance (see [12]). This makes possible the calibration of the all important Cepheid period-luminosity relation using local Cepheids. Nearly all of the *Hipparcos* distances for Cepheids have rather large trigonometric errors (see [13]) giving rise to ambiguous results. A count of Cepheids observed with *Hipparcos* [14] shows

that at least 60 Cepheids are visually brighter than 8^m.

Rapidly rotating stars and hot stars As a group, classical Be stars are particularly well-known for their close to break-up rotational velocities as deduced from photospheric absorption lines. In addition the stars show Balmer line emission firmly established as due to gaseous circumstellar disks, that appear and disappear on timescales of months to years. Photometric observations of Be star disks seem to indicate that they may actually evolve into ring structures before disappearing into the interstellar medium (e.g. [15]). These two phenomena (rapid rotation and circumstellar disks) are somehow related, but many open questions exist regarding the detailed physical processes at play. The Be-phenomenon is important given the large number of stars and fundamental stellar physics involved (fraction of Be stars to normal B-type peaks at nearly 50% for B0 stars, [16]). Absorption line studies cannot provide the final answer to their actual rotational velocity due to strong gravity darkening at the equator and brightening at the pole areas. Direct measurement of the shape of the rotating star is not hampered by gravity darkening, and can provide a direct indication of the rotational speed (see α Eri with the VLTI, [17]). The disk's Bremsstrahlung can constitute $\sim 30\%$ of the total light in V-band [16]. There are about 300 Be stars[1] brighter than $m_v = 8^m$, roughly corresponding to a distance limit of 700 pc.

The signal-to-noise ratio of an optical intensity interferometer improves with the temperature of the target. Since SII is insensitive to atmospheric turbulence, observations in the violet or blue pose no problem. Eliminating the "Achilles' Heel" of standard phase interferometry will enable high resolution studies of hot stars over very long geometric baselines. A rough estimate of the effective temperatures of the objects in the Bright Star Catalog reveals that approximately 2600 stars brighter than visual magnitude 7 and hotter than 9000 K exist in the sky, all of which should be realistic targets even for a fairly modest intensity interferometer. Typical angular sizes for the stellar surface disk range between 0.5 and 5 mas. Of these targets, a handful of especially interesting ones are presented below, along with some brief notes on their possible science potential.

- **Rigel (β Orionis)** Rigel is the nearest blue supergiant (240 pc). It is a very dynamic object with variable absorption/emission lines and oscillations on many different timescales - from minutes to weeks [18]. The physical properties of Rigel have recently been shown to be very similar to the supernova progenitor SN1987A. This realization makes understanding the dynamical nature of Rigel highly relevant.
- **β Centauri** β Centauri is a binary system consisting of two very hot, very massive variable stars. Both components are variable both spatially and in their line profiles. The intricate nature of the system has led to it being called "a challenge for current evolution scenarios in close binaries" [19].
- **Vega (α Lyrae)** While one of the most fundamental stars in the sky for calibration purposes, the nature of Vega has proven to be more complicated than previously thought. Recent phase interferometry studies suggest an 18-fold drop in intensity at 500 nm from center to limb, consistent with a rapidly rotating pole-on model, as contrasted to the 5-fold drop predicted by non-rotating models [20]. Intensity interferometry will direct studies of the intensity distribution at shorter wavelengths and in different passbands. Such observations will lead to a better understanding between the link between rotation and limb darkening in different wavelength regions.
- **η Carinae** η Carinae is the most luminous star known in the Galaxy, and an extremely unstable and complex object. Recent VLTI studies have revealed asymmetries in the stellar

[1] `http://www.astrosurf.com/buil/us/becat.htm`

winds due to the rapid rotation of the star [21]. Like Rigel, η Carinae is believed to be on the verge of exploding as a core-collapse supernova.

- γ^2 **Velorum** γ^2 Velorum is a binary consisting of a hot O-type star and a Wolf-Rayet star. The proximity to the O-type star creates a situation where two stellar winds interact, creating a wealth of interesting phenomena such as wind collision zones, wind-blown cavities and eclipses of spectral lines [22]. The bright emission lines of WR stars make them suitable for comparative studies in different passbands, as discussed above.

Optical emission from AGN Nuclear optical continuum emission from AGN is visible whenever there is a direct view of the accretion disc (although jets can also contribute to this component). NGC 1068 is among the brightest and the most nearby active galaxy (18.5 Mpc), and hence the prototypical AGN. The core of the galaxy is very luminous not only in the optical, but also in ultraviolet and X-rays, and a supermassive black hole is required to account for the nuclear activity. The VLTI has succeeded in resolving structures in the AGN torus at mid-infrared wavelengths [23] on scales of 30 milli-arcsecond. On the other hand, the blue optical continuum emission is dominated by thermal emission from the inner accretion disk (the source of the "big blue bump" in many quasars) and much more compact. The optical emission regions have an expected size of 0.3 milli-arcsecond at the distance of NGC 1068 and resolving it would be a fantastic achievement. The nucleus has a visual magnitude of around 10^{m}.

Gamma-ray bursts and supernovae The energy, spectrum and delay between the spectrally-remote events and their inexplicable energy have long been puzzling. Initial models assumed clashes between expanding shells to explain these bright events [24], and later concentrated on polar shells. Another model tried to explain the effect by assuming relativistic plasma spheres in which directionality sets all these observed parameters [25]. Resolution is required to decide between the many models for these hot spots. The currently available high-spatial resolution instruments are all insufficient as amplitude interferometers cannot operate on long enough baselines in the crucial blue and ultraviolet regime [27]. Early warning systems will allow to obtain some spatial and spectral information at the peak of the optical flux. Since most of these events are extremely far, we can expect only those within z= 1 to be resolvable. There have been at least two such bright ($\mathrm{m_v} < 9^{\mathrm{m}}$) objects, GRB990123 and GRB080319B, and there are others (e.g. GRB050509B) with host galaxies, all of which are of interest.

3. Cherenkov telescope arrays as an optical intensity interferometer

The major observational advantages of an intensity interferometer are its low requirements on path length equalization and its relative insensitivity to atmospheric seeing. However traditional implementation has required huge quantities of light. Cherenkov telescopes are capable of gathering huge quantities of light and recent studies [28] have rediscovered the potential of the next-generation Imaging Air Cherenkov Telescope (IACT) arrays as a multi-element intensity interferometer. Two major IACT array facilities for γ-ray astronomy are currently under design-study: the Advanced Gamma Imaging System (AGIS [29]) in the US and the Cherenkov Telescope Array (CTA [30]) in Europe. Current designs will offer several thousand baselines (tens to a hundred telescopes) from a few tens of meters to more than a kilometer (Figure 2) and would achieve a limiting magnitude for SII of $\mathrm{m_v} \approx 9^{\mathrm{m}}$, achievable within a few hours exposure [28, 31, 32]. CTA is on the roadmap[2] of the European Strategy Forum on Research Infrastructures (ESFRI), is stated as one of the "Magnificent Seven" of the European strategy for astroparticle physics published by ASPERA[3] and is highly ranked in the strategic plan for

[2] ftp://ftp.cordis.europa.eu/pub/esfri/docs/esfri_roadmap_update_2008.pdf

[3] http://www.aspera-eu.org/images/stories/roadmap/aspera_roadmap.pdf

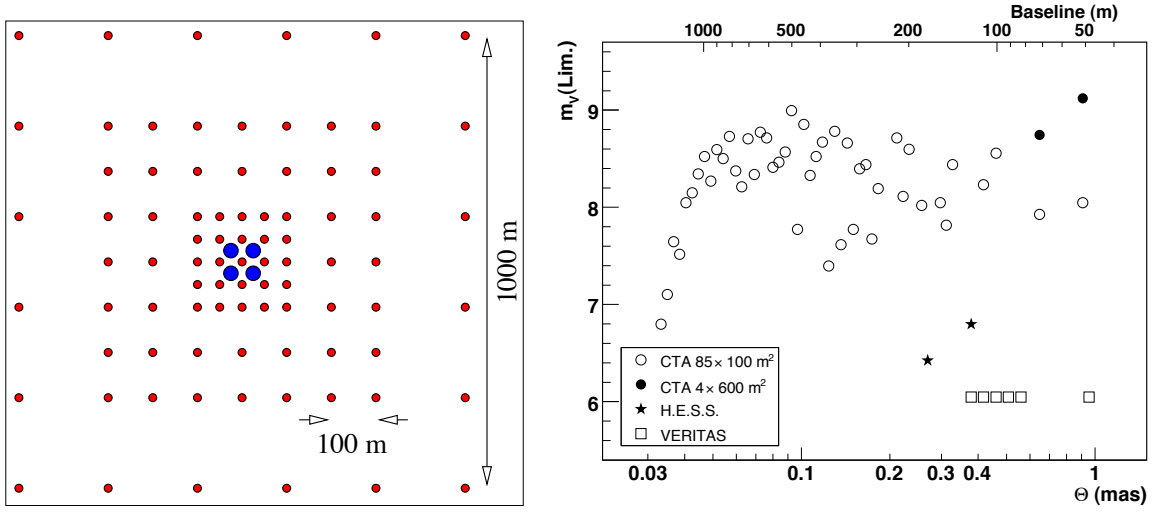

Figure 2. *Left:* Proposed lay-out for the future CTA. Small red dots are the 85 100 m^2 dishes, large blue dots are the four 600 m^2 dishes (adapted from [26]). *Right:* Limiting optical magnitude estimate as function of baseline for a 5σ detection, in a 5 hr integration on a centro-symmetric object with 50% visibility. Sensitivity for *SII* of current ground-based γ-ray facilities (HESS, and VERITAS) are also included. Final limiting magnitudes depend on signal bandwidth and CTA design details, see [28].

European astronomy of ASTRONET[4]. The AGIS collaboration has provided a white paper for the Division of Astrophysics of the American Physical Society on the status and future of ground-based TeV γ-ray astronomy [33]. The next generation of IACT arrays are foreseen to come on-line within the next 10 years. Implementation of *SII* with IACT arrays will result in imaging capabilities with an expected angular resolution of 0.05 mas at 400 nm.

IACT γ-ray observations are done with a low duty cycle due to a requirement for low night-sky background light levels excluding moonlight.Meanwhile *SII* observations in narrow optical bands are much less affected by the background The *SII* exploitation of large IACT arrays will close to double their operational duty cycle for a modest additional cost. The elegant combination of $SII - IACT$ will increase and diversify science output by giving access to unprecedented imaging capabilities.

These new developments across the community have resulted in the formation of a working group on the topic within the IAU commission 54 on optical and infrared interferometry[5]. The group met officially for the first time during a workshop in January 2009[6]. A report for the CTA collaboration is in preparation. Provisions will be included in the high energy γ-ray camera design to make the future installation of *SII* specific hardware possible. The foreseen IACT arrays offer a sufficiently dense coverage of the Fourier plane to perform actual image reconstruction. Implementation of *SII* on IACT arrays is identified as a natural first step towards revival of intensity interferometry.

4. Concluding remarks

The natural synergy of IACT arrays and *SII* will bring together disparate research communities around a single large scale facility with imaging capabilities at an unprecedented angular

[4] http://www.astronet-eu.org/

[5] http://physics.technion.ac.il/~intint/index.html

[6] http://www.physics.utah.edu/~lebohec/SIIWGWS/

resolution. This will usher in true imaging of diverse stellar phenomena such as rapidly rotating stars and mass accretion processes. It will illuminate stellar evolution processes through calibration of pre-main sequence tracks and highly evolved systems close to going supernova. It will significantly improve the distance scale by calibrating the Cepheid period-luminosity relation. Extra-galactic targets are fainter and smaller, but not out of reach of future IACTs. The time for revival of intensity interferometry in astronomy has arrived.

The temporal variant of *SII* has been chosen for a planned quantum optics instrument for the European Extremely Large Telescope, and is in an advanced stage of development. *Quanteye* is designed to perform on sub-nanoseconds time scales allowing photon correlation spectroscopy[34, 35, 36, 37]. It will provide new insights into high-speed astrophysical phenomena and the fine structure of photon emission. As astronomy is ultimately driven by technical innovation rather than theoretical predictions, these and other related developments of intensity interferometry will undoubtedly open up a new vantage point on the universe.

References

[1] Hanbury Brown R and Twiss R Q 1956 *Nature* **178** 1046
[2] Hanbury Brown R and Twiss R Q 1958 *Royal Society of London Proceedings Series A* **248** 199
[3] Hanbury Brown R, Davis J and Allen L R 1974 *MNRAS* **167** 121
[4] Sato T, Wadaka S, Yamamoto J and Ishii J 1978 *Appl. Opt.* **17** 2047
[5] Vildanov R R, Ismatov M S, Kodirov N Z, et al. 1998 *Turkish Journal of Physics* **22** 949
[6] Ofir A and Ribak E N 2006 *MNRAS* **368** 1652
[7] Ofir A and Ribak E N 2006 *MNRAS* **368** 1646
[8] Nunez P, Le Bohec S, et al. 2009 in prep.
[9] Holmes R B and Belen'kii M S 2004 *Journal of the Optical Society of America A* **21** 697
[10] Stauffer J R, Jones B F, Backman D, et al. 2003 *AJ* **126** 833
[11] Zuckerman B and Song I 2004 *ARA&A* **42** 685
[12] Sasselov D and Karovska M 1994 *ApJ* **432** 367
[13] Feast M W and Catchpole R M 1997 *MNRAS* **286** L1
[14] Groenewegen M A T 1999 *A&AS* **139** 245
[15] de Wit W J, Lamers H J G L M, Marquette J B, et al. 2006 *A&A* **456** 1027
[16] Zorec J and Briot D 1997 *A&A* **318** 443
[17] Domiciano de Souza A, Kervella P, Jankov S, et al. 2003 *A&A* **407** L47
[18] Stewart H A, Guinan E F, Wasatonic R, et al. 2009 in *American Astronomical Society Meeting Abstracts* **213** 408
[19] Ausseloos M, Aerts C, Uytterhoeven K, et al. 2002 *A&A* **384** 209
[20] Peterson D M, Hummel C A, Pauls T A, et al. 2006 *Nature* **440** 896
[21] Weigelt G, Kraus S, Driebe T, et al. 2007 *A&A* **464** 87
[22] Millour F, Petrov R G, Chesneau O, et al. 2007 *A&A* **464** 107
[23] Jaffe W, Meisenheimer K, Röttgering H J A, et al. 2004 *Nature* **429** 47
[24] Sari R, Piran T and Narayan R 1998 *ApJ* **497** L17
[25] Dado S, Dar A and De Rújula A 2003 *A&A* **401** 243
[26] Bernlöhr K *et al.* 2007 *Proc. International Cosmic Ray Conference*
[27] Bloom J S, Perley D A, Li W, et al. 2009 *ApJ* **691** 723
[28] Le Bohec S and Holder J 2006 *ApJ* **649** 399
[29] AGIS, 2008, http://www.agis-observatory.org
[30] CTA, 2008, http://www.mpi-hd.mpg.de/hfm/CTA/
[31] Le Bohec S, Daniel M, de Wit W J, et al. 2008 in *American Institute of Physics Conference Series* **984**, 205
[32] Le Bohec S, Barbieri C, de Wit W J, et al. 2008 in *SPIE Conference Series* **7013**
[33] Buckley J, Byrum K, Dingus B, et al. 2008 *ArXiv e-prints 0810.0444*
[34] Barbieri C, da Deppo V, D'Onofrio M, Dravins D, et al. 2006 in *IAU Symposium* **232**, 506
[35] Naletto G, Barbieri C, Dravins D, et al. 2006 in *SPIE Conference Series* **6269**
[36] Barbieri C, Naletto G, Occhipinti T, et al. 2007 *Memorie della Societa Astronomica Italiana Supplement* **11** 190
[37] Dravins D, Barbieri C, Fosbury R A E, et al. 2006 in *IAU Symposium* **232**, 502

Imaging Stars

After 400 years with telescopes, astronomy is still incapable of observing stars; we only see starlight, not the stars themselves!

A few giants are resolved by adaptive optics or interferometers but to resolve others requires kilometric-scale instruments.

Betelgeuse, imaged with adaptive optics at VLT (ESO).

VLT image of the surface and spot of T Tau in near-infrared (ESO).

Atmospheric turbulence limits optical phase interferometers to baselines of some hundred meters. Longer baselines would require complex space missions, unrealistic in the near future.

However, atmospheric turbulence can be circumvented through quantum-optical techniques and intensity interferometry.

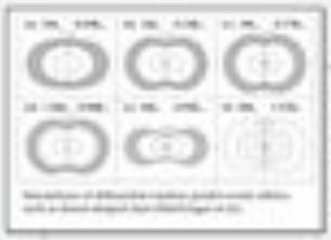

Simulations of diffraction-limited, double-star orbits, such as Kervella's image from Chandon et al. (2).

Novel Science

Stellar imaging reveals the true shapes of stars and their surroundings, opening doors to new discoveries:

- Rotationally deformed stars
- Changing shapes of pulsating stars
- Stellar disks and environments
- Interacting stellar winds

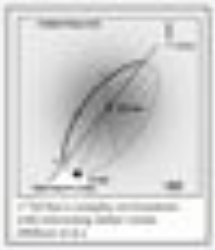

Digital Revival of Intensity Interferometry

Towards a Diffraction-Limited Square-Kilometer Optical Telescope

Hannes JENSEN & Dainis DRAVINS, Lund Observatory

Intensity Interferometry

Intensity interferometry measures second-order coherence of light by correlating intensity fluctuations rather than measuring interference fringes.

Intensity fluctuations are measured over "long" electronic timescales of nanoseconds, being virtually immune to atmospheric disturbances and telescopic imperfections.

In the 1960's, such an interferometer was built by R. Hanbury Brown et al. to measure stellar diameters.

Due to technical limitations at that time, astronomical intensity interferometry was not continued, though it has applications in particle and laboratory physics.

The original Narrabri stellar intensity interferometer in Australia used 6.5 m light collectors moving along a circular track. (University of Sydney.)

The Physics

Quantum effects cause intensity fluctuations in starlight.

The correlation between intensity fluctuations in different telescopes depends on the optical coherence of the light, which in turn depends on the stellar brightness distribution.

$$|V| = |\gamma_{12}| = \sqrt{\frac{\langle \Delta I_1(t+\tau)\Delta I_2(t)\rangle}{\langle I_1\rangle\langle I_2\rangle}}$$

Intensity fluctuations, ΔI, are measured in two telescopes, separated by a time delay of τ.

Using such correlations for different pairs of telescope baselines, the two-dimensional intensity distribution – the image – of the star can be reconstructed.

Digital Revival!

Modern technology enables a "digital revival" of intensity interferometry as a route towards high-brilliance-second imaging in the visible:

- High-speed photon-counting detectors
- Fast digital hardware signal correlators
- Large-flux collectors and big telescopes
- Algorithms for image reconstruction

The electronic connection of multiple optical telescopes has analogies with ν interferometry recently developed at radio wavelengths.

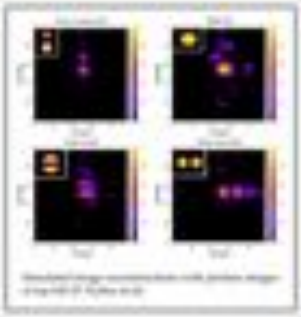

Simulated image reconstruction with position images at top left (V. Fodera et al).

Air Cherenkov Telescopes

Imaging Air Cherenkov Telescopes (IACTs) study Cherenkov light induced in the Earth's atmosphere by energetic gamma rays, but are very suitable also for intensity interferometry.

VERITAS in Arizona has already been used for our experiments, and work is in progress to enable intensity interferometry with the planned Cherenkov Telescope Array, CTA.

Much simpler than space interferometers, such IACTs may become the first kilometric-scale imagers in optical astronomy, revealing stellar features on sub-milliarcsecond scales.

VERITAS in Arizona, with its four 12 m reflectors. The cluster has already been used with a super-Cherenkov experiment. (© VERITAS collaboration, Copyright).

CTA – the planned next-generation IACT, in with concept of optical 100-fold collection beyond even these mega-telescopes. (CTAO).

Further reading:

W. Lee Wild et al., Next Astrophysical Opportunities Exploiting Stellar Temporal Optical Correlations, Astro2010 Science White Papers (http://sites.nationalacademies.org/bpa/BPA_049312)

D.Dravins & S.LeBohec, Towards a diffraction-limited square-kilometer optical telescope: Digital revival of intensity interferometry, SPIE Proc. **6986**, 69860P (2008)

D.Dravins, Photonic Astronomy and Quantum Optics, in High Time Resolution Astrophysics, Astrophys. Space Sci. Lib. **351**, 91 (2008)

Stellar intensity interferometry: Optimizing air Cherenkov telescope array layouts

Hannes Jensen[a], Dainis Dravins[a], Stephan LeBohec[b], Paul D. Nuñez[b]

[a]Lund Observatory, Box 43, SE-22100 Lund, Sweden
[b]Department of Physics and Astronomy, The University of Utah, 115 South 1400 East, Salt Lake City, UT 84112-0830, U.S.A.

ABSTRACT

Kilometric-scale optical imagers seem feasible to realize by intensity interferometry, using telescopes primarily erected for measuring Cherenkov light induced by gamma rays. Planned arrays envision 50–100 telescopes, distributed over some 1–4 km^2. Although array layouts and telescope sizes will primarily be chosen for gamma-ray observations, also their interferometric performance may be optimized. Observations of stellar objects were numerically simulated for different array geometries, yielding signal-to-noise ratios for different Fourier components of the source images in the interferometric (u, v)-plane. Simulations were made for layouts actually proposed for future Cherenkov telescope arrays, and for subsets with only a fraction of the telescopes. All large arrays provide dense sampling of the (u, v)-plane due to the sheer number of telescopes, irrespective of their geographic orientation or stellar coordinates. However, for improved coverage of the (u, v)-plane and a wider variety of baselines (enabling better image reconstruction), an exact east-west grid should be avoided for the numerous smaller telescopes, and repetitive geometric patterns avoided for the few large ones. Sparse arrays become severely limited by a lack of short baselines, and to cover astrophysically relevant dimensions between 0.1–3 milliarcseconds in visible wavelengths, baselines between pairs of telescopes should cover the whole interval 30–2000 m.

Keywords: Instrumentation: high angular resolution – Instrumentation: interferometers – Stars: individual

1. IMAGING STARS WITH INTENSITY INTERFEROMETRY

1.1 Introduction

A small number of the apparently largest stars have now been imaged with phase/amplitude interferometers, revealing their oblate shapes caused by rapid rotation or perhaps being surrounded by circumstellar winds, disks, or shells. Clearly, improving the angular resolution by just another order of magnitude would enable many more phenomena to be resolved.[1] However, atmospheric turbulence makes the required interferometry over hundreds of meters quite challenging for phase/amplitude interferometers which require optical path-length precisions within a fraction of an optical wavelength.

Optical intensity interferometry currently seems the most realistic way to realize imaging of stars on scales well below one milliarcsecond (mas).[2,3] Using a simple λ/D criterion, 1 mas resolution at λ=500 nm requires a baseline around 100 meters, while 1 km enables 100 μas. For the forthcoming large arrays of Cherenkov telescopes, extensions over some 2 km are discussed, and if such could be utilized at λ=350 nm, resolutions could approach 30 μas.

1.2 Theory of Intensity Interferometry

Intensity interferometry measures correlations in light intensity fluctuations between pairs of telescopes.[4,5] This correlation is related to the squared modulus of the complex degree of coherence of the light:

$$|\gamma|^2 = \frac{\langle \Delta I_1 \Delta I_2 \rangle}{\langle I_1 \rangle \langle I_2 \rangle} \tag{1}$$

[a] hannesj1@gmail.com, dainis@astro.lu.se, www.astro.lu.se

where I_i and ΔI_i are the intensity and intensity fluctuations respectively, measured by telescope i and $\langle\rangle$ denotes the time average.

The complex coherence is proportional to the Fourier transform of the stellar surface brightness, Θ, sampled at a point (u, v) in the Fourier plane, according to the van Cittert-Zernike theorem:

$$\gamma(u,v) \propto \iint \Theta(l,m) e^{-2\pi i(ul+vm)} \,\mathrm{d}l \,\mathrm{d}m \tag{2}$$

where l, m are (angular) positions in the sky. So, in short, each pair of telescopes in an intensity interferometer measures the square of the magnitude of the Fourier transform of the target at one point in the Fourier plane.

Long telescope separations, or baselines, measure high-frequency components, corresponding to small structures on the target, while short baselines sample the low frequencies. For a baseline $\mathbf{B} = (B_{\mathrm{North}}, B_{\mathrm{East}})$ the associated Fourier-plane coordinates are $(u, v) = \frac{1}{\lambda}(B_{\mathrm{North}}, B_{\mathrm{East}})$.

For an array of N telescopes there are $N(N-1)/2$ (not necessarily unique) baselines. As the target of observation moves across the sky, the projected baselines, $\mathbf{B}_p$, will change, with each telescope pair tracing out an ellipse in the Fourier plane according to the following expression:[6]

$$(u,v,w) = \frac{1}{\lambda}\mathbf{B}_p = \frac{1}{\lambda}\begin{pmatrix} -\sin l \sin h & \cos h & \cos l \sin h \\ \sin l \cos h \sin\delta + \cos l \cos\delta & \sin h \sin\delta & -\cos l \cos h \sin\delta + \sin l \cos\delta \\ -\sin l \cos h \cos\delta + \cos l \sin\delta & -\sin h \cos\delta & \cos l \cos h \cos\delta + \sin l \sin\delta \end{pmatrix} \begin{pmatrix} B_{\mathrm{North}} \\ B_{\mathrm{East}} \\ 0 \end{pmatrix} \tag{3}$$

where l is the latitude of the telescope array and δ and h are the declination and hour angle of the star. The w component corresponds to the time delay between the two telescopes. This effect, known as *Earth rotation synthesis*, greatly increases the Fourier-plane coverage of a telescope array.

From the Fourier magnitude, it is possible to both reconstruct the image of the target[7] (provided the sampling is good enough), or fit a model to the data.

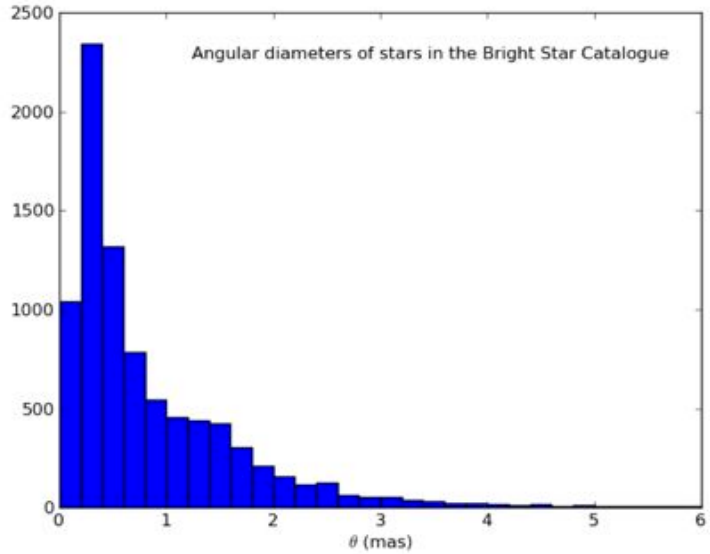

Figure 1. Approximated angular diameters of the stars in the Bright Star Catalogue (BSC),[8] containing all stars in the sky with $m_V < 6.5$ (a few outliers have been omitted for clarity). Effective temperatures were estimated from their $B-V$ color index, and then used to calculate the angular diameters.

Optimizing the telescope placement in an interferometric array is a complex problem that has been widely studied for optical and radio interferometers (e.g., Refs. 9–11). The optimal configuration depends upon the task: if the objective is to study very small structures, long baselines are required. If, on the other hand, one wishes to measure large-scale structures, shorter baselines are necessary. For a general-purpose array, it is usually preferable to have a healthy mixture of short and long baselines, sampling the (u, v)-plane as uniformly as possible. In some interferometers this is satisfied by movable telescopes; in others one maintains similar diffraction-limited resolutions for observations at different wavelengths, placing telescopes in self-similar patterns (e.g., logarithmic spirals), while still others may be constrained by the local geography. In any case it is almost always best to avoid regularly spaced telescopes, since such placement results in duplicate baselines.

1.3 Astrophysical Targets

Ideal targets for intensity interferometry are hot and bright stars.[1] The limiting magnitude depends on the size of the flux collectors, the detectors with their electronics, and the integration time, but simulations and previous experience suggest a limiting magnitude around $m_V \sim 9$,[2] while initial observing programs will likely be limited to $m_V \lesssim 6$.

The Bright Star Catalogue (BSC)[8] lists all stars brighter than $m_V = 6.5$ (a total of 9096), and can be used to illustrate the parameters of likely observational targets. The $B - V$ colors of the BSC entries were converted to theoretical effective temperatures by fitting a polynomial to data relating T_{eff} and $B - V$ color index from Bessel et al.[12] These effective temperatures were then used to calculate the angular diameters assuming the stars are blackbodies with uniform circular disks; see Fig. 1.

Most bright stars have angular diameters on the order of one milliarcsecond (mas) or less. Such a star is resolved by telescopic baselines of ∼100 m, so an array must provide baselines at least this long to be able to observe any significant number of objects. However, it is important to note that short baselines are also crucial. An array lacking baselines shorter than ∼ 100 m will have too narrow a field of view to image the shapes of most stars.

1.4 Technical Requirements

Intensity interferometry places substantial technical requirements on the detection equipment used (for a discussion of its technical aspects, see Ref. 13). Very high time-resolution detectors are required to measure the rapid intensity fluctuations, and fast hardware is needed for calculating correlation functions. However, by far the most expensive components are the flux collectors. The technique is sensitive to the square of the received light intensity, and large amounts of starlight need to be collected. On the other hand, there is no need for high-quality optics – a time resolution on the order of 1 ns, say, corresponds to a light travel distance of 30 cm, and optical imperfections comparable to such a magnitude can be tolerated. Despite the tolerance for optical imperfections, the cost associated with a large array of ∼10 m telescopes is substantial, so a very attractive possibility is to operate intensity interferometry as an auxiliary program on arrays set up for other purposes.

Seemingly ideal for this purpose are those air Cherenkov telescopes that are being erected for gamma-ray astronomy (e.g., Refs. 14,15). These measure the feeble Cherenkov light in air produced by cascades of secondary particles initiated by highly energetic gamma rays. They must have a time resolution of a few nanoseconds (set by the duration of the Cherenkov light flash); they must be sensitive to short optical wavelengths (Cherenkov light is bluish); they must be large (Cherenkov light is faint), and they need to be separated by distances of ∼50 m to ∼200 m (extent of the Cherenkov light-pool onto the ground).

2. EXISTING CHERENKOV TELESCOPE ARRAYS

A number of air Cherenkov telescope facilities are already in operation, with the major ones summarized in Fig. 2 and Table 1.

Table 1. Properties of some existing Cherenkov arrays. N denotes the number of telescopes, A is the light collection area of each telescope, n is the number of unique baselines simultaneously available, B_{min}, B_{max} indicates the range of baselines for observation at zenith. The corresponding range of angular diameters in milliarcseconds ($1.22\lambda/b$) for observations at 400 nm is indicated by $\theta_{min}, \theta_{max}$.

Array	N	A (m^2)	n	B_{min}, B_{max} (m)	$\theta_{min}, \theta_{max}$ (mas)
CANGAROO-III[16]	4	57	6	100, 184	0.5, 1.0
HAGAR[17]	7	7	21	50, 100	1.0, 2.0
H.E.S.S.-I[18]	4	108	6	120, 170	0.6, 0.8
MAGIC[19]	2	227	1	85, 85	1.2, 1.2
PACT[20]	25	9.5	300	20, 128	0.8, 5.0
TACTIC[21]	4	7	6	17, 20	5.0, 6.0
VERITAS[22]	4	113	6	80, 140	0.7, 1.2

2.1 Interferometric capabilities of existing arrays

Already the baselines offered by some of the existing arrays may be adequate for starting intensity interferometry experiments. Their adequately large flux collectors should provice excellent signal-to-noise ratios, but the longest baselines do not reach more than some 200 meters and their achievable angular resolution essentially overlaps with that feasible with existing phase interferometers (though observations could be made in the blue or violet, where the contrast of many stellar features is expected to be higher). Table 1 lists some of their relevant properties.

Figure 3 shows a simulation of the Fourier plane coverage of the baselines possible with the VERITAS array for an 8-hour observation of a star moving through zenith, cf. Eq. (3). While the (u, v)-coverage is increased greatly through Earth rotation, it is still rather sparse and does not extend very far.

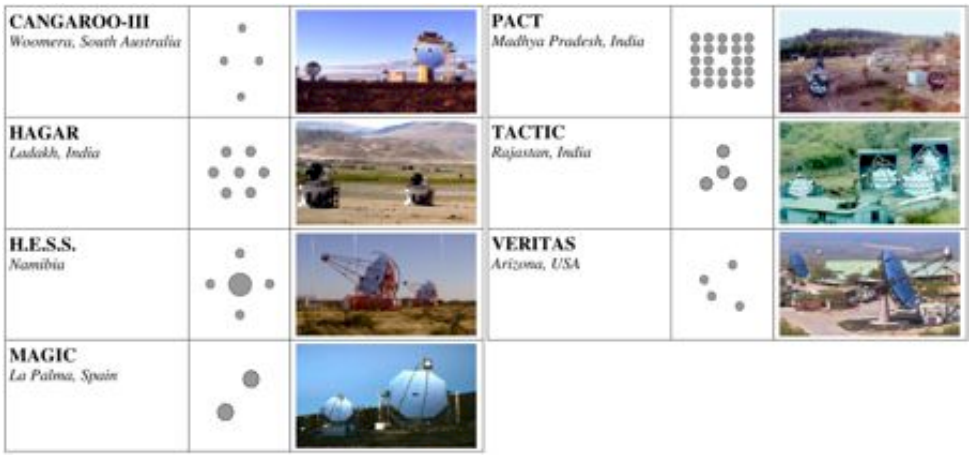

Figure 2. Overview of existing air Cherenkov telescope arrays. The geometric layout is shown with north upwards (the scale varies between different arrays in the figure; see Table 1 for array sizes).

3. FUTURE CHERENKOV TELESCOPE ARRAYS

The largest current projects for future observatories are CTA (Cherenkov Telescope Array),[23] and AGIS (Advanced Gamma-ray Imaging System).[24] Either of them is envisioned to comprise around 50-100 flux collectors with diameters up to ∼20 m spread over kilometer-scale distances. These would be excellent facilities for intensity interferometry, both in terms of resolution and Fourier-plane sampling, and their design studies now also incorporate their possible use for optical interferometrry. For such use, appropriate data analysis software would digitally synthesize baselines between all possible pairs of telescopes.[2,3]

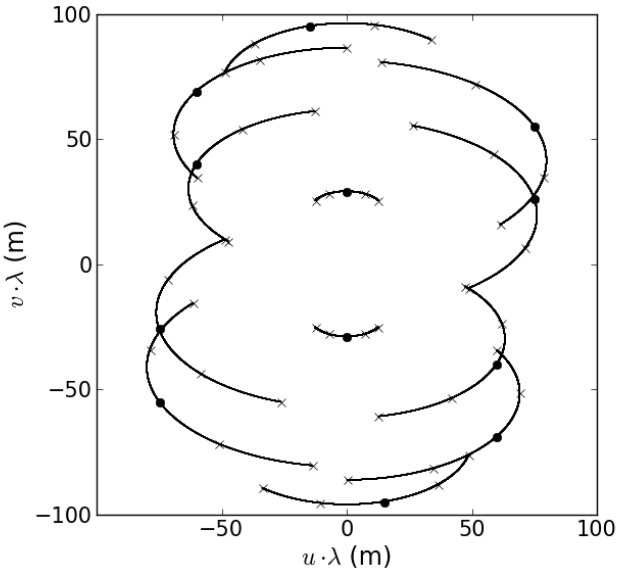

Figure 3. Simulated (u, v)-coverage of the VERITAS array (Fig. 2 and Table 1) for an 8-hour observation of a star moving through zenith. Each pair of telescopes traces out two partial ellipses in the Fourier plane, since the Fourier magnitude in a point (u, v) will be the same as in the point $(-u, -v)$. The filled circles indicate the snapshot Fourier plane coverage when the star is in the zenith. The small crosses mark 2-hour intervals before and after the meridian passage.

3.1 Candidate configurations

Any dedicated interferometer can be optimized for the best coverage of the interferometric (u, v)-plane. However, for Cherenkov telescope arrays, intensity interferometry is a secondary application and telescope placements and sizes will primarily be chosen for their gamma-ray observations. Nevertheless, also the interferometric performance may be optimized, without compromising the gamma-ray performance nor adding extra costs.

A number of candidate array layouts for the CTA are being studied within its design study,[23,25,26] of which a number is shown in Fig. 4. Each of these candidate layouts is a subset of an all-encompassing larger array, shown in the bottom-right corner. Note that several among the configurations are not fundamentally different from each other. Already from a quick glance, one can roughly divide the layouts into three groups: A, B, F and G, whose telescopes are concentrated in a fairly small area and which lack longer baselines; C, D and J which contain telescopes more sparsely spread out over a large area; and E, H, I and K which contain a larger number of telescopes and provide both long and short baselines. For this paper, the configurations B, D and I were selected for more detailed study, as "representatives" of the three groups.

The left column in Fig. 5 shows the telescope placement of the three examined configurations B, D and I.

Table 2. Properties of the three examined candidate configurations. N is the number of telescopes, A is the light collection area of each type of telescope, n is the number of unique baselines available, B_{min}, B_{max} indicates the range of baselines for observations in zenith. The corresponding range of angular diameters in milliarcseconds $(1.22\lambda/b)$ for observations at 400 nm is indicated by $\theta_{min}, \theta_{max}$.

Array	N	A (m^2)	n	B_{min}, B_{max} (m)	$\theta_{min}, \theta_{max}$ (mas)
Conf. B	42	113, 415	253	32, 759	0.13, 3.2
Conf. D	57	113	487	170, 2180	0.05, 0.6
Conf. I	77	28, 113, 415	1606	90, 2200	0.05, 1.13

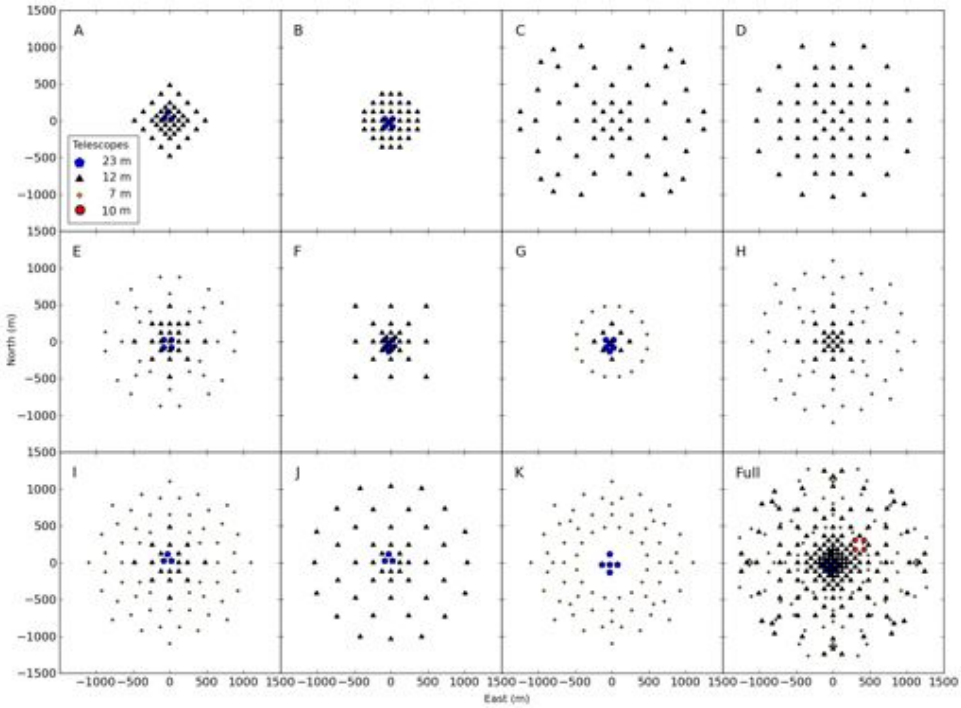

Figure 4. Different telescope array layouts currently being discussed for CTA. Each of the configurations is a subset of the large array shown in the bottom-right corner. For this paper, configurations B, D and I were selected for further study.

The middle column shows a "snapshot" (u, v)-plane coverage of the arrays for a star in the zenith. In the right column, the effect in the (u, v)-plane of the star moving 20 degrees from the zenith to the west is shown.

Already from Fig. 5 and Table 2 something can be said about the designs if applied to intensity interferometry. Configuration B samples the central parts of the Fourier plane very densely and would provide a field of view that is fully capable of imaging the shapes of almost any stellar object. However, since it lacks longer baselines, it is unable to resolve details smaller than ∼0.13 mas.

Configuration D, on the other hand, provides baselines out to 2180 m, permitting studies of very detailed structures, down to around 50 μas. However, its shortest baseline is 170 m, which means that any structures larger than ∼0.6 mas will be lost. This makes it unsuitable for most stars (cf. Fig. 1). Configuration I seems to provide the best of the two worlds: it has baselines short enough to measure the shapes of the disks of most stellar objects, while still providing very long baselines and a very good resolution.

4. SIMULATED OBSERVATIONS WITH CHERENKOV TELESCOPE ARRAYS

An intensity interferometer using two photon-counting detectors A and B and a digital correlator will measure the correlation of Eq. (1) in a discrete form:

$$g^{(2)} = \frac{N_{AB}}{N_A N_B} N, \tag{4}$$

where N_A and N_B are the number of photons detected in A and B respectively, N_{AB} is the number of joint detections and N is the number of sampled time intervals. In the simulations presented below, each measurement was simulated by generating random numbers N_A, N_B and N_{AB} and inserting into Eq. (4). These will be Poisson distributed random variables* with mean values $\lambda_A = P_A \cdot N$, $\lambda_B = P_B \cdot N$ and $\lambda_{AB} = P_{AB} \cdot N$. Here, P_A and

*In reality, the measurement time is always long enough for the Poisson distributions to be adequately approximated as normal distributions.

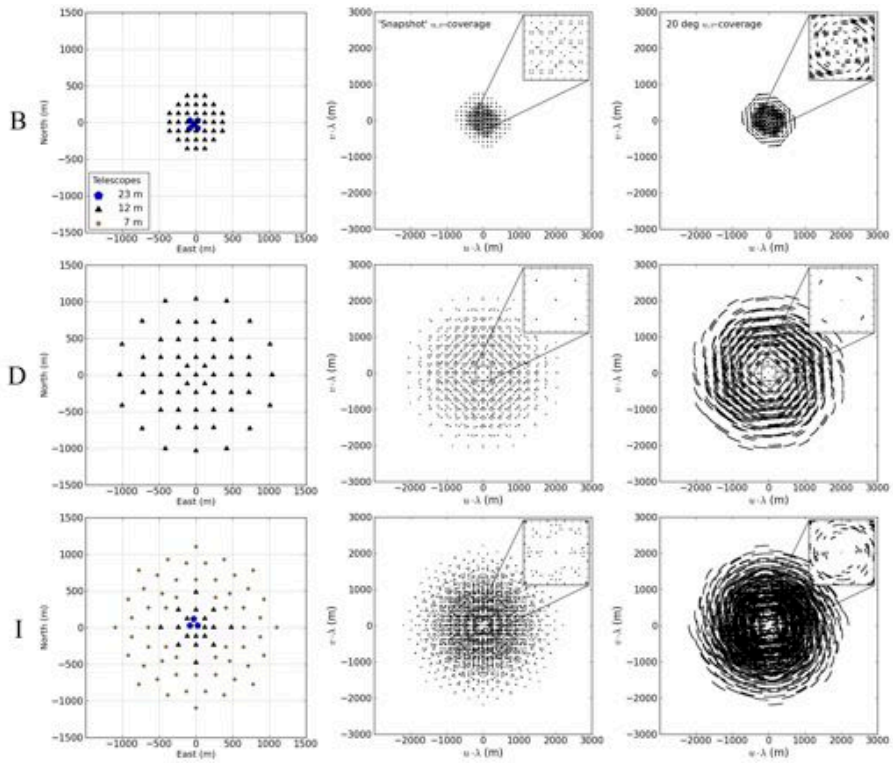

Figure 5. Left column: Telescope placement for the three candidate configurations B, D and I (top to bottom). Middle column: (u, v)-plane coverage at an instant in time for a star in the zenith. Upper right-hand squares show the central 400x400 m area. Right column: (u, v)-plane coverage for a star moving from the zenith through 20 degrees to the west.

P_B are the probabilities of detecting a photon in A and B respectively within a small time interval Δt and P_{AB} is the probability of a joint detection within Δt.

These probabilites can be written out in terms of variables depending only on the instrumentation and the target of study (e.g. Ref. 27):

$$P_A = \alpha_A \langle I_A \rangle \Delta t \tag{5}$$

$$P_B = \alpha_B \langle I_B \rangle \Delta t \tag{6}$$

$$P_{AB} = P_A P_B + \alpha_A \alpha_B \langle I_A \rangle \langle I_B \rangle |\gamma_{AB}|^2 \frac{\tau_c}{\Delta t} \Delta t^2 \tag{7}$$

Here α denotes the quantum efficiency[†] of the detectors, $\langle I \rangle$ is the mean light intensity, τ_c is the coherence time of the light (determined by the wavelength and optical passband) and γ_{AB} is the degree of optical coherence (proportional to the Fourier transform of the target). Such simulations were carried out for the various candidate configurations using the binary star in Fig. 6 as the source to be observed.

4.1 Varying target magnitude

Figure 7 shows the results of varying the brightness of the target. The simulations started with the star in zenith and then moving 50 degrees to the west in steps of 5 degrees, with an integration time of 2 hours at each time step (thus, such an observation would require several nights of integration). The observational wavelength was 500 nm and the detectors were assumed to have a time resolution of 1 ns and a quantum efficiency of 70 %.

[†]The quantum efficiency of a detector is essentially the ratio of detected photons to incoming photons.

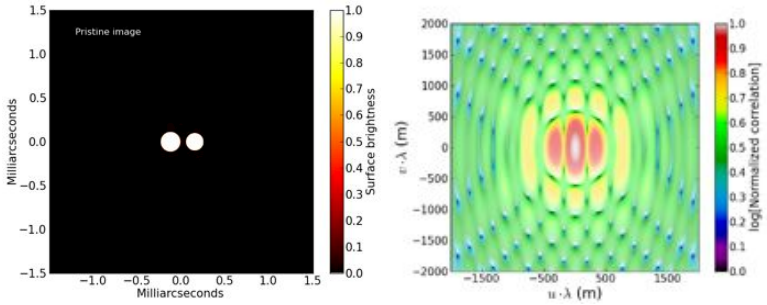

(a) Source image (b) Fourier magnitude

Figure 6. Test image of a binary star used for simulations and its (logarithmized) Fourier magnitude.

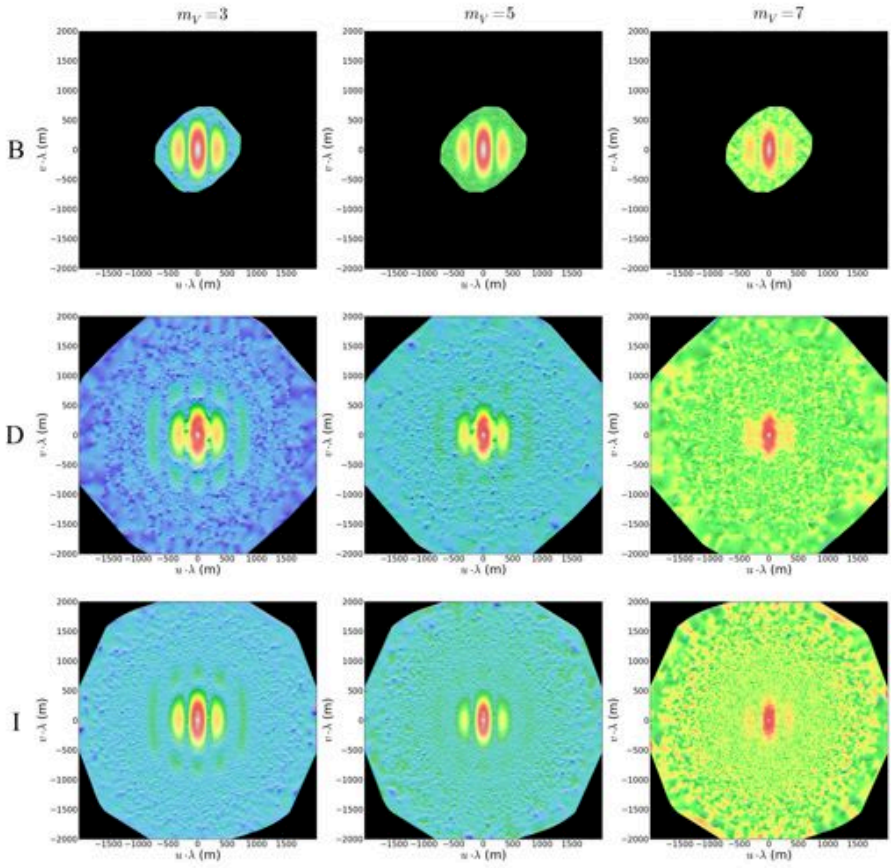

Figure 7. Simulated observations of the binary star in Fig. 6 with configuration B (top row), D (middle) and I (bottom). Vertical columns are for differently bright stars; left is for $m_V = 3$; center for $m_V = 5$, and $m_V = 7$ to the right.

The data from the simulations are shown in the Fourier plane. To better illustrate the locations of low-amplitude structures and of noise, the data were logarithmized and normalized after first performing a linear interpolation between the "observed" points, in order to obtain the Fourier magnitude over a regular grid. A 3D shading was then applied to the data to further highlight the locations of structures (the absolute values of the measured correlations are not of any real significance in this context).

These simulations are consistent with earlier results in that the practical limiting magnitude seems to lie somewhere around $m_V = 6-7$. Configuration B performs well in reproducing the three central lobes of Fig. 6(b), but it lacks the longer baselines needed for higher-frequency components.

Configuration D, on the other hand, measures the higher-frequency components very well but even for a target with such a small angular extent, the central parts of the Fourier plane – which determine the overall shape of the object – are distorted due to poor sampling at short baselines. Configuration I samples the whole Fourier plane well, but its smaller-size telescopes (see Fig. 5) makes it a bit more sensitive to target magnitude.

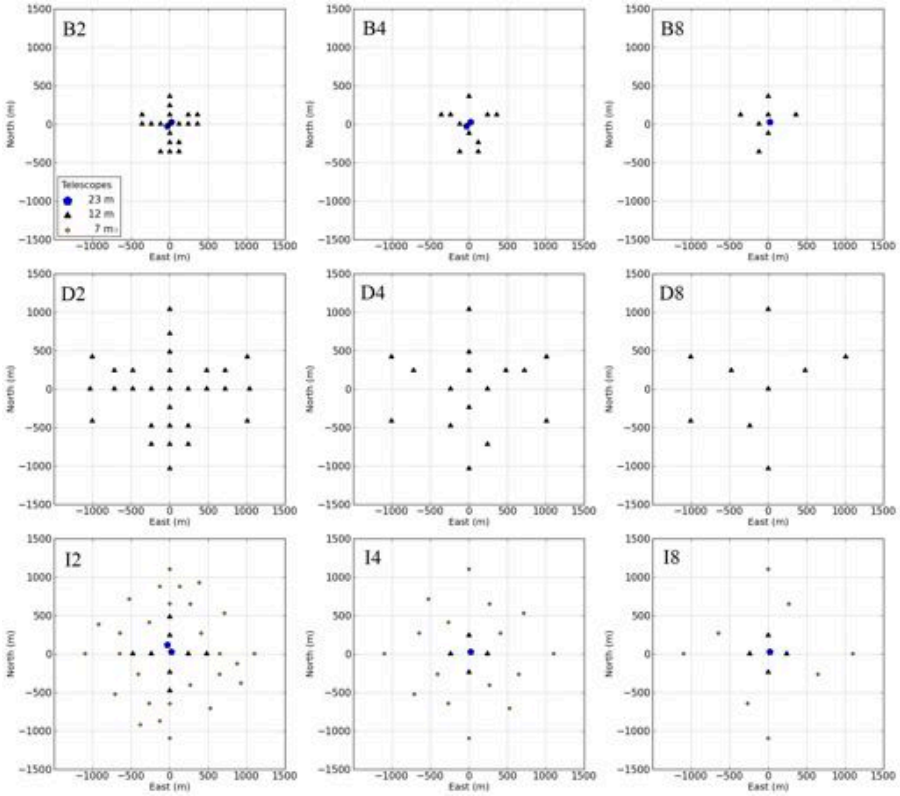

Figure 8. Subsets of the candidate configurations (B, D, I from top to bottom). In the leftmost column half the telescopes of the superset configuration were selected in a pseudo-random fashion. In the middle column, one in four telescopes was selected, and in the rightmost column one in eight.

4.2 Observations with subsets of the configurations

It is interesting to examine the performance of also various smaller subsets of the telescope arrays. It is not known whether some modifications or special equipment might be required at each telescope to be used for intensity interferometry, nor whether the full array will always be available. Observations using only a subset of the telescopes may thus represent a realistic mode of operation, at least initially.

For each of the configurations B, D and I, three subset configurations were generated, as shown in Fig. 8. The configurations shown in the leftmost column, designated B2, D2 and I2, were obtained by selecting half of the full set of telescopes in a semi-random manner (attempting to preserve the overall "shape" of the array). In the middle column, one in four telescopes was retained (these are referred to as B4, D4, and I4) and in the rightmost column only one telescope in eight was kept (B8, D8, and I8).

Figure 9 shows the output from simulations of the binary star in Fig. 6(a) using these subsets. The simulation parameters were the same as in Fig. 7 except that the magnitude of the star was now fixed to m_V =5 and the

integration time was increased to 10 hours per timestep in order to depress measurement noise and thus highlight sampling effects for the various configurations.

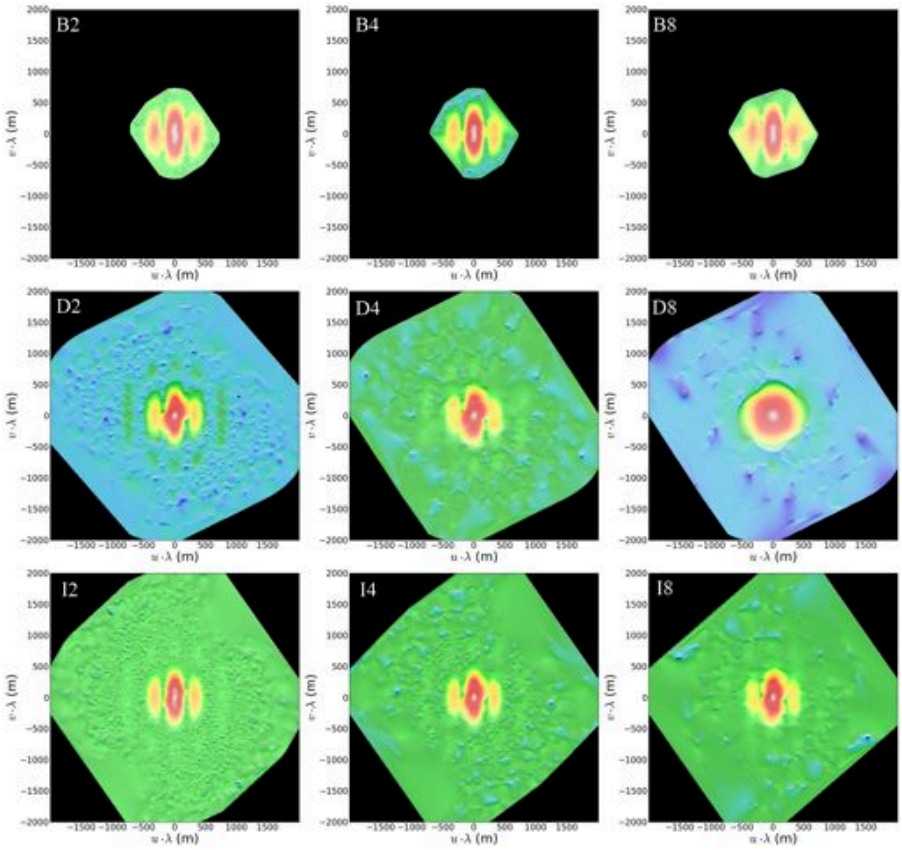

Figure 9. Simulated observations of the binary star in Fig. 6 with subsets of configuration B (top row), D (middle row) and I (bottom row). The left column is for subsets containing half of the telescopes; the center for a quarter, and the rightmost for one eighth (see Fig. 8).

It is obvious that more telescopes are better in terms of Fourier plane sampling, and too few telescopes can ruin the results, as illustrated by the observation with D8. It should be noted, however, that no attempt was made to optimize the selection of telescopes in order to improve the sampling. Once the design for CTA is finalized, this could be one of the first problems to examine in order to determine which telescopes to equip first for intensity interferometry.

4.3 Image reconstruction

The discussion above has only dealt with Fourier magnitudes, which is what is directly measured by an intensity interferometer. Fourier magnitudes alone can be used to fit model parameters such as stellar diameters, binary separations, circumstellar disk thicknesses, etc. As is shown in Ref. 7, model-independent image reconstruction from the Fourier magnitude alone is indeed possible (though with some limitations).

Figure 10 shows a proof-of-concept example of an image reconstructed from simulated data using one of the candidate configurations. However, image reconstruction is an active area of research and many practical issues remain to be improved. Thus, at this stage, it is not yet possible to tell which imperfections are due to fundamental limitations of the algorithms used or simply due to practical issues that can be solved. There is thus a risk that a comparison between reconstructed images from the different candidate arrays would be misleading, which is why the focus here is instead on the algorithm-independent Fourier magnitudes.

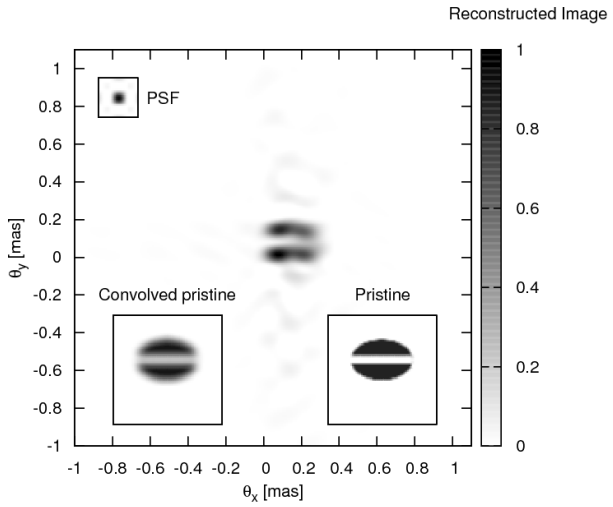

Figure 10. Image reconstructed from simulated data corresponding to 50 hours of observation of a magnitude 6 rotationally flattened star with an obscuring disk. The simulation was done using a telescope array qualitatively similar to those discussed in this paper (see Ref. 7 for details). The image in the bottom-right corner was used as input for the simulation. Also shown is the pristine image convolved with the point-spread-function of the array. The difference in sharpness between this and the pristine image is due to the inability of a finite-sized array to measure all the higher-frequency Fourier components. The convolved pristine image is thus the best image that is theoretically possible to reconstruct.

5. CONCLUSIONS

A facility such as the CTA will most likely be able to produce excellent scientific data if used as an intensity interferometer, providing measurements of spatial structures on scales down to a few tens of μas – orders of magnitude better than what is possible today in visible light.

The candidate configurations examined here – while not optimized for intensity interferometry – all provide very dense sampling of the (u, v)-plane due to the sheer number of telescopes. Apart from the simulations described above, a number of other tests were carried out to determine effects from varying the declination of the star and the geographic orientation of the telescope array. It was found that the very large number of telescopes make the effects of any such variations almost negligible.

However, it must be noted that an array such as configuration D will be severely crippled by its lack of short baselines, essentially limiting such a facility to only studying stars smaller than $\sim$0.5 mas. Also, to improve coverage of the (u, v)-plane and to ensure a wider variety of baselines (enabling better image reconstruction), an exact east-west orientation should be avoided for the grid of many smaller telescopes (since stars rise in the east, and move towards west, the projection of any east-west baseline will vary only in amount, not orientation). For the fewer large telescopes, repetitive geometric patterns should be avoided, in order to avoid redundancy in baselines. To cover astrophysically relevant dimensions between 0.1–3 milliarcseconds, baselines between pairs of telescopes should as far as possible cover the whole interval 30–2000 m.

ACKNOWLEDGMENTS

The work at Lund Observatory is supported by the Swedish Research Council and The Royal Physiographic Society in Lund. S. LeBohec acknowledges support from grants SGER #0808636 of the National Science Foundation.

REFERENCES

[1] Dravins, D., Jensen, H., LeBohec, S., and Nuñez, P. D., "Stellar intensity interferometry: Astrophysical targets for sub-milliarcsecond imaging," *Proc. SPIE* **7734**, 7734–9 (2010).

[2] Le Bohec, S. and Holder, J., "Optical intensity interferometry with atmospheric Cerenkov telescope arrays," *Astrophys. J.* **649**, 399–405 (2006).

[3] LeBohec, S., Barbieri, C., de Witt, W.-J., et al., "Toward a revival of stellar intensity interferometry," *Proc. SPIE* **7013**, 70132E (2008).

[4] Hanbury Brown, R., [*The Intensity Interferometer*], Taylor & Francis, London (1974).

[5] Labeyrie, A., Lipson, S. G., and Nisenson, P., [*An Introduction to Optical Stellar Interferometry*], Cambridge Univ. Press, Cambridge (2006).

[6] Ségransan, D., "Observability and UV coverage," *New Astron. Rev.* **51**, 597–603 (2007).

[7] Nuñez, P. D., LeBohec, S., Kieda, D., et al., "Stellar intensity interferometry: Imaging capabilities of air Cherenkov telescope arrays," *Proc. SPIE* **7734**, 7734–47 (2010).

[8] Hoffleit, D. and Warren, Jr., W. H., "Bright Star Catalogue, 5th revised ed.," *VizieR Online Data Catalog* **5050** (1995).

[9] Keto, E., "The shapes of cross-correlation interferometers," *Astrophys. J.* **475**, 843–852 (1997).

[10] Millour, F., "All you ever wanted to know about optical long baseline stellar interferometry, but were too shy to ask your adviser," *New Astron. Rev.* **52**, 177–185 (2008).

[11] Boone, F., "Interferometric array design: Optimizing the locations of the antenna pads," *Astron. & Astrophys.* **377**, 368–376 (2001).

[12] Bessell, M. S., Castelli, F., and Plez, B., "Model atmospheres broad-band colors, bolometric corrections and temperature calibrations for O - M stars," *Astron. & Astrophys.* **333**, 231–250 (erratum **337**, 321) (1998).

[13] LeBohec, S., Adams, B., Bond, I., et al., "Stellar intensity interferometry: Experimental steps toward long-baseline observations," *Proc. SPIE* **7734**, 7734–48 (2010).

[14] Hinton, J., "Ground-based gamma-ray astronomy with Cherenkov telescopes," *New J. of Phys.* **11**, 055005 (2009).

[15] Völk, H. J. and Bernlöhr, K., "Imaging very high energy gamma-ray telescopes," *Exp. Astron.* **25**, 173–191 (2009).

[16] Kubo, H., Asahara, A., Bicknell, G. V., et al., "Status of the CANGAROO-III project," *New Astron. Rev.* **48**, 323–329 (2004).

[17] Chitnis, V. R., Acharya, B. S., Bhat, P. N., et al., "Status of HAGAR, the High Altitude Gamma Ray Observatory at Hanle," *29th International Cosmic Ray Conference Pune* **5**, 235–238 (2005).

[18] Hinton, J. A., "The status of the HESS project," *New Astron. Rev.* **48**, 331–337 (2004).

[19] Cortina, J., "Status and first results of the Magic telescope," *Astrophys. Space Sci.* **297**, 245–255 (2005).

[20] Bhat, P. N., Acharya, B. S., Chitnis, V. R., et al., "Pachmarhi array of Cherenkov telescopes," *Bull. Astron. Soc. India* **28**, 455–457 (2000).

[21] Koul, R., Tickoo, A. K., Kaul, S. K., et al., "The TACTIC atmospheric Cherenkov imaging telescope," *Nucl. Instr. Meth. Phys. Res. A* **578**, 548–564 (2007).

[22] Holder, J., Atkins, R. W., Badran, H. M., et al., "The first VERITAS telescope," *Astropart. Phys.* **25**, 391–401 (2006).

[23] "CTA, Cherenkov Telescope Array." http://www.cta-observatory.org (2010).

[24] "AGIS, Advanced Gamma-ray Imaging System." http://www.agis-observatory.org (2010).

[25] Bernlöhr, K., Carmona, E., and Schweizer, T., "MC Simulation and layout studies for a future Cherenkov telescope array," *Proc. 30th International Cosmic Ray Conference* **3**, 1469–1472 (2008).

[26] Hermann, G., "Towards the future Cherenkov telescope array CTA," *Nucl. Instr. Meth. Phys. Res. A* (2010).

[27] Mandel, L. and Wolf, E., [*Optical Coherence and Quantum Optics*], Cambridge University Press, Cambridge (1995).

Stellar Intensity Interferometry: Imaging capabilities of air Cherenkov telescope arrays

Paul D. Nuñez[a*], Stephan LeBohec[a], David Kieda[a], Richard Holmes[b], Hannes Jensen[c], Dainis Dravins[c]

[a] University of Utah, Dept. of Physics & Astronomy, 115 South 1400 East, Salt Lake City, UT 84112-0830, USA
[b] Boeing LTS, Inc., 535 Lipoa Parkway, Suite 200, Kihei, Hawaii 96753-6907, USA
[c] Lund Observatory, Box 43, SE-22100 Lund, Sweden

ABSTRACT

Sub milli-arcsecond imaging in the visible band will provide a new perspective in stellar astrophysics. Even though stellar intensity interferometry was abandoned more than 40 years ago, it is capable of imaging and thus accomplishing more than the measurement of stellar diameters as was previously thought. Various phase retrieval techniques can be used to reconstruct actual images provided a sufficient coverage of the interferometric plane is available. Planned large arrays of Air Cherenkov telescopes will provide thousands of simultaneously available baselines ranging from a few tens of meters to over a kilometer, thus making imaging possible with unprecedented angular resolution. Here we investigate the imaging capabilities of arrays such as CTA or AGIS used as Stellar Intensity Interferometry receivers. The study makes use of simulated data as could realistically be obtained from these arrays. A Cauchy-Riemann based phase recovery allows the reconstruction of images which can be compared to the pristine image for which the data were simulated. This is first done for uniform disk stars with different radii and corresponding to various exposure times, and we find that the uncertainty in reconstructing radii is a few percent after a few hours of exposure time. Finally, more complex images are considered, showing that imaging at the sub-milli-arc-second scale is possible.

1. INTRODUCTION

There has been a recent interest in the revival of Stellar Intensity Interferometry (SII) due to the excellent baseline coverage of planned air Cherenkov telescope arrays.[1,2] This interest has lead to developments in instrumentation, experimentation, and simulations of the capabilities of this technique. Various analog and digital correlator technologies[3] are being implemented by LeBohec et. al.,[4] and cross correlation of streams of photons with nanosecond scale resolution has already been achieved. The suitability of various proposed array configurations is being evaluated by Jensen et al.[5] to understand their different sensitivities for interferometric imaging before final choices of the array layouts are made. Image reconstruction algorithms such as the one suggested by Holmes et. al.[6] have opened the possibility of imaging and have become interesting subjects in their own right. In this paper we will focus on the imaging capabilities and limitations of air Cherenkov telescope arrays used as high angular resolution intensity interferometers.

High angular resolution astronomy in the optical range will open a whole new field of exploration. The possibility of viewing stars as extended objects will enable the testing of many current astrophysical models, and the knowledge acquired will have consequences on many fields related to stellar astrophysics. As a first example consider the measurement of stellar diameters, which can be performed to an accuracy of a few percent with the methods discussed in this paper (see section 4.1). When measuring diameters at different wavelengths, we can learn about the behaviour of the optical depth as a function of the radius of a particular star.[7] This type of measurement becomes particularly useful at shorter wavelengths ($\lambda \sim 400nm$) than those feasible with conventional amplitude (Michelson) interferometry. Another interesting science case is the study of fast rotating stars, for which we can measure oblateness, pole brightening, and disk formation. There is also the study of

* pnunez@physics.utah.edu

interacting binaries. An actual image of an interacting binary will not only aid in the determination of the orbital parameters to a high degree of accuracy, but also in the study and imaging of mass transfer and accretion. Although not rigorously discussed in this paper, imaging mass transfer will improve our understanding of late stellar evolution, i.e. the formation of type II supernovae, which are of great importance in cosmology,[8] and our understanding of the formation of compact objects. The number of interesting science cases and astrophysical targets is overwhelmingly large, and a detailed discussion is given by Dravins et al.[9]

We propose the use of Intensity Interferometry for high angular resolution astronomy (see Holder et. al.[1] for more details). This technique was introduced in the 1950's by R. Hanbury Brown[10,11] and implemented in the 1960's with the Narrabri Stellar Intensity Interferometer,[12] accomplishing the measurement of over thirty stellar diameters. The use of planned air Cherenkov telescope arrays poses a unique opportunity to revive Intensity Interferometry. With hundreds of telescopes separated by up to $\sim 1km$, it will be possible to have an unprecedented coverage of the Fourier plane and thus achieving sub-milliarcsecond resolution.

The most important difference between SII and amplitude interferometry is that SII relies on the correlation between the low frequency intensity fluctuations and so does not rely on the relative phase of the individual waves received at different telescopes. Intensity interferometry measures the squared modulus of the complex degree of coherence $|\gamma|^2$.

$$|\gamma|^2 = \frac{< \Delta I_i \, \Delta I_j >}{< I_i >< I_j >} \tag{1}$$

Here $< I_i >$ is the time average of the intensity received at a particular telescope i, and ΔI_i refers to the low frequency intensity fluctuations received at telescope i. Intensity interferometry has several advantages and disadvantages when compared to amplitude interferometry. The main advantages are that it is insensitive to atmospheric turbulence and that it does not require high optical precision[†]. The complex degree of coherence is proportional to the Fourier transform of the object in the sky (Van Cittert-Zernike theorem), and since we measure the modulus squared of γ, the main disadvantage is that the phase of the Fourier transform is lost in the measurement process, posing difficulties in recovering actual images from magnitude information only. In addition to imaging difficulties, measuring a second order effect also results in sensitivity issues,[1] which can be dealt with by using large light collection areas and exposure times. As for the imaging limitations, several phase retrieval techniques exist, and we will implement a two dimensional version of the one dimensional approach introduced by Holmes & Belen'kii.[6] It is important to note that our results pertain to a single phase recovery algorithm,[6] and a comparison to other algorithms is currently being investigated.[13] Once a sufficient coverage of the Fourier plane is available, and phase recovery is performed, a study on imaging capabilities can be performed. Here we will first concentrate on the study of the uncertainty when reconstructing disk-like stars. Then a less exhaustive analysis on the capabilities is performed for more complicated images such as oblate rotators, binary stars and stars with bright & dark features.

The outline of the paper is the following: First we will briefly discuss the phase retrieval technique. Then we will discuss the simulation of our data and how it will be fitted to an analytic function so that the phase retrieval method can be applied. Finally we will discuss the capabilities for imaging disk-like stars, binary stars and more complicated objects.

2. PHASE RECONSTRUCTION

The objective of phase reconstruction is to recover the phase of the Fourier transform of the image from magnitude information only.[6] The resulting image is then reconstructed up to an arbitrary translation and reflection. It is simpler to first understand phase retrieval in one dimension and then generalize to two dimensions . One possible route towards phase retrieval starts by first approximating the continuous Fourier transform $I(x)$ by

[†]For a more detailed discussion on the advantages of Intensity Interferometry see Hanbury Brown[12]

a discrete one ($I(m\Delta x) = \sum_j \mathcal{O}(j\Delta\theta)e^{ijmk_0\Delta x\Delta\theta}$, where $\mathcal{O}(\theta)$ is the image in the sky and k_0 is the usual wave vector). Then the discrete Fourier transform can be expressed as a magnitude times a phasor ($I(z) = R(z)e^{i\Phi(z)}$ where $z \equiv e^{imk_0\Delta x\Delta\theta}$ is complex). The most important step is then to apply the theory of analytic functions i.e. the Cauchy-Riemann equations[‡]. These relate the phase Φ and the log-magnitude $\ln R$ along the real or imaginary axes. One can show by using the Cauchy-Riemann equations, that the phase differences along the radial direction in the complex plane[§] are directly related to the differences in the logarithm of the magnitude (see Holmes & Belen'kii[6] for more details), so that integrating the Cauchy-Riemann equations directly does not immediately solve for the phase. In other words, phase differences along the purely real or imaginary axes are not available directly from the data.

Since z, the independent variable of the Fourier transform ($z \equiv e^{imk_0\Delta x\Delta\theta}$), has modulus equal to 1, the phase differences that we seek lie along the unit circle in the complex plane. Consequently, the procedure to find the phase consists in first assuming a plausible solution form, then taking differences in the radial direction of the complex plane, and finally fitting the data to the radial differences of the assumed solution. A general form of the phase can be postulated by noting that the phase is a solution of the Laplace equation in the complex plane (applying the Laplacian operator on the phase and using the Cauchy-Riemman equations yields zero). Since the phase differences are known along the radial direction in the complex plane we can take radial differences of the general solution and then fit the log-magnitude differences (available from the data) to the radial differences of the general solution.

One can think of this one-dimensional reconstruction as a the phase estimation along a single slice in the Fourier plane. A generalization to two dimensions can be made by doing the same procedure for several slices. The direction of the slices is arbitrary, however for simplicity we reconstruct the phase along horizontal or vertical slices in the Fourier plane, and noting that one can relate all slices with a single orthogonal slice, i.e. once the phase at the origin is set to zero, the single orthogonal slice sets the initial values for the rest of the slices. The resulting reconstructed phase will be arbitrary up to a constant and a linear term, which corresponds to a translation. It should be noted that the above solution approach gave reasonably good results. However, it is not the only possible approach. We have also investigated Gerchberg-Saxton phase retrieval, Generalized Expectation Maximization, and other variants of the Cauchy-Riemann approach.[13]

3. PROCEDURE

Having briefly discussed the phase reconstruction algorithm, our basic procedure for recovering images is the following: First we simulate realistic data as would be obtained from an air Cherenkov telescope array such as CTA or AGIS. Once simulated data are available, they are fitted to an analytic function so that the phase recovery algorithm can be applied in a more straightforward way. Finally, once the phase is recovered, the inverse Fourier transform will provide us with a reconstructed image. Some details concerning the simulations and data fitting approach now follow.

3.1 Simulation of realistic data and array design used

The simulation of the the data that may be produced by an array of telescopes starts from a pristine image, generally 2048×2048 pixels with an arbitrary dynamic range. The squared magnitude of the Fourier transform of this image is obtained by means of an FFT algorithm and it is normalized so its maximum at zero baseline is equal to one. With a wavelength $\lambda = 400\,nm$, and the full scale of the image typically set to 10 mas, this provides a value for the expected degree of coherence on a square grid with a pitch of $\sim 8.2\,m$ extending over a $\sim 16.8\,km \times 16.8\,km$ area.

The squared Fourier magnitude map is sampled by the set of pairs available in the simulated array. Simulations presented here have been obtained with an array of $N = 97$ telescopes, each with a light collecting

[‡]The C-R equations can be applied because $I(z)$ is a polynomial in z, where $z \equiv e^{i\phi}$.

[§]If ξ is the real axis and ψ is the imaginary axis, then a difference along the radial direction is $\Delta\xi + i\Delta\psi$.

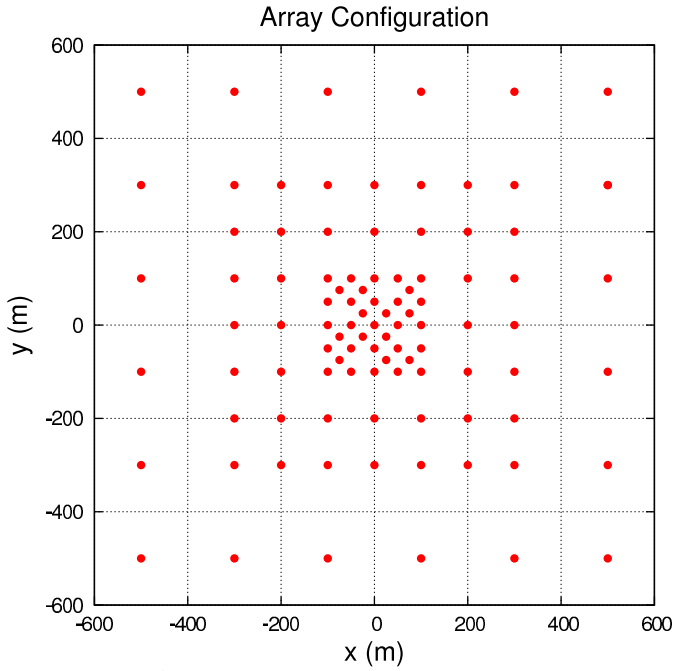

Figure 1. Array configuration used for our analysis.

area of $100\,m^2$ and a quantum efficiency $\alpha = 0.30$ resulting in an effective area of $30\,m^2$. The telescopes are distributed in the field according to an early design of the CTA array shown in figure 2. Such an array provides a coverage of the interferometric (u,v) plane with $N(N-1)/2 = 4656$ baselines many of which are redundant. The baselines are shown in figure 2. The degree of coherence recorded by each baseline is obtained from a linear interpolation between the closest four points in the Fourier magnitude table.

The data recorded by a real array would be affected by the diurnal motion of the observed star which affects the effective baselines by projection. The average correlation must then be recorded for each baseline at time intervals short enough for the baseline change to be negligible. In the first simulation study reported here we have decided to avoid this complication and simulate data that would result from the observation of fixed stars at zenith so the effective baselines used are those shown in figure 2 without any further projective distortion. The implications of this simplification choice are a less uniform sampling of the (u,v) plane compensated by smaller error bars on the degree of coherence from each baseline record. These two effects essentially cancel each other as long as small scale features in the (u,v) plane are not central to the analysis. The benefits from the simplification is a reduction in the volume of data to handle (each simulation produces a single record for each pair of telescopes) and eliminates further arbitrary parameters (such as the site latitude, celestial declination, range of hour angles and time interval between recordings).

Once the degree of correlation within each baseline has been obtained, Gaussian noise is added. The Gaussian nature of the noise was tested with detailed simulation of a pair of photo-multiplier tube signals corresponding to a random stream of photons. The time integrated product of the two traces was Gauss distributed. The magnitude m_V of the star is used to compute a spectral density ($m^{-2}s^{-1}Hz^{-1}$) according to $n = 5 \times 10^{-}5 \times 2.5^{-m_V}$. The standard deviation of the Gaussian noise added to the pair of telescopes (i,j) is calculated as $\sigma = n\sqrt{A_i \cdot A_j \cdot \Delta f \cdot \Delta t/2}$ where A_i is the effective light collection area of the i^{th} telescope, Δf is the signal band-width and Δt is the observation duration. For simulations presented in this paper $\Delta f = 200MHz$ which is a realistic choice when considerations on air Cherenkov telescope optics and electronics are taken into account (See Holder & LeBohec[1] and LeBohec et al.[4]).

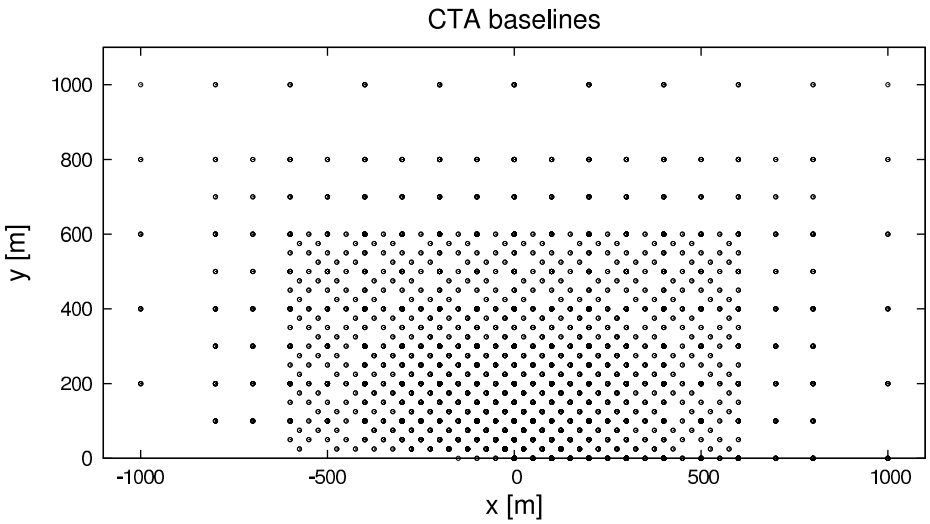

Figure 2. Available baselines for the array design used in this study.

3.2 Fitting the data to an analytic function

The phase reconstruction algorithm is greatly simplified when data are known on a square grid rather than in a 'randomly' sampled way as is directly available from observations. This is because sampling data on a fine square grid enables an easier estimation of the derivatives of the log-magnitude.

Assuming that data $f(x_i)$ are known at positions x_i, with uncertainty $\delta f(x_i)$, our goal is then to find a function that minimizes the following χ^2

$$\chi^2 = \sum_i \left[\frac{(f(x_i) - \sum_k a_k g_k(x_i))}{\delta f(x_i)} \right]^2 . \tag{2}$$

Here, the $a_k{}'s$ are the coefficients of the basis functions g_k that we want to use to fit our simulated data. Any complete basis will suffice in theory, however it is more appropriate to choose a set of basis functions that tend to zero at infinity. The reason for this requirement of our basis functions is so that data are more realistically fitted in regions were there is not much data available. For the case of the CTA array design that we used, we noticed that there is less data at baselines greater than 600 m (see figure 2). We found that basis functions that meet this requirement are the solutions to the two dimensional quantum-mechanical harmonic oscillator, i.e. Hermite polynomials with Gaussian envelopes. These also turn out to be convenient because they are eigenfunctions of the Fourier transform operator.

Now we can turn this problem into a linear system by taking derivatives with respect to the unknowns a_k. Our data fitting typically starts with a small number of basis elements, then we check to see if a certain reduced χ^2 is met (in our case, we chose an acceptable reduced χ^2 to be 1.5), if this condition is not met, then the number of basis elements is increased iteratively until it does.

4. IMAGING CAPABILITIES

We may start by quantifying the resolution of an air Cherenkov telescope array such as the one shown in figure 2 by recalling that quantities that are related to each other by a Fourier transform obey an uncertainty relation. For an order of magnitude estimation it suffices to relate the size of the array to the maximum resolution by

$$\Delta\theta \sim \frac{\lambda}{\Delta x}. \tag{3}$$

With a kilometer size array ($\Delta x \sim 1\,km$), and a wavelength of $\lambda \sim 400nm$ we obtain a resolution of $\Delta\theta \sim 0.1\,mas$. On the other hand, the largest objects observable with an array whose inter-telescope separation is of the order of $\Delta x \sim 50m$ is $\Delta\theta \sim 1\,mas$. These order of magnitude considerations will be taken into account when performing simulations and image reconstructions, i.e. the minimum and maximum size of pristine images will not go far beyond these limits.

We tested the imaging capabilities for simple objects, namely uniform disk-like stars, oblate rotating stars, binaries, and more complex images. First we will concentrate on the capabilities and limitations for reconstructing uniform disk-like stars. We will show that such a preliminary analysis reveals more precisely, when compared to the previous estimate, the sizes of objects that can be observed. Even though using a Cauchy-Riemann based approach to recover images might not be the most efficient way to measure stellar radii, such a study will start to quantify the abilities of measuring other scale parameters in more complicated images (oblateness, distance between binary components, etc.).

4.1 Uniform disks

Simulated data were generated corresponding to uniform disk stars of a particular brightness. We set the brightness to magnitude 6 after noting that an error of a few percent in the simulated data can be achieved in a few hours. Also, 6^{th} magnitude stars are appropriate since they roughly correspond to the upper limit for most of the interesting astrophysical targets found by Dravins et al.[9]

It is interesting to first study the uncertainty for a particular exposure time and a brightness corresponding to 6^{th} magnitude. We simulated data corresponding to uniform disks of random radii up to $1\,mas$ for 50 hours of exposure time. An example of such a reconstruction is shown in figure 3b, where the brightness is shown in arbitrary units between 0 and 1. A first look at the example reconstruction reveals that the edge of the reconstructed disk is not sharp, so a threshold in the brightness was applied for for measuring the radius. The radius was measured by counting pixels above a threshold and noting that the area of the disk is proportional to the number of pixels passing the threshold. After experimenting for different radii, we chose the threshold for measuring the radius to be 0.2. We can now compare the simulated and reconstructed radii as shown in figure 3a, where each point in the figure corresponds to an individual simulation (including noise) and reconstruction.

Figure 3a clearly shows that stellar diameters ranging from 0.05 mas to 0.5 mas can be measured with uncertainties smaller than 5%. The 'tail' seen in the bottom left of figure 3a shows the smallest measurable radius, so we take this radius ($\simeq 0.03\,mas$) to be the point spread function (PSF) of the array. The uncertainty shown in the sub-figure in figure 3 was estimated after running noisy simulations many times as is shown in figure 4.

It can be seen from figure 3a, that the uncertainty increases roughly linearly as a function of the pristine (simulated) radius. This can be understood from the following argument: As the pristine radius decreases, the distance to the first zero in the correlation increases as $\sim r$, so the number of telescopes contained within the Airy disk increases as $\sim r^2$. Consequently, decreasing the pristine radius is equivalent to increasing the number of independent measurements by a factor of $\sim r^2$ at most (at least by a factor of r). Since the uncertainty will decrease as the square root of the number of independent measurements, the error will decrease as $\sim r$ at most. For radii above $0.6\,mas$, there are simply not enough baselines to constrain the Fourier plane information for image reconstruction. For radii greater than $0.6\,mas$, the size of the Airy disk is of the order of $100\,m$, and this results in having less than 100 independent measurements as can be seen in figure 2. Also shown in figure 4 is the percent error as a function of time for two different radii, where it can be seen that a percent error of less than 5% is achieved after only a few hours.

5. COMPLEX IMAGES

Our algorithm has also been tested on more complex images such as oblate rotating stars, binary stars, and stars with brighter or darker regions. Since we have not developed a proper tool for quantitatively comparing

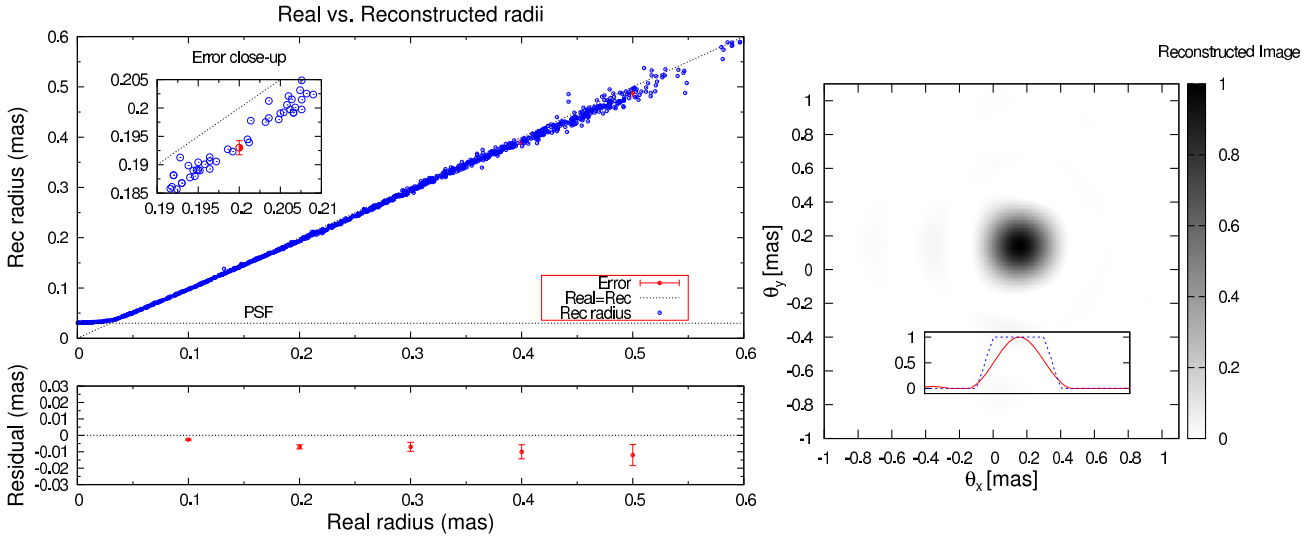

Figure 3. a) Simulated vs. Reconstructed radii for magnitude 6 stars with 50 hours of observation time. The top sub-figure shows the uncertainty for a 0.2 mas measurement. The bottom sub-figure shows the residual (Reconstructed-Real) along with the uncertainty in the radius. b) Example of a reconstructed uniform disk of radius 0.2 mas. Also shown is a slice of the reconstructed image (solid line) compared to a slice of the pristine image (dashed line).

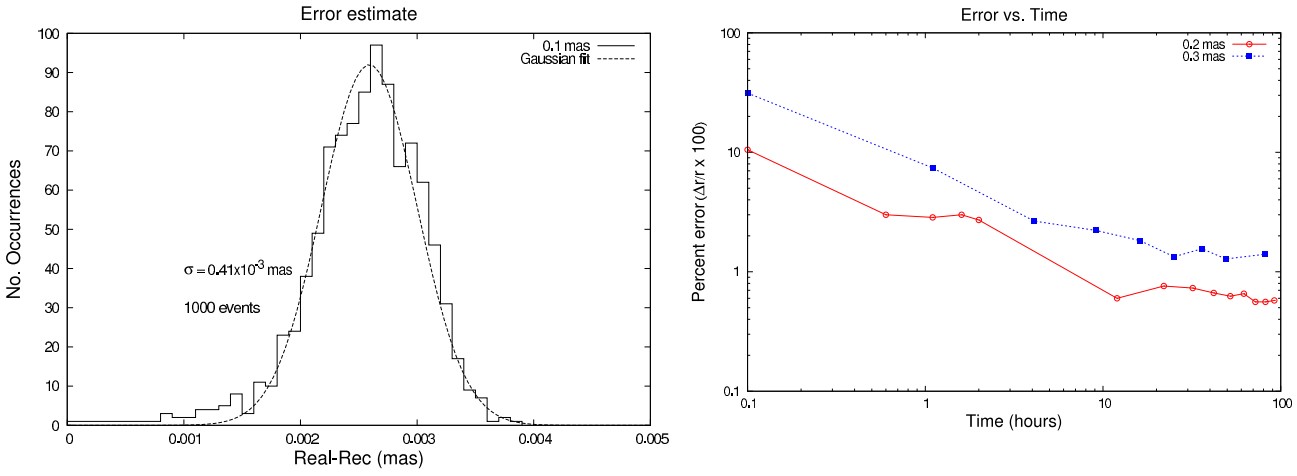

Figure 4. a) Histogram of real radius minus reconstructed radius for 50 hours of exposure time on a 6^{th} magnitude star of 0.2 *mas* radius. b) Percent error as a function of time for several reconstructed radii.

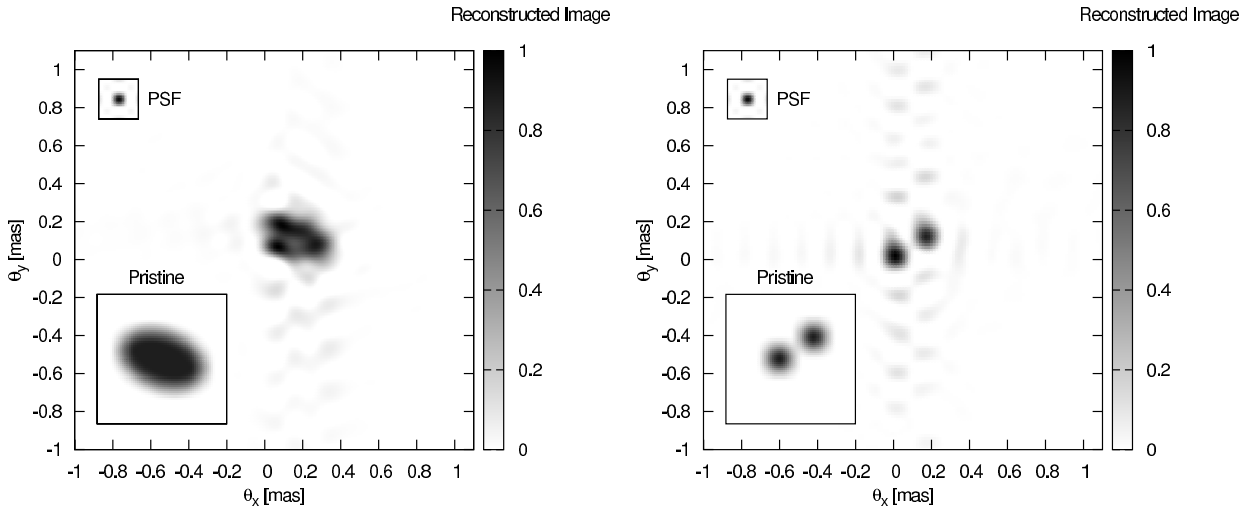

Figure 5. a) Simulated and reconstructed oblate rotator of magnitude 3 and 10 hours of observation time. b) Simulated and reconstructed binary of magnitude 6 and 12 hours of observation time.

simulated and reconstructed images[¶], we will only show a few representative examples of what the algorithm is capable of. Figure 5a shows an example reconstruction of an oblate rotating star of magnitude 3 and 10 hours of observation time, the semi-major axis and semi-minor axis of the pristine ellipse are 0.2 mas and 0.12 mas respectively. Also shown in this figure, and all subsequent ones, is the pristine image convolved with the point spread function of the array (see section 4.1). Reconstructed noise of less than 10% can be seen in the figure. These noise fluctuations are not so much a consequence of noise in the simulated data, but of the reconstruction algorithm itself, and the preferential direction of this reconstructed noise (along the vertical direction) is due to our choice of the slice direction for the phase reconstruction, i.e. the phase was reconstructed by taking horizontal one-dimensional slices of the magnitude, and then related to each other with a single vertical slice. As for the structure (bumps) within the star in figure 5a, these start to appear when either the star becomes bright or enough exposure time is supplied so that information other than the first lobe in the Fourier magnitude is significant. In other words, when high frequency portions are visible in the Fourier magnitude, fictitious structure starts to become visible. This is most likely due to the fact that most of the high frequency information in the Fourier plane is used to reconstruct a dark background of several mas's with a central bright region.

The case of a binary star is shown in figure 5b, corresponding to a magnitude 6 binary star for 12 hours of exposure time. The noise in the reconstructed image has the same origin as in the case of the oblate star. Although the inclination angle was well reconstructed in both cases in figure 5, image reconstruction is degraded when the symmetry axis is neither the x or y axis. Again, this is due to the particular phase recovery method of taking horizontal or vertical slices and the degradation is significantly reduced when aligning one symmetry axis of the magnitude to our x or y axis.

Having this symmetry consideration in mind, a slightly more complicated example is shown in figure 6a, corresponding to a star obscured by a disk (of dust for example). A black streak in the pristine image representing the obscuring disk is aligned with the x axis. The black streak can be easily seen in the reconstruction as well as the contour of the obscured star. This image becomes increasingly easier to reconstruct as the image becomes more and more symmetric, that is, as the black streak in the pristine image moves towards the center

[¶]Since the simulated and reconstructed objects can differ by translations and reflections, developing a tool than can accurately quantify the difference between simulated and reconstructed images is not trivial.

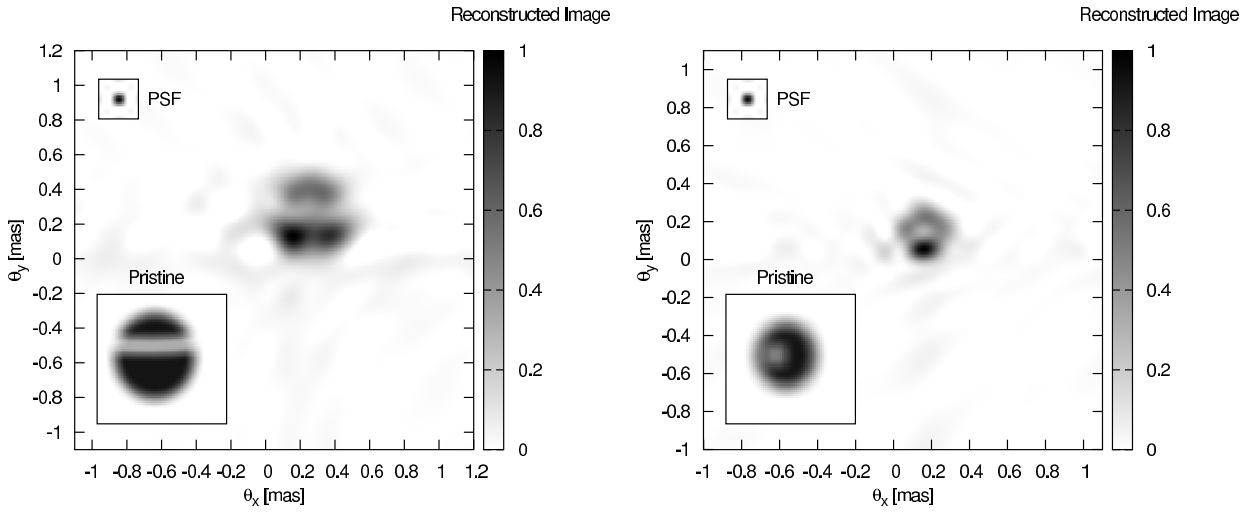

Figure 6. a) Simulated and reconstructed star obscured by a disk. This corresponds to magnitude 4 and 15 hours of observation time. b) Uniform disk of radius 0.2 mas with a dark spot of radius 0.05 mas. The simulation was done for magnitude 6 and 100 hours of observation time.

of the star[‖]. As a final example, we considered the case of a dark spot in a star as shown in figure 6b. The simulation corresponds to a magnitude 6 star and 100 hours of observation. Even though the reconstructed image appears brighter in the bottom, and the location of the spot is more symmetric, the size of the spot (comparable to the PSF) is well reconstructed.

6. CONCLUSION AND OUTLOOK

We have shown that planned air Cherenkov telescope arrays have sufficient baselines to provide an excellent coverage of the (u,v) plane. By first simulating realistic data, we show that it is possible to achieve a signal to noise ratio of the order of 10 within a few hours for relatively faint stars (magnitude 6), and obviously higher S/N for brighter stars. Once data were simulated we also show that imaging is possible using a Cauchy-Riemann[6] phase recovery technique. A study of the error propagation with disk-like stars reveals that the uncertainty in reconstructed radii is of a few percent. We also explored imaging capabilities for more complex images such as oblate rotating stars, binary stars, and stars with dark/bright regions yielding good results. A quantitative analysis of the reconstruction capabilities for complex images is still in progress.

The array design could certainly be improved by including telescopes at shorter distances. This could significantly improve the size range of observable objects, in particular, we could observe objects of more than 1 mas across at 400 nm.

The analysis can also be improved by doing several things: If the pristine object has a symmetry axis, a first reconstruction can be made to find it, and then a second image reconstruction can be made to improve the first results. Something else worth implementing is a first reconstruction only constraining the low frequency components of the phase by using the low frequency part of the magnitude, then a second reconstruction could be performed, only dealing with the internal details of the image.

[‖]This can be understood by noting that the Fourier magnitude of a non symmetric binary becomes almost indistinguishable from the one corresponding to a central bright star with two fainter companions at either side.

To conclude this simulation phase, pristine images generated from astrophysical models should be generated in order to identify how much of the astrophysical model can actually be constrained. This aspect of the simulation phase is currently under development.

Acknowledgements:

This work is supported by grants SGER #0808636 from the National Science Foundation. The work at Lund Observatory is supported by the Swedish Research Council and The Royal Physiographic Society in Lund.

REFERENCES

[1] Holder, J., and LeBohec, S. "Optical intensity interferometry with atmospheric Cerenkov telescope arrays" ApJ 649, 399-405 (2006)

[2] Dravins D, LeBohec S, "Towards a diffraction-limited square-kilometer optical telescope: Digital revival of intensity interferometry" SPIE Proc. 6986, 698609 (2008)

[3] Dravins D., Hagerbo H. O., Lindegren L. et al., "Optical astronomy on milli-, micro-, and nanosecond timescales", Proc SPIE 2198, 289-301 (1994)

[4] LeBohec, S., Adams, B., Bond, I., et al., "Stellar intensity interferometry: Experimental steps toward long-baseline observations", Proc. SPIE 7734, 7734-48 (2010)

[5] Jensen, H., Dravins, D., LeBohec, S. and Nuñez, P.D., "Stellar intensity interferometry: Optimizing air Cherenkov telescope array layouts", Proc. SPIE 7734, 7734-64 (2010)

[6] Holmes R. B. and Belen'kii M. S. "Investigation of the CauchyRiemann equations for one-dimensional image recovery in intensity interferometry", J.Opt.Soc.Am A 21, 697-706 (2004)

[7] Mozurkewich, D., Armstrong, J. T., Hindsley, R. B. et al., " Angular diameters of stars from the Mark III optical interferometer", AJ 126, 2502-2520 (2003)

[8] van Dyk, S. D, "Extragalactic binaries as progenitors of core-collapse supernovae", New Astron. Rev. 48, 749-753 (2004)

[9] Dravins, D., Jensen, H., LeBohec, S. and Nuñez, P. D., "Stellar Intensity Interferometry: Astrophysical targets for sub-milliarcsecond imaging", Proc. SPIE 7734, 7734-9 (2010)

[10] Hanbury Brown, R. and Twiss, R. Q., "Interferometry of the intensity fluctuations in light I. Basic theory: The correlation between photons in coherent beams of radiation", Proc. Roy. Soc. London A 242, 300-324 (1957)

[11] Hanbury Brown, R. and Twiss R. Q., "Interferometry of the intensity fluctuations in light II. An experimental test of the theory for partially coherent light", Proc. Roy. Soc. London A 243, 291-319 (1958)

[12] Hanbury Brown, R., [The Intensity Interferometer], Taylor & Francis, London (1974)

[13] Holmes, R., Nuñez, P. D. and LeBohec, S., "Two-dimensional image recovery in intensity interferometry using the Cauchy-Riemann relations", Proc. SPIE 7818B, 7818B-23, (2010)

Stellar intensity interferometry: Experimental steps toward long-baseline observations

Stephan LeBohec[a]*, Ben Adams[a], Isobel Bond[b], Stella Bradbury[b], Dainis Dravins[c], Hannes Jensen[c], David B. Kieda[a], Derrick Kress[a], Edward Munford[a], Paul D. Nuñez[a], Ryan Price[a], Erez Ribak[d], Joachim Rose[b], Harold Simpson[a], Jeremy Smith[a]

[a] Department of Physics & Astronomy, University of Utah, 115 South 1400 East, Salt Lake City, UT 84112- 0830, USA
[b] School of Physics and Astronomy, E.C. Stoner Building, The University of Leeds, Leeds, LS2 9JT, UK
[c] Lund Observatory, Box 43, SE-22100 Lund, Sweeden.
[d] Physics Department, Technion, Haifa 32000, Israel

ABSTRACT

Experiments are in progress to prepare for intensity interferometry with arrays of air Cherenkov telescopes. At the Bonneville Seabase site, near Salt Lake City, a testbed observatory has been set up with two 3-m air Cherenkov telescopes on a 23-m baseline. Cameras are being constructed, with control electronics for either off- or online analysis of the data. At the Lund Observatory (Sweden), in Technion (Israel) and at the University of Utah (USA), laboratory intensity interferometers simulating stellar observations have been set up and experiments are in progress, using various analog and digital correlators, reaching 1.4 ns time resolution, to analyze signals from pairs of laboratory telescopes.

1. INTRODUCTION

The recent years have seen an increase of interest for the possibility of reviving Stellar Intensity Interferometry (SII), which was pioneered by Robert Hanbury Brown and Richard Twiss who established the technique in 1956.[13] They then exploited[14] it with their colleagues with the Narrabri Stellar Intensity Interferometer (NSII[15]) operated until 1972, after which the technique was abandoned. The present renewed interest draws from a few key ideas. Large baselines ($100\,m$ and more) in the visible band are still challenging for amplitude (Michelson) interferometry while the SII technique is relatively unaffected by poor seeing conditions and large baselines. Several large scale projects including large arrays of large light collectors are currently under development. Technological developments in photo-detection and signal processing since the time of the NSII make it possible to process the high bandwidth signals from a large number of telescopes.

The recent interest for SII induced the formation of a dedicated working group within IAU commission 54[21,23] which had a first meeting in January 2009[25] during which planned imaging atmospheric Cherenkov telescope (IACT) arrays used for very high energy ($E > 100\,GeV$) gamma ray astronomy were identified as the most favorable settings for the deployment of a major Stellar Intensity Interferometer. The working group subsequently contributed to the 2010 Astronomy and

* lebohec@physics.utah.edu

Astrophysics Decadal Survey Astro2010 in the USA with a white paper[3] and a response to a request for information[8] identifying the science potential of a modern version of SII with large telescope arrays as well as technical challenges and options for a successful deployment. This program is now underway as SII gets increasingly integrated in IACT projects in the form of task force groups within the CTA[7] and AGIS[2] collaborations which are planning construction to start in 2013. The recently approved upgrade of the VERITAS gamma ray observatory[30] includes SII in its program and will serve as a test bench for more ambitious SII projects. Efforts are going along four main directions about each of which a report can be found in these proceedings. The science potentials of a modern, large scale SII with imaging capabilities are being better identified and characterized[10] with lists of interesting targets. Imaging possibilities offered by SII are implemented and evaluated[26] using increasingly realistically simulated data. The optimal geometry of telescope arrays to be used as SII is investigated in order to identify and evaluate possible options and compromises that would further improve SII capabilities without being detrimental to the Very High Energy (VHE – $E > 100\,GeV$) observing program.[16] Finally, the present paper is a report on developments concerning the design and testing of various prototypes for the optics, front end electronics and correlation electronics.

This paper is organized as follows. Section 2 gives a brief outline of the principle of intensity interferometry with its capabilities and requirements using IACT arrays. Section 3 presents the telescopes in StarBase which are to be used as a realistic environment testing bed with easy access. Section 4 presents a prototype of secondary optics making SII compatible with VHE instrumentation. Section 5 presents the slow control and front end electronics prototypes under test. Individual photodetector signals are brought to the central recording and correlation station via analog optical fibers. Section 6 presents various correlator options being investigated. This is the critical and most challenging part of an SII as the instantaneous signal to noise ratios are extremely small. Finally section 7 anticipates on the future developments toward the effective deployment and operation of an array of SII receivers.

2. INTENSITY INTERFEROMETRY

Intensity Interferometry relies on the fact that the beating of Fourier components of light results in correlated star light intensity fluctuations in different telescopes. The degree of correlation between the intensity fluctuation δi_1 and δi_2 recorded by two telescopes provides a measurement of the squared mutual coherence, $|\gamma(d)|^2$, of the light at the two telescopes separated by a distance d, which is the square of the normalized magnitude of the Fourier transform of the image.[20] The degree of correlation is obtained by averaging over time the product of the intensity fluctuations (see Equation 1) and the measurement relies on a second order effect implying severe sensitivity limitations which can only be alleviated by using telescopes with very large effective light collecting areas.

$$|\gamma(d)|^2 = \frac{< \delta i_1 \cdot \delta i_2 >}{< i_1 >< i_2 >} \tag{1}$$

However, the intensity fluctuations are of relatively low frequency set by the exploited coherence time and the requirements on optical and mechanical tolerance are much relaxed in comparison to amplitude interferometry. The signal to noise ratio in a single pair of telescopes is given by Equation 2 where A is the light collection area of each telescope, α is the quantum efficiency, n is the spectral density ($m^{-2}s^{-1}Hz^{-1}$), Δf is the intensity fluctuation signal bandwidth and T is the duration of observation.

$$(S/N)_{RMS} = A \cdot \alpha \cdot n(\lambda)|\gamma(d)|^2\sqrt{\Delta f \cdot T/2} = \sqrt{< i_1 >< i_2 >} \cdot |\gamma(d)|^2 \cdot \sqrt{\Delta f \cdot T/2} \tag{2}$$

This equation does not take into account effects such as photo-detector excess noise, night sky background light or partial resolution by individual telescopes.[22] It can however be used to estimate the sensitivity of a realistic pair of telescopes. With $A = 100\,m^2$, $\alpha = 30\%$ and $\Delta f = 100MHz$, a single pair of telescopes used for five hours would provide a five statistical standard deviation detection and measurement of degrees of mutual coherence $|\gamma|^2 = 0.3$ and $|\gamma|^2 = 0.03$ for stars of visual magnitude 4.8 and 2.4 respectively.[8] Crude light collectors composing IACT arrays used for VHE gamma ray astronomy observations are perfectly suited to be used also as SII receivers. VHE gamma ray observations are restricted to low moon light nights during which SII observations could be made through narrow optical passbands. The recent successes in the field of VHE gamma ray astronomy resulted in the ongoing design of much larger arrays counting up to one hundred telescopes which would provide close to five thousand simultaneous baselines[16] ranging from $\sim 50\,m$ to more than $1000\,m$. Such a set of baselines with large telescopes suggests observations of visual magnitude 9 stars with an angular resolution of $50\mu as$ for $\lambda = 400nm$ would be possible. The magnitude limitation is coming from both the practicality of the required observations times ($T < 50\,h$) and from the night sky background signal contamination.[22] The rich coverage of the interferometric plane allows model independent imaging[26] by means of various phase recovery techniques.[17,18]

In order to make it possible to use IACT arrays for SII observations, dedicated instrumentation to measure, communicate, record and correlate the intensity fluctuations at individual telescopes is necessary. The subsequent sections of this paper are dedicated to the ongoing[24] design, construction of testing of prototypes aiming at providing SII capability to the future IACT arrays for which start of constructions is anticipated in the coming three years.

3. THE STAR BASE TELESCOPES

As a first test toward implementing SII with IACT arrays, pairs of 12 m telescopes in the VERITAS array at the Fred Lawrence Whipple Observatory in Arizona were interconnected through digital correlators.[11] These tests were made during parts of nights otherwise shared with VHE observations with a very temporary setup and established the need for a dedicated test bench on which various options of secondary optics and electronics could be evaluated in a realistic environment. In order to satisfy this requirement, the two StarBase[29] telescopes were deployed on the site of the Bonneville Seabase diving resort[6] in Grantsville, Utah, 40 miles west from Salt Lake City. The two telescopes (Figure 1) are on a $23\,m$ East-West base line. The telescopes had earlier been used in the Telescope Array experiment[1] operated until 1998 on the Dugway proving range. Each telescope is a $3\,m$, $f/1$ Davies-Cotton[9] light collector composed of 19 hexagonal mirror facets $\sim 60\,cm$ across. This design is typically used for IACT and secondary optics tested on the StarBase telescopes could be used directly on the VERITAS telescopes for larger scale tests. The telescope mounts are alt-azimuthal with the motion around both axes controlled by tangential screws and absolute encoders with a few arc-seconds resolution. The tracking model parameters are being optimized but the absolute pointing accuracy is better than four arc-minutes and can be compensated by online corrections. This should be compared to the focal plane optical point spread function (PSF) full width at half maximum (FWHM) which is on the order of 0.1°. The PSF is dominated by spherical aberration of individual mirror facets. This is untypical of large Davies-Cotton Cherenkov telescopes for which the PSF FWHM is typically around 0.05°. This difference is due to the facets of the StarBase telescope being much larger in proportion to the telescope diameter than in usual IACTs. For example, the VERITAS telescopes are $12\,m$ in diameter $f/1$ light collectors made of 350 mirror

Figure 1. The StarBase $3\,m$ telescopes are protected by buildings which can be rolled open for observation (left) The control room is located in a smaller building located between the two telescopes. The picture on the right shows a close up view of one telescope before the camera was mounted.

facets $\sim 60\,cm$ across. Interestingly, this lower angular performance of the StarBase light collectors make them ideal test beds for a larger scale implementation of SII as the PSF linear extent measured in the focal plane is very comparable to that in large IACTs such as in VERITAS and the aperture ratio is the same.

4. STELLAR INTENSITY INTERFEROMETRY CAMERAS

The cameras designed for the StarBase telescopes must satisfy two objectives. They must perform as SII cameras providing two channels for zero baseline measurement. They must also demonstrate their compatibility with the VHE Cherenkov camera occupying the focal plane of IACTs. This is achieved by using a large enough mirror making a 45° angle with the telescope optical axis so all the secondary optics is mounted in a plane parallel to the focal plane. The idea is that such a SII camera could simply be mounted in front of the VHE camera or, even better, integrated in the shutter protecting the VHE camera.

The SII camera must collect the light, selecting a narrow optical passband and concentrate it on one or two photodetectors if the zero baseline correlation is to be measured. Interest for narrow optical passbands is two fold. As already seen above, the sensitivity of SII does not depend on optical passband width. For very bright stars, selecting a narrow optical passband preserves the sensitivity while minimizing problems associated with measuring a high photon rate with a high gain photomultiplier tube. For faint stars there is no such need for a narrow passband. However the capability of working with narrow optical passbands will allow measurements through multiple independent optical passbands, thereby improving sensitivity for observations where wavelength dependence is not critical. For example, replacing the beam splitter used to illuminate the two channels with a dichroic mirror would allow the measurement in two different optical passbands simultaneously.

Working with narrow optical passband, say $\Delta\lambda \approx 10\,nm$ typically requires the light to be collimated to within $\sim 5°$. The extent of the PSF measured in the focal plane being $\sim 10\,mm$, this implies using a collimating lens of focal length longer than $\sim 57\,mm$ and since the aperture ratio of the telescopes is unity, the secondary optics need to be of diameter larger than $57\,mm$. This simple estimate does not fully prevent vignetting of some of the point sources in the focal plane, $5\,mm$ from the optical axis so the minimal optics diameter should in fact be set to $67\,mm$. However,

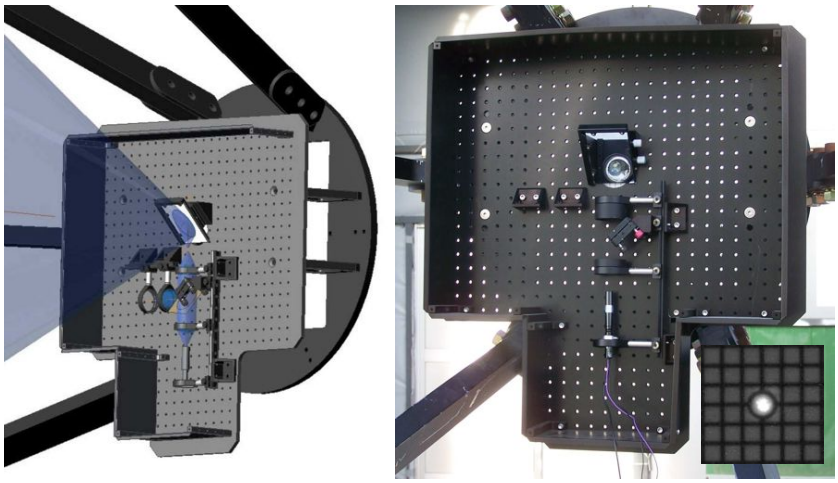

Figure 2. All the optics of the SII camera is mounted on a plate, just above the focal plane of the telescope as shown on the AutoCAD drawing on the left. The light is reflected by a flat mirror at a 45° angle from the optical axis. It is then picked up by a collimating lens on which is mounted an interferometric filter. A beam splitter allows the light to be sent to two independent channels. The light is concentrated onto the photo-detector by an f/1.2 60 mm lens. The electronics can be mounted next to the photo-detectors and on the back of the camera. The actual camera is shown on the right with only one channel in place and no electronics yet. The picture in the lower right corner is an image of the PSF taken while tracking Capella, The grid shows a 1 cm spacing in the focal plane, which corresponds to 0.19°.

and in order to save some of the optics cost, we decided to work with 50 mm optics, setting the focal length of the collimating lens to 37 mm by combining a 100 mm with a 60 mm focal length lens. This results in a collimation within less than 8°. Figure 2 shows an autoCAD drawing of the camera and an actual camera mounted on one of the StarBase telescopes.

5. FRONT END AND SLOW CONTROL ELECTRONICS

The camera electronics consist of two parts. The slow control electronics provide power to the front end, digitize the anode current to monitor the DC light intensity $< i_n >$, provide high voltage to the photo-detector and can be used to program parameters of the front end electronics. The front end electronics convert high frequency intensity fluctuations δi_n down to the single photon level to analog light pulses which can be transported by optical fiber with minimal bandwidth loss over great distances. The optical fiber signals are then converted back to electrical signals which may be correlated at the central control building.

5.1 Slow control electronics

The slow control system is responsible for providing high voltage power to the camera photomultiplier tubes (PMT) as well as capturing the average anode current $< i_n >$. A central microprocessor on the circuit board records the anode current that is optically isolated from the separate capture circuit through a built in ADC. The optical isolation is intended to avoid the injection of correlated noise in the front end electronics. The PMT is powered by an onboard programmable high voltage power supply that is controlled by the microprocessor through a DAC. The circuit also records

the ambient temperature and measures the voltage of its power source. In order to adjust compensation for the temperature sensitivity of the gain of the front end electronics, the slow control system writes to a programmable resistor chip on the front end electronics through a two wire Inter-Integrated Circuit (I^2C) protocol. The anode current, high voltage output, temperature, and power supply voltage data are relayed to a computer using the RS-232 protocol through serial to fiber-optic converters. The graphical software for the slow control board is written in wxPython and can control up to eight boards at a time. The software also records the anode current levels and writes them to a file so their values can be used in the data analysis to obtain measurements of $|\gamma(d)|^2$ by means of Equation 1. In the event that the PMT is exposed to excessive light levels, hardcoded circuit protection shuts off power to the high voltage supply. The slow control system conditions and provides power to the front end electronics. Each channel (two per telescope) is powered by local rechargeable batteries and is only optically connected to the outside of the focal plane instrumentation.

5.2 Front end electronics

Future IACT arrays consisting of several tens of individual reflectors could in principle allow up to a few thousand different baselines. Detectors may be separated by as much as a kilometer, over which distance coherence must be maintained if one is to combine pulses of $3-5\,ns$ FWHM at a centrally located correlator. From Equation 2, we see that the sensitivity for SII observations is proportional to to the square root of the signal bandwidth. Clearly signal transmission via co-axial cable which adds 50% dispersion to the pulse FWHM and perhaps 25% amplitude attenuation over $100\,m$ is not suitable.[24]

The concept of a VCSEL (Vertical Cavity Surface Emitting Laser) based system to transmit undigitized photomultiplier pulses over optical fibre at high bandwidth with minimal attenuation for use in IACTs was proposed by J. Rose.[28] Optical fibres have the additional advantage of immunity to cross-talk and to electromagnetic interference and avoid the difficulty of maintaining a common ground and protection for the receiving electronics against (not uncommon) lightning strikes across the array. They are also relatively lightweight. A 12 channel transmitter of the type tried in the Whipple $10\,m$ telescope weighed 650 g, mainly due to its heatsink, and the weight per channel of the 30 core graded index glass fibre cable used was about a tenth of that of RG59 copper cable.[5] Thus the short-term installation, for interferometric observations in several optical passbands, of a plate carrying secondary optics, photomultipliers and signal transmission electronics in front of an existing IACT camera is conceivable.

The single channel optical fibre signal transmission system being developed in Leeds for deployment between SII instrumentation prototypes is essentially a revision of that described in detail by R.J. White,[31] which was found to give a linear response to within 12% over a dynamic range of 61 dB. In the transmitter, an operational amplifier is used to develop a signal current proportional to the input signal voltage which is then AC coupled to the $850\,nm$ Zarlink ZL60052 VCSEL anode. The bias current supplied to the VCSEL, by a MAX3740A laser-driver chip, can be controlled by the slow control system over an I^2C interface via a DS1859 resistor chip. The DS1859 also monitors temperature and contains a look-up table which can be pre-programmed to maintain a uniform gain by adjusting the bias current in response to the self-heating of the VCSEL. Furthermore, the VCSELs used have been carefully selected from a batch tested for stability in order to avoid the sporadic gain changes observed in the Whipple $10\,m$ telescope system and attributed to laser mode hopping. The signal is communicated via a $62.5\,\mu m$ core, multi-mode optical fibre coupled to a PIN

photodiode based receiver. Both VCSEL and photodiode are encapsulated in E2000 connectors for laser safety.

An RC network and amplifier has been added to the transmitter board to convert the anode DC current to a voltage made available on an RJ45 connector for the slow control system used to provide power, monitoring and control signals. As well as providing the normalization for the measurement of the degree of coherence $|\gamma(d)|^2$, this allows one to record changes in the apparent brightness of a target star due to atmospheric effects and to safely reduce or cut the high voltage supplied to the photomultiplier should stray light flood its field of view. Further additional functionality includes the ability to inject test pulses into the laser-driver to test the link in daylight. The OPA695 amplifier used by R.J. White et al.[31] has been superseded by Analog Devices' AD8000, one of a new generation of amplifiers not previously available, which has a comparable slew rate but a quoted input voltage noise of just $1.6\,nV/\sqrt{Hz}$. Initial laboratory tests show that a photomultiplier pulse rise time of the order of $2ns$ can be well reproduced.

6. CORRELATORS

One of the most critical elements of an SII is the correlator which provides the averaged product of the intensity fluctuations $< \delta i_1 \cdot \delta i_2 >$ to be normalized by the average intensities $< i_1 >$ and $< i_2 >$ provided by the slow control system. Several approaches are investigated in different groups. Different systems are currently being tested in the laboratory at the Lund Observatory, at the University of Utah and in Technion. These laboratory tests also include experimentation with different types of detectors from high quantum efficiency photo-multiplier tubes to single-photon-counting avalanche photodiodes. In these laboratory experiments, an artificial star is provided by an illuminated pinhole at some distance from miniature telescopes whose separation can be varied by moving them on an optical bench perpendicular to the observing direction. Photodetectors and correlators will be further tested on the StarBase telescopes starting summer 2010.

6.1 Analog correlator

At the Technion, a laboratory experiment is set up for testing the applicability of intensity interferometry to space, where large collectors and long base-lines are relatively easier to deploy. Communications between collectors (perhaps on different spacecrafts) might be the bottleneck. In the laboratory, a barely resolvable blue LED is monitored by two Fresnel lenses and photomultiplers. Each photomultiplier current signal is converted to a voltage, and the two voltages are correlated by an analog device (Figure 3). This is a communications RF gain and phase detector, able to reach $2.5\,GHz$. This device serves as a correlator able to find the phase difference between the two inputs. It is operated above $100\,MHz$ because of interference from local radio stations, and below $1\,GHz$ because of detector limitations. The phase signal is found assuming we know approximately the frequency of the inputs, which is of course random. However the frequency is not so important as long as we stay in the zero-phase-difference regime.

For bright objects as encountered in Intensity Interferometry, the Poisson signal is overwhelming, and only deviations from it signify a signal. For example, a 20-bit number of photons will yield a 10-bit Poisson noise. Obviously deviations from Poisson noise on the scale of one or two bits are insufficient, so an even higher signal might be required. This is still difficult to handle with digital electronics, which is why analog processing is the initial choice.

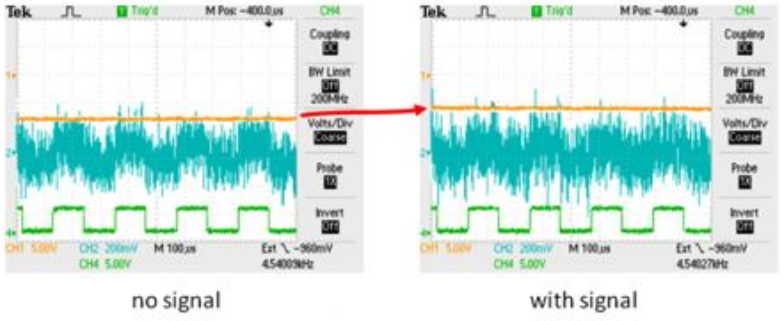

Figure 3. (Left) A modulator at the output of the detector (bottom curve) modulates the signal (middle), and the result is demodulated after the correlator (top). (Right) In the presence of signal, the noise increases, as is obvious from the middle and top curves. This additional noise is actually our correlation output.

At the same time, for the space application, we need to transmit the signals to a central correlator. Here we opted for 8-bit digitizers running at $1\,GHz$, followed by correlation in Field programmable Gate Array (FPGA). This version is now being tested and integrated.

6.2 Digital on-line correlator

A $100\,MHz$ signal bandwidth correlator was designed and constructed at the University of Utah. The two input correlator digitizes the signals into 12 bits at a rate of $200\,MHz$. The digitized signals are collected by an FPGA programmed to provide a $5\,ns$ resolution time delay. In order to obtain a finer control of the relative timing, the FPGA also programs analog delays in st of $0.6\,ns$ up stream for the digitization. After the digital delay, the samples are multiplied and summed up in an accumulation register to obtain the correlation. In order to minimize the effects of offsets and slow drifts, the correlator makes use of a double phase switching. The FPGA controls a programmable periodic phase modulation on both inputs, prior to digitization. The multiplied samples are in fact added or subtracted from the accumulations register in a way that depends on the mutual states of the phase switches do achieve a demodulation of the correlation signal. This system is now fully operational.

6.3 Photon stream correlator

The Narrabri intensity interferometer is often seen as the first experiment in quantum optics, and its subsequent theoretical understanding, together with the development of the laser, led to a number of somewhat analogous applications of light scattering against laboratory specimens[4] It was realized that high-speed photon correlation measurements were required and electronics initially developed in military laboratories were eventually commercialized, first by Malvern Instruments Ltd. in the U.K..[27]

At the Lund Observatory, such digital correlators were acquired and used to pursue experiments for high-speed optical astrophysics, including studies of atmospheric scintillation at the observatory on La Palma.[12] While the first correlators were impressively voluminous rack-mounted units, their electronics have since been miniaturized and current units are very small and easily transportable items, built around FPGAs, accepting many input channels, running at sampling frequencies up to

$700\,MHz$, and with easy USB data transfer to a host computer. It is believed that their electronic performance is now adequate for full intensity interferometry experiments. These have already been used at different observatories, both in searches for high-speed astrophysical phenomena, when connected to the OPTIMA photometric instrument of the Max-Planck-Institute of Extraterrestrial Physics,[19] and also for the first full-scale intensity interferometry experiments with Cherenkov telescopes of the VERITAS array in Arizona.[11]

At present, different correlators (made by the company Correlator.com) are used, with the highest time resolution reaching $1.4\,ns$. The correlators can handle continuous data flows of more than $100\,MHz$ per channel without any deadtimes. Their computer output contains the cross correlation function between the two telescopes (as well as autocorrelation functions for each of them), made up of about a thousand points. For small delays (where most of the intensity interferometry signal resides), the sampling of the correlation functions is made with the smallest timesteps, which increase in a geometric progression to large values to reveal the full function up to long delays of seconds and even minutes. Individual photon events are normally not saved, although that is possible for moderate count rates below about $1\,MHz$. The advantage with such real-time firmware correlators is that they produce correlation functions in real time, and avoid the build-up and storage of huge amounts of photon-count data (e.g., just one of the present correlators, using its 8 input channels, each running at $50\,MHz$ during one 8-hour observing night would process more than $10\,TB$ of photon-count data). Their limitation, of course, is exactly analogous: if something needs to be checked afterwards, the full set of original data is no longer available, and alternative signal processing cannot be applied.

Besides the correlator, another piece of electronics is required for real-time intensity interferometry, namely one to implement the continuously variable time delay from the target star to each telescope, as the star moves across the sky. Since – in contrast to the historic Narrabri interferometer whose telescopes moved on railroad tracks – the locations of Cherenkov telescopes are fixed, there is a need to keep measurements of the target constant within some nanosecond or so, relative to its wavefront. At Lund Observatory, an experimental hardware unit (QVANTOS precision delay) was designed by engineer Bo Nilsson, and verified in the laboratory. This unit enables a continuously variable and programmable delay up to a few μs (corresponding to differential light travel distances of half a km) as applied to a stream of electronic pulses. The pulses are read into a large buffer memory and almost simultaneously read out but then with a slightly different readout frequency, slightly stretching or squeezing the electronic pulsewidths to create the required delay. If such a delay unit is not used, the maximum correlation signal will appear not in the channel for zero time delay between any pair of telescopes, but rather at a delay equal to the light-time difference between telescopes along the line of sight towards the source. In principle, this would be possible to handle already with existing digital correlators since these can be programmed to measure the correlation at full time resolution also at time coordinates away from zero. However, since these delays continuously change as the star moves overhead, such an arrangement would require frequent readouts and might prove not practical for more routine observations.

6.4 Correlation using continuous digitization & software processing

Recent advances in commercial high speed data acquisition has enabled the ability to perform the correlation between the telescope intensity signals entirely in software. Using a National Instruments PXIe-5122 high speed digitizer ($100\,MHz$ sampling, 12 bit resolution, 2 channels), we can continuously digitize the electronic signal stream from each photomultiplier tube. The high speed

backplane of the PXIe mainframe (4 giga-samples per second – Gs/sec) allows the entire data stream to be continuously recorded for several hours onto a high speed RAID disk ($600\,Mb/sec$, NI 6282 Controller + NI 8264 RAID disk) . The data streams from multiple telescopes can then be cross-correlated using a software correlation algorithm, and digital filtering algorithms can be employed to implement narrow-band notch filters to eliminate interference noise from narrow band sources such as cell-phones, motors, computer clocks, etc. This type of systems allows measurement of two-telescope intensity correlations as well as higher order correlations (3 telescopes and higher) which may prove useful for phase recovery.

We are currently testing a two channel continuous digitization stream system built with the above commercial components. The system has demonstrated the ability to stream data continuously to disk for 4 hours at $100\,MHz$ sampling rate (2 channels, 12 bit resolution) without loss of any data. Preliminary FFT studies of the data stream indicate very flat spectral response and only a few very narrow band man-made noise sources. A 2-telescope software correlation algorithm has been developed, and we are currently fine tuning the algorithm to develop optimal sensitivity.

During the summer of 2010, we expect to field test the continuous digization system at the StarBase telescopes. National Instruments is also developing a higher speed continuous streaming digitizer ($500\,MHz$ 8-bit resolution, and $1\,GHz$, 8-bit resolution) which is scheduled to be available during 3Q 2010. The imminent availability of these higher speed commercial digitizers, in conjunction with a substantial reduction in the cost of $10\,Gs/sec$ data transmission using 9/125 single-mode optical fiber may allow a distributed array to stream data from every telescope in an array to a central station for continuous software correlation between every telescope pair in quasi-real time.

The continuous digitization/software correlation approach has strong advantages, including short development time, excellent flexibility and ease of modification, the ability to examine FFT characteristics of each photomultiplier tube, and the ability to look at higher order intensity correlations. These extraordinary advantages are offset by the computational difficulties encountered in handling large (multi TB) data sets. The net result is a very powerful technique which is already strongly competitive with traditional analog and chip-based correlators.

7. OUTLOOK

During the summer of 2010, the camera electronics, front end and slow control should be in place to be tested on the StarBase telescopes so signals will be available for correlation studies using the various techniques available.

Using Equation 2 with conservative parameters for the StarBase telescopes ($A = 6\,m^2$, $\alpha = 0.2$ and $\Delta f = 100\,MHz$), the 5 standard deviation measurement of a degree of coherence $|\gamma(d)|^2 = 0.5$ will require an observation time $T \approx 10\,min \times 2.5^{2V}$ where V represents the visual magnitude and where we have made the crude approximation $n = 5 \times 10^{-5} \times 2.5^{-V} m^{-2} \cdot s^{-1} \cdot Hz^{-1}$. This corresponds to one hour for $V = 1$ and 6.5 hours for V=2 and when considering the measurement of $|\gamma(d)|^2 \approx 1$, these observation times should be divided by four.

The first objective will be the detection of the degree of coherence for an unresolved object ($|\gamma(d)|^2 \approx 1$). The distance between the two telescopes being $23\,m$ (smaller baselines can be obtained during observations to the East and to the West due to the projection effect), at $\lambda = 400\,nm$ the stars have to be smaller than typically $\sim 3\,mas$ in diameter. An essentially unresolved star suitable for calibration should be less than $\sim 1\,mas$ in diameter. Good candidates for this are in increasing order of magnitude $\alpha\,Leo$, $\gamma\,Ori$, $\beta\,Tau$ or even $\eta\,UMa$ which, with a magnitude of 1.76 should

be observable as a unresolved object for calibration within 50 minutes. Alternatively, it will be possible to measure any star as an unresolved object by correlating the signals from two channels mounted on the same telescope by means of the camera beam splitter. These observations should allow to establish methods for adjusting the signal time delays optimally and also to identify the most effective correlator. A next phase will be dedicated to the measurement of a few bright stars in order to further demonstrate the technique. This second phase will possibly include the observation of coherence modulation resulting from orbital motion in the binary star Spica with a $a = 1.5\,mas$ semi major axis and $V = 1.0$, or even, possibly Algol ($a = 2.18\,mas$, $V = 2.1$).

These tests over the coming year or two will be ported to the VERITAS telescopes and will permit to clearly identify all the aspects of a larger scale implementation and converge with confidence toward a practical and effective design of SII instrumentation to be integrated into future IACT arrays such as CTA and AGIS.

8. ACKNOWLEDGEMENT

This work is supported by grants SGER #0808636 from the National Science Foundation. The work at Lund Observatory is supported by the Swedish Research Council and The Royal Physiographic Society in Lund. The authors are grateful to Linda Nelson and George Sanders for hosting the StarBase observatory on the site of the Bonneville Seabase diving resort[6] .

REFERENCES

[1] S. Aiso, M. Chikawa, Y. Hayashi et al., "The detection of TeV gamma rays from the Crab using the Telescope Array prototype", Proc. 25th International Cosmic Ray Conference, Durban, 5, 177-181, (1997)

[2] Advanced Gamma-ray Imaging System (AGIS) home page: http://www.agis-observatory.org

[3] C. Barbieri, M.K. Daniel, W.J. de Wit et al., "New astrophysical opportunities exploiting spatio-temporal optical correlations", Astro2010 white paper, arXiv:0903.0062, (2009)

[4] W. Becker, [Advanced time-correlated single photon counting techniques], Springer, Berlin, (2005)

[5] Bond, I. H.; Bradbury, S. M.; Ogden et al., "Design and performance of analog fiber optics links used on the Whipple 10m Cherenkov telescope", Proceedings of the 27th ICRC, 2904 - 2907, Hamburg, (2001)

[6] Bonneville Seabase Utah web page: http://www.seabase.net

[7] Cherenkov Telescope Array (CTA) home page: http://www.cta-observatory.org

[8] M. Daniel, W.J. de Wit, D. Dravins et al., "Towards the intensity interferometry stellar imaging system", Astro2010 RFI submitted by D. Kieda, arXiv:0906.3276, (2009)

[9] J.M. Davies and E.S. Cotton, "Design of the quartermaster solar furnace", Journal of Solar Energy, 1,16-22, (1957)

[10] D. Dravins, H. Jensen, S. LeBohec and P.D. Nuñez, "Stellar Intensity Interferometry: Astrophysical targets for sub-milliarcsecond imaging", Proc. SPIE 7734, 7734-9, (2010)

[11] D. Dravins and S. LeBohec, "Towards a diffraction-limited square kilometer optical telescope: Digital revival of intensity interferometry", Proc. SPIE 6896, 689609, (2008)

[12] D. Dravins, L. Lindegren, E. Mezey and A.T. Young, "Atmospheric intensity scintillation of stars. I. Statistical distributions and temporal properties", PASP 109, 173-207, (1997)

[13] R. Hanbury Brown and R. Twiss, "A test of a new type of stellar interferometer on Sirius", Nature 178, 1046-1048, (1956)

[14] R. Hanbury Brown, J. Davis and L.R. Allen, "The angular diameters of 32 stars", MNRAS 167, 121-136, (1974)

[15] R. Hanbury Brown, [The Intensity Interferometer, its Application to Astronomy], Taylor & Francis, London, (1974)

[16] H. Jensen, D. Dravins, S. LeBohec and P.D. Nuñez, "Stellar intensity interferometry: Optimizing air Cherenkov telescope array layouts", Proc. SPIE 7734, 7734-64, (2010)

[17] R.B. Holmes and M.S.Belen'kii, "Investigation of the Cauchy-Riemann equations for the one-dimensional image recovery in intensity interferometry" , J.Opt.Soc.Am.A 21,697-706, (2004)

[18] R. B. Holmes, P. D. Nuñez and S. LeBohec, "Two-dimensional image recovery in intensity interferometry using the Cauchy-Riemann relations," Proc. SPIE 7818B, Paper 23., (2010)

[19] G. Kanbach, A. Stefanescu, S. Duscha et al., "OPTIMA: A high time resolution optical photopolarimeter", in D.Phelan, O.Ryan and A.Shearer, eds.: High Time Resolution Astrophysics, Astrophys. Space Sci. Lib. 351, 153-169, Springer, Berlin, (2008)

[20] A. Labeyrie, S.G. Lipson and P.Nisenson, [An Introduction to Optical Stellar Interferometry], Cambridge Univ. Press, Cambridge, (2006)

[21] P.R. Lawson, Optical Long Baseline Interferometry News (OLBIN) web-page: http://olbin.jpl.nasa.gov

[22] S. LeBohec and J.Holder, "Optical intensity interferometry with atmospheric Cherenkov telescope arrays", ApJ 649, 399-405, (2006)

[23] S. LeBohec, C. Barbieri, W.-J. de Wit et al., "Toward a revival of stellar interferometry", Proc. SPIE 7013, 70132B, (2008)

[24] S. LeBohec, M. Daniel, W. J. de Wit et al., "Stellar intensity interferometry with air Cherenkov telescope arrays", AIP Conf. Proc. The Universe et sub-second timescales, 984, 205-215, Ed. D. Phelan, O. Ryan and A. Shearer, (2008)

[25] S. LeBohec, SII working group 2009 meeting: http://www.physics.utah.edu/∼lebohec/SIIWGWS

[26] P. D. Nuñez, S. LeBohec, D.B. Kieda et al., "Stellar intensity interferometry: Imaging capabilities of air Cherenkov telescope arrays", Proc. SPIE 7734, 7734-47 ,2010

[27] E.R. Pike, "The Malvern Correlator: Case study in development", Phys.Technol. 10, 104-109, (1979)

[28] J. Rose, I. Bond, A. Karle et al., "Analog signal transmission for an air Cherenkov photomultiplier camera using optical fibers", Nucl. Instrum. Meth. Phys. A, 442, 113 - 116, (2000)

[29] StarBase telescopes web page: http://www.physics.utah.edu/starbase

[30] Very Energetic Radiation Imaging Telescope Array System (VERITAS) home page: http://veritas.sao.arizona.edu/

[31] R.J. White, J. Rose and S. Bradburry, "A temperature-stable optical link for the transmission of fast analogue signals", Nucl. Instrum. Meth. Phys. A 595, 332 - 338, (2008)

Stellar Intensity Interferometry: Astrophysical targets for sub-milliarcsecond imaging

Dainis Dravins[*a], Hannes Jensen[a], Stephan LeBohec[b], Paul D. Nuñez[b]
[a]Lund Observatory, Box 43, SE-22100 Lund, Sweden
[b]Department of Physics and Astronomy, The University of Utah, 115 South 1400 East, Salt Lake City, UT 84112-0830, U.S.A.

ABSTRACT

Intensity interferometry permits very long optical baselines and the observation of sub-milliarcsecond structures. Using planned kilometric arrays of air Cherenkov telescopes at short wavelengths, intensity interferometry may increase the spatial resolution achieved in optical astronomy by an order of magnitude, inviting detailed studies of the shapes of rapidly rotating hot stars with structures in their circumstellar disks and winds, or mapping out patterns of nonradial pulsations across stellar surfaces. Signal-to-noise in intensity interferometry favors high-temperature sources and emission-line structures, and is independent of the optical passband, be it a single spectral line or the broad spectral continuum. Prime candidate sources have been identified among classes of bright and hot stars. Observations are simulated for telescope configurations envisioned for large Cherenkov facilities, synthesizing numerous optical baselines in software, confirming that resolutions of tens of microarcseconds are feasible for numerous astrophysical targets.

Keywords: Instrumentation: high angular resolution — Instrumentation: interferometers — Stars: individual

1. HIGHEST RESOLUTION IN ASTRONOMY

Science cases for constantly higher angular resolution in astronomy are overwhelming, driving many instrumentation developments. Tantalizing results from current optical interferometers – revealing circumstellar shells or oblate shapes of rapidly rotating stars – show how we are beginning to view stars as a vast diversity of objects, and a great leap forward will be enabled by improving angular resolution by just another order of magnitude. Bright stars have typical sizes of a few milliarcseconds, requiring optical interferometry over hundreds of meters to enable surface imaging. However, phase/amplitude interferometers require precisions to a fraction of an optical wavelength, while atmospheric turbulence makes their operation challenging for baselines much longer than 100 m, and at shorter visual wavelengths.

Together with very long baseline radio interferometry at the shortest radio wavelengths, optical intensity interferometry seems the currently most realistic way to realize astronomical imaging on submilliarcsecond scales (Figure 1). Using a simple λ/D criterion for the required baseline, a resolution of 1 milliarcsecond (mas) at λ 500 nm requires a length around 100 meters, while 1 km enables 100 μas. For the forthcoming large arrays of Cherenkov telescopes, extensions over some 2 km are discussed, and if such could be utilized at λ 350 nm, resolutions could approach 30 μas.

The tantalizing potential of very long baseline optical interferometry has been realized by several[1,2], and proposed concepts include very large optical and ultraviolet phase interferometer arrays placed in space: *Stellar Imager*[3] and the *Luciola* hypertelescope[4], or possibly placed at high-altitude locations in Antarctica[5]. However, the complexity and probable expense of these projects make the timescales for their realization somewhat uncertain.

Compared to ordinary phase interferometry, optical intensity interferometry presents both advantages and challenges. One great advantage is to be practically insensitive to either atmospheric turbulence or to telescope imperfections, enabling very long baselines as well as observing at short optical wavelengths, even through large airmasses far away from zenith. However, it requires large photon count rates (thus large flux collectors), and very fast electronics.

Seemingly ideal flux collectors for this purpose are those air Cherenkov telescopes that are being erected for gamma-ray

* dainis@astro.lu.se ; www.astro.lu.se/~dainis

astronomy. These measure the feeble and brief flashes of Cherenkov light in air produced by cascades of secondary particles initiated by very energetic gamma rays. Time resolution has to be no worse than a few nanoseconds (duration of the Cherenkov light flash); they must be sensitive to short optical wavelengths (Cherenkov light is bluish); they must be large (Cherenkov light is faint), and they must be spread out over hundreds of meters (size of the Cherenkov light-pool onto the ground). Currently planned large arrays: CTA (Cherenkov Telescope Array)[6] or AGIS (Advanced Gamma-ray Imaging System)[7] envision on the order of 50-100 telescopes with various apertures between about 5-25 meters, distributed over at least some square kilometer. For their use as an intensity interferometer, appropriate data analysis software would digitally synthesize very many pairs of baselines between all possible pairs of telescopes[8,9].

Baselines in existing air Cherenkov telescope arrays (CANGAROO, HAGAR, H.E.S.S., MAGIC, PACT, VERITAS, etc.) do not exceed some 200 meters, and their achievable angular resolution largely overlaps with that feasible with existing phase interferometers (although one could observe in the blue or violet, where the contrast of many stellar features is expected to be higher). Experiments in connecting pairs of Cherenkov telescopes for intensity interferometry have already been carried out at VERITAS[10], and although some observations might be made already with existing facilities, any significant leap in optical astronomy will require the planned large arrays. Their use for also intensity interferometry is now part of their respective design studies, and preparatory experimental work is already in progress[11].

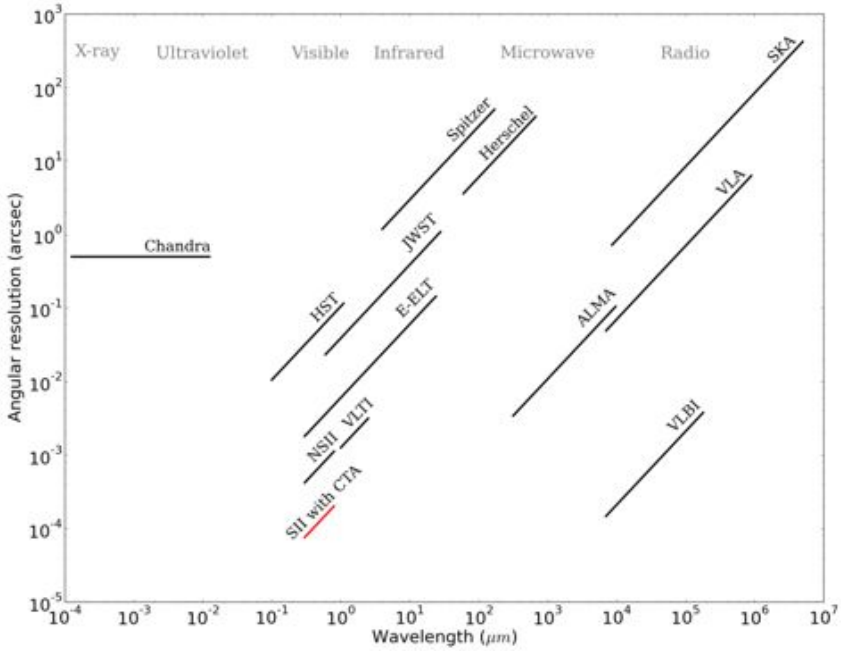

Fig.1. Angular resolution for existing and future observatories at different wavelengths. Except for X-rays, resolutions were taken as diffraction-limited. HST = Hubble Space Telescope; JWST = James Webb Space Telescope; NSII = Narrabri Stellar Intensity Interferometer; E-ELT = European Extremely Large Telescope; VLTI = Very Large Telescope Interferometer; SKA = Square Kilometer Array; VLA = Very Large Array; ALMA = Atacama Large Millimeter Array; VLBI = Very Long Baseline Interferometry (here for a baseline equal to the Earth diameter); CTA = Cherenkov Telescope Array. Stellar intensity interferometry (SII) offers unprecedented angular resolution, challenged only by radio interferometers operating between Earth and deep space.

2. CHOICE OF ASTROPHYSICAL TARGETS

Pushing into microarcsecond domains with kilometric-scale interferometry will require attention not only to optimizing the instrumentation but also to a careful choice of targets to be selected. These must be both astronomically interesting and realistic to observe; discussing such a target selection is the purpose of this paper.

The now historical Narrabri Stellar Intensity Interferometer (NSII) in Australia[12] was primarily used to measure angular diameters of hot and bright stars (indeed, its design parameters with a track of 188 m diameter are said to have been chosen to enable it to spatially resolve the O5 star ζ Puppis). With that instrument, 32 stars brighter than about $m_V = 2.5$

and hotter than $T_{eff} = 7000$ K were measured, producing an effective-temperature scale for early-type stars of spectral types between O5 and F8.

With longer baselines, the scientific aims can be enhanced; stars can be not only spatially resolved but one may start analyzing structures on and around them. However, it is essential to understand what can (and what cannot) realistically be done with intensity interferometry. While the sensitivity of the method has characteristics that make it suitable for observations of hot and small sources at short wavelengths, it is impractical for studying cool or extended sources in the near-infrared. Since the latter is a specialty of phase interferometry, this is a good example of complementarity between both these interferometric methods.

If a source can be studied with either phase-, or intensity interferometry, it should normally be simpler to attain low-noise data from measuring the first-order coherence in phase interferometry. Intensity interferometry should become the method of choice when other methods run into limitations set by atmospheric turbulence.

2.1 Signal-to-noise in intensity interferometry

Intensity interferometry measures the second-order coherence of light, and the noise properties in its measurement are essential to understand for defining realistic observing programs. For one pair of telescopes, the signal-to-noise ratio[12] is *proportional to*:

(1) Effective telescope area
    [geometric mean of the areas (not diameters) of the two telescopes]
(2) Detector quantum efficiency
(3) Square root of the integration time
(4) Square root of the electronic bandwidth
(5) Photon flux per unit optical frequency bandwidth

The first four parameters depend on the instrumentation but (5) is a property of the source itself, a function of its radiation temperature. Thus, for a given number of photons detected per unit time [determined by (1)–(4)], the signal-to-noise ratio is better for sources where those photons are squeezed into a narrower optical passband. This can be understood from a quantum optics point of view: the method is based upon two-photon correlations – more photons inside one optical coherence volume imply a higher probability for detecting two of them simultaneously. Alternatively, from a classical wave-optics point of view, a narrower passband implies a more monochromatic source with a longer coherence time, and smaller loss of temporal coherence during the electronic integration time. A corollary is that the signal-to-noise is *independent of:*

(6) Width of optical passband

The latter property implies that the S/N remains equal, whether observing only the limited light inside a narrow spectral feature or a much greater broad-band flux. Although at first perhaps somewhat counter-intuitive, the explanation is that realistic electronic resolutions of nanoseconds are very much slower than the temporal coherence time of broad-band light (perhaps 10^{-14} s). While narrowing the spectral passband does decrease the photon flux, it also increases the temporal coherence with the same factor, canceling the effects of increased photon noise. This property was exploited already in the Narrabri interferometer by Hanbury Brown et al. to identify the extended emission-line volume from the stellar wind around the Wolf-Rayet star γ^2 Vel.

The dependence on photon flux per unit frequency bandwidth implies that the method is particularly sensitive to hot objects. Only those are feasible targets for kilometric-scale interferometry since a source must not only provide a significant photon flux, but also be small enough for its structures to produce significant visibility over such long baselines (Figure 2). A cool source would have to be large in extent to give a sizeable flux, but then it will be spatially resolved already over short baselines. Seen alternatively, for stars with the same angular diameter but decreasing temperature (thus decreasing fluxes), telescope diameter must successively increase to maintain the same S/N. When the star is resolved by a single mirror, the S/N begins to drop (the spatial coherence of the light decreases), and no gain results from larger mirrors.

Given that the electronic signal bandwidth cannot realistically be higher than about a gigahertz, the temporal coherence of the light is diluted (compared to a hypothetical full time resolution of 10^{-14} s, say), and a significant photon flux is required in order to measure the second-order coherence to a good precision. Calculations, simulations, and extrapolations from work with the Narrabri instrument demonstrate that, for realistic optical and electronic parameters[8], the limiting visual magnitude for a continuum source will be on order $m_V = 9$. This limit is conservative as it could be pushed by employing larger flux collectors, higher signal bandwidth, and/or simultaneously observing in multiple spectral channels. For the present discussion, however, we restrict ourselves to stars brighter than m_V=7.

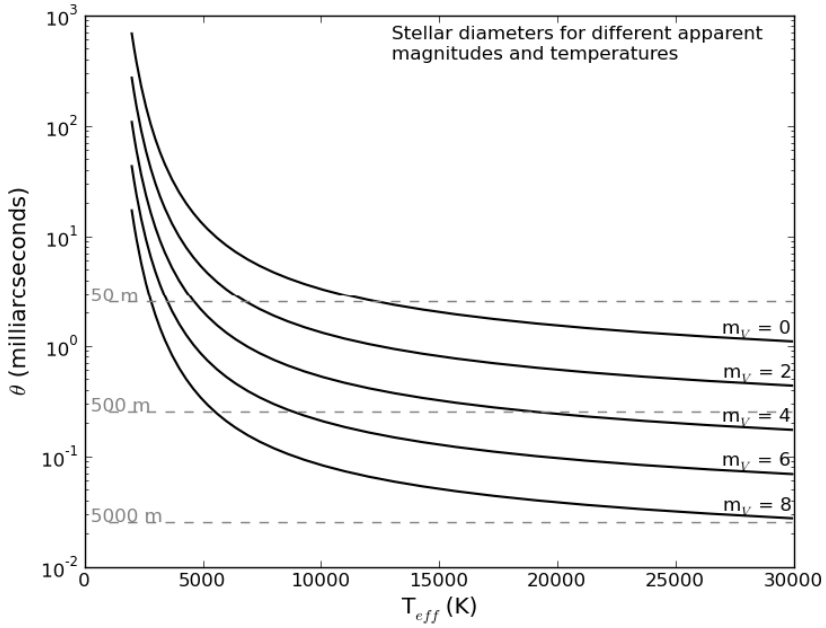

Fig.2. Relationship between stellar diameter and effective temperature for different apparent magnitudes. Stars are assumed to be blackbodies with uniform circular disks, observed in the V band (centered on λ 545 nm). Dashed lines show baselines at which different diameters are resolved, i.e., where the first minimum of the spatial coherence function is reached.

Since the S/N does not depend on the width of the spectral passband, it follows that a source with bright emission lines may be observed in just those lines to enhance the S/N to a level corresponding to the emission-line radiation temperature, while the integrated light from the source could be fainter than those magnitude limits. Already in work preceding the Narrabri intensity interferometer, estimates of possible S/N (using then current instrumental parameters, and integrating for 1 hour) were given by Hanbury Brown and Twiss[13] (their Figure 6) as function of stellar temperature: about 200 for 10,000 K, reaching 1000 for 20,000 K. For any given electronic performance, stars cooler than a certain temperature will not give any sensible signal-to-noise ratio, no matter how bright the star, or how large the telescopes.

In principle, the signal could be enhanced by increasing the electronic bandwidth (up to that of the light itself, of 10^{15} Hz or so), but then one would essentially have re-created a phase/amplitude interferometer with all its requirements to control optical and electronic delays to within 10^{-15} s or less, equivalent to the light-travel distance over a fraction of an optical wavelength, exactly the requirement that intensity interferometry was set out to circumvent in the first place.

With one single pair of telescopes one measures the second-order spatial coherence corresponding to that particular Fourier component of the source intensity distribution which corresponds to the baseline vector between the telescopes, projected along the line of sight to the source and which (for stationary telescopes) gradually changes as the source moves across the sky. While, for a small number of telescopes, the coverage in the two-dimensional Fourier-transform *(u,v)*-plane remains sparse, arrays with *N* telescopes enable *N(N−1)/2* baselines, and the planned large Cherenkov arrays will permit thousands of baselines to be synthesized in software. Not only does this greatly decrease the noise and improve the *(u,v)*-plane coverage but it also enables the stable reconstruction of full two-dimensional images. This could

have been an issue because intensity interferometry provides the *squares* of the amplitudes of the corresponding Fourier-transform components (in contrast to phase interferometry, the phases are not directly obtained). While this does provide information on the sizes of structures in the source, the reconstruction of an actual source image involves certain mathematical operations which become much easier for any more complete coverage of the *(u,v)*-plane[14].

2.2 Hot and bright sources

Primary targets are hot stars brighter than about $m_V = 7$, such as listed among the about 9000 objects of the *Bright Star Catalogue*[15]. Some 2600 objects are both hotter than 9000 K and brighter than $m_V = 7$, among which the brightest and hottest should be those easiest to observe. Table 1 lists such a subset of 35 stars brighter than $m_V = 2$ *or* hotter than $T_{eff} = 25{,}000$ K (effective temperatures were approximated from measured B−V colors, using a polynomial fit to values from Bessel et al.[16]). Naturally, this list of potential targets partially overlaps with those that were selected for diameter measurements already with the Narrabri interferometer[17]; those are marked with asterisks. However, the present list is biased more towards hotter stars, with typically smaller diameters θ, as appropriate for longer baselines.

Table 1. Candidate sources from The Bright Star Catalogue[15]: 35 stars brighter than $m_V = 2$ **or** hotter than $T_{eff} = 25{,}000$ K. Those whose angular diameters were measured already with the Narrabri intensity interferometer[17] are marked with an asterisk (*).

Name	**θ** [mas]	**V**rot [km/s]	**Spectr. class**	**T_{eff}** [K]	**V** [mag]	**Notes**
Achernar, α Eri, HR 472	1.9	250	B3 Ve	15 000	0.46	High Vrot, *
Rigel, β Ori, HR 1713	2.4	30	B8 Iab	9 800	0.12	Emission-line star, supernova candidate, *
λ Lep, HR 1756		70	B0.5 IV	28 000	4.29	
Bellatrix, γ Ori, HR 1790	0.7	60	B2 III	21 300	1.64	Variable, *
Elnath, β Tau = γ Aur [*sic*], HR 1791	1.5	70	B7 III	13 500	1.65	Binary system
υ Ori, HR 1855		20	B0 V	28 000	4.62	Variable
HR 1887, HD 36960		40	B0.5 V	26 000	4.78	Binary system
Alnilam, ε Ori, HR 1903	0.7	90	B0 Iab	18 000	1.7	Emission-line star, *
μ Col, HR 1996		150	O9.5 V	33 000	5.17	
β CMa, HR 2294	0.5	35	B1 II-III	23 000	1.98	β Cep-type variable, *
Alhena, γ Gem, HR 2421	1.4	30	A0 IV	9 100	1.93	*
S Mon, HR 2456		60	O7 Ve	26 000	4.66	Pre-main-sequence
Sirius, α CMa, HR 2491	5.9	10	A1 V	9 100	-1.46	*
EZ CMa, HR 2583			WN4	33 000	6.91	Highly variable W-R star
Adara, ε CMa, HR 2618	0.8	40	B2 Iab	20 000	1.5	Binary, *
Naos, ζ Pup, HR 3165	0.4	210	O5 Ia	28 000	2.25	BY Dra variable, *
γ^2 Vel, HR 3207	0.4		WCv+	21 300 35 000	1.78	Wolf-Rayet binary, WC8 + O7.5, *
β Car, HR 3685	1.5	130	A2 IV	9 100	1.68	*
Regulus, α Leo, HR 3982	1.4	330	B7 V	12 000	1.35	High Vrot,*
η Car, HR 4210	5.0		peculiar	36 000	6.21	Extreme object, variable
Acrux, α^1 Cru, HR 4730		120	B0.5 IV	24 000	1.33	Close binary to α^2 Cru
Acrux, α^2 Cru, HR 4731		200	B1 V	28 000	1.73	Close binary to α^1 Cru
β Cru, HR 4853	0.7	40	B0.5 IV	23 000	1.25	β Cep-type variable, *
ε UMa, HR 4905		40	A0 p	9 500	1.77	α^2 CVn-type variable, chemically peculiar
Spica, α Vir, HR 5056	0.9	160	B1 III-IV	23 000	0.98	β Cep-type variable
Alcaid, η UMa, HR 5191	< 2	200	B3 V	18 000	1.86	Variable
β Cen, HR 5267	0.9	140	B1 III	23 000	0.61	β Cep-type variable
τ Sco, HR 6165		25	B0.2 V	26 000	2.82	
λ Sco, HR 6527		160	B2 IV+	21 000	1.63	β Cep-type variable
Kaus Australis, ε Sgr, HR 6879	1.4	140	B9.5 III	9 800	1.85	Binary, *
Vega, α Lyr, HR 7001	3.2	15	A0 V	9 100	0.03	*
Peacock, α Pav, HR 7790	0.8	40	B2 IV	19 000	1.94	Spectroscopic binary, *
Deneb, α Cyg, HR 7924	2.2	20	A2 Iae	9 300	1.25	Variable
α Gru, HR 8425	1.0	230	B6 V	13 000	1.74	*
Fomalhaut, α PsA, HR 8728	2	100	A4 V	9 300	1.16	With imaged exoplanet, *

2.3 Primary targets

2.3.1. Rapidly rotating stars

Rapidly rotating stars are normally hot and young ones, of spectral types O, B, and A; some are indeed rotating so fast that the effective gravity in their equatorial regions becomes very small and easily enables mass loss or the formation of circumstellar disks. Rapid rotation causes the star itself to become oblate**,** and induces gravity darkening. The von Zeipel theorem[18] states that the radiative flux in a uniformly rotating star is proportional to the local effective gravity and implies that equatorial regions are dimmer, and polar ones brighter. Spectral-line broadening reveals quite a number of early-type stars as rapid rotators and their surface distortion was looked for already with the Narrabri interferometer, but not identified due to then insufficient signal-to-noise levels[19,20].

A number of these have now been studied with phase interferometers. By measuring diameters at different position angles, the rotationally flattened shapes of the stellar disks are determined. For some stars, also their asymmetric brightness distribution across the surface is seen, confirming the expected gravitational darkening and yielding the inclination of the rotational axes. Aperture synthesis has permitted the reconstruction of images using baselines up to some 300 m, corresponding to resolutions of 0.5 mas in the near-infrared H-band around λ 1.7 μm[21].

Two stars illustrate different extremes: Achernar (α Eridani) is a highly deformed Be-star ($V\sin i$ = 250 km/s; > 80 % of critical). Its disk is the flattest so far observed – the major/minor axis ratio being 1.56 (2.53 and 1.62 mas, respectively); and this projected ratio is only a lower value – the actual one could be even more extreme[22]. Further, the rapid rotation of Achernar results in an outer envelope seemingly produced by a stellar wind emanating from the poles[23,24]. There is also a circumstellar disk with Hα-emission, possibly structured around a polar jet[25]. The presence of bright emission lines is especially interesting: since the S/N of an intensity interferometer is independent of the spectral passband, studies in the continuum may be combined with observations centered at an emission line.

Vega (α Lyrae, A0 V) has been one of the most fundamental stars for calibration purposes but its nature has turned out to be quite complex. First, space observations revealed an excess flux in the far infrared, an apparent signature of circumstellar dust. Later, optical phase interferometry showed an enormous (18-fold) drop in intensity at λ 500 nm from stellar disk center to the limb, indicating that Vega is actually a very rapidly rotating star which just happens to be observed nearly pole-on. The true equatorial rotational velocity is estimated to 270 km/s while the projected one is only 22 km/s[26,27]. The effective polar temperature is around 10,000 K, the equatorial only 8,000 K. The difference in predicted ultraviolet flux between such a star seen equator-on, and pole-on, amounts to a factor 5, obviously not a satisfactory state for a star that should have been a fundamental standard.

Predicted classes of not yet observed stars are those that are rotating both rapidly and differentially, i.e. with different angular velocities at different depths or latitudes. Such stars could take on weird shapes, midway between a donut and a sphere[28]. There exist quite a number of hot rapid rotators with diameters of one mas or less, and clearly the angular resolution required to reveal such stellar shapes would be 0.1 mas or better, requiring kilometric-scale interferometry for observations around λ 400 nm.

2.3.2. Be-stars with circumstellar disks

Rapid rotation lowers the effective gravity near the stellar equator which enables centrifugally driven mass loss and the development of circumstellar structures. Be-stars make up a class of rapid rotators with dense equatorial gas disks; the "e" in "Be" denotes the presence of emission in Hα and other lines. Observations indicate the coexistence of a dense equatorial disk with a variable stellar wind at higher latitudes, and the disks may evolve, develop and disappear over timescales of months or years[29].

The detailed mechanisms for producing such disks are not well understood, although the material in these decretion (mass-losing) disks seems to have been ejected from the star rather than accreted from an external medium. The rapid rotation of the central B star certainly plays a role[30]. Some Be-stars show outbursts, where the triggering mechanism is perhaps coupled to non-radial pulsations. Some of their disks have been measured with phase interferometers, e.g., ζ Tau[31,32]. A related group is the B[e] one, where emission is observed in forbidden atomic lines from [Fe II] and other species. A few of those stars are within realistic magnitude limits (e.g., HD 62623 = *l* Pup of m_V=4.0).

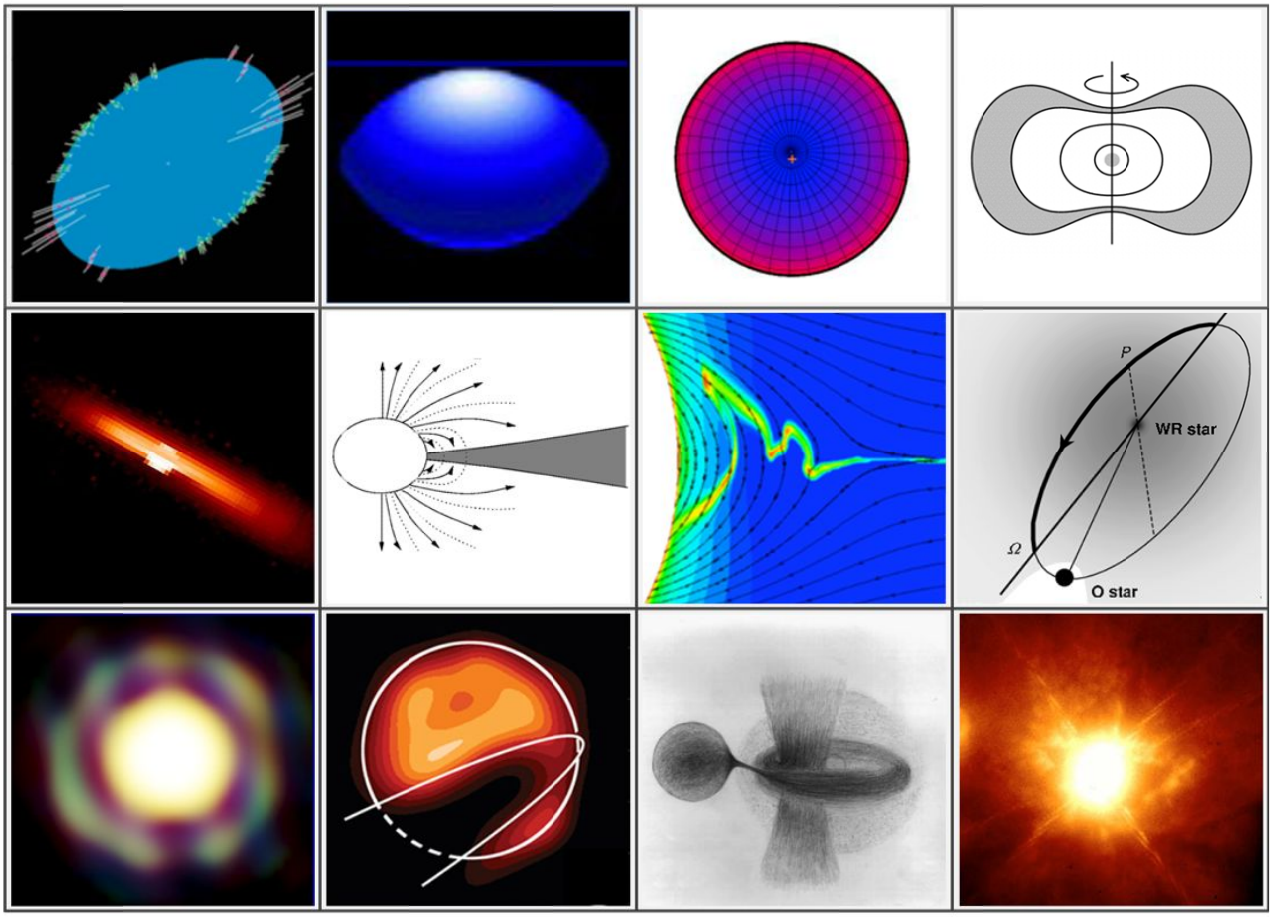

Fig.3. Astrophysical targets for kilometric-scale intensity interferometry. *Top row:* Stellar shapes and surfaces affected by rapid rotation – The measured shape of Achernar[22]; expected equatorial bulge and polar brightening of a very rapid rotator[30]; deduced surface brightness of the rapidly rotating star Vega, seen pole-on[27]; possible donut-shape for a rapidly and differentially rotating star[28]. *Middle row:* Disks and winds – Modeled interferometric image of the circumstellar disk of the Be-star ζ Tauri[32]; a magnetic stellar wind compresses a circumstellar disk[29]; simulation of how stronger magnetic fields distort wind outflow from hot stars[33]; the strongest stellar wind in a binary opens up cavities around the other star: the geometry around the Wolf-Rayet star γ^2 Vel as deduced from interferometry[34]. *Bottom row:* Stellar surroundings – Interferometric image of the giant star T Lep surrounded by its molecular shell[35]; an analogous image of the giant ε Aur, while partially obscured by a circumstellar disk[36]; artist's view of the interacting β Lyr system with a gas stream, accretion disk, jet-like structures and scattering halo[37]; an adaptive-optics, high-resolution image of the mysterious object η Car, the brightest star in the Galaxy[38].

2.3.3. Winds from hot stars

The hottest and most massive stars (O-, B-, and Wolf-Rayet types) have strong and fast stellar winds that are radiatively driven by the strong photospheric flux being absorbed or scattered in spectral lines formed in the denser wind regions. Not surprisingly, their complex time variability is not well understood. Stellar winds can create co-rotating structures in the circumstellar flow in a way quite similar to what is observed in the solar wind. These structures have been suggested as responsible for discrete absorption components observed in ultraviolet P Cygni-type line spectra.

Rapid stellar rotation causes higher temperatures near the stellar poles, and thus a greater radiative force is available there for locally accelerating the wind. In such a case, the result may be a poleward deflection of wind streamlines, resulting in enhanced density and mass flux over the poles and a depletion around the equator (opposite to what one would perhaps "naively" expect in a rapidly rotating star). Surface inhomogeneities such as cooler or hotter starspots

cause the local radiation force over those to differ, leading to locally faster or cooler stellar-wind streamers which may ultimately collide, forming co-rotating interaction regions. Further, effects of magnetic fields are likely to enter and – again analogous to the case of the solar wind – such may well channel the wind flow in complex ways.

2.3.4. Wolf-Rayet stars and their environments

Being the closest and brightest Wolf-Rayet star, and residing in a binary jointly with a hot O-type star, γ^2 Velorum is an outstanding object for studies of circumstellar interactions. The proximity to the O-star causes the dense Wolf-Rayet wind to collide with the less dense but faster O-star wind, generating shocked collision zones, wind-blown cavities and eclipses of spectral lines emitted from a probably clumpy wind[34,39]. The bright emission lines enable studies in different passbands, and already with the Narrabri interferometer, Hanbury Brown et al.[40] could measure how the circumstellar emission region (seen in the C III-IV feature around λ 465 nm) was much more extended than the continuum flux from the stellar photosphere, and seemed to fill much of the Roche lobe between the two components of the binary.

A few other binary Wolf-Rayet stars with colliding winds are bright enough to be realistic targets. One is WR 140 ($m_V = 6.9$), where the hydrodynamic bow shock has been followed with milliarcsecond resolution in the radio, using the Very Long Baseline Array (VLBA), revealing how the bow-shaped shock front rotates as the orbit progresses during its 7.9 yr period[41].

2.3.5. Blue supergiants and related stars

Luminous blue variables occupy positions in the Hertzsprung-Russell diagram adjacent to those of Wolf-Rayet stars, and some of these objects are bright enough to be candidate targets, e.g. P Cyg ($m_V = 4.8$). Luminous blue variables possess powerful stellar winds and are often believed to be the progenitors of nitrogen-rich WR-stars. Rigel (β Orionis; B8 Iab) is the closest blue supergiant (240 pc). It is a very dynamic object with variable absorption/emission lines and oscillations on many different timescales. Actually, the properties of Rigel resemble those of the progenitor to supernova SN1987A.

β Centauri (B1 III) is a visual double star, whose primary component is a spectroscopic binary with two very hot, very massive, pulsating and variable stars in a highly eccentric orbit ($e = 0.82$)[42,43]. Its binary nature was first revealed with the Narrabri interferometer[17], then measuring a significantly lower intensity correlation than expected from a single star. The formation history of such massive and highly eccentric systems is not understood; a few others are known but β Cen is the by far brightest one (also the brightest variable of the β Cep type), and thus a prime target.

The most remarkable luminous blue variable in our part of the Galaxy is η Carinae. This, the most luminous star known in the Galaxy, is an extremely unstable and complex object which has undergone giant eruptions with huge mass ejections during past centuries. The mechanisms behind these eruptions are not understood but, like Rigel, η Car may well be on the verge of exploding as a core-collapse supernova. Interferometric studies reveal asymmetries in the stellar winds with enhanced mass loss along the rotation axis, i.e., from the poles rather than from the equatorial regions, resulting from the enhanced temperature at the poles that develops in rapidly rotating stars[44,45].

2.3.6. Interacting binaries

Numerous stars in close binaries undergo interactions involving mass flow, mass transfer and emission of highly energetic radiation: indeed many of the bright and variable X-ray sources in the sky belong to that category. However, to be a realistic target for intensity interferometry, they must also be optically bright, which typically means B-star systems. One well-studied interacting and eclipsing binary is β Lyrae (Sheliak; $m_V = 3.5$). The system is observed close to edge-on and consists of a B7-type, Roche-lobe filling and mass-losing primary, and an early B-type mass-gaining secondary. This secondary appears to be embedded in a thick accretion disk with a bipolar jet seen in emission lines, causing a light-scattering halo above its poles. The donor star was initially more massive than the secondary, but has now shrunk to about 3 $\mathcal{M}_\odot$, while the accreting star now has reached some 13 $\mathcal{M}_\odot$. The continuing mass transfer causes the 13-day period to increase by about 20 seconds each year[37].

Using the CHARA interferometer with baselines up to 330 m, the β Lyrae system has been resolved in the near-infrared H and K bands[46]. The images resolve both the donor star and the thick disk surrounding the mass gainer, 0.9 mas away. The donor star appears elongated, thus demonstrating the photospheric tidal distortion due to Roche-lobe filling. Numerous other close binaries invite studies of mutual irradiation, tidal distortion, limb darkening, rotational distortion,

gravity darkening, and oscillations. These include Spica (α Vir; m_V =1.0; primary B1 III-IV); the pre-main sequence 15 Mon (S Mon; m_V=4.7; O7 V(f) + O9.5 Vn); HD 193322; m_V=5.8 (primary O9 V); δ Sco (m_V=2.3; primary B0 IVe); δ Ori (m_V=2.2; O9 II + B0 III); and the complex of stars in the Trapezium cluster, e.g., θ^1 Ori C (m_V=5.1; primary O6pe), and others.

Another class of interacting stars is represented by Algol (β Persei; m_V=2.1), a well-known eclipsing binary in a triple system, where the large and bright primary β Per A (B8 V) is regularly eclipsed by the dimmer K-type subgiant β Per B, for several hours every few days. It could appear as a paradox that the more massive β Per A is still on the main sequence, while the presumably coeval but less massive β Per B already has evolved into a subgiant: significant mass transfer must have occurred from the more massive companion and influenced stellar evolution. Algol is also a flaring radio and X-ray source, and analyses of its variability suggest that to be related to magnetic activity. Magnetic fields of the components apparently interact with the mass transfer and the accretion structure. Possibly, not only the cooler (solar-type) star is magnetically active, but magnetic fields are generated also by hydrodynamically driven dynamos inside the accretion structures (circumstellar disks or annuli). The disk and stellar fields interact, with magnetic reconnection causing energy release in flares and acceleration of relativistic particles[47]. As discussed already for Be-type stars, magnetic fields can in addition channel the gas flows in the system and generate quite complex geometries.

3. OBSERVING WITH INTENSITY INTERFEROMETERS

3.1. Observing programs

The most promising targets for early intensity interferometry observations thus appear to be relatively bright and hot, single or binary O-, B-, and WR-type stars with their various circumstellar emission-line structures, as exemplified in Figure 3. The expected diameters of their stellar disks are typically on the order of 0.2–0.5 mas and thus lie [somewhat] beyond what can be resolved with existing phase/amplitude interferometers. However, several of their outer envelopes or disks extend over a few mas and have been resolved with existing facilities, thus confirming their existence and providing valuable information on what types of features to expect when next pushing the resolution by another order of magnitude. Also, when observing at short wavelengths (and comparing to phase interferometer data in the infrared), one will normally observe to a different optical depth in the source, thus beginning to reveal also its three-dimensional structure.

Also some classes of cooler objects are realistic targets. Some rapidly rotating A-type stars of temperatures around 10,000 K should be observable for their photospheric shapes (maybe one could even observe how the projected shapes change with time, as the star moves in its binary orbit, or if the star precesses around its axis?). Stars in the instability strip of the Hertzsprung-Russell diagram, of spectral types around F and temperatures below 7,000 K, undergo various types of pulsations. For example, the classic Cepheid *l* Car (m_V=3.4) was monitored at λ 700 nm with the SUSI interferometer over a 40 m baseline, finding its mean diameter of 3.0 mas to cyclically vary over its 35-day pulsation period with an amplitude of almost 20 %[48].

However, the diameters of such brighter Cepheids (typically 1-3 mas) can be resolved already at modest baselines, and those that would require kilometric baselines are too faint for presently foreseen intensity interferometry. Nevertheless, several such stars are expected to undergo non-radial pulsations, with sections of the stellar surface undulating in higher-order modes. The modulation amplitudes in temperature and white light presumably are modest (not likely to realistically be detectable) but the corresponding velocity fluctuations could perhaps be observed. If the telescope optics permit an adequate collimation of light to enable measurements through a narrow-band spectral filter centered on a stronger absorption line of 50 % residual intensity, say, the local stellar surface will appear at that particular residual intensity (if at rest relative to the observer), but will reach full continuum intensity if the local velocities have Doppler-shifted the absorption line outside the narrow filter passband. If such spatially resolved observation of stellar non-radial oscillations can be realized, they would provide highly significant input to models of stellar atmospheres and interiors[49,50,51].

3.2. Positions of potential targets

Potential sources are distributed over large parts of the sky and permit vigorous observing programs from both northern and southern sites. However, several of the hot and young stars belong to Gould's Belt, an approximately 30 million year old structure in the local Galaxy, sweeping across the constellations of Orion, Canis Major, Carina, Crux, Centaurus, and Scorpius, centered around right ascensions 5-7 hours, not far from the equator. Thus, many primary targets are suitable to observe during northern-hemisphere winter or southern-hemisphere summer. For intensity interferometry, this might be a further advantage in coordinating work with Cherenkov telescopes. Not only can observations be made during full moonlight (when observations of the feeble Cherenkov light induced by gamma rays are problematic), but they can preferentially be made during those parts of the year when it is not possible to observe the many gamma-ray sources near the center of the Galaxy (which is at right ascension 18 hours).

3.3. Simulated observations

Observations of various types of targets have been numerically simulated for telescope configurations envisioned for currently planned facilities. The example in Figure 4 shows an assumed pristine image and simulated observations of the magnitude of its two-dimensional Fourier transform in the interferometric *(u,v)*-plane with an array of Cherenkov telescopes distributed over baselines of up to 2 km between the outermost pairs. The source is a rapidly rotating and rotationally flattened star, ($m_V = 6$; $T_{eff} = 7000$ K), some 0.4 mas across, seen equator-on, with a very thin (10 μas) disk visible in the He I emission line at λ 587 nm, assumed to be six times stronger than the local continuum (a not uncommon value for Be emission-line stars). For an electronic time resolution of 1 ns and a detector quantum efficiency of 70 %, data were assumed to be integrated for 10 hours with a telescope configuration analogous to one being discussed for the Cherenkov Telescope Array.

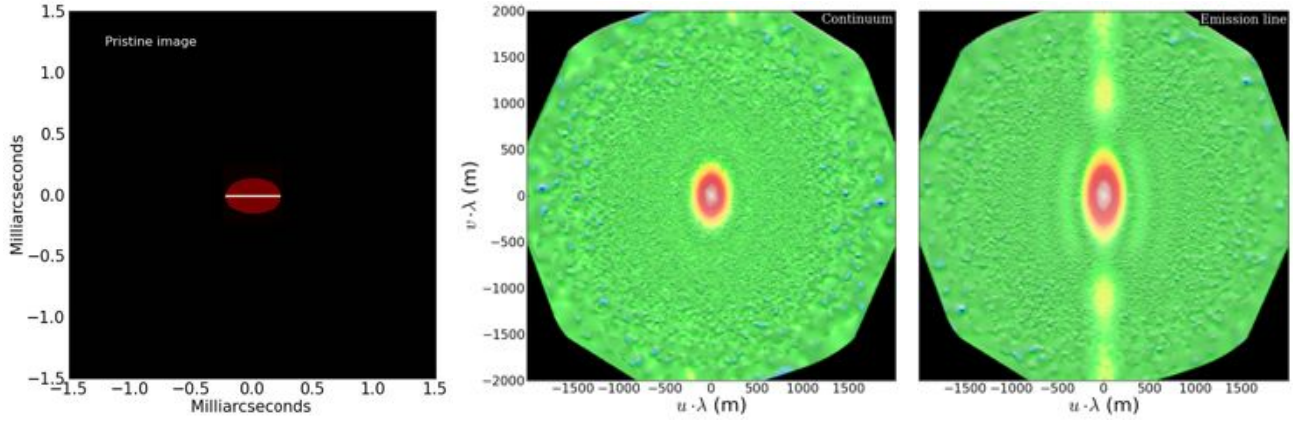

Fig.4. Simulated observations of a rotationally flattened star with an emission-line disk. *Left:* Assumed pristine image. *Center:* Simulated observations of the magnitude of the two-dimensional Fourier transform of the source's intensity distribution in continuum light, as sampled by a large number of telescopes. The flattening of the stellar disk is visible as an asymmetry in the *(u,v)*-plane. *Right:* The same, but for a narrow-bandpass filter centered on the He I emission line, showing the distinct signature of a narrow equatorial disk. The simulated observations were interpolated between measured points, plotted on a logarithmic scale, and with a pseudo-3D shading to better show the geometric patterns in various parts of the *(u,v)*-plane.

The center and right-hand panels illustrate the roles of different baselines: The flattened stellar disk is resolved already by the innermost few-hundred-meter baselines while the signal from the very narrow (10 μas) emission disk clearly continues beyond the assumed longest baselines, and is thus not fully resolved. Although phase information is not directly obtained, such measures of the Fourier transform magnitudes permit the two-dimensional image to be reconstructed[14], confirming the feasibility of submilliarcsecond imaging through intensity interferometry with Cherenkov telescope arrays. More details about such simulations with further examples are presented elsewhere, also illustrating the response of different array layout configurations[52].

Acknowledgements

The work at Lund Observatory is supported by the Swedish Research Council and The Royal Physiographic Society in Lund. S. LeBohec acknowledges support from grants SGER #0808636 of the National Science Foundation.

REFERENCES

[1] Labeyrie, A., "Resolved imaging of extra-solar planets with future 10-100 km optical interferometric arrays", A&AS **118**, 517-524 (1996)
[2] Quirrenbach, A., "Design considerations for an extremely large synthesis array", Proc. SPIE **5491**, 1563-1573 (2004)
[3] Carpenter, K. G., Lyon, R. G., Schrijver, C., Karovska, M. and Mozurkewich, D., "Direct UV/optical imaging of stellar surfaces: The Stellar Imager (SI) vision mission", Proc. SPIE **6687**, 66870G (2007)
[4] Labeyrie, A., Le Coroller, H., Dejonghe, J. et al., "Luciola hypertelescope space observatory: Versatile, upgradable high-resolution imaging, from stars to deep-field cosmology", Exp.Astron. **23**, 463-490 (2009)
[5] Vakili, F., Belu, A., Aristidi, E. et al., "KEOPS: Kiloparsec Explorer for Optical Planet Search, a direct-imaging optical array at Dome C of Antarctica", Bull.Soc Roy.Sci. Liège **74**, 73-78 (2005)
[6] *CTA*: Cherenkov Telescope Array http://www.cta-observatory.org/ (2010)
[7] *AGIS:* Advanced Gamma-ray Imaging System, http://www.agis-observatory.org/ (2010)
[8] Le Bohec, S. and Holder, J., "Optical intensity interferometry with atmospheric Cerenkov telescope arrays", ApJ **649**, 399-405 (2006)
[9] LeBohec, S., Barbieri, C., de Witt, W.-J. et al., "Toward a revival of stellar intensity interferometry", Proc. SPIE **7013**, 70132E (2008)
[10] Dravins, D. and LeBohec, S., "Towards a diffraction-limited square-kilometer optical telescope: Digital revival of intensity interferometry", Proc. SPIE **6986**, 698609 (2008)
[11] LeBohec, S., Adams, B., Bond, I. et al., "Stellar intensity interferometry: Experimental steps toward long-baseline observations", Proc. SPIE **7734**, 7734-48 (2010)
[12] Hanbury Brown, R., [The Intensity Interferometer], Taylor & Francis, London (1974)
[13] Hanbury Brown, R. and Twiss, R. Q., "Interferometry of the intensity fluctuations in light. III. Applications to astronomy", Proc.Roy.Soc. London. Ser.A, Math.Phys.Sci. **248**, 199-221 (1958)
[14] Nuñez, P. D., LeBohec, S., Kieda, D. et al., "Stellar intensity interferometry: Imaging capabilities of air Cherenkov telescope arrays", Proc. SPIE **7734**, 7734-47 (2010)
[15] Hoffleit, D. and Warren, W. H., [Bright Star Catalogue, 5th Revised Ed.], VizieR on-line catalog, http://cdsarc.u-strasbg.fr/ (1995)
[16] Bessell, M. S., Castelli, F. and Plez, B., "Model atmospheres broad-band colors, bolometric corrections and temperature calibrations for O-M stars", A&A **333**, 231-250 (1998); erratum *ibid.* **337**, 321 (1998)
[17] Hanbury Brown, R., Davis, J. and Allen, L. R., "The angular diameters of 32 stars", MNRAS **167**, 121-136 (1974)
[18] von Zeipel, H., "The radiative equilibrium of a rotating system of gaseous masses", MNRAS **84**, 665-683 (1924)
[19] Hanbury Brown, R., Davis, J., Allen, L. R. and Rome, J. M., "The stellar interferometer at Narrabri Observatory-II. The angular diameters of 15 stars", MNRAS **137**, 393-417 (1967)
[20] Johnston, I. D. and Wareing, N. C., "On the possibility of observing interferometrically the surface distortion of rapidly rotating stars", MNRAS **147**, 47-58 (1970)
[21] Zhao, M., Monnier, J. D., Pedretti, E. et al., "Imaging and modeling rapidly rotating stars: α Cephei and α Ophiuchi", ApJ **701**, 209-224 (2009)
[22] Domiciano de Souza, A., Kervella, P., Jankov, S. et al., "The spinning-top Be star Achernar from VLTI-VINCI", A&A **407**, L47-L50 (2003)
[23] Kervella, P. and Domiciano de Souza, A., "The polar wind of the fast rotating Be star Achernar. VINCI/VLTI interferometric observations of an elongated polar envelope", A&A **453**, 1059-1066 (2006)
[24] Kervella, P., Domiciano de Souza, A., Kanaan, S. et al., "The environment of the fast rotating star Achernar. II. Thermal infrared interferometry with VLTI/MIDI", A&A **493**, L53-L56 (2009)
[25] Kanaan, S., Meilland, A., Stee, Ph. et al.,"Disk and wind evolution of Achernar: The breaking of the fellowship", A&A **486**, 785-798 (2008)

[26] Aufdenberg, J. P., Mérand, A., Coudé du Foresto, V. et al., "First results from the CHARA Array. VII. Long-baseline interferometric measurements of Vega consistent with a pole-on, rapidly rotating star", ApJ **645**, 664-675 (2006); erratum *ibid.* **651**, 617 (2006)
[27] Peterson, D. M., Hummel, C. A., Pauls, T. A. et al., "Vega is a rapidly rotating star", Nature, **440**, 896-899 (2006)
[28] MacGregor, K. B., Jackson, S., Skumanich, A. and Metcalfe, T. S., "On the structure and properties of differentially rotating, main-sequence stars in the 1-2 $\mathcal{M}_\odot$ range", ApJ **663**, 560-572 (2007)
[29] Porter, J. M. and Rivinius, T., "Classical Be stars", PASP **115**, 1153-1170 (2003)
[30] Townsend, R. H. D., Owocki, S. P. and Howarth, I. D., "Be-star rotation: How close to critical?", MNRAS **350**, 189-195 (2004)
[31] Gies, D. R., Bagnuolo, W. G., Baines, E. K. et al., "CHARA array K'-band measurements of the angular dimensions of Be star disks", ApJ **654**, 527-543 (2007)
[32] Carciofi, A. C., Okazaki, A. T., Le Bouquin, J.-B. et al., "Cyclic variability of the circumstellar disk of the Be star ζ Tauri. II. Testing the 2D global disk oscillation model", A&A **504**, 915-927 (2009)
[33] ud-Doula, A. and Owocki, S. P., "Dynamical simulations of magnetically channeled line-driven stellar winds. I. Isothermal, nonrotating, radially driven flow", ApJ **576**, 413-428 (2002)
[34] Millour, F., Petrov, R. G., Chesneau, O. et al., "Direct constraint on the distance of γ^2 Velorum from AMBER/VLTI observations", A&A **464**, 107-118 (2007)
[35] Le Bouquin, J.-B., Millour, F., Merand, A., and VLTI Science Operations Team, "First Images from the VLT Interferometer", ESO Messenger 137, 25-29 (2009)
[36] Kloppenborg, B., Stencel, R., Monnier, J.D. et al., "Infrared images of the transiting disk in the Aurigae system", Nature **464**, 870-872 (2010)
[37] Harmanec, P., "The ever challenging emission-line binary β Lyrae", Astron.Nachr. **323**, 87-98 (2002)
[38] European Southern Observatory press release eso0313, "Sharper and deeper views with MACAO-VLTI", http://www.eso.org/public/news/eso0313/ (2003)
[39] North, J. R., Tuthill, P. G., Tango, W. J. and Davis, J., "γ^2 Velorum: Orbital solution and fundamental parameter determination with SUSI", MNRAS **377**, 415-424 (2007)
[40] Hanbury Brown, R., Davis, J., Herbison-Evans, D. and Allen, L. R., "A study of γ^2 Velorum with a stellar intensity interferometer", MNRAS **148**, 103-117 (1970)
[41] Dougherty, S. M., Beasley, A. J., Claussen, M. J. et al., "High-resolution radio observations of the colliding-wind binary WR 140", ApJ **623**, 447-459 (2005)
[42] Ausseloos, M., Aerts, C., Uytterhoeven, K. et al., "β Centauri: An eccentric binary with two β Cep-type components", A&A **384**, 209-214 (2002)
[43] Davis, J., Mendez, A., Seneta, E. B. et al., "Orbital parameters, masses and distance to β Centauri determined with the Sydney University Stellar Interferometer and high-resolution spectroscopy", MNRAS **356**, 1362-1370 (2005)
[44] van Boekel, R., Kervella, P., Schöller, M. et al., "Direct measurement of the size and shape of the present-day stellar wind of η Carinae", A&A **410**, L37–L40 (2003)
[45] Weigelt, G., Kraus, S., Driebe, T. et al., "Near-infrared interferometry of η Carinae with spectral resolutions of 1500 and 12000 using AMBER/VLTI", A&A **464**, 87-106 (2007)
[46] Zhao, M., Gies, D., Monnier, J. D. et al., "First resolved images of the eclipsing and interacting binary β Lyrae", ApJ **684**, L95-L98 (2008)
[47] Retter, A., Richards, M. T. and Wu, K., "Evidence for superhumps in the radio light curve of Algol and a new model for magnetic activity in Algol systems", ApJ **621**, 417-424 (2005)
[48] Davis, J., Jacob, A. P., Robertson, J. G. et al., "Observations of the pulsation of the Cepheid *l* Car with the Sydney University Stellar Interferometer", MNRAS **394**, 1620-1630 (2009)
[49] Jankov, S., Vakili, F., Domiciano de Souza, A. and Janot-Pacheco, E., "Interferometric-Doppler imaging of stellar surface structure", A&A **377**, 721-734 (2001)
[50] Schmider, F.-X., Jankov, S., Vakili, F. et al., "Impact of next generation interferometers on asteroseismology", Bull.Soc.Roy.Sci. Liège **74**, 115-131 (2005)
[51] Cunha, M. S., Aerts, C., Christensen-Dalsgaard, J. et al., "Asteroseismology and interferometry", A&ARv **14**, 217-360 (2007)
[52] Jensen, H., Dravins, D., LeBohec, S. and Nuñez, P.D., "Stellar intensity interferometry: Optimizing air Cherenkov telescope array layouts", Proc. SPIE **7734**, 7734-64 (2010)